



Politecnico di Bari

Repository Istituzionale dei Prodotti della Ricerca del Politecnico di Bari

Investigating the feasibility of using Sentinel-1 data to determine the damage state of Ukrainian territory
= Indagare sulla fattibilità dell'utilizzo dei dati

This is a PhD Thesis

Original Citation:

Availability:

This version is available at <http://hdl.handle.net/11589/252080> since: 2023-04-26

Published version

DOI:10.60576/poliba/iris/caporusso-giacomo_phd2023

Publisher: Politecnico di Bari

Terms of use:

(Article begins on next page)



LIBERATORIA PER L'ARCHIVIAZIONE DELLA TESI DI DOTTORATO

Al Magnifico Rettore
del Politecnico di Bari

Il sottoscritto Giacomo Caporusso nato a Barletta il 18/07/1982 residente a Barletta in via Vito Antonio Lattanzio 1/B e-mail giacomo.caporusso@poliba.it iscritto al 3° anno di Corso di Dottorato di Ricerca in Rischio e Sviluppo Ambientale, Territoriale ed Edilizio ciclo XXXV ed essendo stato ammesso a sostenere l'esame finale con la prevista discussione della tesi dal titolo: "Investigating the feasibility of using Sentinel-1 data to determine the damage state of Ukrainian territory."

DICHIARA

- 1) di essere consapevole che, ai sensi del D.P.R. n. 445 del 28.12.2000, le dichiarazioni mendaci, la falsità negli atti e l'uso di atti falsi sono puniti ai sensi del codice penale e delle Leggi speciali in materia, e che nel caso ricorrero dette ipotesi, decade fin dall'inizio e senza necessità di nessuna formalità dai benefici conseguenti al provvedimento emanato sulla base di tali dichiarazioni;
- 2) di essere iscritto al Corso di Dottorato di ricerca in Rischio e Sviluppo Ambientale, Territoriale ed Edilizio ciclo XXXV, corso attivato ai sensi del "Regolamento dei Corsi di Dottorato di ricerca del Politecnico di Bari", emanato con D.R. n.286 del 01.07.2013;
- 3) di essere pienamente a conoscenza delle disposizioni contenute nel predetto Regolamento in merito alla procedura di deposito, pubblicazione e autoarchiviazione della tesi di dottorato nell'Archivio Istituzionale ad accesso aperto alla letteratura scientifica;
- 4) di essere consapevole che attraverso l'autoarchiviazione delle tesi nell'Archivio Istituzionale ad accesso aperto alla letteratura scientifica del Politecnico di Bari (IRIS-POLIBA), l'Ateneo archiverà e renderà consultabile in rete (nel rispetto della Policy di Ateneo di cui al D.R. 642 del 13.11.2015) il testo completo della tesi di dottorato, fatta salva la possibilità di sottoscrizione di apposite licenze per le relative condizioni di utilizzo (di cui al sito <http://www.creativecommons.it/Licenze>), e fatte salve, altresì, le eventuali esigenze di "embargo", legate a strette considerazioni sulla tutelabilità e sfruttamento industriale/commerciale dei contenuti della tesi, da rappresentarsi mediante compilazione e sottoscrizione del modulo in calce (Richiesta di embargo);
- 5) che la tesi da depositare in IRIS-POLIBA, in formato digitale (PDF/A) sarà del tutto identica a quelle **consegnate**/inviolate/inviati da inviarsi ai componenti della commissione per l'esame finale e a qualsiasi altra copia depositata presso gli Uffici del Politecnico di Bari in forma cartacea o digitale, ovvero a quella da discutere in sede di esame finale, a quella da depositare, a cura dell'Ateneo, presso le Biblioteche Nazionali Centrali di Roma e Firenze e presso tutti gli Uffici competenti per legge al momento del deposito stesso, e che di conseguenza va esclusa qualsiasi responsabilità del Politecnico di Bari per quanto riguarda eventuali errori, imprecisioni o omissioni nei contenuti della tesi;
- 6) che il contenuto e l'organizzazione della tesi è opera originale realizzata dal sottoscritto e non compromette in alcun modo i diritti di terzi, ivi compresi quelli relativi alla sicurezza dei dati personali; che pertanto il Politecnico di Bari ed i suoi funzionari sono in ogni caso esenti da responsabilità di qualsivoglia natura: civile, amministrativa e penale e saranno dal sottoscritto tenuti indenni da qualsiasi richiesta o rivendicazione da parte di terzi;
- 7) che il contenuto della tesi non infrange in alcun modo il diritto d'Autore né gli obblighi connessi alla salvaguardia di diritti morali ed economici di altri autori o di altri aventi diritto, sia per testi, immagini, foto, tabelle, o altre parti di cui la tesi è composta.

Luogo e data: Bari, 26/04/2023

Firma

Il sottoscritto, con l'autoarchiviazione della propria tesi di dottorato nell'Archivio Istituzionale ad accesso aperto del Politecnico di Bari (POLIBA-IRIS), pur mantenendo su di essa tutti i diritti d'autore, morali ed economici, ai sensi della normativa vigente (Legge 633/1941 e ss.mm.ii.),

CONCEDE

- al Politecnico di Bari il permesso di trasferire l'opera su qualsiasi supporto e di convertirla in qualsiasi formato al fine di una corretta conservazione nel tempo. Il Politecnico di Bari garantisce che non verrà effettuata alcuna modifica al contenuto e alla struttura dell'opera.
- al Politecnico di Bari la possibilità di riprodurre l'opera in più di una copia per fini di sicurezza, back-up e conservazione.

Luogo e data: Bari, 26/04/2023

Firma



D.R.S.S.

POLITECNICO DI BARI

05

Doctor of Philosophy in Environmental
and Building Risk and Development

2023

Coordinator: Prof. Michele Mossa

XXXV CYCLE
Curriculum ICAR/06 – Topography and
Cartography

DICATECh

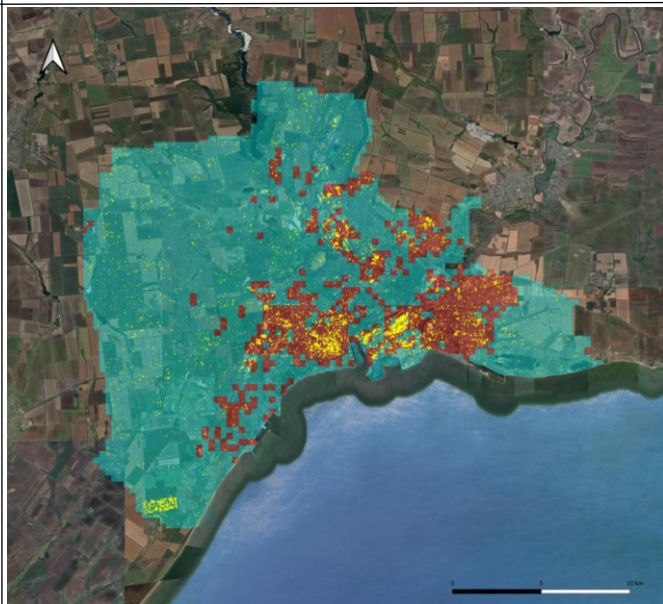
Department of Civil, Environmental, Building
Engineering and Chemistry

Giacomo Caporusso

**Investigating the feasibility of using Sentinel-1
data to determine the damage state of
Ukrainian territory.**

Prof. Eufemia Tarantino
DICATECh
Politecnico di Bari

Dr. Ir. Alessandra Capolupo, Ph.D.
DICATECh
Politecnico di Bari





D.R.S.S.

POLITECNICO DI BARI

05

Dottorato di Ricerca in Rischio e Sviluppo Ambientale, Territoriale ed Edilizio

2023

Coordinatore: Prof. Michele Mossa

XXXV CICLO
Curriculum ICAR/06 – Topografia e Cartografia

DICATECh

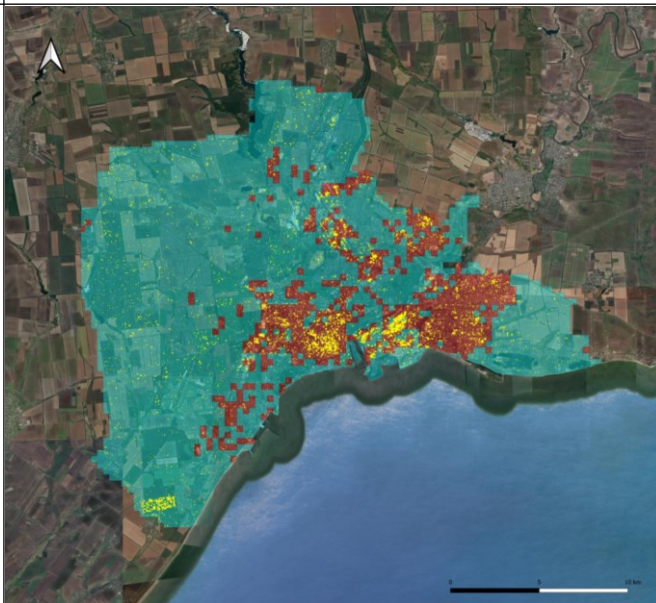
Dipartimento di Ingegneria Civile, Ambientale, Edile e Chimica

Giacomo Caporusso

Indagare sulla fattibilità dell'utilizzo dei dati Sentinel-1 per determinare lo stato di danneggiamento del territorio Ucraino.

Prof. Eufemia Tarantino
DICATECh
Politecnico di Bari

Dr. Ir. Alessandra Capolupo, Ph.D.
DICATECh
Politecnico di Bari



EXTENDED ABSTRACT (eng)

Since February 24, 2022, the Ukrainian population and territory have been exposed to warlike events that have resulted in victims, destruction, and severe consequences on the European and international levels. Unfortunately, it will not be feasible to resurrect any of the victims, but it will most likely be possible to act in order to recover the damaged or completely destroyed buildings, infrastructures, and parts of urban realities. These interventions necessitate an assessment of the damaged areas in order to plan and fund the necessary actions in an acceptable manner. The maps produced by the United Nations Satellite Center (UNOSAT), part of the United Nations Institute for Training and Research (UNITAR), prove to be a useful support given the very high spatial resolution of the WorldView-3 satellite images to which they refer, which can reach 30cm of spatial resolution. However, these maps derive from rapid photo-interpretation operations mainly affected by human errors and involve economic costs. Research in the field of Remote Sensing therefore attempts to obtain damage maps using free images and innovative algorithms based on the use of classification indexes often compared with UNOSAT sources. The thesis work tries to respond to this general objective by using free Sentinel-1 high-resolution data derived from Synthetic Aperture Radar (SAR) sensors to create the damage maps in the context of the war in Ukraine taking as reference the UNOSAT maps. The choice of this imagery is appropriate since the average spatial resolution of 10m can be compared with the footprints of urban buildings and SAR technology, through the use of microwaves, allows for investigation the territory both during the day and night and in any weather conditions. The work examines three different sites in terms of extension, urban density, geographical position and concentration of damaged areas: the set of areas west of Kyviv, Mariupol and Chernihiv. The effectiveness of 3 polarimetric indices, 6 coherence indices and 6 intensity indices is examined, trying to achieve the secondary objective of identifying the element capable of discriminating the damaged from the undamaged

in the best way. A new element in the specific field of damage analysis is represented by the idea of considering the definition of the coherence and intensity indices in a series of 15 calculation boxes increasing around the reference pixel. As a result, 183 rasters data were created for each study area, for a total of 549 rasters data evaluated. The examination of the polarimetric variables largely proved what is frequently stated in the literature about the inadequacy of Sentinel-1 data of the dual-pol type to fully characterize the scatterometric behavior of the investigated surfaces. The relevance of the information content was reduced in each of the three series of rasters data consisting of coherence and polarimetric variables by controlling the signal to noise ratio (SNR). The subsequent analysis of the principal components applied to the residual rasters of the SNR control enabled the generation of damage maps relating to the first principal component with an overall accuracy greater than 75% and to identify the RC VH index defined in the fourth calculation window as the best damaged/undamaged discriminant from a qualitative and quantitative point of view. Some inconsistencies with respect to the accuracy of the UNOSAT sources found in the union of maps of the area west of Kyviv in which elements simultaneously classified as damaged and undamaged were detected, leaving some room for debate about the certainty attributed to the sources comparison of this work and others of its kind.

Key Words: Ukraine, War Damage, Sentinel-1, UNOSAT, Polarimetry, Coherence, Intensity, SNR, PCA, QGIS, SNAP, R Studio, CATALYST.

EXTENDED ABSTRACT (ita)

Dal 24 febbraio 2022 la popolazione e il territorio ucraini sono stati esposti a eventi bellici che hanno provocato vittime, distruzioni e gravi conseguenze a livello europeo e internazionale. Purtroppo, non sarà possibile resuscitare nessuna delle vittime, ma molto probabilmente sarà possibile agire per recuperare gli edifici, le infrastrutture e le parti delle realtà urbane danneggiate o completamente distrutte. Tali interventi necessitano di una valutazione delle aree danneggiate al fine di programmare e finanziare in maniera accettabile gli interventi necessari. Le mappe prodotte dal Centro Satellitare delle Nazioni Unite (UNOSAT), parte dell'Istituto delle Nazioni Unite per la Formazione e la Ricerca (UNITAR), si rivelano un utile supporto data l'altissima risoluzione spaziale delle immagini satellitari WorldView-3 a cui si riferiscono, che può raggiungere i 30 cm. Tuttavia, queste mappe derivano da rapide operazioni di fotointerpretazione affette principalmente da errori umani e comportano costi economici. La ricerca nel campo del Telerilevamento cerca quindi di ottenere mappe di danno utilizzando immagini libere e algoritmi innovativi basati sull'utilizzo di indici di classificazione spesso confrontati con fonti UNOSAT. Il lavoro di tesi cerca di rispondere a questo obiettivo generale utilizzando i dati gratuiti Sentinel-1 ad alta risoluzione derivati dai sensori radar ad apertura sintetica (SAR) per creare le mappe dei danni nel contesto della guerra in Ucraina prendendo come riferimento le mappe UNOSAT. La scelta di queste immagini è opportuna in quanto la risoluzione spaziale media di 10m può essere confrontata con le impronte degli edifici urbani e la tecnologia SAR, attraverso l'uso delle microonde, consente di indagare il territorio sia di giorno che di notte e con qualsiasi condizione atmosferica. Il lavoro prende in esame tre diversi siti in termini di estensione, densità urbana, posizione geografica e concentrazione delle aree danneggiate: l'insieme delle aree ad ovest di Kyviv, Mariupol e Chernihiv. Viene esaminata l'efficacia di 3 indici polarimetrici, 6 indici di coerenza e 6 indici di intensità, cercando di raggiungere l'obiettivo secondario di individuare l'elemento in grado di

discriminare al meglio il danneggiato dall'intero. Un elemento nuovo nello specifico campo dell'analisi del danno è rappresentato dall'idea di considerare la definizione degli indici di coerenza e di intensità in una serie di 15 finestre di calcolo crescenti intorno al pixel di riferimento. Di conseguenza, sono stati creati 183 dati raster per ciascuna area di studio, per un totale di 549 dati raster valutati. L'esame delle variabili polarimetriche ha ampiamente dimostrato quanto spesso affermato in letteratura circa l'inadeguatezza dei dati Sentinel-1 di tipo dual-pol per caratterizzare compiutamente il comportamento scatterometrico delle superfici indagate. La rilevanza del contenuto informativo è stata ridotta in ciascuna delle tre serie di dati raster costituiti da variabili di coerenza e polarimetriche controllando il rapporto segnale/rumore (SNR). La successiva analisi delle componenti principali applicata ai raster residui del controllo SNR ha permesso di generare mappe di danno relative alla prima componente principale con un'accuratezza complessiva superiore al 75% e l'individuazione dell'indice RC VH definito nella quarta finestra di calcolo come il miglior discriminante danneggiato/non danneggiato dal punto di vista qualitativo e quantitativo. Alcune incongruenze rispetto all'accuratezza delle fonti UNOSAT riscontrate nell'unione di mappe dell'area ad ovest di Kyiv in cui sono stati rilevati elementi classificati contemporaneamente come danneggiati e non danneggiati, lasciano spazio al dibattito circa la certezza attribuita al confronto delle fonti di questo lavoro e altri del suo genere.

Parole Chiave: Ukraine, War Damage, Sentinel-1, UNOSAT, Polarimetry, Coherence, Intensity, SNR, PCA, QGIS, SNAP, R Studio, CATALYST.

INDEX

INTRODUCTION	1
THESIS AIMS AND STRUCTURE.....	6
<i>Aims</i>	6
<i>Summary of the chapters</i>	6
1. PRINCIPLES OF ACTIVE REMOTE SENSING	9
1.1 <i>Generalities of Active Remote Sensing</i>	10
1.2 <i>Signal Characteristics</i>	13
1.3 <i>Signal Polarizations</i>	15
1.4 <i>Backscatter Contributors</i>	16
1.5 <i>Acquisition Geometry</i>	18
1.6 <i>Geometric Distortions</i>	23
1.7 <i>Radiometric Distortions</i>	26
1.8 <i>Interferometry</i>	27
2. FRAMEWORK	29
3. GROUND TRUTH	33
3.1 <i>UNOSAT Maps of West Kyviv area</i>	35
3.2 <i>UNOSAT Map of Mariupol</i>	43
3.3 <i>UNOSAT Map of Chernihiv</i>	44
4. SENTINEL-1 DATASET	47
4.1 <i>Copernicus Programme</i>	47
4.2 <i>Sentinel-1 Mission</i>	47
4.3 <i>Sentinel-1 Products</i>	50

4.4.	<i>Sentinel-1 Data Acquisition</i>	52
5.	STUDY AREAS	55
5.1	<i>West Kyviv area</i>	56
5.2	<i>Mariupol</i>	58
5.3	<i>Chernihiv</i>	59
5.4	<i>Synthesis of the Investigated Surfaces</i>	60
6.	EVENTS IN THE STUDY AREAS	61
2.1.	<i>West Kyviv area: events from 20/02/2022 to 01/04/2022.</i>	61
2.2.	<i>Mariupol: events from 20/02/2022 to 26/03/2022.</i>	63
2.3.	<i>Chernihiv: events from 20/02/2022 to 22/03/2022.</i>	65
7.	SOFTWARE	67
7.1.	<i>SNAP</i>	67
7.2.	<i>CATALYST</i>	68
7.3.	<i>QGIS</i>	69
7.4.	<i>R Studio</i>	69
8.	GENERAL IMAGE PROCESSING OPERATIONS	71
8.1.	<i>TOPS Split</i>	71
8.2.	<i>Apply Orbit File</i>	72
8.3.	<i>Calibration</i>	72
8.4.	<i>TOPS Deburst</i>	74
8.5.	<i>Subset</i>	74
8.6.	<i>Multilook</i>	74
8.7.	<i>Terrain Correction</i>	76
8.8.	<i>Coregistration - Sentinel-1 Back Geocoding</i>	77
8.9.	<i>Enhanced Spectral Diversity</i>	79
8.10.	<i>Speckle Filter</i>	79

9.	POLARIMETRY VARIABLES	83
9.1.	<i>SAR Polarimetry</i>	83
9.2.	<i>Polarimetry Variables</i>	89
9.3.	<i>Polarimetry Image processing</i>	90
9.4.	<i>Polarimetry Results</i>	92
10.	COHERENCE VARIABLES	95
10.1.	<i>SAR Coherence</i>	95
10.2.	<i>Coherence Variables</i>	96
10.3.	<i>Coherence Image processing</i>	97
10.4.	<i>Coherence Results</i>	99
11.	INTENSITY VARIABLES	101
11.1.	<i>Correlation Coefficient</i>	101
11.2.	<i>Intensity Variables</i>	102
11.3.	<i>Intensity Image processing</i>	103
11.4.	<i>Intensity Results</i>	105
12.	SNR DISCRIMINATION	109
12.1.	<i>SNR Coefficient</i>	109
12.2.	<i>SNR Determination</i>	110
12.3.	<i>Variables Discrimination</i>	111
13.	PCA ANALYSIS	115
13.1.	<i>Principal Component Analysis</i>	115
13.2.	<i>PCA Implementation</i>	117
13.3.	<i>PCA Results</i>	118
13.4.	<i>Damage Maps</i>	129
14.	DISCUSSION OF THE RESULTS	133
14.1.	<i>Polarimetry Discussion</i>	133

14.2. PCA Discussion.....	134
14.3. Damage Map Discussion.....	135
CONCLUSIONS	141
APPENDIX	147
A – Polarimetry Outputs	147
B – Coherence Boxplots	153
C – Intensity Boxplots	171
D – SNR Graphs.....	189
ACKNOWLEDGEMENTS	201
REFERENCES	203
BIBLIOGRAPHY	203
SOURCES OF WAR NEWS.....	224
CURRICULUM	237

INTRODUCTION

Since 24 February 2022, the Ukrainian territory has been the scene of a conflict with Russia such that as of 12 December 2022 there are certain 17,362 civilian victims, of which 6,755 are dead. Tens of millions of people are still in 'potential danger of death' (United Nations. Regional Information Centre for Western Europe, 2022). On the same date, UNESCO found damage to 227 sites including 101 religious buildings, 17 museums, 79 buildings of historical and/or artistic interest, 19 monuments, 11 libraries (UNESCO, 2022). This war, like all wars, is a source of damage to the territory of the Ukrainian nation and of social and economic crisis both for the Ukrainian people and for the European context (Khudaykulov et al., 2022).

The knowledge of the damage to the urban territory represents an element at the basis of post-war resettlement and in urban reconstruction plans (Bolorani et al., 2021). Land damage information can be acquired in several ways. Earth Observation is a safe and quick way to map damage under these circumstances (Arturo et al., 2020). For example, Muller et al. (2021) have developed an automated method of measuring destruction in high-resolution satellite images using deep-learning techniques combined with label augmentation and spatial and temporal smoothing (Mueller et al., 2021). Lubin and Saleem (2019) performed a Remote sensing-based mapping of the destruction to Aleppo during the Syrian Civil War between 2011 and 2017 (Lubin & Saleem, 2019). Braun (2018) conducted an Assessment of building damage in Raqqa during the Syrian civil war using time-series of radar satellite imagery (Braun, 2018). Ghandour and Jezzini (2018) developed a post-war building damage detection over a Syrian war-affected zone near Damascus (Ghandour & Jezzini, 2018).

Active remote sensing makes use of synthetic aperture radar sensors that use microwaves to investigate the earth's surface (Dubovik et al., 2021). Unlike multispectral optical images, SAR images offer the advantage of being able to detect

the territory by day and by night and regardless of weather conditions (Singh et al., 2021a). The European Space Agency makes the SAR Sentinel-1 images available free of charge, often used to analyze the problems that characterize the territory also through Change Detection techniques, defined as a process of identifying differences in the state of an object by observing the pre- and post-event data (Ashbindu sensing & 1989, 20101989). For example, Refice et al. (2020) exploited the integration of C- and L-band SAR images for detailed flood monitoring of remote vegetated areas (Refice et al., 2020). Caporusso et al. (2022a, 2022b) used Sentinel-1 imagery to characterize the surfaces of oil spills that occurred in the Persian Gulf in 2017 and in Venezuela in 2020 (Caporusso et al., 2022b, 2022a). Lu et al. (2018) identified earthquake-induced disasters in urban areas by coherence analysis of the SAR interferogram derived from Sentinel-1 images (Lu et al., 2018).

Many works that make use of high-resolution images assume ground-based maps made available by the United Nations Satellite Center (UNOSAT) which is part of The United Nations Institute for Training and Research (UNITAR). These maps are based on the photointerpretation of very high-resolution images such as the WorldView 3. The spatial resolution of these images is such that information on elements of the order of tens of centimeters may be acquired, as in the case of the leaf area index retrieval (Tarantino et al., 2015a). In the case of land damage, Meneses III and A. C. Blanco (2022) worked out rapid mapping and assessment of damages due to typhoon rai using Sentinel-1 synthetic aperture radar data. This study also examined the potential of SAR data for assessing the severity of the damages by quantitatively comparing the rapid damage assessment maps to damage tags from UNITAR and UNOSAT (Meneses III & Blanco, 2022). Kim Junwoo et al. (2021) tested the synergistic use of geospatial data for water body extraction from Sentinel-1 images for operational flood monitoring across southeast Asia implementing deep neural networks on UNOSAT maps (Kim et al., 2021). Pulvirenti et al. (2020) used the UNOSAT maps for calibration and validation phases of their InSAR work to detect floodwater in Beletweyne, Somalia (Pulvirenti et al., 2020). Hasanlou et al. (2021) defined earthquake damage region detection by

multitemporal coherence map analysis of radar and multispectral Imagery and two UNOSAT maps like ground truths (Hasanlou et al., 2021).

Sentinel-1 images are also used in the analysis of the damage caused to the territory by war events. In fact, Tapete and Cigna (2016) analyzed the transformations that occurred in the urban reality of Homs during the war in Syria in 2009, 2014 and 2015 through a change detection analysis executed on Sentinel-1 and TerraSAR-X images (Tapete & Cigna, 2016). Furthermore, in several cases, the joint use of Sentinel-1 images and UNOSAT maps was tested, as in the case of Bolorani et al.(2021) that compared their post-war urban damage mapping for Musul city in Iraq using InSAR techniques, to the available post-war destruction map of UNITAR (Bolorani et al., 2021). In 2018, Braun evaluated building damages in Raqqa during the Syrian Civil War using time-series of Radar satellite imagery validated by UNOSAT maps (Braun, 2018). Aimaiti et al., (2022) specifically dealt with the analysis of the damages found in the city of Kyiv during the ongoing conflict with Russia using a SAR log ratio of intensity for the Sentinel-1, and a texture analysis for the Sentinel-2. Also, in this study he referred to the UNOSAT maps for the evaluation of the accuracy and considered.

Change Detection techniques based on the use of Sentinel-1 data often consist in observing the variations assumed by polarimetric, coherence and intensity indices. The polarimetric indices describe the signal bounce mechanisms in relation to the scatterometric characteristics of the surfaces hit by the wave (Boerner, 2007). Migliaccio et al.(2015) proposed a SAR polarimetry review for sea oil slick observation (Migliaccio et al., 2015). Delgado et al. (2020) studied Effects on the Double Bounce Detection in Urban Areas of San Francisco Based on SAR Polarimetric Characteristics (Delgado Blasco et al., 2020). Malmgren-Hansen et al. (2020) applied Sentinel-1 Change Detection Polarimetry Analysis for Idai Cyclone Damage Assessment in Urban Environments that hit Mozambique in March 2019 (Malmgren-Hansen et al., 2020). The coherence indices consider the phase change undergone by the radar signal in relation to the position variation of the hit target. There are various uses of these indices

to evaluate land changes. Washaya et al. (2018) used a Coherence Change-Detection with Sentinel-1 for Natural and Anthropogenic Disaster Monitoring in Syria, Puerto Rico, California, and Iran Urban Areas (Washaya et al., 2018). Oxoli et al. (2020) used Coherent Change Detection in an application to earthquake damage assessment on buildings (Oxoli et al., 2020). ElGharbawi and Zarzoura (2021) dealt with a Damage detection using SAR coherence statistical analysis, applied to Beirut city. (ElGharbawi & Zarzoura, 2021). The intensity indices, on the other hand, consider the energy variation undergone by the electromagnetic wave as the characteristics of the incident surface vary. For example, Ge et al. (2019) produced a Building Damage Assessment Using Intensity SAR Data with Different Incidence Angles and Longtime Interval analyzing over the Gorkha area following the earthquake that occurred in Nepal in 2015 (Ge et al., 2019). Stramondo et al. (2006) analyzed the damage in urban areas in the cases of Izmit (1999; Turkey) and Bam (2003; Iran) both affected by strong earthquakes. Both coherence and intensity indices were used in this study (Stramondo et al., 2006a). Akhmediya and Zeng (2018) also used coherence and intensity indices in their study regarding the damage caused by the earthquake in Amatrice in 2016 and in Sarpol E-Zahab in 2017 (Akhmediya & Zeng, 2018). Studies are still being conducted to assess the efficacy of these indexes in relation to the various calculation windows. Kang and Baek (2021) performed a study with respect to SAR Image Change Detection via Multiple-Window Processing with Structural Similarity (Kang & Baek, 2021). Chae et al. (2019) analysed the displacements caused by the Hector Mine earthquake in California in 1999 developing an enhanced SAR offset tracking method based on a multi-kernel data processing developed to find an optimized measurement from the trade-off between resolution and measurement accuracy (Chae et al., 2019).

The different indices used in the context of remote sensing generated raster images whose information content was subject to control of the signal to noise ratio (SNR). For example, Long et al. (2018) in their New Approaches to Processing Ground-Based SAR (GBSAR) Data for Deformation Monitoring, selected their Permanent Scatterer points using an estimated signal to noise ratio (SNR) threshold (Long et al., 2018). An SNR limit value was also frequently used in SAR vessel recognition applications (Pan et al.,

2020; Heiselberg et al., 2022) as observed in the SAR and TomoSAR applications aimed at the recognition and monitoring of buildings in urban areas (Wu et al., 2021; Liu et al., 2022a).

In problems where there is a large number of variables, or in remote sensing applications where there are many indexes in raster format, it is often necessary to identify a small number of variables to describe the phenomenon efficiently and effectively. The Principal Component Analysis (PCA) allows to identify a small number of linearly independent variables that derive from the statistical synthesis of the starting variables (Bajwa & Hyder, 2005). Capolupo et al. (2020) used PCA in their study combining internal orientation variables to predict the accuracy of 3D Rpas-Sfm models (Capolupo et al., 2020). There are numerous applications of PCA using Sentinel-1 SAR data. (Espín Bedón et al., 2022; Liu et al., 2022b; Lee et al., 2021).

In keeping with the concepts presented, this dissertation investigates the feasibility of producing damage maps associated to conflict scenarios on Ukrainian territory using SAR Sentinel-1 SLC and GRDH imagery and an index-based approach. The three study areas of West Kyiv, Mariupol and Chernihiv were analysed for which there is availability of UNOSAT maps of the RBDA and BDA type. The proposal of evaluating the effectiveness of using three polarimetric, six coherence, and six intensity indices is addressed, employing free (QGIS, SNAP, R) and commercial (CATALYST) desktop software. The polarimetric indices do not allow to distinguish the damaged from the undamaged and therefore they are not useful for achieving the objective of the thesis. The analysis of the coherence and intensity indices was performed on 15 computation windows, defining a total of 183 raster data (549 in total) for each study area. Because of the large number of raster data, the SNR check and PCA analysis were required, resulting in the creation of a damage map for each study area based on the first principal component, as well as qualitative and quantitative assessments of the contributions of the coherence and intensity indices.

THESIS AIMS AND STRUCTURE

Aims

The major goal of the thesis study was to investigate the effectiveness of Sentinel-1 SAR satellite images in identifying places that have experienced and continue to suffer damage in Ukraine during the conflict between Russia and Ukraine that began on February 24th, 2022. This objective was achieved by selecting three study areas (Western Kyiv, Mariupol, and Chernihiv) and employing three polarimetric indices, six coherence indices, and six intensity indices as examined and discussed in the bibliography relating to the analysis of changes in the territory caused by natural disasters (earthquakes, floods, etc.) or man-made disasters (earthquakes, floods, etc.) (wars). The second goal, which was the most novel aspect of the research, was to investigate the impact of the six coherence indices and six intensity indices on 15 calculation windows that differed in size with regard to the calculation pixel, for a total of 549 tested indices (90 coherence indices, 90 intensity indices, 3 polarimetric indices, 3 investigation sites). The further objective, constituting the innovative aspect of the work carried out, was to examine the effects of the 6 coherence indices and the 6 intensity indices with respect to 15 calculation windows different in size with respect to the calculation pixel for a total of 549 tested indices (90 coherence indices, 90 intensity indices, 3 polarimetric indices, 3 investigation sites).

Summary of the chapters

The document's chapters are organized in a logical sequential manner, showing the important theoretical principles required to properly understand the consistency of the practical tasks performed.

Chapter 1: illustrates the general information relating to active remote sensing and reports the details necessary to understand what is described in the following chapters. Essentially the elements relating to the geometry and physics of the Synthetic Aperture Radar (SAR) are specified as well as the geometric and radiometric distortions that characterize the images used.

Chapter 2: the chapter summarizes the work scheme implemented in the thesis work and the logical relationships existing between the different steps subsequently detailed in specific chapters.

Chapter 3: reports the details of the UNOSAT maps distributed by UNITAR and taken as a reference for the comparison and validation of the work done. Within the study area west of Kyiv fall maps of different areas, while the areas of Mariupol and Chernihiv are represented in individual maps. For the 3 study areas, UNOSAT distributes Rapid Damage Building Assessment (RBDA) maps free of charge, divided into cells of side equal to 500, colored in red for the condition of damage, otherwise not colored for the condition of undamaged. The Building Damage Assessment (BDA) type maps (available only for some of the areas in the western area of Kyiv) identify the level of damage ascertained for some structures.

Chapter 4: presents a review of the Copernicus program followed by specifics about Sentinel-1 mission to then arrive at the precise identification of the series of images acquired free of charge for each study area within a specific list.

Chapter 5: describes in detail the three chosen study areas reporting their basic geographic and urban characteristics, as well as the maps created in QGIS from which the administrative borders and those of the areas of interest can be deduced obtained through the shapefiles of the UNOSAT maps and falling within the selected Sentinel-1 images.

Chapter 6: For each of the three research locations, sequences of occurrences from globally credible journalistic sources are documented, the damages of which are possibly identifiable both in UNOSAT maps and in classification maps produced from Sentinel-1 processing. The event chronologies are information about true events that must be reported technically and morally in order to offer impartiality and relevance to the work done.

Chapter 7: describes the characteristics of the software used. SNAP is open-source software that is used for polarimetric and coherence analysis as well as the generation of relative indices. CATALYST is commercial software that is used for intensity analysis and the generation of associated indicators. QGIS is open-source software for creating

maps and analyzing raster and shapefile data. R Studio is open-source software that is used to produce statistical results and to execute Principal Component Analysis (PCA).

Chapter 8: covers Sentinel-1 image processing methods that are used in polarimetric, coherence, and intensity analyses. This is done to eliminate redundant information in each of the chapters devoted to the individual analyses.

Chapter 9: describes the procedures necessary for the creation of polarimetric variables by first defining their general characteristics and then reporting their determination in SNAP through Sentinel-1 images of the SLC type.

Chapter 10: starting from the definition of Coherence in the SAR context, the determination of the Coherence variables in SNAP through Sentinel-1 images of the SLC type is reported.

Chapter 11: explains the generation of intensity variables through Sentinel-1 GRDH images in the CATALYST environment starting from the definition of the Intensity Correlation Coefficient.

Chapter 12: once the signal to noise ratio (SNR) has been defined, the procedure for selecting polarimetric and intensity indices with SNR greater than 5 using the R software is reported.

Chapter 13: Describes the characteristics of the Principal Component Analysis and its implementation in R both in order to identify the coherence and intensity indices that best describe the damage condition in each area of interest, and their linear combinations for different levels of explained variance. Finally, the realization of the classification maps produced through the first principal component in QGIS for each of the study areas is depicted.

Chapter 14: The results related to the polarimetric analysis, and the confusion matrices associated with the classification maps are discussed.

Conclusions: they connect the results and discussions to the thesis goals, identifying their strengths and limitations as well as possible future developments.

Appendix: this section contains the collections of images referred to in various chapters of the thesis.

1. PRINCIPLES OF ACTIVE REMOTE SENSING

According to the United States Geological Survey (USGS), Remote sensing is the process of detecting and monitoring the physical characteristics of an area by measuring its reflected and emitted radiation at a distance (typically from satellite or aircraft). Special cameras collect remotely sensed images, which help researchers "sense" things about the Earth (USGS, 2022). The term is applied specially to acquiring information about Earth and other planets. Remote sensing is used in numerous fields, including geography, land surveying and most Earth science disciplines (e.g. hydrology, ecology, meteorology, oceanography, glaciology, geology); it also has military, intelligence, commercial, economic, planning, and humanitarian applications, among others. In current usage, the term remote sensing generally refers to the use of satellite- or aircraft-based sensor technologies to detect and classify objects on Earth. It includes the surface and the atmosphere and oceans, based on propagated signals

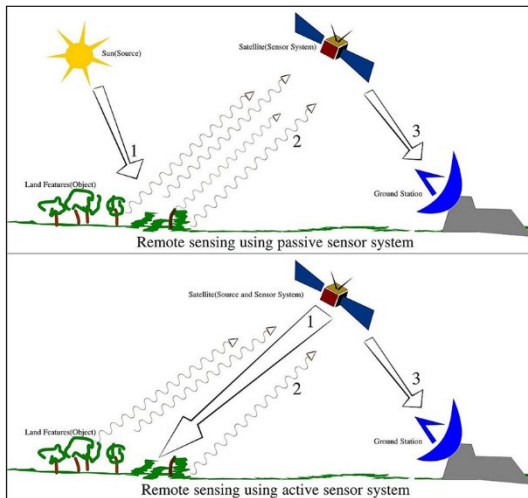


Fig. 1 – Passive and Active Remote Sensing.
https://upload.wikimedia.org/wikipedia/commons/6/61/Remote_Sensing_Illustration.jpg

(e.g. electromagnetic radiation) (Liu & Mason, 2009; Guo et al., 2013; Schott, 2007; Schowengerdt, 2007). Remote sensing can be divided into two types of methods: Passive remote sensing and Active remote sensing (Fig. 1) (Woodhouse, 2017a). Passive sensors gather radiation that is emitted or reflected by the object or surrounding areas. Reflected sunlight is the most common source of radiation measured by passive sensors. Examples of passive remote sensors include film photography, infrared, charge-coupled devices, and radiometers.

1.1 Generalities of Active Remote Sensing

Active sensors, on the other hand, in which the sensor emits the electromagnetic wave and records the reflected and/or naturally emitted radiation from the observed object. RADAR and LiDAR are examples of active remote sensing where the time delay between emission and return is measured, establishing the location, speed and direction of an object. Remote sensing makes it possible to collect data of dangerous or inaccessible areas. Remote sensing also replaces costly and slow data collection on the ground, ensuring in the process that areas or objects are not disturbed. Remote sensing makes use of various parts of the electromagnetic spectrum: visible light (380-780 nm), infrared (780 nm – 0.1 mm) and microwaves (0.1 mm – 1 m) (Fig. 2) (Ball, 2007). The red spectrum together with the near infrared (NIR) is typically used for vegetation applications such as, for example, the NDVI (Normalized Difference Vegetation Index); microwaves, on the other hand, are typically used to obtain information about the atmosphere, land and ocean in the context of weather forecasting (Pettorelli et al., 2011).

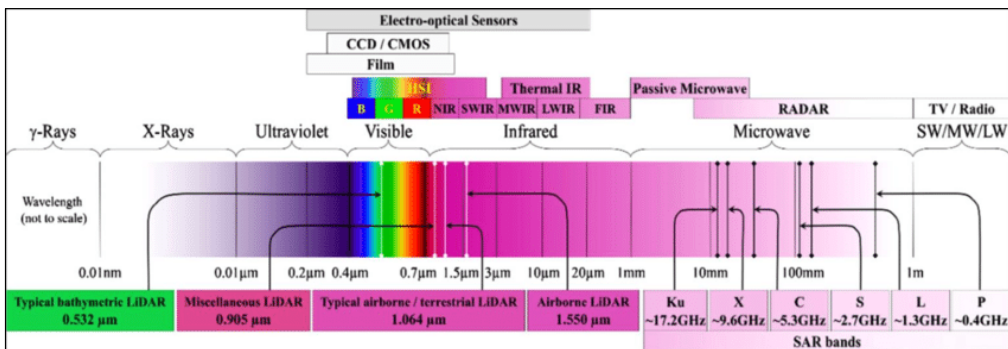


Fig. 2 – Electromagnetic Spectrum Sections in Remote Sensing. Source:(Devrani, 2018).

Active remote sensing allows measurements to be obtained at any time: microwave energy can penetrate rain, snow, cloud, haze and operate independently of sunlight, making it extremely versatile in use, regardless of the time of day and atmospheric conditions in which the image acquisition takes place (Liang, 2017). Furthermore, in

the microwave spectral region, the atmosphere can be considered transparent, especially at lower frequencies (Fig. 3) (Cheney & Borden, 2009).

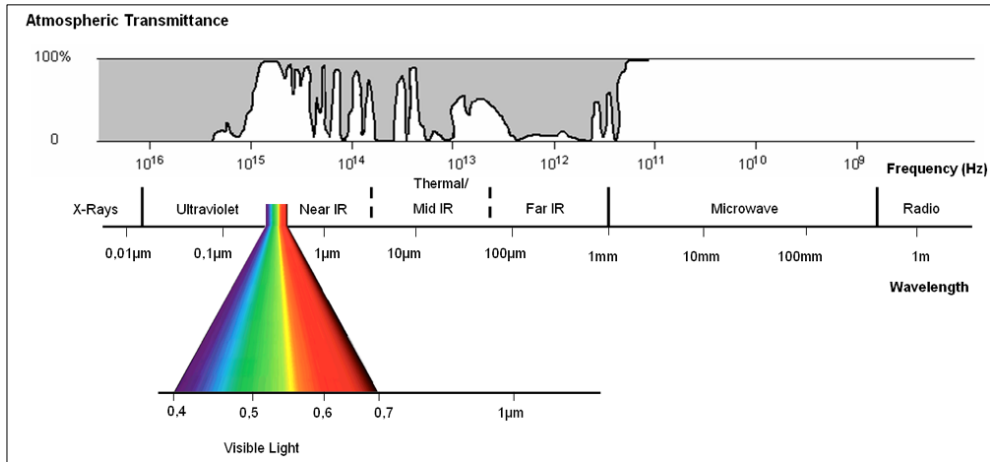


Fig. 3 – The electromagnetic spectrum and atmospheric transmittance. Source: Albertz (2007) with modifications.

Active remote sensing is achieved through satellite missions carried out by different countries around the world which for years have been putting satellites equipped with RADAR-type sensors into orbit around the earth. Among these different kinds of sensors, Synthetic Aperture Radar (SAR) is popularly. A synthetic-aperture radar is an imaging radar mounted on an instant moving platform (Moreira et al., 2013a). SAR makes use of the Doppler effect of the motion of platforms to increase the “aperture” and thus the resolution of the images. Electromagnetic waves are transmitted sequentially, the echoes are collected, and the system electronics digitizes and stores the data for subsequent processing. As transmission and reception occur at different times, they map to different small positions. The well-ordered combination of the received signals builds a virtual aperture that is much longer than the physical antenna width. That is the source of the term "synthetic aperture," giving it the property of an imaging radar (Ramakrishnan et al., 2002).

The past few years have seen the launch of numerous SAR sensors, like TerraSAR-X, CosmoSkyMed, ALOS-2 and more recently Sentinel-1. New sensors will also be launched soon, such as TSX-NG, Cosmo-SkyMed second generation, Radarsat

constellation and NISAR (Zhao, 2019). The Fig. 4 shows the different radar satellites put into orbit since 1991, distinguished by the three acquisition bands X, L and C.

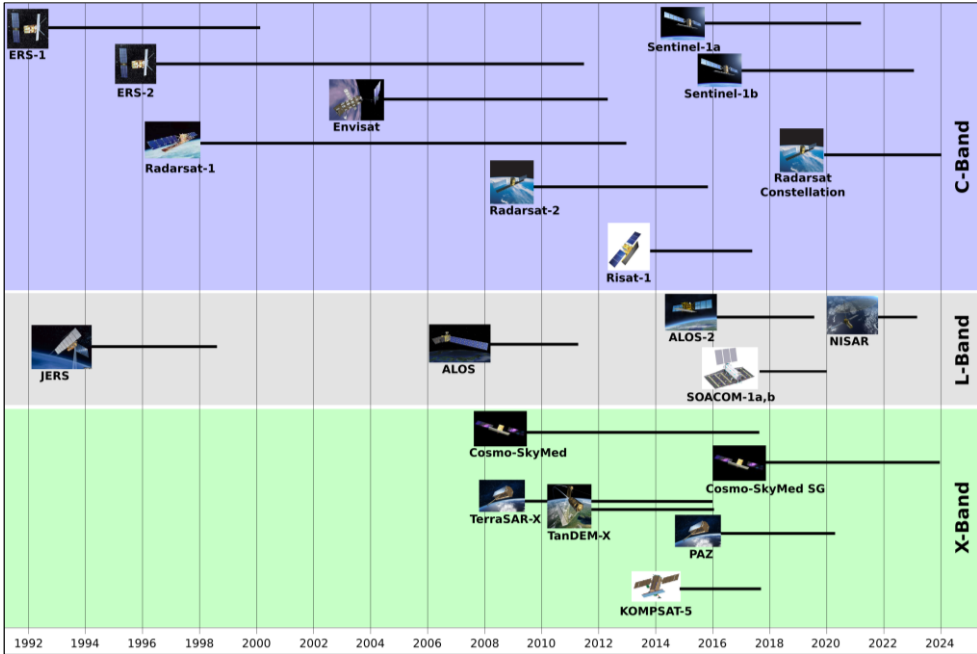


Fig. 4 – SAR satellite programs (presented by UANVCO with some modifications) (Zhao, 2019).

A RADAR device consists of a transmitter, a receiver, an antenna and a recorder. The transmitter generates a series of pulses of duration t , having a certain frequency and bandwidth. The receiver filters and amplifies the backscattered signal. The recorder stores the received signal. Finally, the antenna is used to radiate and/or receive energy. We speak of monostatic radar if there is only one antenna that acts as both transmitter and receiver, we speak of bi-static radar when there are two different antennas for transmission and reception (Skolnik, 1980). The ability of a RADAR to locate a target (observed object) is determined by the radar equation which defines the strength of the signal received by the antenna:

$$P_r = \frac{P_t G^2 \lambda^2}{(4\pi)^3 R^4} \sigma \quad (1)$$

where P_r is the average received power per pixel, P_t is the antenna transmitted power, G is the antenna gain, R is the antenna-to-target distance, λ is the wavelength of the incident radar beam, and σ is the backscattering coefficient, i.e. the reflectivity per unit area of the scene. The latter, and therefore the backscattered energy, depends on many parameters which include both the construction characteristics of the radar systems (frequency, polarization, acquisition geometry) and the characteristics of the detected object (roughness, humidity content and electrical properties of the object) (Hanssen, 2001).

1.2 Signal Characteristics

It is useful to take into account the different physical and mathematical characteristics concerning the wave (Fig. 5).

Considering the harmonic motions associated with the y and x axes of the Cartesian reference as projections of a point that moves with uniform circular motion, the following equations are obtained:

$$\begin{cases} e(t) = A \sin(\omega t + \phi) \\ s(t) = A \cos(\omega t + \phi) \end{cases} \quad (2)$$

where $e(t)$ is the projection of the point on the y -axis at time t , $s(t)$ is the projection of the point on the x -axis at time t , A is the amplitude or the radius of the circle on which the point moves, ω is the angular velocity and ϕ is the angle of phase at time $t=0$ (Crecraft & Gergely, 2002).

Considering the phasor as a representation of the function for $t=0$, independent of time, frequency and pulsation, in terms of complex number in the plane (Im, Re):

$$\begin{cases} a = A \cos \phi \\ b = A \sin \phi \end{cases} \quad (3)$$

$$\mathbf{A} = \mathbf{a} + j\mathbf{b} \quad (4)$$

also writable in Eulerian form:

$$\mathbf{A} = A \cos \phi + A \sin \phi = A e^{j\phi} \quad (5)$$

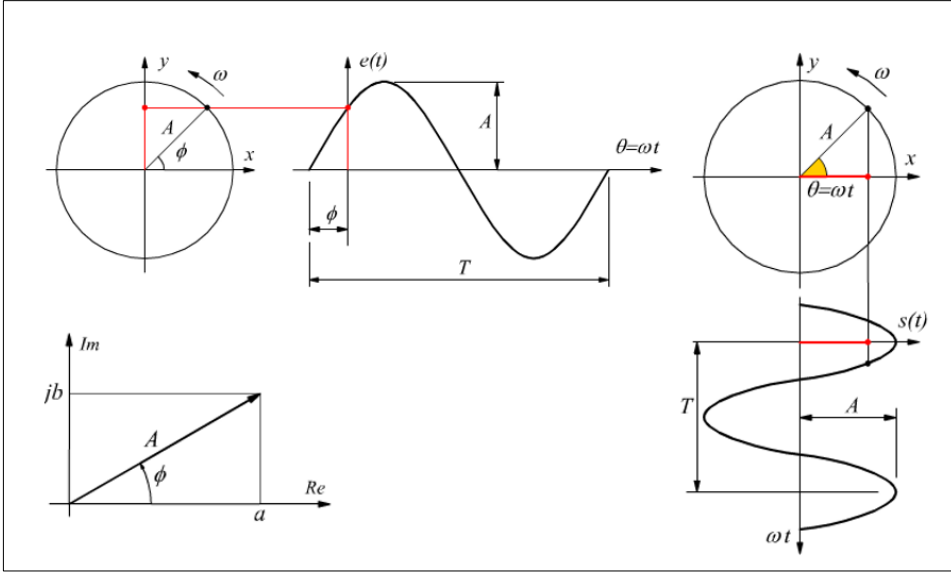


Fig. 5 – Sinusoidal, Cosinusoidal and Phasor representations related to a wave.

Far from the antenna in the far field region (Stratton, 1941; Mott, 1992), the radial waves of take on plane wave characteristics. The general expression for the electric field of a plane electromagnetic wave, which is a solution of the Maxwell equations, is:

$$\mathbf{E} = \mathbf{E}_0(R, t) e^{i(\mathbf{k} \cdot \mathbf{R} - \omega t)} = \mathbf{E}_0(R, t) e^{i\phi} \quad (6)$$

where $\mathbf{k} = k\hat{\mathbf{e}}$ is the complex wave vector ($\hat{\mathbf{e}}$ is a unit vector in the propagation direction), k is the complex wave number, depending on dielectric constant. The wave propagates along space vector \mathbf{R} (slant range). ω is the wave angular frequency and t the time. Thus, the echo received by the antenna of an imaging radar from a ground pixel is characterized by two quantities: amplitude and phase (Zhou et al., 2009). The phase is used to determine the distance from the sensor to a target, and amplitude indicates the amount of the sent signal that returns to the sensor. Amplitude measurements provide information about the roughness, geometry, wetness, and

dielectric constant of that target, while phase measurements are used for SAR interferometry.

1.3 Signal Polarizations

An important property of electromagnetic waves is polarization, which represents the direction along which the electric field oscillates during wave propagation. The polarization is called horizontal (H) if the vibration of the wave insists on a plane perpendicular to the plane of incidence, vertical (V) if the vibration occurs in the plane of incidence. There are four combinations (Fig. 6):

- HH: horizontal transmission and horizontal reception
- VV: vertical transmission and vertical reception
- HV: horizontal transmission and vertical reception
- VH: vertical transmission and horizontal reception.

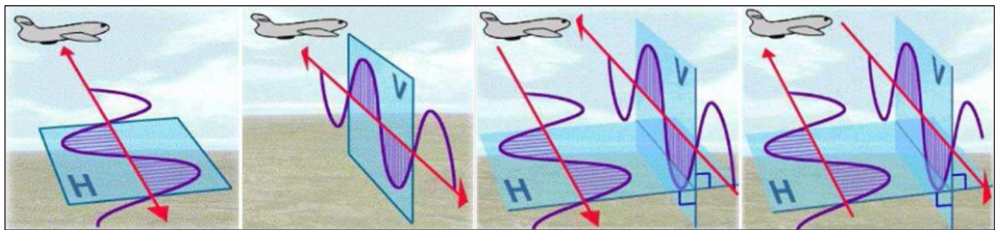


Fig. 6 – SAR Polarizations. Source: (Sarscape, 2009).

In particular, the HH and VV polarizations are called copolarizations, while the HV and VH polarizations are called cross polarizations (Mayer, 2019). The simplest SAR systems often operate with only one polarization due to the high cost of implementation. SAR systems used for research purposes instead tend to have multiple polarizations, and in some cases have all possible polarizations (in which case they are called "quad-pol"). Depending on the polarization of the transmitted and received radar wave, the radiation will interact differently with the target (it will be backscattered differently) and the resulting RADAR images will be different (Richards, 2009). Therefore, using RADAR images acquired with different polarizations, we can have different and complementary information on the investigated target.

1.4 Backscatter Contributors

Examining the signal strength from different polarizations carries information about the structure of the imaged surface, based on the following types of scattering: rough surface, volume, and double bounce (Fig. 7):

- Rough surface scattering, such as that caused by bare soil or water, is most sensitive to VV scattering.
- Volume scattering, for example, caused by the leaves and branches in a forest canopy, is most sensitive to cross-polarized data like VH or HV.
- Double Bounce is caused by buildings, tree trunks, or inundated vegetation and is most sensitive to an HH polarized signal.

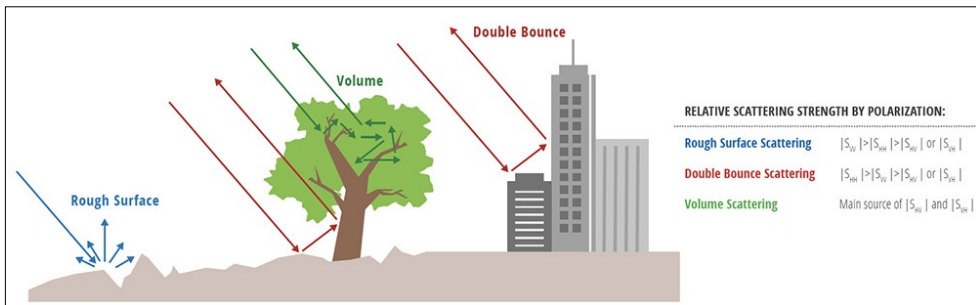


Fig. 7 – Types of scattering: rough surface, volume, and double bounce. Source: (Mayer, 2019).

Smooth water surfaces (Fig. 8 i) can easily be detected by their very low backscatter signal since they act as a specular reflector and the transmitted radiation is almost completely scattered away from the sensor, resulting in a very low backscatter signal (Schmitt & Brisco, 2013; Töyrä & Pietroniro, 2005; Haal, 1996). Volume scattering occurs primarily in tree crowns (Fig. 8 b), while surface scattering can be found on bare soil (Fig. 8 g, h) or the canopy (Fig. 8 a) dependent on leaf size, density etc. The presence of standing water beneath the vegetation cover (surface inundation) significantly leads to double-bounce backscattering and increases radar backscatter from forests and grasslands. Double bounce scattering occurs as soon as vegetation—grass or even trees—is flooded (Fig. 8 c, e) and the radar signal is reflected from the

water surface and then re-directed back to the sensor by the vegetation trunk (Schmitt & Brisco, 2013; Töyrä & Pietroniro, 2005; Ottinger & Kuenzer, 2020).

It is important to note that the amount of signal attributed to different scattering types may change as a function of wavelength, as wavelength changes the penetration depth of the signal. For example, a C-band signal penetrates only into the top layers of the canopy of a forest, and therefore will experience mostly roughness scattering mixed with a limited amount of volume scattering. However, a L-band or P-band signal will have much deeper penetration and therefore experience strongly enhanced volume scattering as well as increasing amounts of double-bounce scattering caused by the tree trunk (Fig. 9).

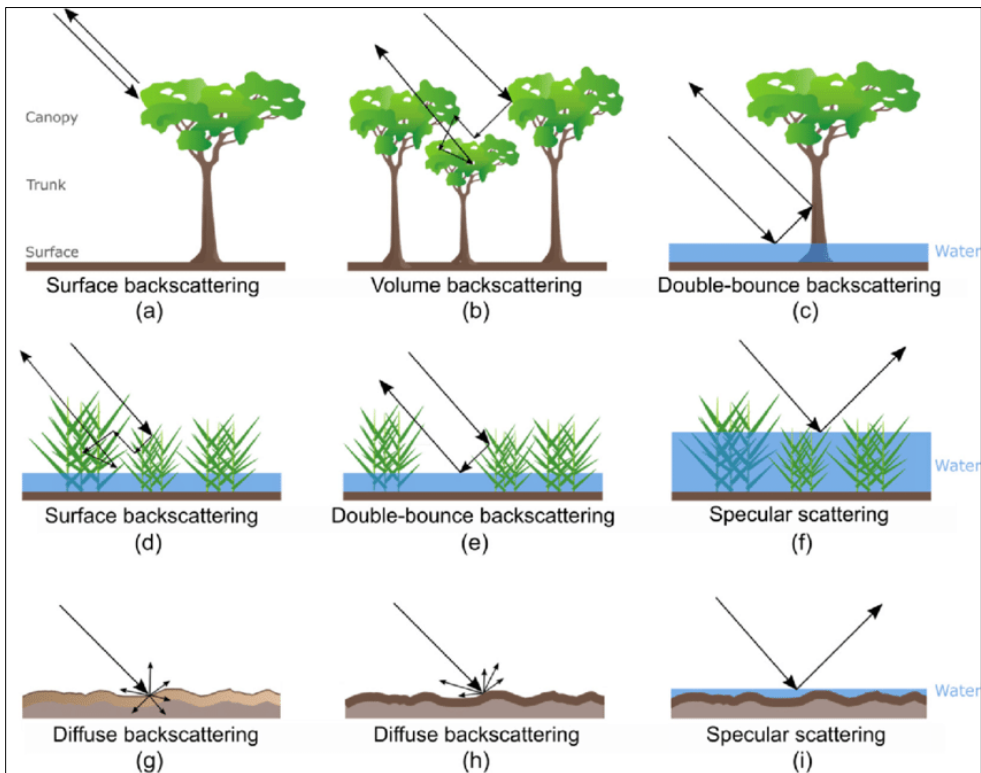


Fig. 8 – Radar backscattering mechanisms for forest, wetland and soil surfaces. (a,b,g,h): Nonflooded condition; signal scattering in the crown and on the ground. (c–f,i): submerged wetland/open water; strong double-bounce reflection between the tree trunks and the water surface. (g–i): Ground surface in (Ottinger & Kuenzer, 2020; Lu & Kwoun, 2008). (Ottinger & Kuenzer, 2020; Lu & Kwoun, 2008).

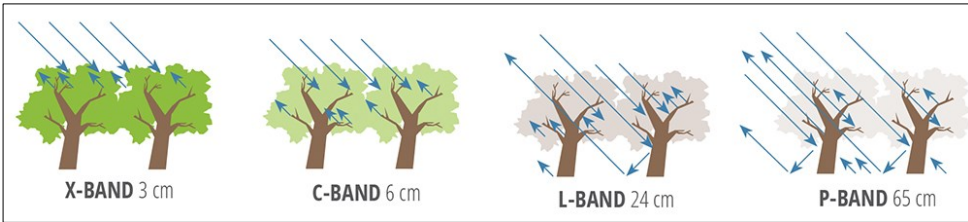


Fig. 9 - Sensitivity of SAR measurements to forest structure and penetration into the canopy at different wavelengths used for airborne or spaceborne remote sensing observations of the land surface (Mayer, 2019).

1.5 Acquisition Geometry

Optical instruments can distinguish between targets based on their angular distance from the sensor's nadir. RADAR can distinguish returns from various targets only on the basis of the return time of the signal. A nadiral acquisition radar would not be able to distinguish between two targets placed at equal distance from the sensor since a single incident wavefront illuminates both points at the same instant, and consequently the backscattered returns from both points arrive at the receiving antenna simultaneously (Fig. 10). A monostatic SAR imaging system consists of a microwave transmitter and receiver, which is placed on a moving platform such as an airplane or a satellite. The radar sensor flies at an approximately constant height h_s above the ground and speed v_s along the radar track (or azimuth, or along-track) direction.

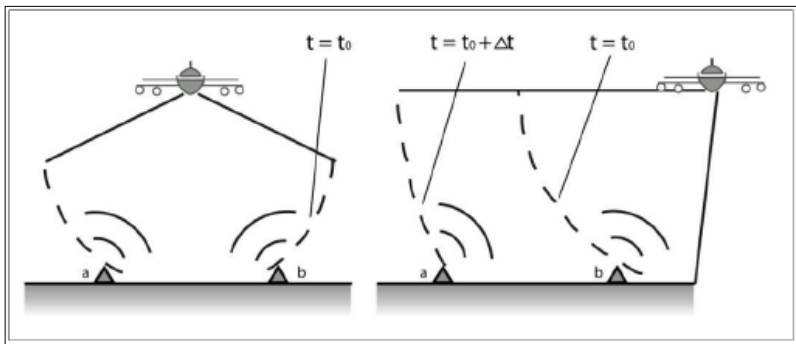


Fig. 10 – Nadir image acquisition (left) and Side Looking image acquisition (right). Source: <https://appliedsciences.nasa.gov/sites/default/files/Session1-SAR-English.pdf>.

The antenna height and length are indicated by L_e and L_a (where the subscripts stand for elevation and azimuth, respectively). The slant range identifies the direction

perpendicular to the radar track pointing to the target T, whereas the ground range is the projection of the slant range on ground, η is the angle of incidence and R_0 is the slant range distance of closest approach between the sensor and the target T (Fig. 11) (Martone, 2019). The microwave energy radiated by the antenna illuminates an area on ground which is defined as the antenna footprint. This extends over L_s along azimuth direction and W_g from near to far range (the so-called swath width), which are expressed as:

$$L_s = \frac{\lambda R_0}{L_a} \quad (7)$$

$$W_g = \frac{\lambda R_0}{L_e \cos(\eta)} \quad (8)$$

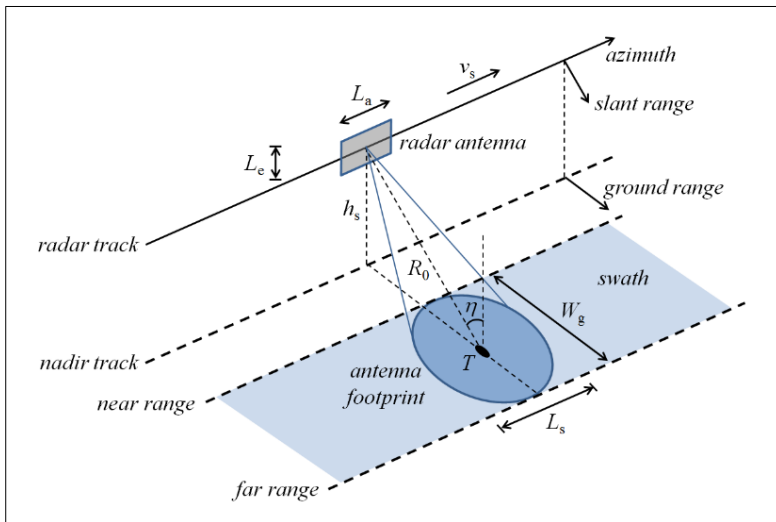


Fig. 11 – SAR Acquisition Geometry (Martone, 2019).

The eq.(7) points out that to increase the resolution in the azimuth direction it is necessary to increase the L_s dimension of the antenna. The SAR transmitter unit emits short pulses of electromagnetic radiation each of duration τ_p at speed of light c_0

(300.000 Km/s in vacuum) at a constant pulse repetition frequency (PRF) (Fig. 12).
 The Pulse Length is:

$$PL = c_0 \cdot \tau_p \quad (9)$$

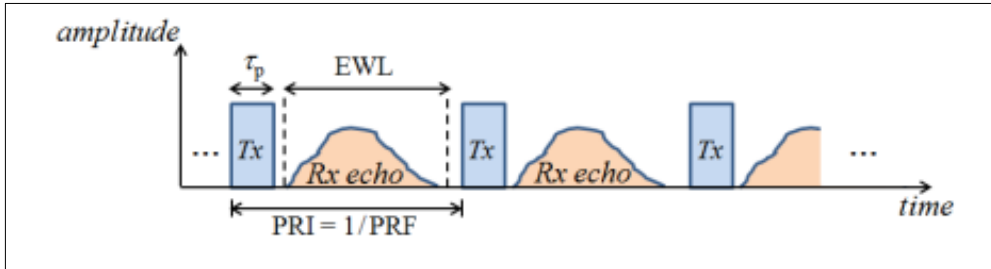


Fig. 12 – SAR pulses and echo (Martone, 2019).

In the time interval τ_p the distance is covered twice, therefore the resolution in the slant range direction can be expressed as:

$$r_{ss} = \frac{c_0 \tau_p}{2} \quad (10)$$

It can be seen in the Fig. 13 that If the distance between the two houses labeled A and B were greater than half Pulse Length, then they would be discerned as two separate features. Since, in this figure the slant range distance is less than half Pulse Length, the reflected signals are "blurred." Slant range resolution does not vary with increasing distance from the aircraft, but ground range does.

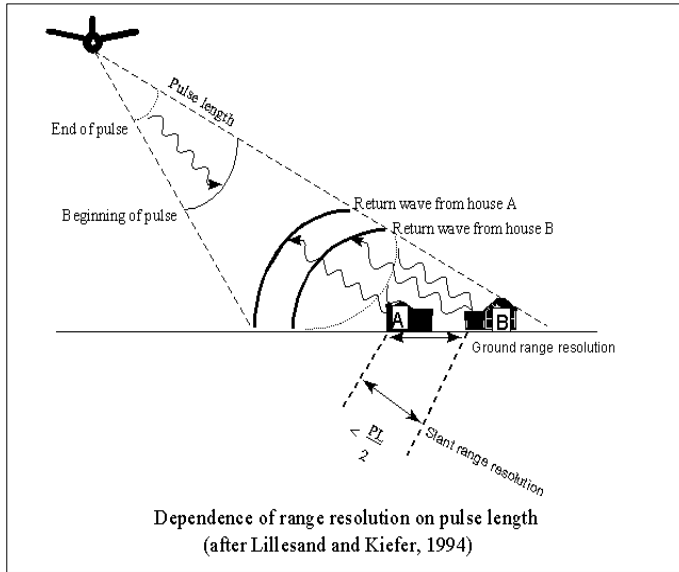


Fig. 13 – RADAR Discrimination Ability.
Source <http://www.geo.hunter.cuny.edu/terrain/radarii.html>

For spaceborne SAR the resulting PRF values are in the range of a few kilohertz (kHz). The echo window length (EWL) is the time interval allowed for the echo reception. Due to the large range distance, each pulse takes several pulse repetition intervals (PRIs, being $PRI = 1/PRF$) to travel from the sensor to the target T and back, i.e., $\Delta t \approx n \cdot PRI$, where n is also known as rank. Given a range R_0 , the rank of a SAR system is defined as:

$$rank(R_0) = \frac{2R_0}{c_0} \cdot \frac{1}{PRI} \quad (11)$$

The echo window length (EWL) directly determines the effective imaged swath width:

$$W_{g,eff} = \frac{c_0 \cdot (EWL - \tau_p)}{2 \cdot \sin(\eta)} \quad (12)$$

The maximum swath width $W_{g,max}$ is achieved by selecting the largest possible EWL, which is given by:

$$EWL_{max} = PRI - \tau_p \quad (13)$$

Synthetic aperture radar makes it possible to significantly improve the performance of a real aperture radar by increasing the azimuth resolution. The principle on which the method is based can be justified by resorting to two different interpretative schemes (Stramondo et al., 2006b; Hanssen, 2001):

- 1) the alignment of elementary antennas (Antennas Array)
- 2) the concept of Doppler beamforming.

According to the Antennas Array approach (Fig. 14), the opening of the alignment of elementary antennas is:

$$\phi_A = \frac{\lambda}{Nd} \quad (14)$$

and is inversely proportional to the length of the alignment.

The radar system, moving along a straight trajectory, transmits and receives the relative echo in correspondence with N positions distant d from each other. In this case, if we assume to add the received echoes, we obtain a formula analogous to eq.1: the only difference is that we need to consider the return path of the signal and therefore replace $\lambda/2$ in place of λ . The resulting virtual alignment has an aperture:

$$\phi_A = \frac{\lambda}{2Nd} \quad (15)$$

From this consideration we obtain that the length of the synthetic alignment is:

$$L_{AR} = Nd = \theta_{az} R_0 = \frac{\lambda h_s}{L_a \cos \eta} \quad (16)$$

And the (15) becomes:

$$\phi_A = \frac{L_a \cos \eta}{2h_s} \quad (17)$$

The footprint of the synthetic alignment determines the resolution of the SAR system in the azimuth direction is:

$$\Delta_x = \phi_A R_0 = \frac{L_a}{2} \quad (18)$$

It can be seen how, unlike the eq.(7) relating to a generic radar antenna, the resolution in the azimuth direction of the SAR increases as the dimensions of the real antenna decrease, in a way that is decidedly more compatible with the technological construction requirements.

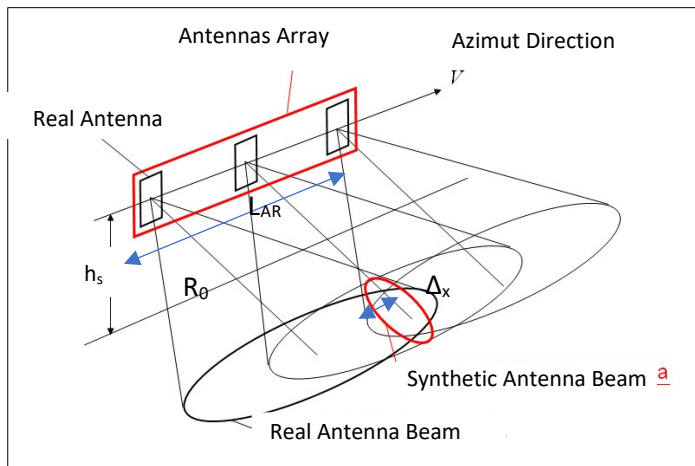


Fig. 14 – SAR Antennas Array Approach.

1.6 Geometric Distortions

The radar measures distances in the slant range and consequently sloping areas are compressed. In fact, the acquisition method, not perpendicular to the ground, but according to an angle of view θ , creates perspective deformations due to the topography of the terrain (Fig. 15, Fig. 16).

- Foreshortening: depending on the angle created between the ground surface and the radar beam, the real surface will be compressed more or less

accentuated. Distortion is greatest when the ground surface tends to be perpendicular to the sensor-target connection. The compressed areas are very bright in the radar images because the return signal from several points is compressed into a few cells, producing very bright pixels (that is, having high Digital Numbers). Therefore, a relief is compressed in the side facing the radar and stretched in the opposite direction.

- Layover: if the radar beam reaches the top of the mountain before its base, in slant range geometry, the return from the top is placed before the return from the base of the mountain. In practice, we have an inversion of the real geometry. The layover effect occurs when the terrain has a greater slope than the angle of incidence of the RADAR and is an extreme case of foreshortening.
- Shadow: if the angle of incidence is too large, the radar beam fails to illuminate mountainsides facing away from the sensor. Thus, there is no energy that can be scattered back to the sensor and these regions remain black in the image.

The foreshortening effect can be corrected during the geometric and radiometric calibration of the SAR images thanks to the use of a digital terrain elevation model (DEM, Digital Elevation Model). Areas where layover and shadow effects are present can be detected, but not corrected. In the shadow areas there is no data, in the layover areas the back-diffused energy from various targets is compressed into a few pixels and there is therefore a strong distortion of the image which prevents the correct interpretation of the signal and any quantitative analysis.

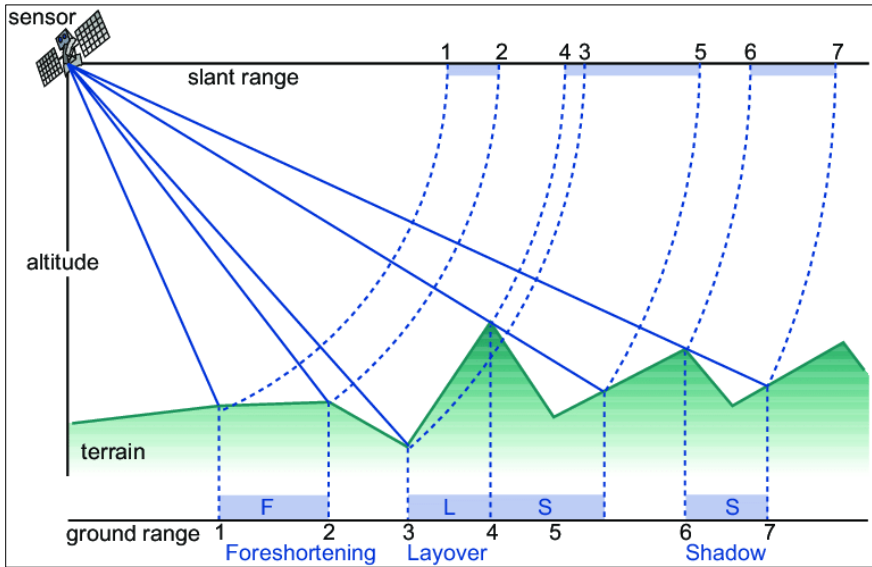


Fig. 15 – RADAR Geometric Distortions. Source: (Tempfli et al., 2009).

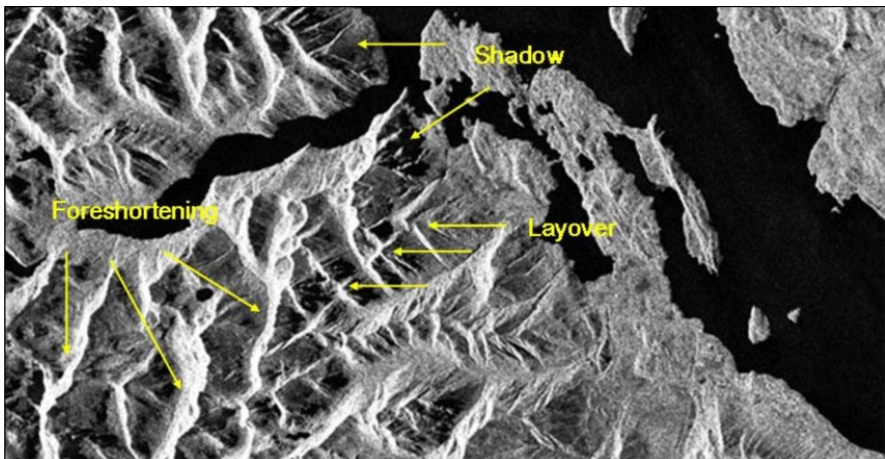


Fig. 16 - RADAR Geometric Distortions in RADAR Image. Source: (Marchionni & Cavayas, 2014).

To know the areas subject to geometric distortions, it is possible proceed in two ways. If a SAR image of the area is available, a layover and shadow map can be created, which identifies the areas affected by these effects; in the absence of the SAR image and knowing the morphological parameters of the territory and the satellite parameters,

a visibility map of the area is created (Plank et al., 2012; Peduto, 2008; Cascini et al., 2009).

1.7 Radiometric Distortions

Speckle, speckle pattern, or speckle noise is radiometric distortion that appears as a granular noise texture degrading the quality as a consequence of interference among wavefronts in coherent imaging systems, such as radar, synthetic aperture radar (SAR), medical ultrasound and optical coherence tomography (Lecompte et al., 2006; Hua et al., 2011; Goodman, 1976; Dainty, 1984). The speckle effect is a result of the interference of many waves of the same frequency, having different phases and amplitudes, which add together to give a resultant wave whose amplitude, and therefore intensity, varies randomly (Fig. 17) (Singh et al., 2021b). When a surface is illuminated by a light wave, according to diffraction theory, each point on an illuminated surface acts as a source of secondary spherical waves. The light at any point in the scattered light field is made up of waves which have been scattered from each point on the illuminated surface. If the surface is rough enough to create path-length differences exceeding one wavelength, giving rise to phase changes greater than 2π , the amplitude, and hence the intensity, of the resultant light varies randomly (Bender et al., 2018, 2019; Dainty, 1984; Goodman, 1976). If light of low coherence (i.e., made up of many wavelengths) is used, a speckle pattern will not normally be observed, because the speckle patterns produced by individual wavelengths have different dimensions and will normally average one another out. However, we can observe speckle patterns in polychromatic light in some conditions (McKechnie, 1976).

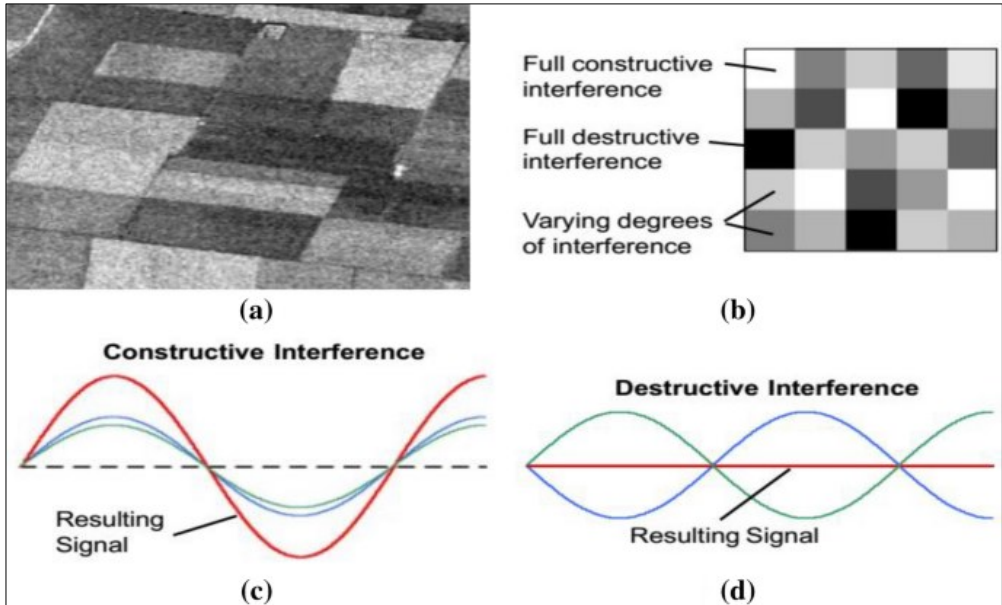


Fig. 17 – Speckle Description: a) Speckle effect in SAR image, b) Detail of Speckle effect in the SAR image, c) Constructive Interference, d) Destructive Interference. Source: (Singh et al., 2021b).

1.8 Interferometry

Interferometry studies the difference in phase and amplitude of the backscattered signal, measuring the variation between two different SAR images observing the same object (GENS & van GENDEREN, 1996). In fact, it is possible to observe the same scene with different observation angles, in order to exploit the phase difference to deduce the "differential range", i.e. the distance perceived by the sensor which operates from two different points of view, and/or the "range change", i.e. the difference between two pairs of images in which there was a movement of the target between the two acquisitions that took place at different times. The interferometric data is obtained through a cross product between the two images:

$$\Delta\phi = \Delta\phi_{topo} + \Delta\phi_{flat} + \Delta\phi_{disp} + \Delta\phi_{atm} + \Delta\phi_{noise} + 2N\pi \quad (19)$$

where $\Delta\phi_{topo}$ is the component due to the height difference between the surface and the surveyed point, $\Delta\phi_{flat}$ is the flatearth component, proportional to the difference between the position along the surface slant-range direction and the surveyed point, $\Delta\phi_{disp}$ is the component proportional to the displacement along the direction of the slant range, $\Delta\phi_{atm}$ is the contribution due to the presence of the atmosphere, $\Delta\phi_{noise}$ is the contribution due to noise and $2N\pi$ is the ambiguity factor (Ferretti et al., 2001).

2. FRAMEWORK

The work envisaged a preliminary exploration of the UNOSAT damage maps related to various Ukrainian territories as scenarios of actions of war-like acts publicly released online by UNITAR following the outbreak of the conflict between Russia and Ukraine. The maps are available both in pdf and shapefile format and derive from the photo-interpretation of WorldView-3 very high resolution satellite images (50 cm). This means that these maps are commonly assumed as ground truths against which to test products derived from lower resolution images such as Sentinel-1 and Sentinel-2 (about 10 m).

At the same time, the availability of Sentinel-1 images corresponding to the UNOSAT maps in spatio-temporal terms was verified. The choice therefore fell on the three study areas (West Kyviv, Mariupol, Chernihiv), having heterogeneous features in order to offer the study a more comprehensive approach. In fact, the area west of Kyviv, in the hinterland, has an extension of about 183 km², is made up of the aggregation of small urban centers (area west of Kyviv, Hostomel, Bucha, Irpin and Horenka,). Mariupol is a coastal city with an area of about 400 km² and a high level of urbanization. Chernihiv is a small inland center with an area of about 87 km² and is not densely urbanized.

The imperfect temporal overlap between the UNOSAT maps and the Sentinel-1 images, the peculiarity of the visual survey containing the UNOSAT maps and the need to refer to true events, have reasonably led to the reporting of the chronology of significant events in terms of origin and extent of the damage (mainly air raids and missile attacks), probably verifiable in the survey work conducted through Sentinel-1 images at each of the three sites.

Polarimetric and coherence analysis were implemented using SLC-type Sentinel-1 pictures, whereas intensity analysis was possible using GRDH-type Sentinel-1 images. Change Detection data processing (i.e. coherence and intensity analysis) on two pairs

of images refers to a sequence of three perfectly overlapping images, the first of which precedes the start of the damage events, the second not before the start of the damage events, and the third with ongoing damage, possibly contemporaneous with the ground truth date. The operations of polarimetric analysis refer to each single image.

The variables Entropy, Anisotropy, and Alpha were generated according to each of the three dates using polarimetric analysis in SNAP software. The average, minimum, and maximum values pertaining to the total area, the damaged section, and the undamaged portion were observed for each of the three variables using boxplots created in R software and Alpha/Entropy diagrams generated in SNAP.

The coherence analysis generated the DC VV, DC VH, RC VV, RC VH, NDCC VV, and NDCC VH variables in the SNAP environment with regard to 15 coherence calculation windows. Following that, boxplots of the average, minimum, and maximum values referenced to the entire region, the damaged section, and the undamaged portion were constructed in R and grouped by analysis window.

In the CATALYST environment, the intensity analysis generated the variables DI VV, DI VH, RI VV, RI VH, NDIC VV, and NDIC VH with regard to 15 coherence calculation windows. As a result, boxplots showing the average, minimum, and maximum values for the entire region, the damaged section, and the undamaged portion were created in R and grouped by analysis window.

The raster data series of the coherence and intensity variables were submitted to a signal to noise ratio (SNR) analysis in R, and only those variables with $SNR > 5$ were considered for each site.

These raster data were identified as inputs to the Principal Components Analysis (PCA), which was always carried out in R. In QGIS, a damage/undamaged classification map was prepared for each study area by using just the raster of the first component and iteratively determining and visualizing the value for which the damage area is closest to

the ground truth. Unlike the damage/undamaged classification work done by Aimaiti et al., (2022), in this case only Sentinel-1 data and a classification technique based on the analysis of polarimetric, coherence and intensity indices were used.

Finally, some considerations about the validity of the study were made by looking at both the polarimetric outputs and the confusion matrices connected to the classification maps. The Fig. 18 depicts a flowchart of the work done.

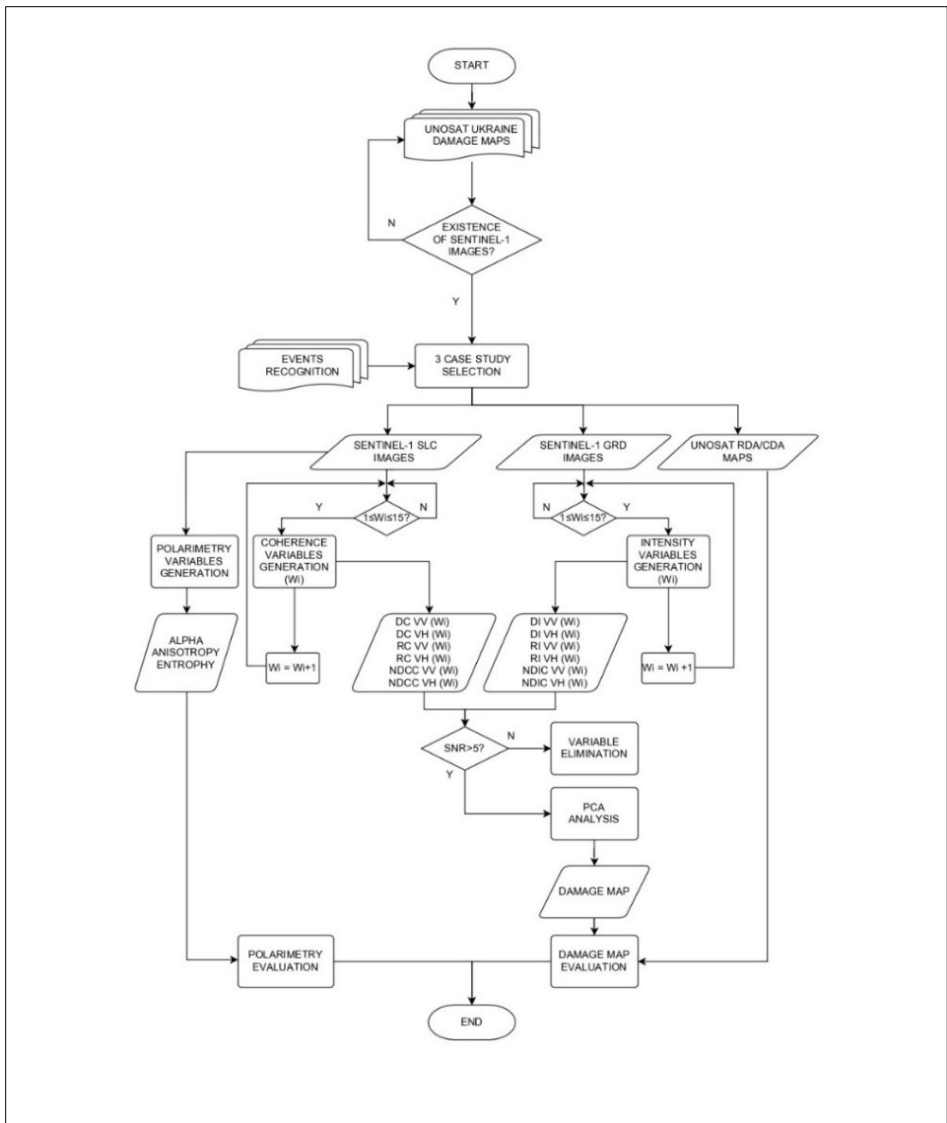


Fig. 18 – Global Framework

3. GROUND TRUTH

The United Nations Institute for Training and Research (UNITAR) provides innovative learning solutions to individuals, organizations and institutions to enhance global decision-making and support country-level action for shaping a better future. UNITAR was created in 1963 to train and equip young diplomats from newly-independent UN Member States with the knowledge and skills needed to navigate through the diplomatic environment. UNITAR provides training and capacity development activities to assist mainly developing countries with special attention to Least Developed Countries (LDCs), Small Island Developing States (SIDS) and other groups and communities who are most vulnerable, including those in conflict situations. The Institute is a project-based organization and does not receive any funds from the regular United Nations budget. UNITAR is financed entirely from voluntary contributions derived mainly from UN Member States, other UN agencies, international and intergovernmental organizations, foundations NGOs and the private sector. UNOSAT is the United Nations Satellite Centre, it is part of the UNITAR, with a mandate to provide United Nations funds, programmes and specialized agencies with satellite analysis, training and capacity development, at their request as well as support Member States with satellite imagery analysis over their respective territories and provide training and capacity development in the use of geospatial information technologies. Operational since 2003, UNOSAT's Emergency Mapping service provides satellite image analysis during humanitarian emergencies related to disasters, complex emergencies and conflict situations. With a 24/7 year-round availability to process requests, the team of experienced analysts ensure timely and tailored delivery of satellite imagery derived maps (both web and static maps), reports and data ready for direct inclusion in Geographic Information Systems (GIS) for evidence-based decision making and operational planning. UNOSAT can distribute both Rapid Building Damage Assessment Overview maps (RBDA) and Building Damage Assessment Overview maps (BDA). The RBDA maps are based on WorldView satellite images with a spatial

resolution of 30X30 cm. The RDBA divides the city into 500m x 500m cells, each of which is analyzed to determine whether or not there are damaged buildings inside the cell. Also, the BDA satellite maps are based on WorldView satellite images with a spatial resolution of 30X30 cm, but inside them the buildings that have suffered damage are reported with an indication of the level of damage and the level of reliability of the information derived from a visual analysis and in any case an in-situ investigation should follow. The choice of the investigation sites and the reconnaissance of the events whose damages are supposed to be detected through this thesis work take the UNOSAT maps described below as a reference, directly downloaded from the appropriate section of the UNOSAT website (<https://unosat.org/products/#map-section>) both in pdf, shapefile and geopackage format. All maps derive from a preliminary analysis and have not yet been validated in the field.

In detail, a shapefile allows to replicate pdf maps in interactive digital maps in GIS environments and in the case of the maps in question it consists of files with the following characteristics:

- .cpg file: describes a set of characters for displaying text in shapefiles; helps localize maps for specific languages.
- .dbf file: the file that stores feature attributes in a tabular format.
- .prj file: the file that contains information on projection format including the coordinate system and projection information. It is a plain text file describing the projection using well-known text (WKT) format.
- .qmd file: The QMD data files are related to Intuit Quicken. The QMD file is an Intuit Quicken Backup Data. Quicken is a personal finance management tool, with a vast array of features.
- .shp file: the file that contains the geometry for all features.
- .shx file: the file that indexes the geometry.

GeoPackage is a universal file format created for sharing and transferring vector and raster spatial data. It is therefore the alternative to raster and shapefile formats. It consists of a single .gpkg file, so it's ideal for transferring geospatial information. From

an operational point of view, in a GIS environment, digital maps are created by overlaying a base map of the area of interest (OSM standard) with the set of files constituting the shapefile or the single GeoPackage file.

In the present work, the RBDA files superimpose on each study area the georeferenced squares of side 500m colored in red for the damaged areas and in blue for the undamaged ones. the BDA files superimpose on each study area the series of points representing the damaged buildings georeferenced and colored differently based on the level of damage and the ascertained level of confidence.

West Kyiv, Hostomel, Bucha, Horenka and Irpin area RBDA shapefiles allow to digitally assemble single map of West Kyiv AOI. For the parts of Hostomel, Bucha and Irpin the BDA shapefiles allow to add to the assembled map the series of points containing the information of the damage concerning some buildings.

Mariupol and Chernihiv RBDA shapefiles require no assembly and allow to digitally replicate Mariupol AOI and Chernihiv AOI maps directly in your GIS environment. There are no BDA files for these areas of interest.

3.1 UNOSAT Maps of West Kyiv area

Unlike the study areas of Mariupol and Chernihiv, the area west of Kiev is divided into 5 parts according to UNOSAT sources: West-Kyiv, Hostomel, Horenka, Irpin and Bucha RBDA maps are available for all these parts, while BDA maps are available only for Hostomel, Irpin and Bucha. The map in Fig. 19 illustrates a satellite imagery-based Rapid Building Damage Assessment (RBDA) in Kotsiubynske and the western part of Kyiv City, Kyiv Oblast, Ukraine. Based on imagery collected on 31 March 2022 and on 25 March 2022, analysts found that 66 out of 4672 cells in western Kyiv sustained visible damage. This represents approximately 1.4% of the cells over the area. This analysis is based on structures visibly damaged as of 31 March 2022 and 25 March

2022 as seen in marginally degraded satellite imagery affected by light clouds and other limiting factors.



Fig. 19 – UNOSAT West Kyiv RBDA map. <https://www.unitor.org/maps/map/3524>.

The map in Fig. 20 illustrates a satellite imagery-based Rapid Damage Building Assessment (RDBA) in the Horenka, Kyiv region, Ukraine. The RDBA divides the city into 500m x 500m cells, each of which is analyzed to determine whether or not there are damaged buildings inside the cell. Based on imagery collected on 31 March 2022, analysts found that 51 cells out of 66 cells in Horenka sustained visible damage. This represents approximately 77% of the cells over the area. This analysis is based on structures visibly damaged as of 31 March 2022 as seen in marginally degraded satellite imagery affected by light clouds and other limiting factors.

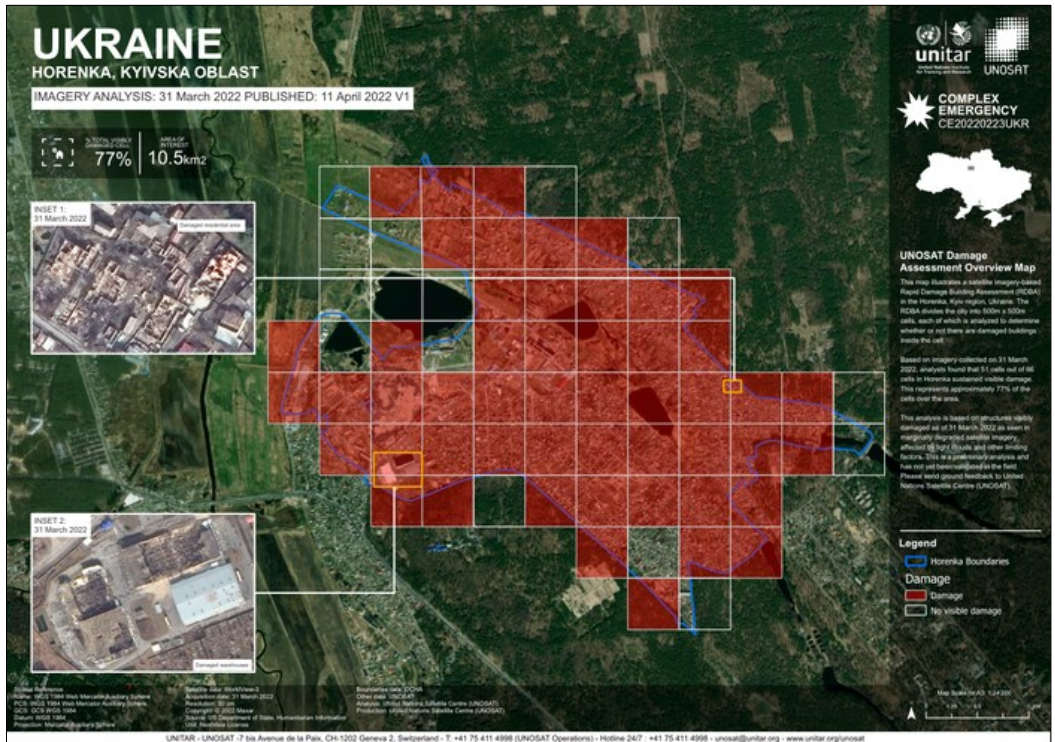


Fig. 20 – UNOSAT Horenka RBDA map. <https://www.unitar.org/maps/map/3523>.

The map in Fig. 21 illustrates a satellite imagery-based Rapid Damage Building Assessment (RBDA) in Hostomel City, Ukraine. The RBDA divides the city into 500m x 500m cells, each of which is analyzed to determine whether or not there are damaged buildings inside the cell. Based on imagery collected on 31 March 2022, analysts found that 125 cells out of 217 in the City of Hostomel sustained visible damage. This represents approximately 58% of the cells over the city. This analysis is based on structures visibly damaged as of 31 March 2022 as seen in marginally degraded satellite imagery affected by light clouds and other limiting factors. This analysis is based on structures visibly damaged as of 31 March 2022 as seen in marginally degraded satellite imagery affected by light clouds and other limiting factors. This analysis is based on structures visibly damaged as of 31 March 2022 as seen in marginally degraded satellite imagery affected by light clouds and other limiting factors. This analysis is based on structures visibly damaged as of 31 March 2022 as seen in marginally degraded satellite imagery affected by light clouds and other limiting factors.

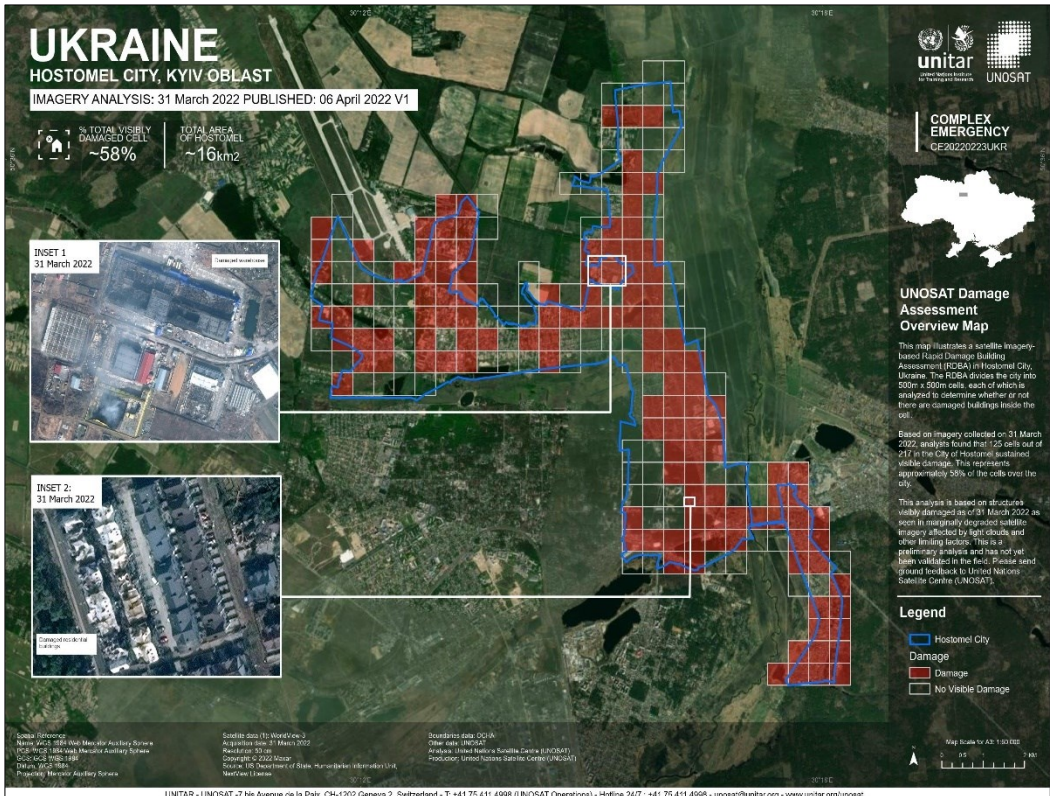


Fig. 21 – UNOSAT Hostomel RBDA map. <https://www.unisar.org/maps/map/3520>.

The map in Fig. 22 illustrates a satellite imagery-based building damage assessment (BDA) within an area of interest including Hostomel City, Ukraine, and the area of Antonov Airport. Based on imagery collected on 31 March 2022 and 20 February 2022, analysis show that 865 structures sustained damage visible in the satellite imagery. Out of these, 260 are destroyed, 138 severely damaged, 397 moderately damaged and 70 possibly damaged. While no complete count of buildings for Hostomel is available an open-source dataset which is visibly incomplete indicates at least 3,116 structures in the area. This analysis is based on structures visibly damaged as of 31 March 2022 as seen in marginally degraded satellite imagery affected by light clouds and other limiting factors.

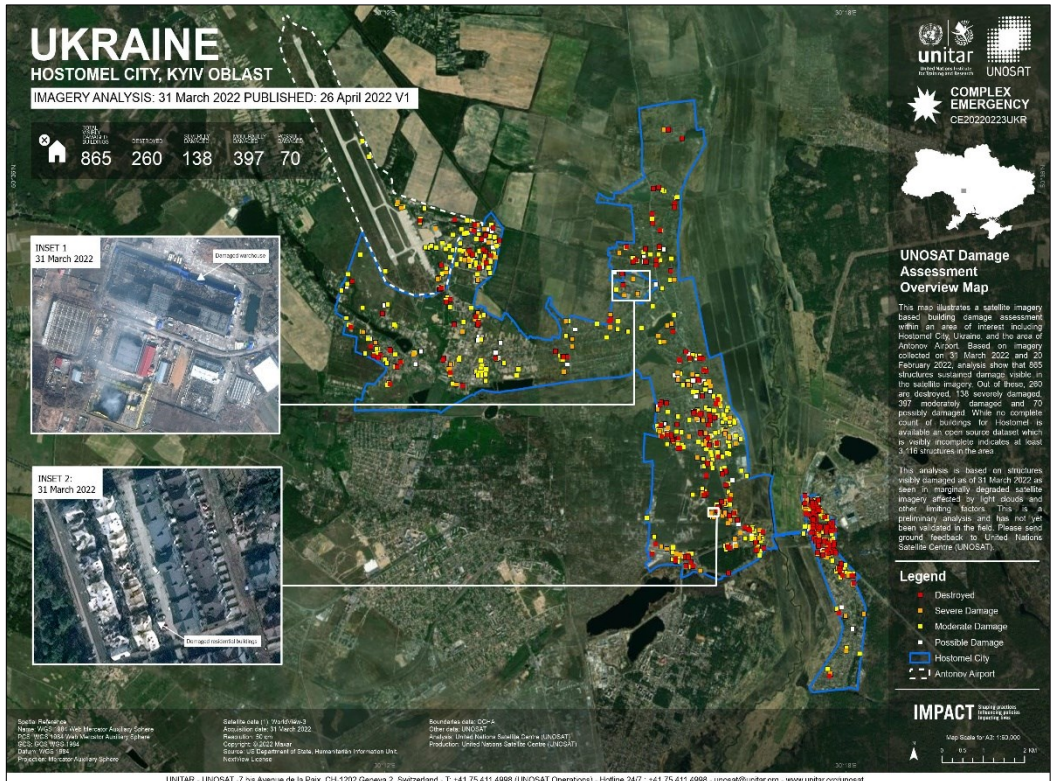


Fig. 22 – UNOSAT Hostomel BDA map. <https://www.unitor.org/maps/map/3533>.

The map in Fig. 23 illustrates a satellite imagery-based Rapid Damage Building Assessment (RDBA) in Irpin City, Kyiv Oblast, Ukraine. The RDBA divides the city into 500m x 500m cells, each of which is analyzed to determine whether or not there are damaged buildings inside the cell. Based on imagery collected on 31 March 2022, analysts found that 176 cells out of 246 in the City of Irpin sustained visible damage. This represents approximately 71% of the cells over the city. This analysis is based on structures visibly damaged as of 31 March 2022 as seen in marginally degraded satellite imagery affected by light clouds and other limiting factors.

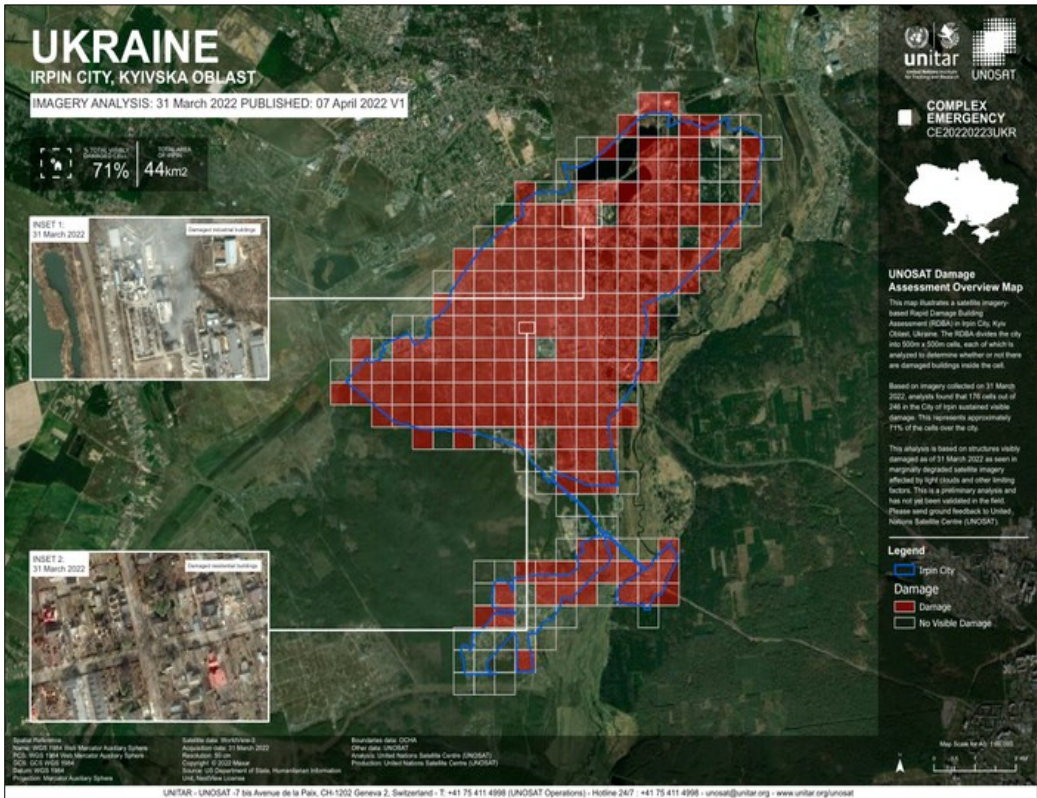


Fig. 23 – UNOSAT Irpin RBDA map. <https://www.unitar.org/maps/map/3521>.

The map in Fig. 24 illustrates a satellite imagery-based building damage assessment in Irpin City, Ukraine, based on imagery collected on 31 March 2022, analysts found that 1,060 structures sustained damage visible on the satellite imagery. Out of these, 115 are destroyed, 698 severely damaged, 187 moderately damaged and 60 possibly damaged. This includes 4 education facilities and 3 health facilities. While no complete count of buildings for Irpin is available, an open-source dataset which is visibly incomplete indicates at least 3,732 structures in the area. This analysis is based on

structures visibly damaged as of 31 March 2022 as seen in marginally cloudy satellite imagery.

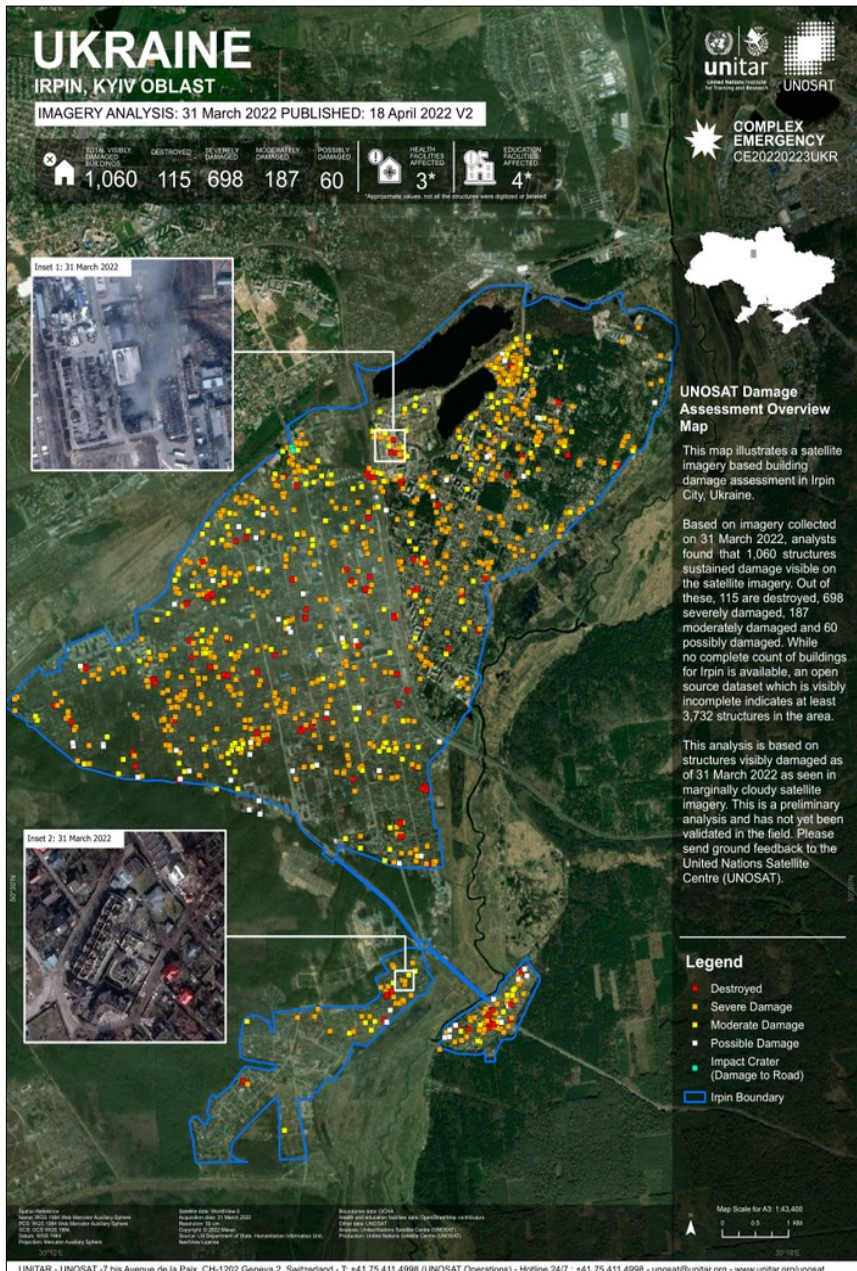


Fig. 24 – UNOSAT Irpin BDA map. <https://unosat.org/products/3360>.

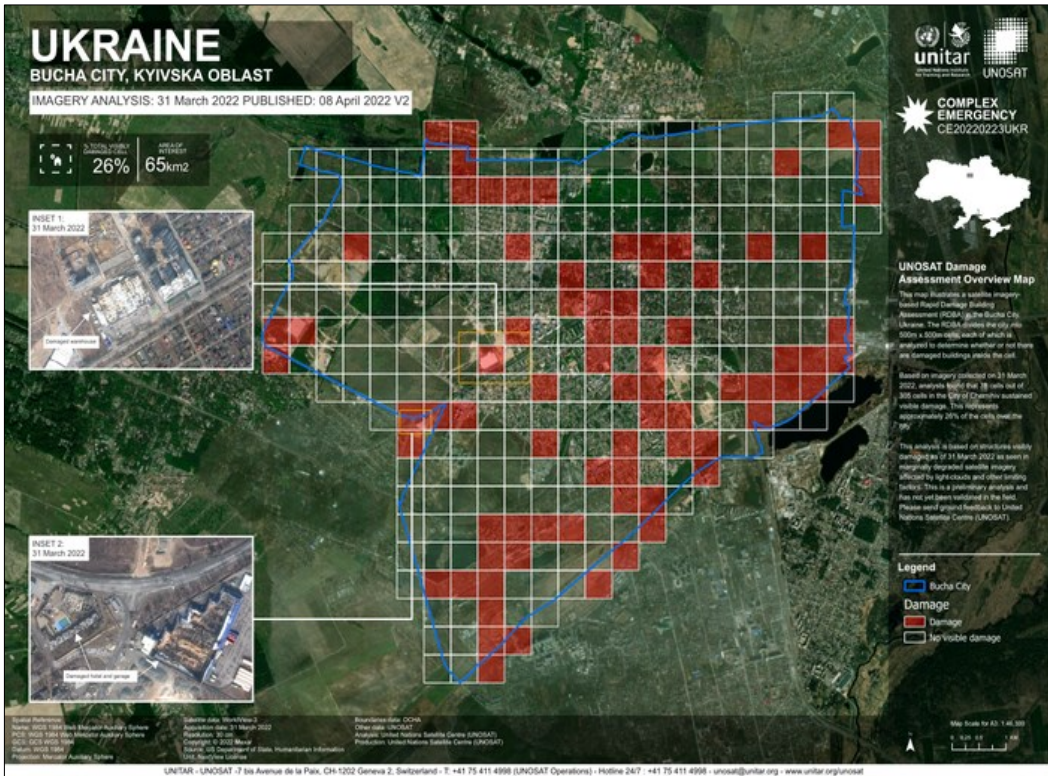


Fig. 25 – UNOSAT Bucha RBDA map. <https://unosat.org/products/3367>.

The map in Fig. 25 illustrates a satellite imagery-based Rapid Damage Building Assessment (RDBA) in the Bucha City, Ukraine.

The RDBA divides the city into 500m x 500m cells, each of which is analyzed to determine whether or not there are damaged buildings inside the cell. Based on imagery collected on 31 March 2022, analysts found that 82 cells out of 305 cells in the City of Bucha sustained visible damage. This represents approximately 27% of the cells over the city. This analysis is based on structures visibly damaged as of 31 March 2022 as seen in marginally degraded satellite imagery affected by light clouds and other limiting factors.

The map in Fig. 26 illustrates a satellite imagery-based building damage assessment within an area of interest (AOI) including Bucha City, Ukraine, and a small area on the western edge. Based on imagery collected on 31 March 2022 and 20 February 2022,

analysts found that 147 structures sustained damage visible in the satellite imagery. Out of these, 19 are destroyed, 72 severely damaged, 27 moderately damaged and 29 possibly damaged. This includes 3 health facilities. While no complete count of buildings for Bucha is available an open-source dataset which is visibly incomplete indicates at least 2,373 structures in the area. This analysis is based on structures visibly damaged as of 31 March 2022 as seen in marginally degraded satellite imagery affected by light clouds and other limiting factors.

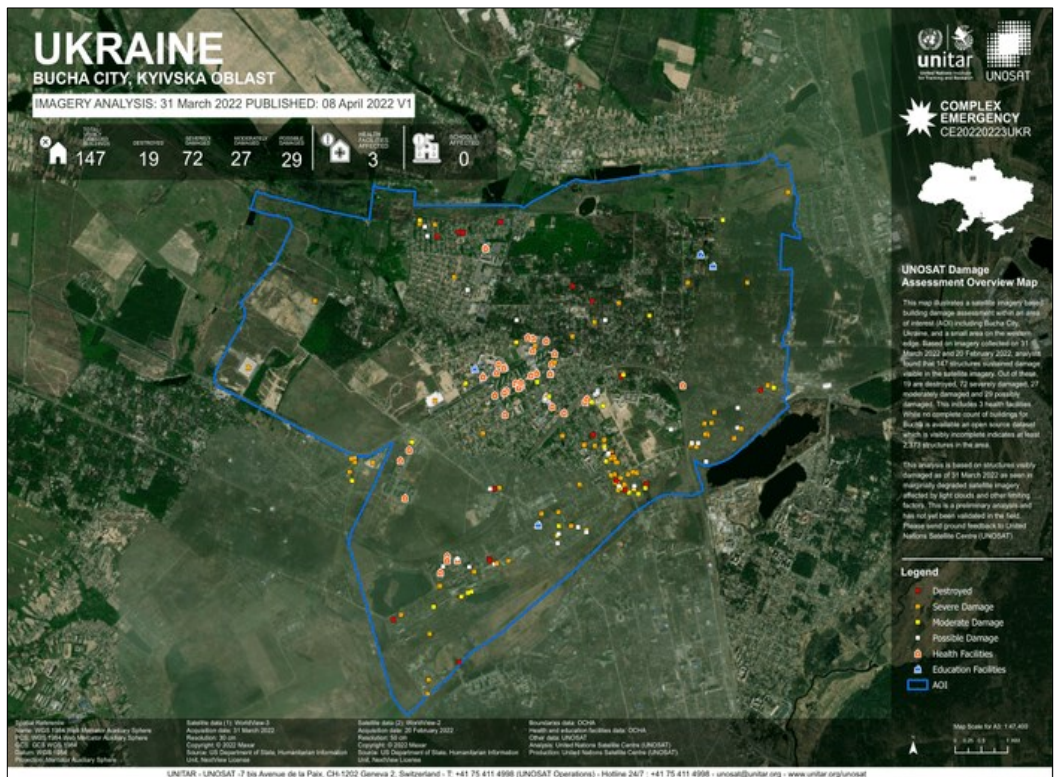


Fig. 26 – UNOSAT Bucha BDA map. <https://www.unitar.org/maps/map/3522>.

3.2 UNOSAT Map of Mariupol

At the time of the study, the Mariupol area was only equipped with the RBDA-type UNOSAT Map. Fig. 27 illustrates a satellite imagery-based Rapid Damage Building Assessment (RBDA) of the Mariupolska Hromada, Ukraine.

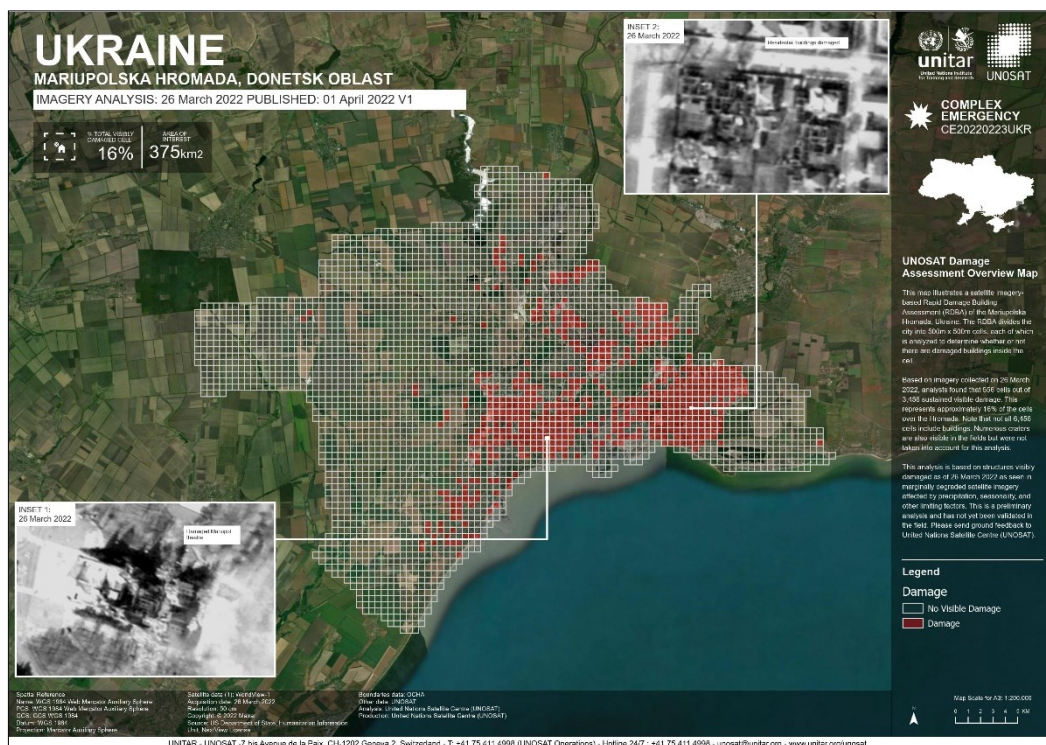


Fig. 27 – UNOSAT Mariupol RBDA map. <https://www.unitar.org/maps/map/3514>.

The RBDA divides the city into 500m x 500m cells, each of which is analyzed to determine whether or not there are damaged buildings inside the cell. Based on imagery collected on 26 March 2022, analysts found that 556 cells out of 3,456 sustained visible damage. This represents approximately 16% of the cells over the Hromada. Note that not all 3,456 cells include buildings. Numerous craters are also visible in the fields but were not taken into account for this analysis. This analysis is based on structures visibly damaged as of 26 March 2022 as seen in marginally degraded satellite imagery affected by precipitation, seasonality, and other limiting factors.

3.3 UNOSAT Map of Chernihiv

Even the Chernihiv area, at the time of the study, was only equipped with the RBDA-type UNOSAT Map.

The RBDA illustrates in Fig. 28 divides the city into 500m x 500m cells, each of which is analyzed to determine whether or not there are damaged buildings inside the cell. Based on imagery collected on 22 March 2022, analysts found that 191 cells out of 901 cells in the City of Chernihiv sustained visible damage. This represents approximately 21% of the cells over the city. This analysis is based on structures visibly damaged as of 22 March 2022.

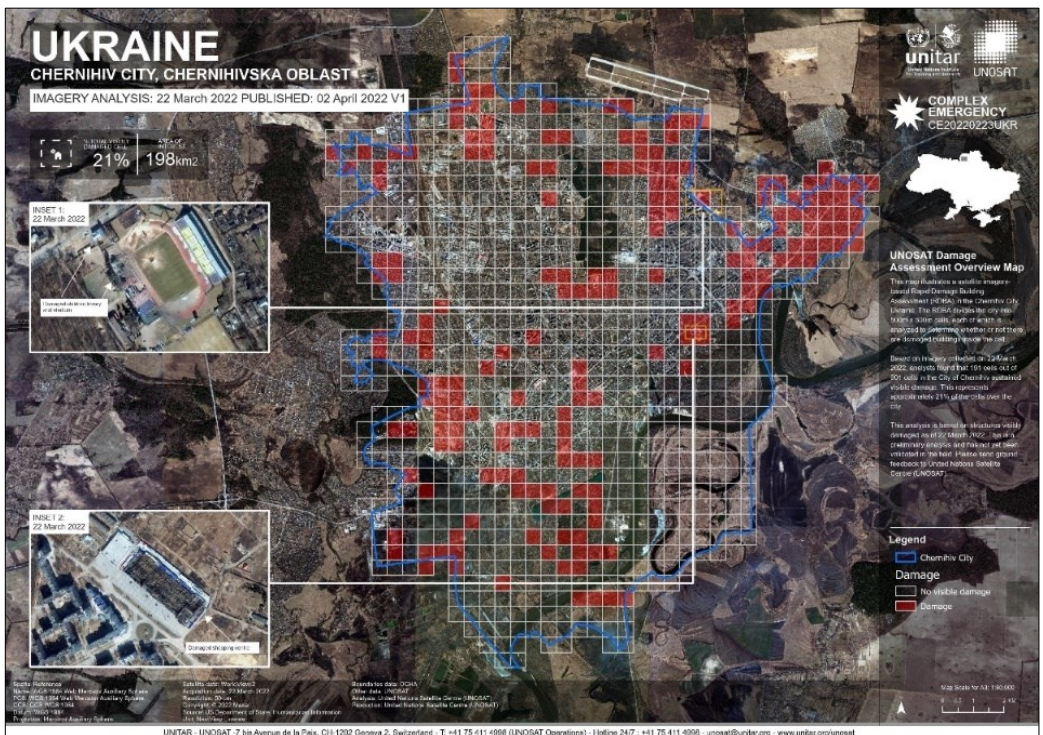


Fig. 28 – UNOSAT Chernihiv RBDA map. <https://www.unitar.org/maps/map/3515>.

4. SENTINEL-1 DATASET

The dataset of the satellite images used in the thesis work consists of images obtained from a C band synthetic aperture radar sensor placed on board the Sentinel-1A satellite belonging to the Sentinel-1 mission of the European Copernicus Program. Descriptions of the items in question follow.

4.1. Copernicus Programme

Copernicus is the European Union's Earth observation programme, looking at our planet and its environment to benefit all European citizens. It offers information services that draw from satellite Earth Observation and in-situ (non-space) data. The European Commission manages the Programme. It is implemented in partnership with the Member States, the European Space Agency (ESA), the European Organization for the Exploitation of Meteorological Satellites (EUMETSAT), the European Centre for Medium-Range Weather Forecasts (ECMWF), EU Agencies and Mercator Océan. Vast amounts of global data from satellites and ground-based, airborne, and seaborne measurement systems provide information to help service providers, public authorities, and other international organizations improve European citizens' quality of life and beyond. The information services provided are free and openly accessible to users. Copernicus is served by a set of dedicated satellites (the Sentinel families) and contributing missions (existing commercial and public satellites). The Sentinel satellites are specifically designed to meet the needs of the Copernicus services and their users. Since the launch of Sentinel-1A in 2014, the European Union set in motion a process to place a constellation of almost 20 more satellites in orbit before 2030 (sentinel.copernicus.eu, 2022).

4.2. Sentinel-1 Mission

The Sentinel-1 mission is composed of a constellation of two satellites, Sentinel-1A and Sentinel-1B. Sentinel-1A was launched on 3 April 2014. Sentinel-1B was launched

on 25 April 2016. Two other spacecraft (Sentinel-1C and Sentinel-1D) are planned to replace the first two satellites at the end of their operational lifespan. Sentinel-1 is in a near-polar, sun-synchronous orbit with a 12 day repeat cycle and 175 orbits per cycle for a single satellite, have a height of 693 km and an inclination of 98.18° inclination. Both Sentinel-1A and Sentinel-1B share the same orbit plane with a 180° orbital phasing difference. With both satellites operating, the repeat cycle is six days.

The satellites are equipped with a Synthetic Aperture Radar (SAR) sensor which has the advantage of operating at wavelengths of the C-band (centre frequency of 5.405 GHz corresponding to a wavelength of ~5.546 cm) not impeded by cloud cover or a lack of illumination and can acquire data over a site during day or night time under all weather conditions. Sentinel-1 provides dual polarization capability (VV+VH, HH+HV, HH, VV) (sentinel.copernicus.eu, 2022).

The Sentinel-1 imaging operating in four exclusive imaging modes with different resolution: Stripmap (SM), Interferometric Wide swath (IW), Extra-Wide swath (EW) and Wave mode (WV) (Fig. 29). Stripmap imaging mode is provided for continuity with ERS and Envisat missions. Stripmap provides coverage with a 5 m by 5 m resolution over a narrow swath width of 80 km. One of six imaging swaths can be selected by changing the beam incidence angle and the elevation beamwidth. The Interferometric Wide swath (IW) mode allows combining a large swath width (250 km) with a moderate geometric resolution (5 m by 20 m). The IW mode images three sub-swaths using Terrain Observation with Progressive Scans SAR (TOPSAR). With the TOPSAR technique, in addition to steering the beam in range as in SCANSAR, the beam is also electronically steered from backward to forward in the azimuth direction for each burst, avoiding scalloping and resulting in a higher quality image. Interferometry is ensured by sufficient overlap of the Doppler spectrum (in the azimuth domain) and the wave number spectrum (in the elevation domain). The TOPSAR technique ensures homogeneous image quality throughout the swath. The IW mode is the default

acquisition mode over land. The Extra Wide swath imaging mode is intended for maritime, ice and polar zone operational services where wide coverage and short revisit times are demanded (Fig. 29).

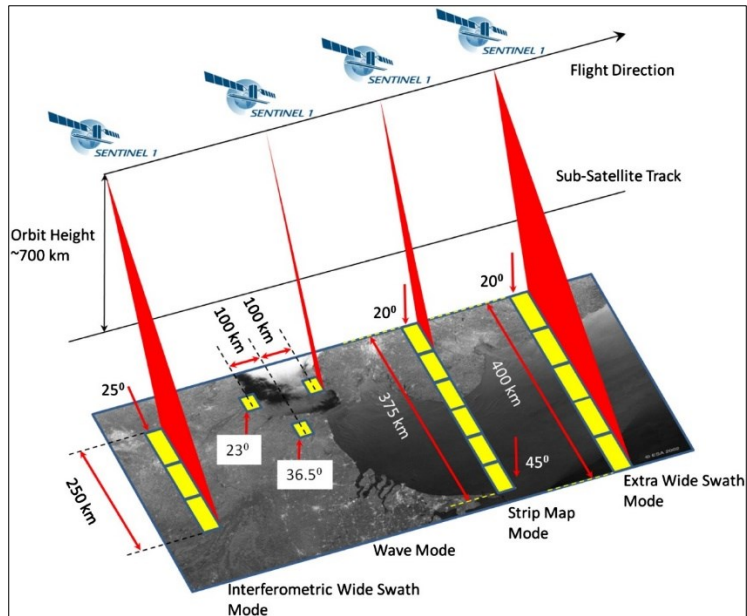


Fig. 29 – Sentinel-1 acquisition modes.

<https://sentinel.esa.int/web/sentinel/missions/sentinel-1/instrument-payload>

The EW mode works similarly to the IW mode employing a TOPSAR technique using five sub-swaths instead of three, resulting in a lower resolution (20 m by 40 m). The EW mode can also be used for interferometry as with the IW mode. Wave mode, in conjunction with global ocean wave models, can help determine the direction, wavelength and heights of waves on the open oceans. Wave mode acquisitions are composed of stripmap imageries of 20 km by 20 km, acquired alternately on two different incidence angles. Wave imageries are acquired every 100 km, with imageries on the same incidence angle separated by 200 km (sentinel.copernicus.eu, 2022).

The objectives of the Sentinel-1 mission are:

- Land monitoring of forests, water, soil and agriculture

- Emergency mapping support in the event of natural disasters
- Marine monitoring of the maritime environment
- Sea ice observations and iceberg monitoring
- Production of high-resolution ice charts
- Forecasting ice conditions at sea
- Mapping oil spills
- Sea vessel detection
- Climate change monitoring (sentinel.copernicus.eu, 2022).

4.3. Sentinel-1 Products

Sentinel-1 data products are made available systematically and free of charge to all data users including the public, scientific and commercial users. The data will be delivered within an hour of reception for Near Real-Time (NRT) emergency response, within three hours for NRT priority areas and within 24 hours for systematically archived data. All data products are distributed in the Sentinel Standard Archive Format for Europe (SAFE) format. Each mode can potentially produce products at SAR Level-0, Level-1 SLC, Level-1 GRDH, and Level-2 OCN. Data products are available in single polarization (VV or HH) for Wave mode and dual polarization (VV+VH or HH+HV) or single polarization (HH or VV) for SM, IW and EW modes (Fig. 30).

Level-0 products consist of the sequence of Flexible Dynamic Block Adaptive Quantization (FDBAQ) compressed unfocused SAR raw data. For the data to be usable, it will need to be decompressed and processed using a SAR processor. Level-1 data are the generally available products intended for most data users. Level-1 products are produced as Single Look Complex (SLC) and Ground Range Detected (GRDH). Level-1 Single Look Complex (SLC) products consist of focused SAR data geo-referenced using orbit and attitude data from the satellite and provided in zero-Doppler slant-range geometry. The products include a single look in each dimension using the full transmit signal bandwidth and consist of complex samples preserving the phase information.

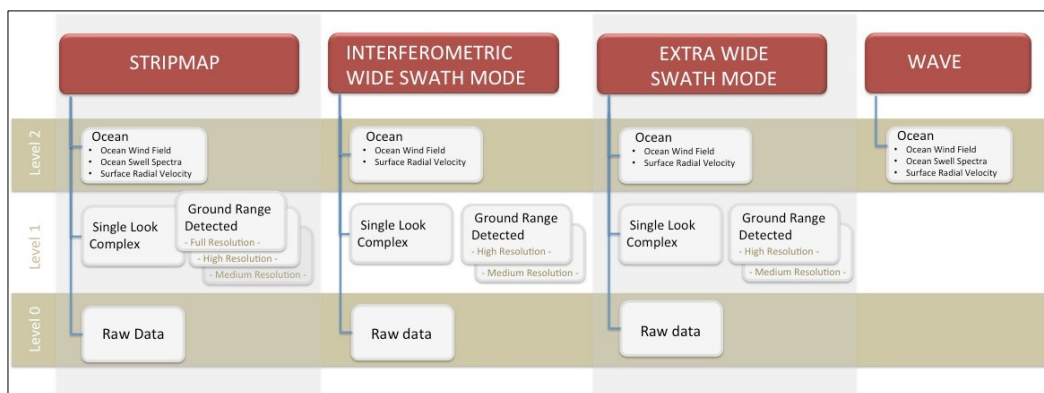


Fig. 30 – Graphical Representation of Sentinel-1 Core Products.
<https://sentinels.copernicus.eu/web/sentinel/missions/sentinel-1/data-products>

Level-1 Ground Range Detected (GRDH) products consist of focused SAR data that has been detected, multi-looked and projected to ground range using an Earth ellipsoid model. Phase information is lost. The resulting product has approximately square spatial resolution pixels and square pixel spacing with reduced speckle at the cost of worse spatial resolution. GRDH products can be in one of three resolutions: Full Resolution (FR), High Resolution (HR) Medium Resolution (MR). The resolution is dependent upon the amount of multi-looked performed. Level-1 GRDH products are available in MR and HR for IW and EW modes, MR for WV mode and MR, HR and FR for SM mode.

Level-2 OCN products include components for Ocean Swell spectra (OSW) providing continuity with ERS and ASAR WV and two new components: Ocean Wind Fields (OWI) and Surface Radial Velocities (RVL). The OSW is a two-dimensional ocean surface swell spectrum and includes an estimate of the wind speed and direction per swell spectrum. The OSW is generated from Stripmap and Wave modes only. For Stripmap mode, there are multiple spectra derived from internally generated Level-1 SLC images. For Wave mode, there is one spectrum per vignette. The OWI is a ground range gridded estimate of the surface wind speed and direction at 10 m above the surface derived from internally generated Level-1 GRDH images of SM, IW or EW modes. The RVL is a ground range gridded difference between the measured Level-2 Doppler grid and the Level-1 calculated geometrical Doppler (sentinels.copernicus.eu, 2022).

4.4. Sentinel-1 Data Acquisition

Sentinel-1 images were acquired through NASA's "Alaska Satellite Facility (ASF) Data Search" portal (<https://search.asf.alaska.edu/#/>), which allows the search and download of all types of images acquired and made available by the Copernicus program. The ASF is a structure that deals with ground processing of data from satellite devices; it is located in the geophysical institute of the University of Alaska at Fairbanks. The goal of the facility is to make remote sensing data accessible for research on climate change in the polar areas, marine pollution and changes occurring in the Amazon rainforest (Kaupp & Holt, 1998).

The determination of the variables in each of the study areas took place through a change detection operation between two pairs of images (Plank, 2014a). Considering the start of the war on February 24, 2022, as the reference date (Choudhary et al., 2022), the first pair is made up of image 1 (pre-war 1) and image 2 (pre-war 2) of which the first is temporally prior to the second. The second pair consists of image 2 (pre-war 2) and image 3 (war in progress) (Fig. 31).

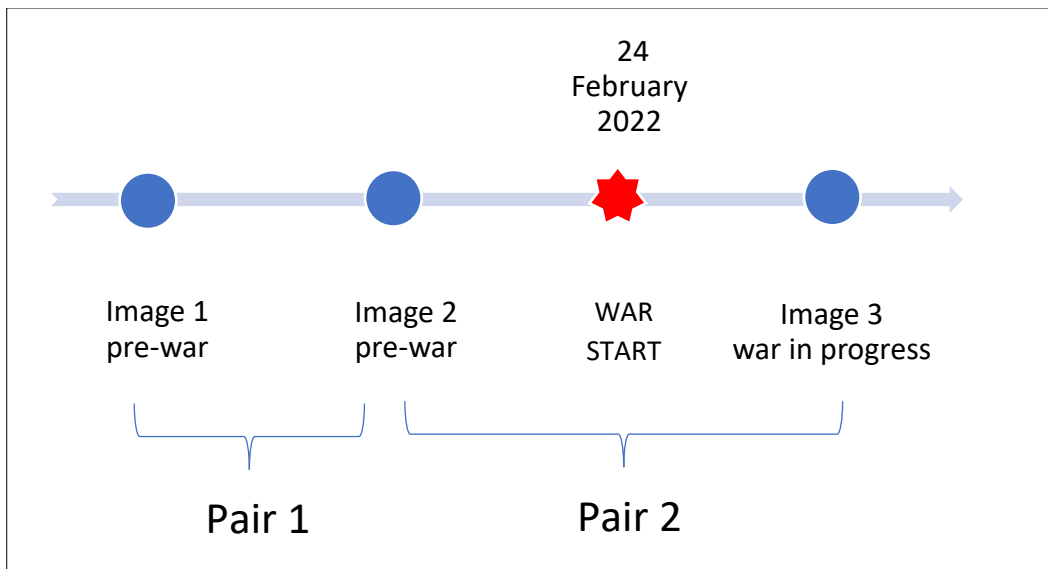


Fig. 31 – Images Scheme

Coherence variables and the polarimetric analysis require the phase data only present in the SLC type images (Wegmüller et al., 2015a; Ma et al., 2019; Wegmüller et al., 2015b), while for intensity variables it is possible to make use of the GRDH type images equipped with a greater number of pre-processing compared to SLC images and can be processed with fewer steps and in less time than the same SLCs (Malmgren-Hansen et al., 2020; Bhogapurapu et al., 2022). Therefore, both the SLC data and the GRDH data were downloaded for each scene. The three scenes relating to each of the study areas have the same acquisition geometry or the same relative number of orbit, the same path, as well as the same acquisition moment within the three dates considered. Image 3 was chosen on the same date or closest to that of the basic satellite data of the UNOSAT image assumed as ground truth.

Image 2 was chosen in correspondence with the date of February 24, 2022, or on a date in which no damage events are recorded within the study area.

Image 1 was chosen at a date prior to February 24th in such a way as to overlap perfectly with image 2 and image 3.

Although the thesis refers exclusively to Sentinel-1 images due to the series of advantages deriving from them, including the possibility of investigating the territory even in the absence of light or in conditions of cloud cover (Chuvieco et al., 2019), the choice of radar images fell in diurnal circumstances and with a cloud cover percentage lower than 30% in order to allow future developments based on the comparison with outputs deriving from the field of passive remote sensing.

Considering the reading key of the name associated with the file directly downloaded from the ASF Portal shown in Fig. 32, Tab. 1 shows the list of Sentinel-1 files used to investigate each of the study areas.

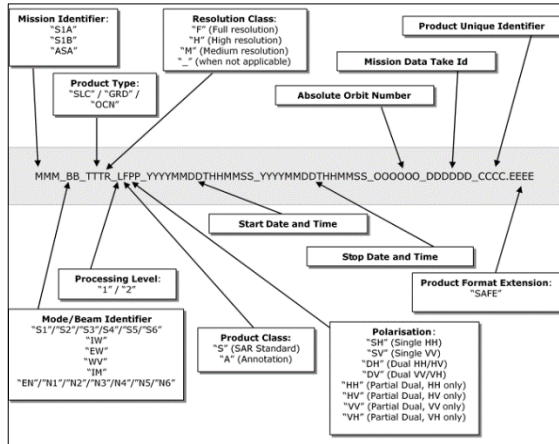


Fig. 32 – Product Naming Convention. <https://sentinels.copernicus.eu/web/sentinel/technical-guides/sentinel-1-sar/products-algorithms/level-1-product-formatting>.

WEST KYVIV AREA	
Image 1	S1A_IW_SLC_1SDV_20220212T155417_20220212T155445_041882_04FC79_5E5E.SAFE
	S1A_IW_GRDH_1SDV_20220212T155418_20220212T155443_041882_04FC79_6C49.SAFE
Image 2	S1A_IW_SLC_1SDV_20220224T155417_20220224T155445_042057_05028F_74F5.SAFE
	S1A_IW_GRDH_1SDV_20220224T155418_20220224T155443_042057_05028F_AEE3.SAFE
Image 3	S1A_IW_SLC_1SDV_20220401T155417_20220401T155445_042582_05145B_1A4C.SAFE
	S1A_IW_GRDH_1SDV_20220401T155418_20220401T155443_042582_05145B_711E.SAFE
MARIUPOL AREA	
Image 1	S1A_IW_SLC_1SDV_20211112T152023_20211112T152050_040540_04CED3_059E.SAFE
	S1A_IW_GRDH_1SDV_20211112T152024_20211112T152049_040540_04CED3_04D8.SAFE
Image 2	S1A_IW_SLC_1SDV_20220111T152020_20220111T152047_041415_04ECA5_FED1.SAFE
	S1A_IW_GRDH_1SDV_20220111T152022_20220111T152047_041415_04ECA5_EFB4.SAFE
Image 3	S1A_IW_SLC_1SDV_20220324T152019_20220324T152046_042465_05106A_C4A7.SAFE
	S1A_IW_GRDH_1SDV_20220324T152021_20220324T152046_042465_05106A_CC37.SAFE
CHERNIHIV AREA	
Image 1	S1A_IW_SLC_1SDV_20220202T153802_20220202T153837_041736_04F764_3B47.SAFE
	S1A_IW_GRDH_1SDV_20220202T153803_20220202T153837_041736_04F764_AE7F.SAFE
Image 2	S1A_IW_SLC_1SDV_20220214T153802_20220214T153837_041911_04FD80_5217.SAFE
	S1A_IW_GRDH_1SDV_20220214T153803_20220214T153837_041911_04FD80_95CE.SAFE
Image 3	S1A_IW_SLC_1SDV_20220322T153802_20220322T153837_042436_050F68_7949.SAFE
	S1A_IW_GRDH_1SDV_20220322T153803_20220322T153837_042436_050F68_A3A1.SAFE

Tab. 1 – Sentinel-1 Dataset

5. STUDY AREAS

Three study areas affected by war events found in UNOSAT maps were chosen in order to try to define a criterion/algorithm for identifying damaged areas using Sentinel-1 data valid throughout the Ukrainian territory during the current war. It was opted for the choice of urbanized territories of different extensions, one of which is densely urbanized (West Kyviv area), one located on the coast (Mariupol) and the other of small extension (Chernihiv) (Fig. 33). Details about each site are given below.

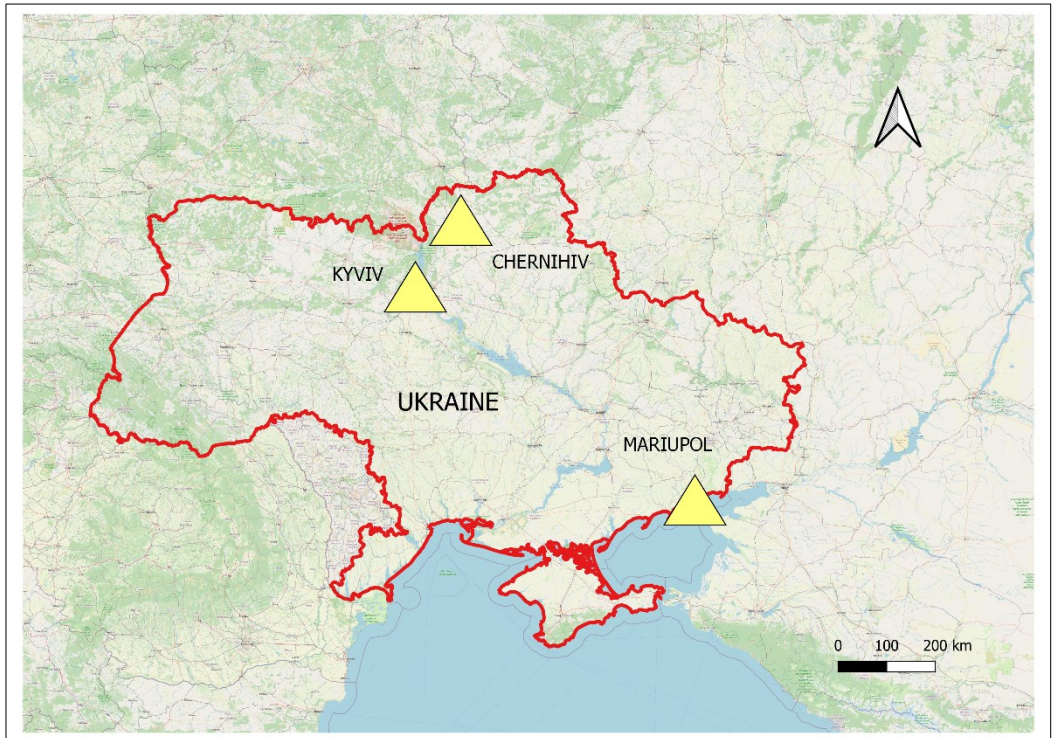


Fig. 33 – The location of the three sites within the Ukrainian territory.

5.1 West Kyviv area

The study area covers part of the cities of Kyviv, Bucha, Hostomel, Horenka and Irpin. Kyiv, also known as Kiev, is the capital and most populous city of Ukraine. It is located at 50°27'00" Latitude and 30°31'25" Longitude. It is in north-central Ukraine along the Dnieper River. Kyiv has an area of about 839 km², is located at an altitude of 179 m a.s.l. As of 1 January 2021, its population was 2.962.180 (3.299 ab/Km²) (Service for State Statistics of Ukraine, 2022).

Bucha is a city in Ukraine's Kyiv Region. Administratively, it serves as the administrative center of Bucha District. It hosts the administration of Bucha urban community. It is located at 50°32'55" Latitude and 30°13'15" Longitude. Bucha has an area of about 26.57 km², is located at an altitude of 148 m a.s.l. In 2021 its population was 36.971 (1.400 ab/Km²) (www.bucha-rada.gov.ua, 2022).

Hostomel is a city in northern Ukraine located in Kyiv Region and Bucha District. It is mainly known for the nearby Kiev-Hostomel Airport, hub of the cargo airline Antonov Airlines and military base of the Ukrainian Air Force. it is located at 50°35'21,4" Latitude and 30°15'30,03" Longitude. Hostomel has an area of about 6,4 km², is located at an altitude of 109 m a.s.l. In 2021 its population was 17.534 (2739 ab/Km²) (Service for State Statistics of Ukraine, 2022).

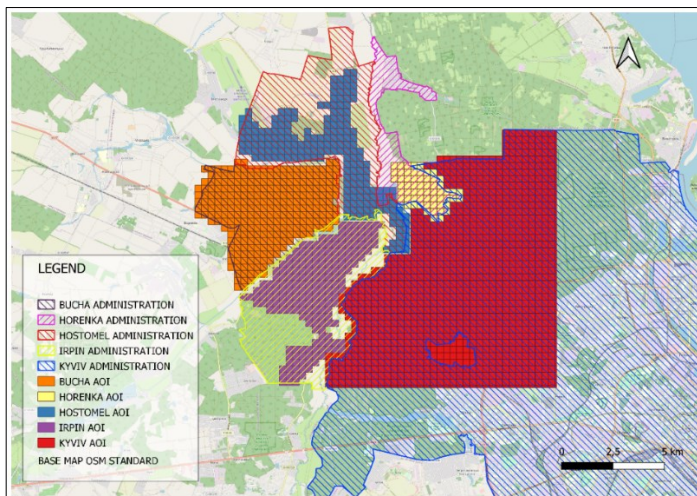


Fig. 34 – West Kyiv AOI.

Horenka is a village in Bucha District in Kyiv Region of Ukraine, on the NW border of the city of Kyiv. It belongs to Hostomel settlement community. It is located at 50°33'25" Latitude and 30°19'03" Longitude. Horenka has an area of about 29,1 km², is located at an altitude of 116 m a.s.l. In 2021 its population was 8.972 (308 ab/Km²) (Service for State Statistics of Ukraine, 2022).

Irpın is a city in northern Ukraine in Kyiv Region and Bucha District. It is located in the northern portion of Ukraine west of Kiev on the banks of the river of the same name. It is located at 50°31' Latitude and 30°15' Longitude. Irpın has an area of about 110,83 km², is located at an altitude of 121 m a.s.l. In 2021 its population was 62.456 (563,53 ab/Km²) (Service for State Statistics of Ukraine, 2022). The Fig. 34 shows all the areas of interest relating to the western area of Kyiv. The Fig. 35 shows the single map of the West of Kyiv Area of Interest in which it is possible to distinguish in red the squares of 500X500 meters defined as affected by damage and in blue those defined as not affected by damage according to UNOSAT analyses.

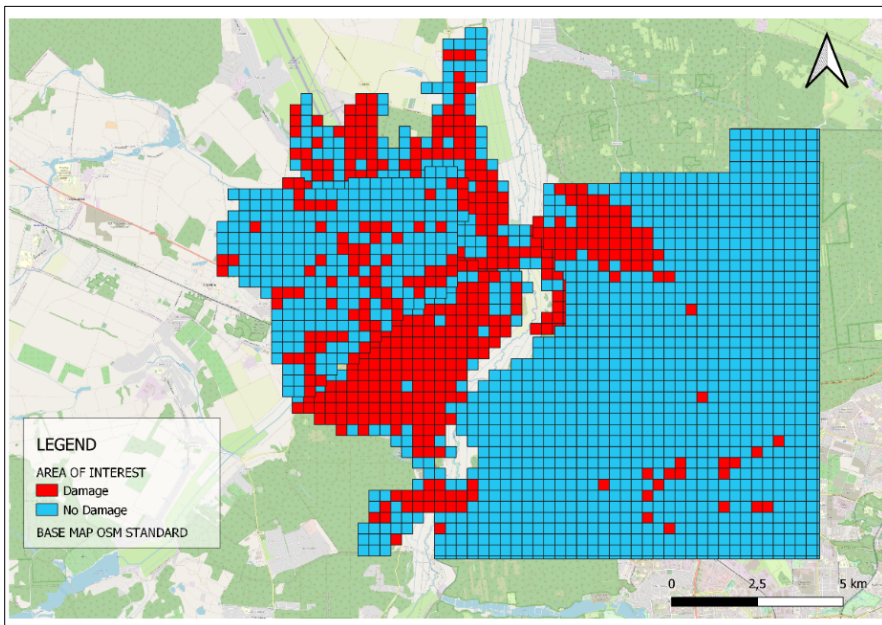


Fig. 35 – West Kyiv AOI. Damage and No Damage squares

5.2 Mariupol

Mariupol is a city in southeastern Ukraine in the Priazovia Region, located in Donetsk District and the capital of district of the same name. Since May 2022, it has been a de facto part of the Donetsk People's Republic. The city is located on the northern coast of the Sea of Azov at the mouth of the Kalmius River. The Port of Mariupol is located in the Taganrog Bay, Sea of Azov. The port is governed by the port authority managed by Ukrainian Sea Ports Authority. Mariupol is located at 47°07'50" Latitude and 37°33'50" Longitude. Mariupol has an area of about 166 km², is located at an altitude of 166 m a.s.l. As of 1 January 2021, its population was 421.859 (2.601,56 ab/Km²) (Service for State Statistics of Ukraine, 2022). The Fig. 36 shows the map of the Mariupol Area of Interest in which it is possible to distinguish in red the squares of 500X500 meters defined as affected by damage and in blue those defined as not affected by damage according to UNOSAT analyses.

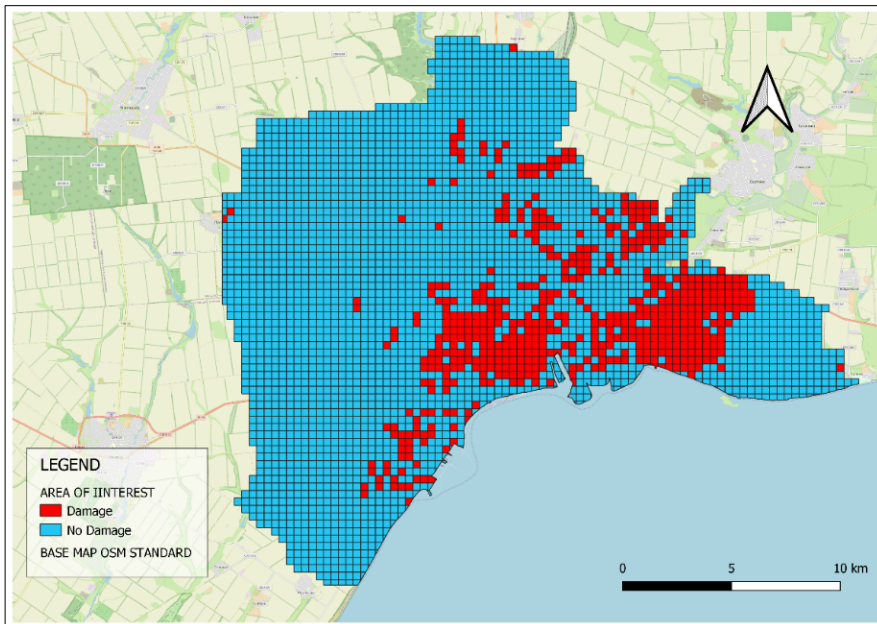


Fig. 36 – Mariupol AOI. Damage and No Damage squares.

5.3 Chernihiv

Chernihiv is a city in northern Ukraine, the capital of the homonymous region and of the homonymous district. Chernihiv is situated on the northern tip of the Dnipro Lowland on the banks of the Desna River, the left tributary of the Dnipro. Chernihiv is located at 51°29'38" Latitude and 31°17'41" Longitude. Chernihiv has an area of about 79 km², is located at an altitude of 136 m a.s.l. As of 1 January 2021, its population was 285.234 (36010,55 ab/Km²) (Service for State Statistics of Ukraine, 2022). The Fig. 37 shows the map of the Mariupol Area of Interest in which it is possible to distinguish in red the squares of 500X500 meters defined as affected by damage and in blue those defined as not affected by damage according to UNOSAT analyses.

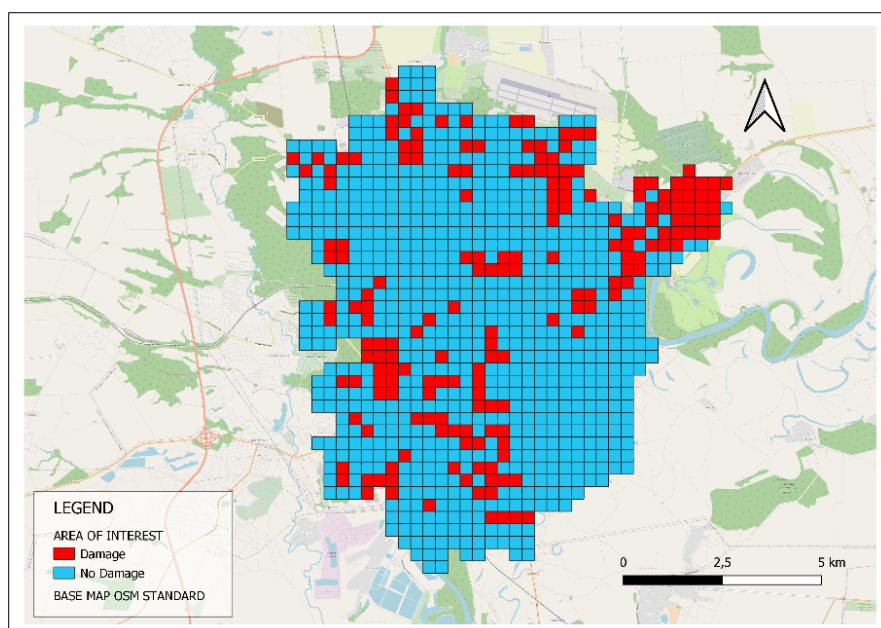


Fig. 37 – Chernihiv AOI. Damage and No Damage squares.

5.4 Synthesis of the Investigated Surfaces

Tab. 2 and Fig. 38 illustrate the synthesis of the analysis of the shapefiles of the UNOSAT maps which took place in QGIS, distinguishing for each study area the total surface investigated visually, the total surfaces of the cells defined as damaged and the total of those defined as undamaged.

AOI	Total Area [m ²]	Damage Area [m ²]	No Damage Area [m ²]
West Kyviv	183.174.608	46.508.874	136.665.734
Mariupol	400.194.779	64.402.364	335.792.415
Chernihiv	87.423.739	18.527.453	68.896.285

Tab. 2 – Synthesis of UNOSAT surfaces investigated.

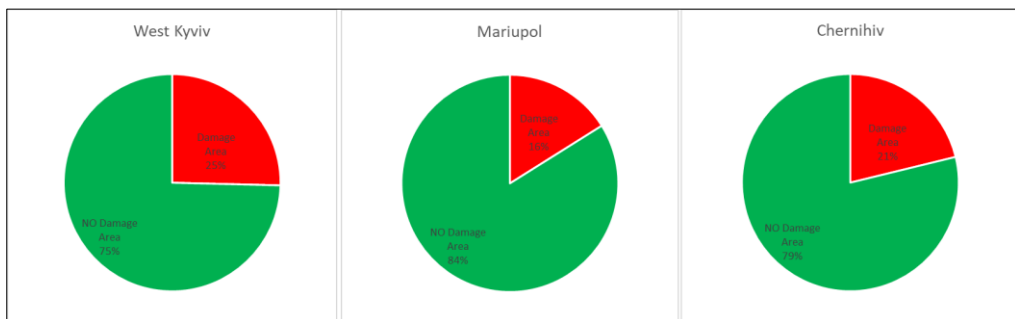


Fig. 38 – Aerograms of UNOSAT surfaces investigated.

6. EVENTS IN THE STUDY AREAS

For each of the three study areas, the series of events that caused damage to the urban territory potentially detectable with high-resolution satellite images is reported. Therefore, events concerning missile launches, rockets and bombings confirmed by news articles of international significance are listed, omitting guerrilla events and everything that, at least in this context, would not have any effect. The three collections end on dates such that the reported events can be found in the UNOSAT maps and in those created in this work starting from the Sentinel-1 images.

2.1. West Kyiv area: events from 20/02/2022 to 01/04/2022.

25/02/2022 - a Ukrainian Sukhoi Su-27 fighter aircraft piloted by Colonel Oleksandr Oksanchenko was shot down over the city, eventually crashing into an apartment building led the city for more than 30 minutes (O'Grady et al., 26AD).

27/02/2022 - a rocket fell and exploded in the courtyard of a 16-story highrise in Troieshchyna, destroying several automobiles (Skotnikova, 2022). A Russian armored unit was recorded attacking a memorial for the War in Afghanistan memorial in Bucha (Tiefenthaler et al., 2022; Lysyckina, 2022). Ukrainian forces used rocket and artillery bombardments and airstrikes to halt the Russian advances into Bucha (Tyschenko, 2022). Ukrainian forces destroyed a bridge connecting Bucha and Irpin, killing an OMON officer and preventing Russian forces from advancing into Irpin (Horbach, 2022).

28/02/2022 - a fresh wave of Russian troops advanced towards Kyiv, but little direct combat occurred, with only three missiles were fired at the city that day (The Associated Press, 2022c, 2022b).

01/03/2022 - a Russian missile struck the Kyiv TV Tower, killing five people and injuring five others (Harding, 2022b). Meanwhile, the Babi Yar Holocaust Memorial Center confirmed an accidental hit by a second missile intended for the tower on a memorial dedicated for the Babi Yar Massacre (Brown, 2022; Gavirelov, 2022; Ari Gross, 2022).

A Russian airstrike also struck and damaged an occupied maternity clinic (Spektor, 2022; Sagal et al., 2022).

Further Russian shelling struck the neighborhoods of Rusanivka and Kurenivka and the suburbs of Boyarka and Vyshneve, as well as the area around Kyiv International Airport (Giuliani, 2022).

02/03/2022 - debris from an intercepted Russian rocket fell on the Kyiv-Pasazhyrskiy railway station, damaging a major heating pipeline. The resulting explosion caused minor damage to the station (Liam, 2022; Trofimov & Marson, 2022). Two Russian Sukhoi Su-25s conducted airstrikes in Irpin. Two missiles struck a residential building, killing a child and injuring a woman (24tv, 2022; TCH Ukraine, 2022).

04/03/2022 - a new wave of shelling struck downtown Kyiv, including the Borshchahivka neighbourhood (Vasovic, 2022b). A CNN investigation found that the strikes had hit a business center and many multi-story buildings in the western areas of the city (Yeung et al., 2022).

06/03/2022 - Russia intensified its shelling of Bucha, resulting in some civilian casualties (Balachuck, 2022).

07/03/2022 - Volodymyr Karplyuk, the former mayor of Irpin, stated that Russian forces had destroyed the Glass Plastic and Fiber Research Institute in Bucha, releasing fumes of acetone and other chemicals (Interfax Ukraine, 2022).

09/03/2022 - Russian forces shelled the city again (Maloletka, 2022a).

12/03/2022 - a Russian loitering munition, identified as Cube, was shot down over the Podil neighborhood, causing a fire in the State Savings Bank of Ukraine building (Polishchuk, 2022; Gerashchenko, 2022). Another fire occurred on Synioozerna Street in the northwestern edge of the city (Balachuk, 2022b).

14/03/2022 - a Russian shell struck a 9-story residential building on Bohatyrskaya Street in Obolon. The building was partially destroyed, with at least one person killed and 12 wounded (Agence France Presse, 2022; Balachuk, 2022a). Another Russian rocket was shot down over Kyiv, with its fragments damaging a 5-story residential building in Kurenivka, killing one person (Petrenko, 2022). In addition, Russian forces fired 3

rockets at the Antonov Serial Production Plant, injuring seven people (Singh, 2022; Yurichenko, 2022).

15/03/2022 - the Lukianivska metro station was damaged due to a blast, later in the morning, Russian forces shelled residential areas, including the Sviatoshynski, Podilskyi and Osokorky districts, setting multiple buildings ablaze (The Free Press Journal, 2022; Singh, 2022).

20/03/2022 - a shopping centre in Podilskyi was destroyed by a Russian missile killing at least 8 people. The missile and subsequent explosion also damaged nearby buildings and destroyed cars (BBC News, 2022c; Mackenzie, 2022). In Sviatoshynskiyi, fragments of a missile fell on a residential area. According to local officials, 6 houses and 4 schools were damaged; about 200 people were evacuated (BBC News, 2022d).

24/03/2022 - Russian forces unleashed a new wave of bombardment (The Associated Press, 2022a). Shelling hit a parking lot in the northern area of the city (National Post, 2022a).

25/03/2022 - the Russian military claimed it had successfully destroyed the largest major oil terminal in the country, which was close to Kyiv (BBC News, 2022b).

31/03/2022 -the occupation of Bucha lasted more than a month. The fighting continued constantly until the city was liberated on March 31, 2022. During this time, there were 2,512 buildings in the city, 301 of which were completely or severely destroyed (Kyiv School of Economics, 2022).

2.2. Mariupol: events from 20/02/2022 to 26/03/2022.

24/02/2022 - Russian artillery bombarded the city, reportedly injuring 26 people (UN News, 2022; Vasovic, 2022a).

26/02/2022 - Russian forces continued to bombard Mariupol with artillery (ABC News, 2022).

28/02/2022 - the city remained under Ukrainian control, despite being surrounded by Russian troops and constantly shelled (Trevithick, 2022; ukrinform.net, 2022).

01/03/2022 - Russian artillery later bombarded Mariupol, causing over 21 injuries (Novynarnia, 2022).

02/03/2022 - Russian artillery targeted a densely populated neighborhood of Mariupol, shelling it for nearly 15 hours. The neighborhood was massively damaged as a result, with deputy mayor Sergiy Orlov reporting that "at least hundreds of people are dead" (Crane, 2022; Gunter, 2022c).

03/03/2022 - the city was shelled again by Russian troops (Gunter, 2022b).

04/03/2022 - Boychenko stated that Russian BM-21 Grads were shelling the city's hospitals and that Mariupol residents no longer had heat, running water, or electricity (ukrinform.ne, 2022).

05/03/2022 - Civilians began to evacuate from Mariupol along a humanitarian corridor to the city of Zaporizhzhia. As civilians entered the evacuation corridor, Russian forces continued shelling the city, forcing evacuees to turn back (Gunter, 2022a).

06/03/2022 - Anton Herashchenko, a Ukrainian official, said the second attempt at a humanitarian corridor for civilians in Mariupol ended with a Russian bombardment (Deutsche Welle, 2022). Inna Sovsun, a Ukrainian member of parliament, stated that the fuel pipeline that supplies Mariupol was damaged by Russian forces, leaving more than 700,000 people without heat, and suggested that people might freeze to death, as the temperature at the time often fell below 0 °C (32 °F) (Braithwaite, 2022). The bombardment also hit the city's last functioning cellular tower (Marsi, 2022).

08/03/2022 - another attempt to evacuate civilians was made, but the Ukrainian government accused Russia of violating the ceasefire again by bombing the evacuation corridor (Zaks & Clark, 2022). Russian shelling had hit the cemetery the previous day, interrupting the burials and damaging a wall (BBC News, 2022a).

09/03/2022 - the Mariupol City Council issued a statement that a Russian airstrike had struck and destroyed a maternity ward and children's hospital (Harding, 2022a; Maloletka, 2022b; National Post, 2022b).

13/03/2022 - Boychenko stated that Russian forces had bombed the city at least 22 times in the previous 24 hours, with a hundred bombs, and added that the last food and water reserves in the city were being depleted (Zinets et al., 2022; Devdiscourse, 2022).

16/03/2022 - The Donetsk Regional Drama Theatre, sheltering hundreds of civilians, was hit by a Russian airstrike on 16 March and destroyed (Andrea, 2022). Pavlo Kyrylenko, the governor of Donetsk Oblast, later stated that Russian forces had also targeted the Neptune swimming pool (Dreier, 2022).

19/03/2022 - Major Mykyta Nadochii, commander of the Azov Regiment's second battalion, was wounded in a Russian airstrike (Ukrayinska Pravda, 2022).

20/03/2022 - an art school building, which had sheltered some 400 people, was destroyed in a Russian bombing (Kesaieva & Carey, 2022). An order by Russia's Ministry of Defence to surrender, lay down arms and evacuate the city was submitted on 20 March, requesting a written response by 02:00 UTC the next day. The ultimatum was rejected by the Ukrainian government and the mayor of Mariupol. By this point, one of the Ukrainian battalion commanders in the city described "bombs falling every 10 minutes (Bondarenko et al., 2022).

2.3. Chernihiv: events from 20/02/2022 to 22/03/2022.

25/02/2022 - Russian BM-21 Grad multiple rocket launchers (MRL) hit hospitals and kindergartens in Chernihiv (Interfax Ukraine news agency, 2022). An archive of the Security Service of Ukraine (SBU) was bombed by Russian forces (Meduza, 2022; Chernihiv Society, 2022).

27/02/2022 - On 27 February, Ukrainian officials said that Russian forces damaged most of Chernihiv's city center with missiles and destroyed the historic Shchors cinema (CHERNIHIV REGIONAL MILITARY ADMINISTRATION, 2022; Government of Ukraine., 2022) .

28/02/2022 - the village of Kyinka came under fire. Cluster munitions repudiated by most countries were used in the attack (Ukrinform, 2022).

02/03/2022 - two missiles hit a hospital in the city, according to the health administration chief Serhiy Pivovar (ABC News. Associated Press, 2022).

03/03/2022 - a Russian airstrike was reported to have hit residential buildings and two schools (Polityuk et al., 2022; SKY News, 2022).

06/03/2022 - attacks continued as the Russian Air Force dropped heavy bombs intended for fortifications on residential buildings (Myronchuk, 2022).

10/03/2022 - Mayor Vladyslav Atroshenko said that Russian forces had completed the encirclement of Chernihiv, adding that the city was completely isolated and critical infrastructure for its 300,000 residents was rapidly failing as it came under repeated bombardment (Santora, 2022). A Russian airstrike also damaged the Chernihiv Arena (FC Chernihiv, 2022).

11/03/2022 - the Chernihiv Stadium and a library were badly damaged by a Russian airstrike (Sangal et al., 2022).

12/03/2022 - the "Hotel Ukraine" building in the city was destroyed (ABC News, 2022).

13/03/2022 - a Russian airstrike at 05:46 hit a dormitory (Kurpita, 2022). Ukrainian forces later claimed to have shot down a Russian fighter jet while it was bombing Chernihiv (Romanenko, 2022).

14/03/2022 - Chaus stated that Russian airstrikes had destroyed the Chernihiv Polytechnic National University (Roshchina, 2022).

7. SOFTWARE

During the thesis work, a series of software was used to perform specific Sentinel-1 image processing operations, analyze and create maps, analyze data and produce graphical and tabular outputs.

In particular:

- SNAP was used to process the Sentinel-1 SLC images in the polarimetric analysis and to produce the rasters associated with the coherence variables.
- Catalyst was used for the processing of Sentinel-1 GRDH images in order to produce the rasters associated with the intensity variables.
- QGIS has been used to analyze the UNOSAT maps in shapefile format and to produce the final maps of the thesis work.
- R was used for the basic statistical analysis of the raster data and for the production boxplots, graphs and finally for the implementation of the PCA and for the production of the principal component maps.

Below are the details of each of the software mentioned.

7.1. SNAP

The Sentinel Application Platform (SNAP) is a common architecture for all Sentinel Toolboxes. The software is developed by Brockmann Consult, Skywatch, Sensar and C-S. The SNAP architecture is ideal for Earth observation (EO) processing and analysis due to the following technological innovations: extensibility, portability, modular rich client platform, generic EO data abstraction, tiled memory management, and a graph processing framework. SNAP and the individual Sentinel Toolboxes support numerous sensors other than Sentinel sensors. ESA/ESRIN is providing the SNAP user tool free of charge to the Earth Observation Community (The European Space Agency, 2022).

The Sentinel-1 Toolbox (S1TBX) consists of a collection of processing tools, data product readers and writers and a display and analysis application to support the large archive of data from ESA SAR missions including Sentinel-1, ERS-1 & 2 and ENVISAT, as well as third party SAR data from ALOS PALSAR, TerraSAR-X, COSMO-SkyMed and RADARSAT-2. The Toolbox includes tools for calibration, speckle filtering, coregistration, orthorectification, mosaicking, data conversion, polarimetry and interferometry. The Sentinel-1 Toolbox is being developed for ESA by Array in partnership with DLR, Brockmann Consult and OceanDataLab (The European Space Agency, 2022).

It is possible to download SNAP with the Sentinel 1 Toolbox directly from ESA's website <https://step.esa.int/main/download/snap-download/>.

7.2. CATALYST

CATALYST Professional is a geospatial desktop suite, specializing in Remote Sensing, Photogrammetry & Earth Observation Science for optical, and SAR imagery. It integrates image analysis, ortho-mosaicking, and image processing capabilities into a geospatial technology stack (catalyst.earth, 2022).

The CATALYST platform offers flexibility to complete InSAR processing steps manually, or through full automation. Multiple approaches can be addressed including Differential InSAR (DInSAR), Small Baseline Subset (SBAS), and Persistent Scatterer Interferometry (PSI). Change detection is predicated on highly accurate image coregistration, which is a key strength of the CATALYST platform.

Change detection algorithms can help to leverage intensity or the phase-and-magnitude elements of the signal, and quickly derive change information layers. It is possible to work with many different types of SAR images in the CATALYST platform and maintain the integrity of the signal to fully leverage the information contents. Work with slant range, complex data formats natively without having to resample or project to ground range. Support for single, dual, full, and compact polarizations (catalyst.earth,

2022c). The full CATALYS Professional bundle currently costs \$1335 per month (catalyst.earth, 2022b).

7.3. QGIS

QGIS is a professional application that is built on top of and proud to be itself). QGIS is a user-friendly Open-Source Geographic Information System (GIS) licensed under the GNU General Public License, Free and Open Source Software (FOSS). QGIS is an official project of the Open-Source Geospatial Foundation (OSGeo).

It runs on Linux, Unix, Mac OSX, Windows and Android and supports numerous vector, raster, and database formats and functionalities. QGIS is a volunteer driven project that provides a continuously growing number of capabilities provided by core functions and plugins. QGIS functions as geographic information system (GIS) software, allowing users to analyze and edit spatial information, in addition to composing and exporting graphical maps (qgis.org, 2022).

QGIS version 3.20 - Odense was used in the thesis work.

QGIS supports shapefiles, personal geodatabases, dxf, MapInfo, PostGIS, and other industry-standard formats (Gray, 2008). Web services, including Web Map Service and Web Feature Service, are also supported to allow use of data from external sources. QGIS integrates with other open-source GIS packages, including PostGIS, GRASS GIS, and MapServer (Cavallini, 2007). Plugins written in Python or C++ extend QGIS's capabilities. Plugins can geocode using the Google Geocoding API, perform geoprocessing functions similar to those of the standard tools found in ArcGIS, and interface with PostgreSQL/PostGIS, SpatialLite and MySQL databases. QGIS can also be used with SAGA GIS and Kosmo.

7.4. R Studio

R is free software as it is distributed under the GNU GPL license, and is available for various operating systems (e.g. Unix, GNU /Linux, macOS, Microsoft Windows). Its

object-oriented language derives directly from the S package distributed under a non-open-source license and developed by John Chambers and others at Bell Laboratories. RStudio is an integrated development environment for R, a programming language for statistical computing and graphics. It is available in two formats: RStudio Desktop is a regular desktop application while RStudio Server runs on a remote server and allows accessing RStudio using a web browser (Gandrud, 2018).

R Studio is often used in image analysis; for example, Mengen et al. performed discharge estimation in R Studio within their new approach for estimating river discharge is applied using river width measurements derived from Sentinel-1A and 1B time series (Mengen et al., 2020). Arjasakusuma et al. also used R Studio for mapping paddy extent in central Java using time-series of Sentinel-1 SAR data (Arjasakusuma et al., 2021).

R can be downloaded from the <https://cran.r-project.org/bin/windows/base/> website. R Studio version 2022.02.3+492 was used in the thesis work.

8. GENERAL IMAGE PROCESSING OPERATIONS

Many image processing operations are common among the algorithms used to create polarimetric variables, coherence variables, and intensity variables. In order to avoid useless repetitions, these operations are reported in this chapter.

8.1. TOPS Split

IW SLC products consist of three sub-swaths (Fig. 39, red labels) image per polarization channel, for a total of three (single polarizations) or six (dual polarization) images in an IW product. Each sub-swath image consists of a series of bursts (Fig. 39, white labels), where each burst has been processed as a separate SLC image. The individually focused complex burst images are included, in azimuth-time order, into a single sub-swath image with black-fill demarcation in between, similar to ENVISAT ASAR Wide ScanSAR SLC products.

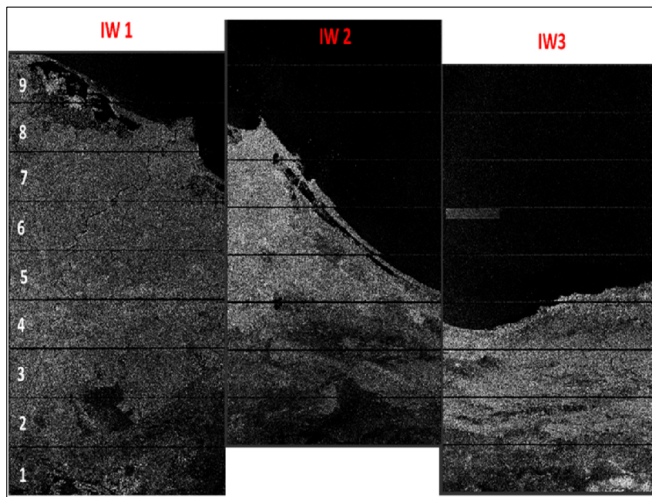


Fig. 39 – Sub-swaths (red) and bursts (white) of S1 IW products. Source:(Darwish et al., 2021)

In SNAP, S-1 TOPS Split is applied to the data to select only those bursts which are required for the analysis. Currently, each Sub-Swath is processed separately. Note: If

the area of interest covers several Sub-Swaths, they have to be merged with the S-1 TOPS Merge operator after the Sub-Swaths were debursting. To reduce the loaded data to the area of interest, open the S-1 TOPS Split operator (under Radar > Sentinel-1 TOPS) and select sub-swath number and polarization type in the Processing Parameters. Then reduce the bursts by dragging the grey triangles towards the middle. Use the preview to check the location of the selected area. Confirm with Run (Braun & Veci, 2021).

8.2. Apply Orbit File

Products from Synthetic Aperture Radar (SAR) require a state orbital vector to correct spatial position accuracy. This information is contained in externally hosted files that need to be downloaded separately and are used by SNAP to update product metadata (Filipponi, 2019). In SNAP, The Apply Orbit File process automatically downloads the Orbit State Vector (OSV) file and updates the metadata. The processing parameters, used both for SLC and GRDH images, pre and post event, are:

- Orbit State Vectors: Sentinel Precise (Auto Download).
- Polynomial Degree: 3.

8.3. Calibration

Calibration is the procedure that converts digital pixel values to radiometrically calibrated SAR backscatter. The information required to apply the calibration equation is included within the Sentinel-1 product; specifically, a calibration vector included as an annotation in the product allows simple conversion of image intensity values into sigma naught values. The calibration reverses the scaling factor applied during level-1 product generation and applies a constant offset and a range-dependent gain, including the absolute calibration constant.

Level-1 products provide four calibration Look Up Tables (LUTs) to produce β_i^0 , σ_i^0 and γ_i^0 or to return to the Digital Number DN_i . The LUTs apply a range-dependent gain including the absolute calibration constant. For GRDH products a constant offset is also applied. The radiometric calibration is applied by the following equation:

$$value(i) = \frac{|DN_i|^2}{A_i^2} \quad (20)$$

where, depending on the selected LUT:

$value(i)$ is one of β_i^0 , σ_i^0 , γ_i^0 or original DN_i ;

$A_i =$ one of $betaNought(i)$, $sigmaNought(i)$, $gamma(i)$ or $dn(i)$.

Bi-linear interpolation should be used for any pixels that fall between points in the LUT. In the proposed preprocessing workflow, a LUT to produce sigma nought values is proposed, in order to generate radiometrically calibrated SAR backscatter with respect to the nominally horizontal plane (Fig. 40). Sigma specifies the strength of reflection in terms of the geometric cross section of a conducting sphere and represents the radar cross section of a distributed target over that expected from an area of one square meter. The sigma nought has a significant variation with the incidence angle, wavelength, and polarization, as well as with properties of the scattering surface (Filipponi, 2019; Atwood et al., 2012).

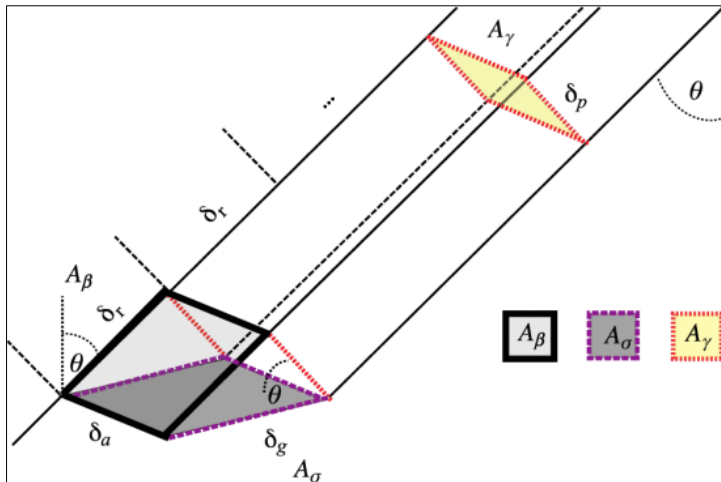


Fig. 40 – Illustration of the reference areas for the three radar backscatter conventions: beta, sigma, and gamma nought taken from (Small, 2011).

8.4. TOPS Deburst

To remove the seamlines between the single bursts, the S-1 TOPS Deburst operator (under Radar > Sentinel-1 TOPS) is applied to the last product. It does not require any user input (Fig. 41). The output contains the same bands as the input, but with merged bursts according to their zero Doppler time.

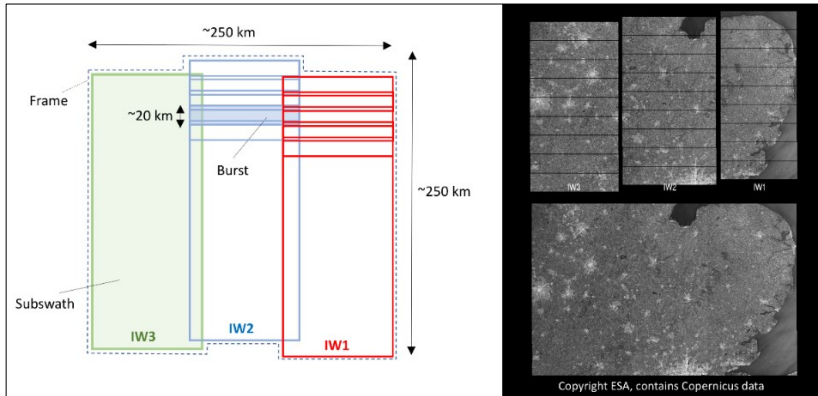


Fig. 41 – SNAP: TOPS Deburst. Source: https://github.com/isce-framework/isce2-docs/blob/master/Notebooks/UNAVCO_2020/TOPS/topsApp.ipynb.

8.5. Subset

To focus the analysis on the area of interest, reduce errors and increase processing speed a subset is required. Among the various ways available in Subset tab to create a subset, the manual entry of the coordinates of the area of interest obtained in WKT format via QGIS was chosen. Fig. 43 illustrates the coordinates obtained for the area of interest relating to the western area of Kiev subsequently inserted in the SNAP subset tab.

8.6. Multilook

An SLC type image is acquired with a resolution ranging from 1.5x3.6m to 2.3x14.1m; it therefore has a different spatial resolution along the two directions. To obtain an acquisition with a square pixel, comparable to reality, a multilooking process of a square pixel is carried out.

As a side result of this operation, multilooking can also be used to produce an image with reduced speckle effect.

The elaboration can be generated by calculating the average resolution, along the range direction or the azimuth direction, degrading the image quality but obtaining square pixels. The number of resampled pixels and those considered for calculation processing are not the same: in the process it is possible to select the "number of Looks" which allows you to choose how many pixels go to form the data (Fig. 42).

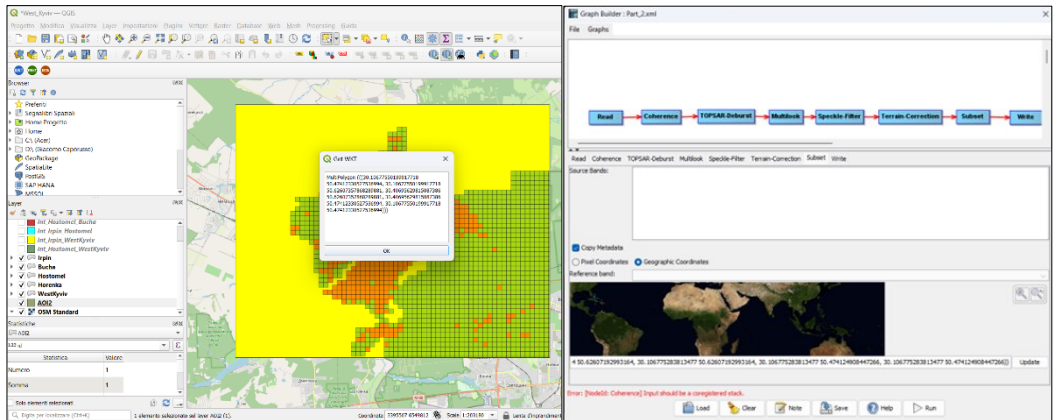


Fig. 43 - Acquisition of the WKT coordinates of the area of interest in QGIS (left); entering WKT coordinates in the SNAP subset tab (right).

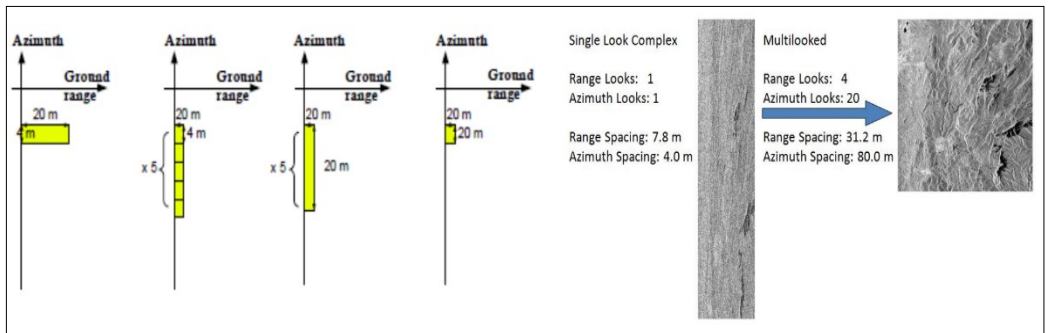


Fig. 42 – Multilook Process. Sources (Boerner, 2007), <https://amslaurea.unibo.it/>

Typically, a SAR image appears marred by the “salt and pepper noise” typical of all images of digital origin. To reduce the presence of this effect several images are

combined incoherently, as if they corresponded to different captures of the same scene (Filipponi, 2019).

In SNAP the Multilook algorithm has been implemented with the following parameters:

- Number of Range Looks: 4
- Number of Azimuth Looks: 1
- Mean GR Square Pixel: 14.36 m

8.7. Terrain Correction

Due to topographical variations of a scene and the tilt of the satellite sensor, distances can be distorted in the SAR images. Image data not directly in the nadir position of the sensor has foreshortening, layover and shadowing distortions. Terrain corrections are intended to compensate for these distortions so that the geometric representation of the image will be as close as possible to the real world. In SNAP, Terrain Correction allows geometric overlays of data from different sensors and/or geometries. The Range Doppler Terrain Correction Operator implements the Range Doppler orthorectification method for geocoding SAR images from single 2D raster radar geometry (Small et al., 2008). It uses available orbit state vector information in the metadata or external precise orbit (only for ERS and ASAR), the radar timing annotations, the slant to ground range conversion parameters together with the reference DEM data to derive the precise geolocation information. Currently, only the DEMs with geographic coordinates (Plat, Plon, Ph) referred to global geodetic ellipsoid reference WGS84 (and height in meters) are properly supported. Various different types of Digital Elevation models can be used (ACE2_5Min, ACE_30, ASTER_1Sec, CFEM, Copernicus30m, Copernicus90m, GETASSE30, SRTM 1Sec, SRTM 3Sec GeoTiff). The STRM v.4 (3" tiles) from the Joint Research Center FTP (xftp.jrc.it) will automatically be downloaded in tiles for the area covered by the image to be orthorectified. User can also use external DEM file in Geotiff format which, as specified above, must be with geographic coordinates (Plat, Plon, Ph) referred to global geodetic ellipsoid reference WGS84 (and height in meters). Besides the default suggested pixel spacing computed with parameters in the metadata, user

can specify output pixel spacing for the orthorectified image. The pixel spacing can be entered in both meters and degrees.

It's possible use the radiometric normalization option; this option implements a radiometric normalization based on the equation proposed by (Kellendorfer et al., 1998):

$$\sigma_{NORM}^0 = \sigma_{Ellipsoid}^0 = \frac{\sin \vartheta_{DEM}}{\sin \vartheta_{Ellipsoid}} \quad (21)$$

Where ϑ_{DEM} is the local incidence angle projected into the range plane and defined as the angle between the incoming radiation vector and the projected surface normal vector into range plane (Small et al., 2008). The range plane is the plane formed by the satellite position, backscattering element position and the earth centre.

8.8. Coregistration - Sentinel-1 Back Geocoding

The sub-pixel coregistration of SAR images is a strict requirement and critical component of any interferometric processing chain. It is an essential step for the accurate determination of phase difference, and applications such as DEM map generation, interferometric deformation analysis, etc.

In SNAP, the interferometric modules of the toolbox will accurately co-register one or more secondary images with respect to a reference image. The co-registration procedure is completely automatic. Apart from defining the processing parameters, no additional input nor intervention from the user is required. For example, the distribution of correlation (optimization) windows are done in automatic manner for both reference and secondary image. Also, the refinement of the coregistration offsets is done in a fully automatic way, including downloading and interpolation of the a-priori digital-elevation-model. The implementation of the co-registration procedure is based on the cross-correlation technique as illustrated in the Fig. 44 . Input SAR images may be fully ("full frame") or only partially overlapping ("subset"), they have to be from acquisitions taken at different times using compatible, in the interferometric sense, sensors, and input images must belong to the same type (i.e., them must be complex). While in

principle the implementation of the InSAR coregistration is flexible enough to allow processing of real (detected) products, for now only complex (single-look-complex) data is supported. The Create Stack operator collocates the reference and secondary images based into a single reference (reference) geometry. Basically, the secondary image data is subset into geometry of the reference image. With performing this

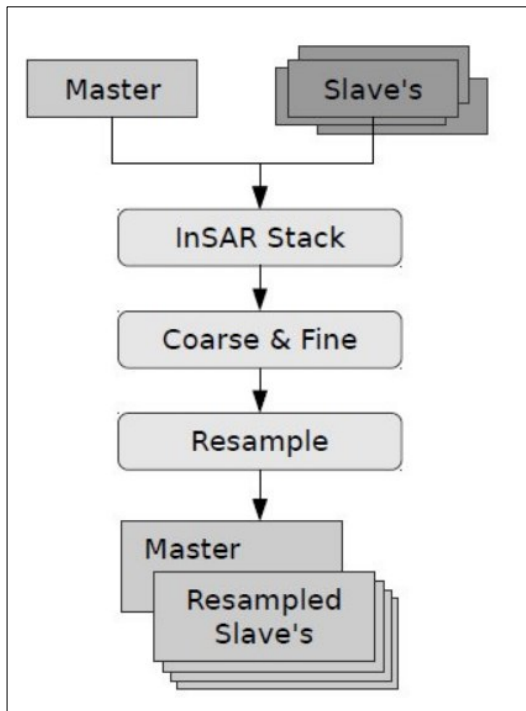


Fig. 44 – Coregistration Procedure. Source: SNAP, help page software.

operation, the reference and secondary images share the same geo-positioning information and have the similar dimensions. For overlap and geometry calculation either orbital data, or annotated tie-point-grids (i.e., ground-control-points) can be used. In other words, the coarse coregistration is performed using orbital information or annotated GCPs. The Cross Correlation operator creates an alignment between reference and secondary images by matching automatically distributed correlation optimization windows to their corresponding secondary windows. There are two steps: coarse and fine registration. The offsets

between reference and secondary are computed by maximizing the cross-correlation between reference and secondary images on a series of imagerettes defined across the images. First on coarse level, with large windows and lower oversampling factors, later on fine level, with smaller windows and higher oversampling factors. With the reference-secondary offsets computed, a coregistration polynomial (CPM) is estimated by the Warp operator, which resamples pixels in the secondary image into pixels in the reference image. This resampling is performed in two-steps: (1) reconstruction of the continuous signal from its sampled

version by convolution with an interpolation kernel, and (2) sampling of the constructed signal at the new sampling locations (ESA, 2022). In particular, Sentinel-1 Back Geocoding co-registers two S-1 SLC split products (reference and secondary) of the same sub-swath using the orbits of the two products and a Digital Elevation Model (DEM). In resampling the secondary images into reference frame, deramp and demodulation are performed first to the secondary image, then the truncated-sinc interpolation is performed. Finally, the reramp and remodulation are applied to the interpolated secondary image. In this work the back geocoding has been set with the following parameters:

- Digital Elevation Model: SRTM 1Sec HGT (Auto Download).
- DEM Resampling Method: Bicubic Interpolation.
- Resampling Type: Bisinc 5 Point Interpolation.

8.9. Enhanced Spectral Diversity

In SNAP, this operator implements the Network Enhanced Spectral Diversity (NESD) method for TOPS coregistration (Fattahi et al., 2017).

It performs the joint coregistration of a Sentinel-1 stack by creating a network (graph) of images and then estimating range and azimuth offsets by solving an optimization problem. This operator estimates rigid azimuth and range offsets (i.e., constant for each image) with respect to a reference image considering the offsets of multiple secondary-secondary pairs (ESA, 2022).

8.10. Speckle Filter

SAR images have inherent salt and pepper like texturing called speckles which degrade the quality of the image and make interpretation of features more difficult. Speckles are caused by random constructive and destructive interference of the de-phased but coherent return waves scattered by the elementary scatters within each resolution cell. Speckle noise reduction can be applied either by spatial filtering or multilook processing (Lee & Pottier, 2017a; Robinson, 1977; Frost et al., 1982; Mansourpour et al., 2006). SNAP supports the following speckle filters for handling speckle noise of

different distributions (Gaussian, multiplicative or Gamma): Boxcar (mean), Median, Frost, Lee, Refined Lee, Gamma-MAP, Lee Sigma and IDAN. For most filters, the following parameters should be selected:

- Source Band: all bands (real or virtual) of the source product. User can select one or more bands for producing filtered images. If no bands are selected, then by default all bands will be selected. For complex product, only the intensity band can be selected.
- Filter: the speckle filter.
- Size X: the filtering kernel width.
- Size Y: the filtering kernel height.
- Frost Damping Factor: the damping factor for Frost filter.

In this work the Refined Lee filter was chosen.

Lee Filter is developed by Jong Sen Lee in 1981(Lee, 1980). It is better than above filters in edge preservation. It is based on multiplicative speckle model and uses local statistics to preserve details. Lee filter works on the variance basis, i.e. if variance of the area is low then it performs smoothing operation but not for high variance. That means it can preserve details in low as well as in high contrast hence it has adaptive nature. Mathematical model for Lee filter is given in equations:

$$Img(i, j) = Im + W^*(Cp - Im) \quad (22)$$

$$W = \sigma^2 (\sigma^2 + \rho^2) \quad (23)$$

$$\sigma^2 = \frac{1}{N} \sum_{j=0}^{N-1} (X_j)^2 \quad (24)$$

$$\rho^2 = \frac{1}{M} \sum_{j=0}^{M-1} (Y_j)^2 \quad (25)$$

Where,

- M = size of image
- Y_j = pixel value of each pixel in the image
- ρ^2 = additive noise, the variance in the image
- N = size of the filter window
- X_j = pixel value at j
- σ^2 = the variance of the pixel in the window
- W = filter window
- C_p = value of the center pixel
- Im = mean intensity of filter window
- Img = pixel value after filtering

For no smoothing filter output is the only mean intensity value (Im). Disadvantage of Lee Filter is it cannot effectively remove the speckle noise near edges (Uddin et al., 2015). Refined Lee Filter is an enhancement of Lee filter and can preserve prominent edges, linear features, point target, and texture information. Refined Lee (Lee, 1981) algorithm using edge directed windows. Eight non-square windows for eight edge orientations are created within a 7×7 window. The local mean and local variance are computed using only those pixels in the edge directed window and then, the local statistics filter is applied. The noise in the edge and high contrast areas is effectively removed and, in fact, the edges are enhanced (Lee et al., 1994). In SNAP, Refined Lee filter doesn't need any settings.

9. POLARIMETRY VARIABLES

9.1. SAR Polarimetry

Radar Polarimetry (Polar: polarization, Metry: measure) is the science of acquiring, processing and analyzing the polarization state of an electromagnetic field (Boerner, 2007). Whenever there are abrupt or gradual changes in the index of refraction (or permittivity, magnetic permeability, and conductivity), the polarization state of a narrow band (single-frequency) wave is transformed, and the electromagnetic “vector wave” is re-polarized. When the wave passes through a medium of changing index of refraction, or when it strikes an object such as a radar target and/or a scattering surface and it is reflected; then, characteristic information about the reflectivity, shape and orientation of the reflecting body can be obtained by implementing ‘polarization control’ (Poelman et al., 1985). Coherent sources of electromagnetic field radiation emit fully-polarized states in which the oscillation of the electric field vector is well defined (Woodhouse, 2017b). For sinusoidal waveform, the complex direction of the electric field vector, in general describing an ellipse, in a plane transverse to propagation, plays an essential role in the interaction of electromagnetic ‘vector waves’ with material bodies, and the propagation medium (Beckmann & Keller, 1972; Azzam et al., 1978; Boerner, 1981; Boerner et al., 1988, 1981). This polarization transformation behavior, expressed in terms of the “polarization ellipse” is named “Ellipsometry” in Optical Sensing and Imaging (Azzam et al., 1978; Chipman, 1990) , instead it is denoted as “Polarimetry” in Radar, Lidar/Ladar and SAR Sensing and Imaging (W. M. Boerner et al., 1988; Boerner et al., n.d.; Boerner & North Atlantic Treaty Organization. Scientific Affairs Division., 1985). In the extremes of eccentricity, the traced ellipse becomes the special case of a circle or degenerates into a line (Purcell & Morin D.J., 2013). A plane electromagnetic wave is said to be linearly polarized. The transverse electric field wave is accompanied by a magnetic field wave. Circularly polarized light consists of two perpendicular electromagnetic plane waves of equal amplitude and 90° difference in

phase. Elliptically polarized light consists of two perpendicular waves of unequal amplitude which differ in phase by 90° (Fujiwara, 2007) (Fig. 45).

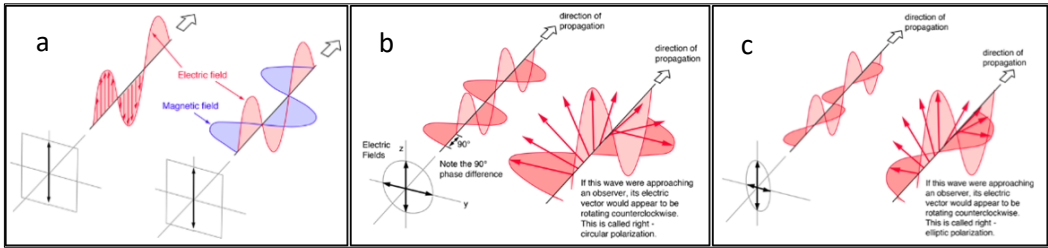


Fig. 45 – a) Linear Polarization, b) Circular Polarization, c) Elliptical Polarization. Image source: <http://hyperphysics.phy-astr.gsu.edu/hbase/phyopt/polclas.html>

Any wave can be characterized by two parameters: Orientation Angle ψ ($-90^\circ \leq \psi \leq 90^\circ$) and Ellipticity Angle χ ($-45^\circ \leq \chi \leq 45^\circ$) (Fig. 46) ((Sletten & Mc Laughlin, 2005).

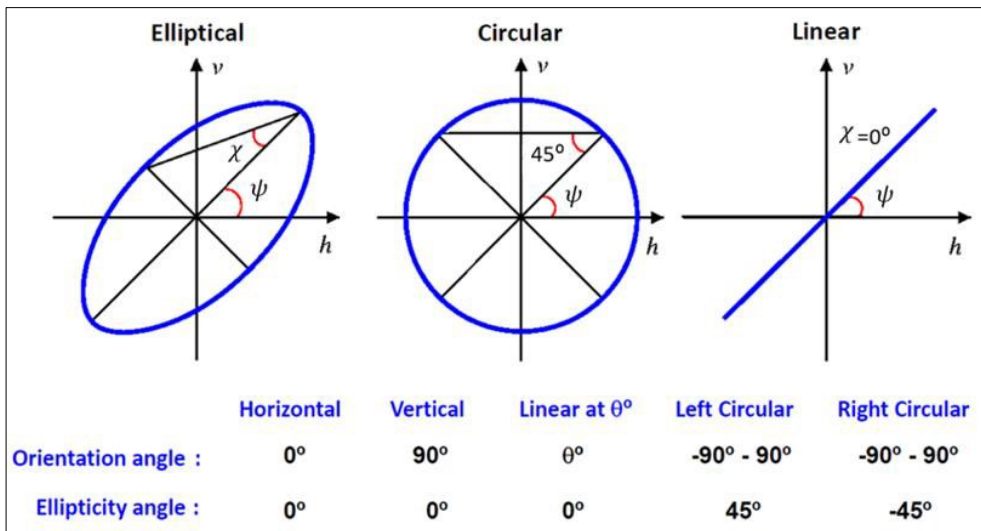


Fig. 46 – Orientation Angle and Ellipticity Angle in Elliptical, Circular and Linear Polarization. Image source: <https://eo-college.org/>.

The Jones Vector is used to describe a fully polarized wave. It represents the amplitude and phase information of the two components of the electric field vector as a two-

dimensional complex vector.(Collett & Society of Photo-optical Instrumentation Engineers., 2005):

$$|E_H|e^{j\phi_H} \tag{26}$$

$$|E_V|e^{j\phi_V} \tag{27}$$

Stokes Parameters $S_0 S_1 S_2 S_3$ describe the fully or partially polarization state of an EM wave. These parameters are derived from the Jones Vector. The Stokes parameters describe the total intensity (H and V directions) of the wave and its geometry (Chandrasekhar, 1960):

$$S_0 = |E_H|^2 + |E_V|^2 \tag{28}$$

$$S_1 = |E_H|^2 - |E_V|^2 \tag{29}$$

$$S_2 = 2|E_H||E_V| \cos \phi_{HV} \tag{30}$$

$$S_3 = 2|E_H||E_V| \sin \phi_{HV} \tag{31}$$

$$\phi_{HV} = \phi_V - \phi_H \tag{32}$$

The incident wave and the wave reflected from the struck element have their own Jones Vector representation (Fig. 47).

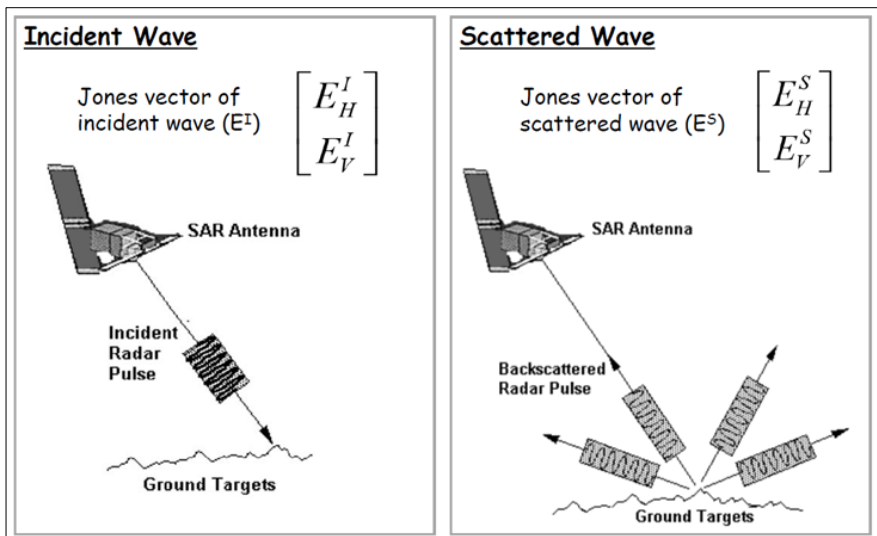


Fig. 47 – Incident Wave and Scattered Wave. Image source: <https://crisp.nus.edu.sg/~research/tutorial/mw.htm>.

The Scattering or Sinclair matrix is used to derive the scattered wave from the incident wave (Lee & Pottier, 2017a):

$$\begin{bmatrix} E_H^S \\ E_V^S \end{bmatrix} = \frac{e^{ikr}}{r} \begin{bmatrix} S_{HH} & S_{HV} \\ S_{VH} & S_{VV} \end{bmatrix} \begin{bmatrix} E_H^I \\ E_V^I \end{bmatrix} ; k = \frac{2\pi}{\lambda}$$

$r = \text{distance from target to receiver}$ (33)

$k = \text{wave number}$

$\lambda = \text{wavelength}$

$S = \text{scattered}$

$I = \text{Incident}$

Monostatic antenna is when the transmit and receive antenna are the same and the Reciprocity Theorem is valid (van Zyl & Kim, 2011):

$$S_{VH} = S_{HV} = S_{XX} \quad (34)$$

$$\begin{bmatrix} S_{HH} & S_{HV} \\ S_{VH} & S_{VV} \end{bmatrix} \Rightarrow \begin{bmatrix} S_{HH} & S_{XX} \\ S_{XX} & S_{VV} \end{bmatrix} \quad (35)$$

The scattering matrix contains all the information about the scattering process and the scatterer itself. The matrix is used to derive two different types of information: those derive directly from the Scattering matrix (First Order) and those derived indirectly from the Covariance and Coherency matrices (Second Order). In detail, First Order information are σ_0 (eq.(36)) (Oliver & Quegan, 1998) and Polarimetric Phase Difference Second Instead Second Order information are Polarimetric Decompositions parameters (Cloude & Pottier, 1996).

$$\sigma_0(dB) = 10 \log_{10} \left(\frac{\text{received energy by the sensor}}{\text{energy reflected in an isotropic way}} \right) \quad (36)$$

In literature it is convenient to express the scatter matrix in vectorial form in Lexicographic basis (eq.(37)) or in Pauli basis (eq.(38)) (Cloude & Pottier, 1996; van Zyl & Kim, 2011; Yamaguchi et al., n.d.).

$$K_L = [S_{HH}, S_{VH}, S_{HV}, S_{VV}]^T \quad (37)$$

$$K_P = \frac{1}{\sqrt{2}} [S_{HH} + S_{VV}, S_{HH} - S_{VV}, S_{VH} + S_{HV}, i(S_{VH} - S_{HV})]^T \quad (38)$$

By applying the reciprocity theorem, they become:

$$K_L = [S_{HH}, \sqrt{2}S_{XX}, S_{VV}]^T \quad (39)$$

$$K_P = \frac{1}{\sqrt{2}} [S_{HH} + S_{VV}, S_{HH} - S_{VV}, 2S_{XX}]^T \quad (40)$$

Only a Single scatter, Deterministic scatterer or Coherent scatterer can be described with the Scattering Matrix (Fig. 48). The description of Multiple targets, Undeterministic scatterer or Incoherent scatterer takes place through the Covariance or Consistency matrices(Ferguson & Gunn, 2022).

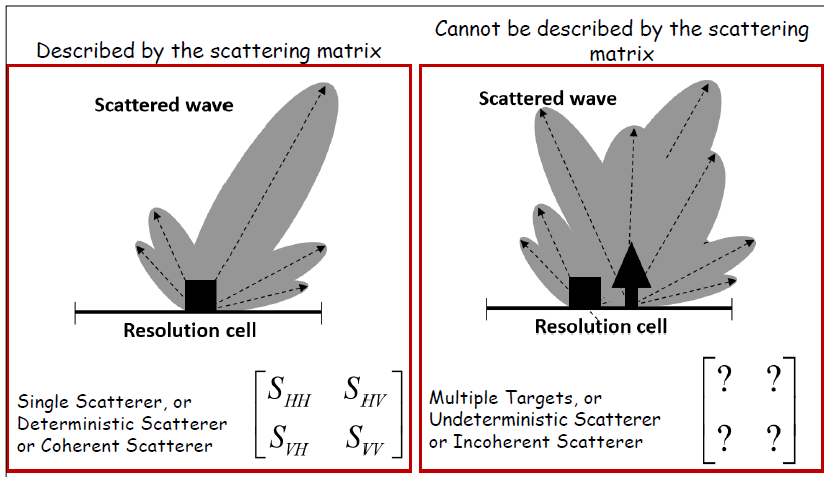


Fig. 48 – Single Scatterer and Multiple Targets Mechanism. Image source: <https://eo-college.org/>.

The Covariance matrix is obtained by multiplying the Scattering vector by its conjugate transpose. The Covariance matrix is a 3 by 3 matrix and contains 9 elements which the diagonal elements (real numbers) describe the intensities and the non-diagonal (complex numbers) describe the intensity and phase between different polarizations (Cloude & Pottier, 1996):

$$[C] = \begin{bmatrix} S_{HH} \\ \sqrt{2}S_{XX} \\ S_{VV} \end{bmatrix} [S_{HH}^* \quad \sqrt{2}S_{XX}^* \quad S_{VV}^*] = \begin{bmatrix} C_{11} & C_{12} & C_{13} \\ C_{21}^* & C_{22} & C_{23} \\ C_{31}^* & C_{32}^* & C_{33} \end{bmatrix} \quad (41)$$

$$[C] = \begin{bmatrix} |S_{HH}|^2 & \sqrt{2}S_{XX}^*S_{HH} & S_{VV}^*S_{HH} \\ \sqrt{2}S_{HH}^*S_{XX} & 2|S_{XX}|^2 & \sqrt{2}S_{VV}^*S_{XX} \\ S_{HH}^*S_{VV} & \sqrt{2}S_{XX}^*S_{VV} & |S_{VV}|^2 \end{bmatrix}$$

The Coherency matrix is obtained by multiplying the Pauli Scattering vector by its conjugate transpose. The Coherency matrix is a 3 by 3 matrix and contains 9 elements which the diagonal elements (real numbers) describe the intensities and the non-diagonal (complex numbers) describe the intensity and phase between different polarizations (Gunn et al., 2018; Zhang et al., 2019; Shokr & Dabboor, 2020):

$$[T] = \frac{1}{2} \begin{bmatrix} S_{HH} + S_{VV} \\ S_{HH} - S_{VV} \\ 2S_{XX} \end{bmatrix} [(S_{HH} + S_{VV})^* \quad (S_{HH} - S_{VV})^* \quad 2S_{XX}^*] = \begin{bmatrix} T_{11} & T_{12} & T_{13} \\ T_{21}^* & T_{22} & T_{23} \\ T_{31}^* & T_{32}^* & T_{33} \end{bmatrix} \quad (42)$$

$$[T] = \begin{bmatrix} |S_{HH} + S_{VV}|^2 & (S_{HH} + S_{VV})(S_{HH} - S_{VV})^* & 2(S_{HH} + S_{VV})S_{XX}^* \\ (S_{HH} - S_{VV})(S_{HH} + S_{VV})^* & |S_{HH} - S_{VV}|^2 & 2(S_{HH} - S_{VV})S_{XX}^* \\ 2(S_{HH} + S_{VV})^*S_{XX} & 2(S_{HH} - S_{VV})^*S_{XX} & 4|S_{XX}|^2 \end{bmatrix}$$

Polarimetric decomposition expresses scattering matrices as the sum of submatrices which correspond to individual mechanisms, targets, or types of polarimetric interaction (Ferguson & Gunn, 2022). Decompositions allow the separation of different scattering contributions and can be used to describe the scattering properties

(geometry and intensity) of the target. There are different decomposition algorithms to extract the scattering mechanisms: eigenvector and eigenvalue-based decomposition and model-based decomposition (Russelle et al., 1984). The Fig. 49 shows the possible polarimetric decompositions deducible from the Sinclair [S], Covariance [C] and Coherence [T] matrices.

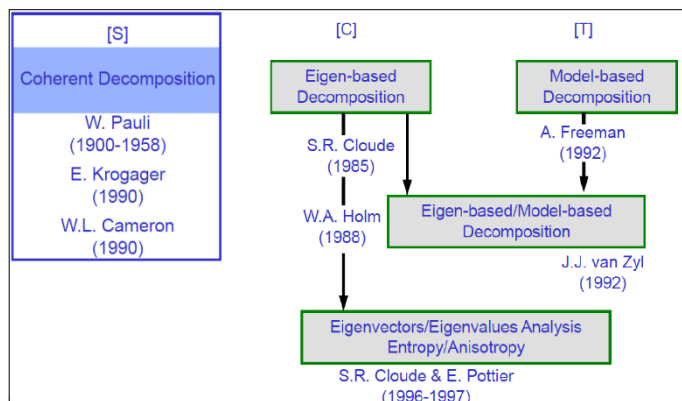


Fig. 49 – Polarimetric Decompositions. Image source: <https://eo-college.org/>

9.2. Polarimetry Variables

In this work, considering the dual polarimetric characteristic of the Sentinel -1 data, it is possible to apply the eigenvector and eigenvalue-based H-A- α decomposition by Cloude and Pottier (Lacoste et al., 2007; Ji & Wu, 2015a; Harfenmeister et al., 2021). This approach used the eigenvalues and the eigenvector of the covariance matrix [C] (eq.(41)) or coherency matrix [T] (eq.(42)) to calculate the three parameters entropy (H), anisotropy (A), and alpha angle (α) (Moreira et al., 2013b; Lee & Pottier, 2017b). Entropy is a measure of the randomness of the scattering process and ranges from 0 to 1. The lower the value, the purer and more polarised the surface, whereas a high value indicates a random scattering process with a completely depolarised wave (Moreira et al., 2013b). It is calculated using the logarithmic sum of the eigenvalues of the coherency matrix [T] (43). P_i refers to the probability of each eigenvalue contribution, whereas n assumes 2 in the dual-polarimetric case and 3 for full-polarimetric data, depending on the size of [T]:

$$H = - \sum_{i=1}^n P_i \log_n P_i \quad (43)$$

$$P_i = \frac{\lambda_i}{\sum_{j=1}^n \lambda_j} \quad (44)$$

Anisotropy indicates the presence of a second scattering mechanism and is therefore complementary to entropy. It is particularly useful to improve the separation of different scattering mechanism when entropy is high. In the dual-polarimetric case, it is calculated using the first and second eigenvalues (Lee & Pottier, 2017b):

$$A_{dual} = \frac{\lambda_1 - \lambda_2}{\lambda_1 + \lambda_2} \quad (45)$$

Alpha angle describes the dominant scattering mechanism. It is defined as the mean of the scattering angles of the eigenvector \mathbf{u} . Values close to 0° indicate surface scattering, values close to 45° refer to volume scattering, and values close to 90° indicate dihedral scattering:

$$\alpha = - \sum_{i=1}^n P_i \alpha_i \quad (46)$$

$$\alpha_i = \cos(|v_{1i}|)^{-1} \quad (47)$$

9.3. Polarimetry Image processing

In SNAP the graph represented in Fig. 50 was created which represents the sequence of processing operations applied to each of the three SLC-type SEntinel-1 images belonging to each of the three areas of interest. The Topsar-Split, Apply Orbit File, Calibration, Topsar-Deburst, Subset, Multilook and Terrain Correction operations were defined in Chapter 8. Details of the remaining operations of the graph are reported here.

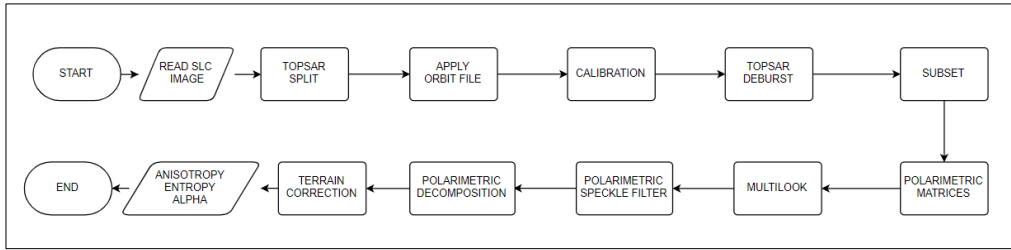


Fig. 50 - Graph of Polarimetric Variables.

Polarimetric Matrices. According to the PolSAR theory, SNAP can generate the [C2] matrix for a dual-pol mode (e.g. Sentinel-1 VV-VH) (Nielsen et al., 2017):

$$[C2] = \begin{bmatrix} \langle S_{VV}S_{VV}^* \rangle & \langle S_{VV}S_{VH}^* \rangle \\ \langle S_{VH}S_{VV}^* \rangle & \langle S_{VH}S_{VH}^* \rangle \end{bmatrix} \quad (48)$$

Polarimetric Speckle Filter. For polarimetric SAR data, the speckle filtering is based on incoherent averaging and requires handling statistical second order representations. Thus, the speckle filtering is applied to covariance or coherency matrix. In SNAP, this operator provides the following polarimetric speckle filterings: Box Car filter, Refined Lee filter, IDAN filter, Improved Lee Sigma filter.

The Lee Sigma assumes Gaussian noise distribution and filters the center pixel in a sliding window with the average of pixels within the two-sigma range. One major drawback of the algorithm is that the mean of pixels within the two-sigma range is always underestimated due to the fact that the noise distributions are not symmetric, and the symmetric thresholds are used in the pixel selection. The new Lee Sigma filter extends and improves the Lee Sigma filter in the following aspects:

- The bias problem is solved by redefining the sigma range based on the speckle probability density functions.
- A target signature preservation technique is developed to prevent point target from being filtered.

The minimum-mean-square-error (MMSE) estimator is used for adaptive speckle reduction. The input to this operator can be full polarimetric data, it can also be covariance or coherency matrix produced by Polarimetric Matrix Generation operator.

The parameters related to the filter have been set as follows:

- Number of Looks (the number of looks of SAR data, which is used in estimating the speckle noise standard deviation): 1
- Window Size (the dimension of the edge-aligned window): 5X5
- Sigma: 0.9
- Target Windows Size: 3X3.

Polarimetric Decompositions. In SNAP, this operator performs the following polarimetric decompositions for a full polarimetric SAR product (ALOS, RADARSAT, TERRASAR etc.): Sinclair Decomposition, Pauli Decomposition, Freeman-Durden Decomposition, Yamaguchi Decomposition, H-a Alpha Decomposition, Touzi Decomposition, Van Zyl Decomposition, Cloude Decomposition, Generalized Freeman-Durden Decomposition, Model-Free 3-Component Decomposition (MF3CF), Model-Free 4-Component Decomposition (MF4CF). Sentinel-1 SLC products are Dual-Pol and SNAP only allows H-Alpha decomposition for them. The chosen window size is 5X5.

9.4. Polarimetry Results

For each study area and for each of the three Sentinel-1 SLC scenes, the three rasters relating to the Entropy, Anisotropy and Alpha variables were obtained, as well as the separate Alpha/Entropy diagrams for the entire study area, for the damaged portion and for the undamaged portion. The areas identified by the diagrams comply with the following legend:

Z1 - Dihedral Reflector

Z2 - Dipole

Z3 - Bragg Surface

Z4 - Double Reflection

Z5 - Anisotropic Particles

Z6 - Random Surface

Z7 - Complex Structures

Z8 - Random Anisotropic Scatterers

Z9 - Non-feasible

All the diagrams obtained in SNAP are shown in Appendix – A (Fig. 79, Fig. 80, Fig. 81).

Moreover, in R, the boxplots of the average values and of the maximum and minimum values assumed by the variables of Entropy, Anisotropy and Alpha were created. In particular, the two series of boxplots have been distinguished by study area and with respect to each of them there is an analysis referring to each of the three reference dates. Therefore, for each date, a grouping has been made which allows the distinction of the boxplots for the entire study area, for the damaged portion and for the undamaged portion. Fig. 82, Fig. 83 and Fig. 84 in Appendix – A, show the results obtained.

10. COHERENCE VARIABLES

10.1. SAR Coherence

The degree of similarity between the two radar measurements is called correlation. The correlation between two SAR images is generally expressed by coherence (Liang et al., 2022). Interferometry is the complex coherence value estimated by the absolute value of the correlation coefficient between corresponding samples of two SAR images (Tamkuan & Nagai, 2017; Arciniegas et al., 2007a; Hajeb et al., 2020; Karimzadeh et al., 2018; Natsuaki et al., 2018).

The coherence γ is calculated according to equation:

$$\gamma = \frac{E\langle c_1 c_2^* \rangle}{\sqrt{E\langle c_1 c_1^* \rangle E\langle c_2 c_2^* \rangle}} \quad (49)$$

where c_1 and c_2 are the corresponding complex pixel values of the two acquisition dates t_1 and t_2 , c^* is the complex conjugate of c , and E indicates the expected value (Stramondo et al., 2006b; Takeuchi et al., n.d.; Yonezawa & Takeuchi, n.d.). The coherence is calculated over a certain window of pixels. Given two SAR images, one master M and one slave S , the estimator is:

$$\hat{\gamma} = |\gamma| = \frac{\frac{1}{N} \sum_1^N MS^*}{\sqrt{\frac{1}{N} \sum_1^N MM^*} \sqrt{\frac{1}{N} \sum_1^N SS^*}} \quad (50)$$

where N is the number of pixels in a moving window.

The value of Coherence ranges from 0 to 1; for values close to 1 we are dealing with highly coherent pixels, typical behavior of built structures or rocky areas, which undergo

a minimal change over time; for values close to 0 there is a low coherence content, typical behavior of changing elements such as vegetables or water (Touzi et al., 1999).

10.2. Coherence Variables

On the basis of what has been proposed by various authors for damage assessment, the variables derived from the simple difference, ratio and normalized ratio both in VV and VH polarization of the coherence values between image pair 1 and image pair 2 (Fig. 31) are taken into consideration in eq.(51),(52),(53),(54),(55),(56) (Suga et al., 2001; Yonezawa & Takeuchi, 2001; Takeuchi et al., n.d.; Arciniegas et al., 2007b; Plank, 2014b; Akhmadiya & Zeng, 2018; Hoffmann, 2007):

$$DC VV = C_{pre}^{VV} - C_{co}^{VV} \quad (51)$$

$$DC VH = C_{pre}^{VH} - C_{co}^{VH} \quad (52)$$

$$RC VV = \frac{C_{pre}^{VV}}{C_{co}^{VV}} \quad (53)$$

$$RC VH = \frac{C_{pre}^{VH}}{C_{co}^{VH}} \quad (54)$$

$$NDCC VV = \frac{C_{pre}^{VV} - C_{co}^{VV}}{C_{pre}^{VV} + C_{co}^{VV}} \quad (55)$$

$$NDCC VH = \frac{C_{pre}^{VH} - C_{co}^{VH}}{C_{pre}^{VH} + C_{co}^{VH}} \quad (56)$$

where C_{pre}^{VV} and C_{pre}^{VH} representing the pre-disaster SAR Coherence calculated for image pair 1 (t_1 and t_2 in Fig. 31) and C_{co}^{VV} and C_{co}^{VH} representing the pre - and post-

disaster SAR Coherence calculated for image pair 2 (t_2 and t_3 in Fig. 31) in the VV and VH polarizations, respectively.

10.3. Coherence Image processing

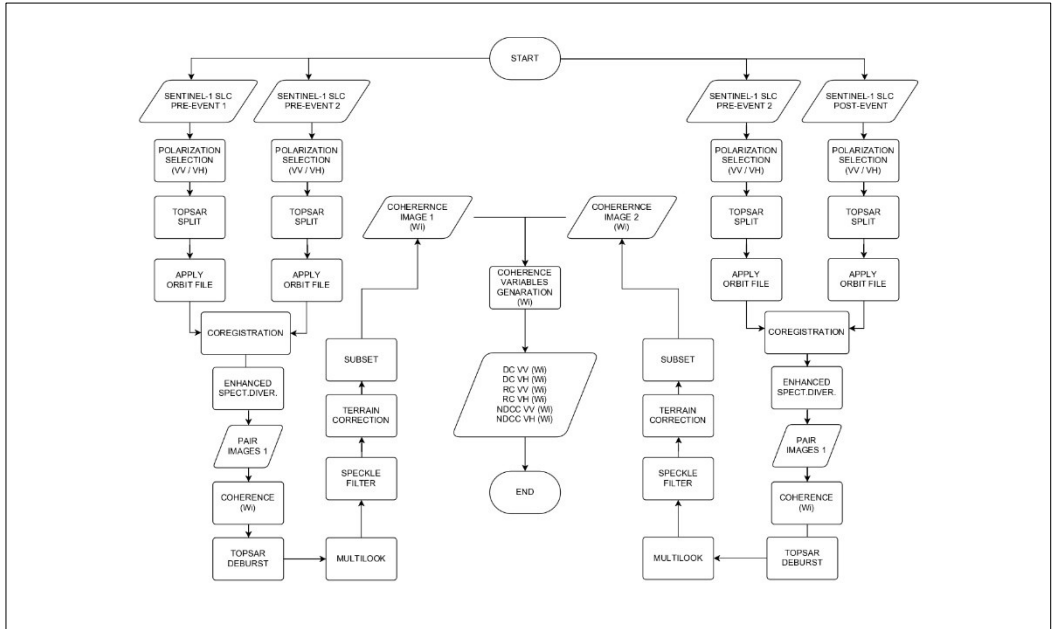


Fig. 51 – Coherence Workflow

The processing of the images took place entirely in SNAP in two phases applied with special graphs for each study area according to the scheme illustrated in the Fig. 51.

The graph used for the first phase was implemented both for the pair of Sentinel-1 SLC images pre-event 1 and pre-event 2 and for the pair pre-event 2 and post-event. The images of each pair were separately read by the software, their VV polarization was selected, the Topsar-Split was applied to select the swaths of interest, the orbit file was applied to consider precise positions, they were co-registered and improved on a spectral level by merging into a single element made up of two perfectly superimposed layers.

The graph used for the second phase was applied to each of the two elements generated at the end of phase 1 and with respect to each of the 15 calculation windows, generating the coherence variable, removing the discontinuities with the Topsar-Deburst, applying the Multilook to obtain a square pixel and reduce the speckle, applying the specific Improved Lee Sigma speckle filter, correcting geometric distortions through Terrain-Correction and finally creating the subset referred to the area of interest. The 3 variables referring to the specific coherence window (DC VV (Wi), RC VV (Wi), NDCC VV (Wi)) were then created using the Band Maths for a total of 45 variables for the VV polarization.

By repeating the procedure, selecting the VH polarization in graph 1, the 3 variables referring to each coherence window (DC VH (Wi), RC VH (Wi), NDCC VH (Wi)) were obtained for a total of 45 variables for the VH polarization.

Topsar-Split, Apply Orbit File, Coregistration operations; Enhanced Spectral Diversity, Topsar-Deburst, Multilook, Speckle Filter, Terrain Correction and Subset have been described in Chapter 8, Therefore only the detail related to the Coherence Estimation algorithm is reported here.

Coherence Estimation. This operator computes/estimates the coherence image, with or without subtraction of the reference phase. The reference phase is subtracted if there is a 2d-polynomial computed -- result of "Compute Interferogram" operator. While, it is not subtracted if this information is not in the metadata, or if the number of polynomial coefficients in "Compute Interferogram" operator is set to 0. Note that this is a "general" coherence estimation operator and not exclusive only for InSAR applications. It can be utilized to estimate the coherence information from any stack of coregistered complex images. In order to reduce the noise, as the post-processing step, you can perform multilooking (with Multilook Operator). Of course, the resolution decreases if multilooking is applied. The input parameters are size of the shifting window for the coherence estimation. The window size is defined, in both azimuth and range

directions. Source Bands are set of, usually coregistered, bands of the complex product. The Fig. 52 shows the settings window of the Coherence algorithm in SNAP and with the details of the section dedicated to the choice of the calculation window changed from time to time to obtain the different outputs.

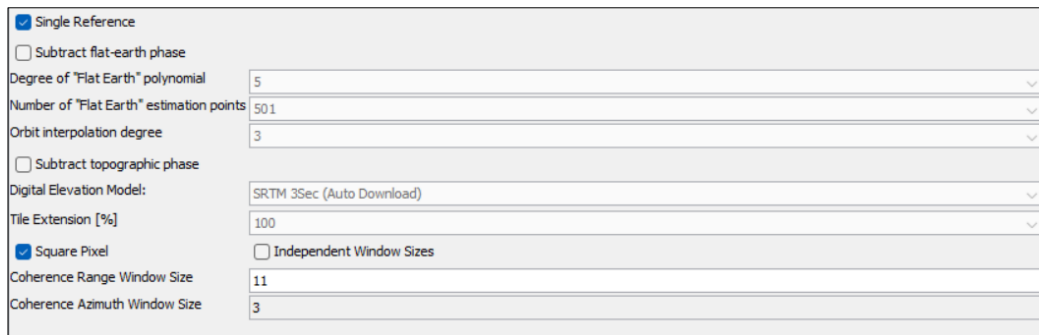


Fig. 52 – SNAP: Coherence Estimation Settings

10.4. Coherence Results

The outputs of this phase of work made it possible to obtain 90 rasters representing the following variables for each of the 3 areas of interest:

- 15 rasters for the DC VV variable
- 15 rasters for the DC VH variable
- 15 rasters for the RC VV variable
- 15 rasters for the RC VH variable
- 15 rasters for the NDCC VV variable
- 15 rasters for the NDCC VH variable

for a total of 270 rasters processed in SNAP.

The Fig. 53 shows some examples of the NDCC VV coherence index rasters processed in SNAP for 2 different calculation windows for each of the 3 study areas and subsequently brought into QGIS for comparison with the UNOSAT map shapefiles.

In QGIS, for the raster of each index, the average, minimum and maximum values assumed within each 500mX500m cell of the UNOSAT shapefile of each of the study areas were extrapolated. Subsequently, each data table was imported into R and it was

possible to create 2 diagrams: the first diagram shows the boxplot sequence of the average values while the second diagram shows the boxplot sequence of the minimum and maximum values. The boxplots have a main grouping referring to the index calculation window and a subgrouping that distinguishes the boxplots of the area investigated as a whole (blue), of the portion defined as damaged (red) and of that defined as undamaged (green) in the references UNOSAT. The figures in Appendix – B from Fig. 85 to Fig. 102 show the pair of diagrams associated with each index for each of the areas of interest.

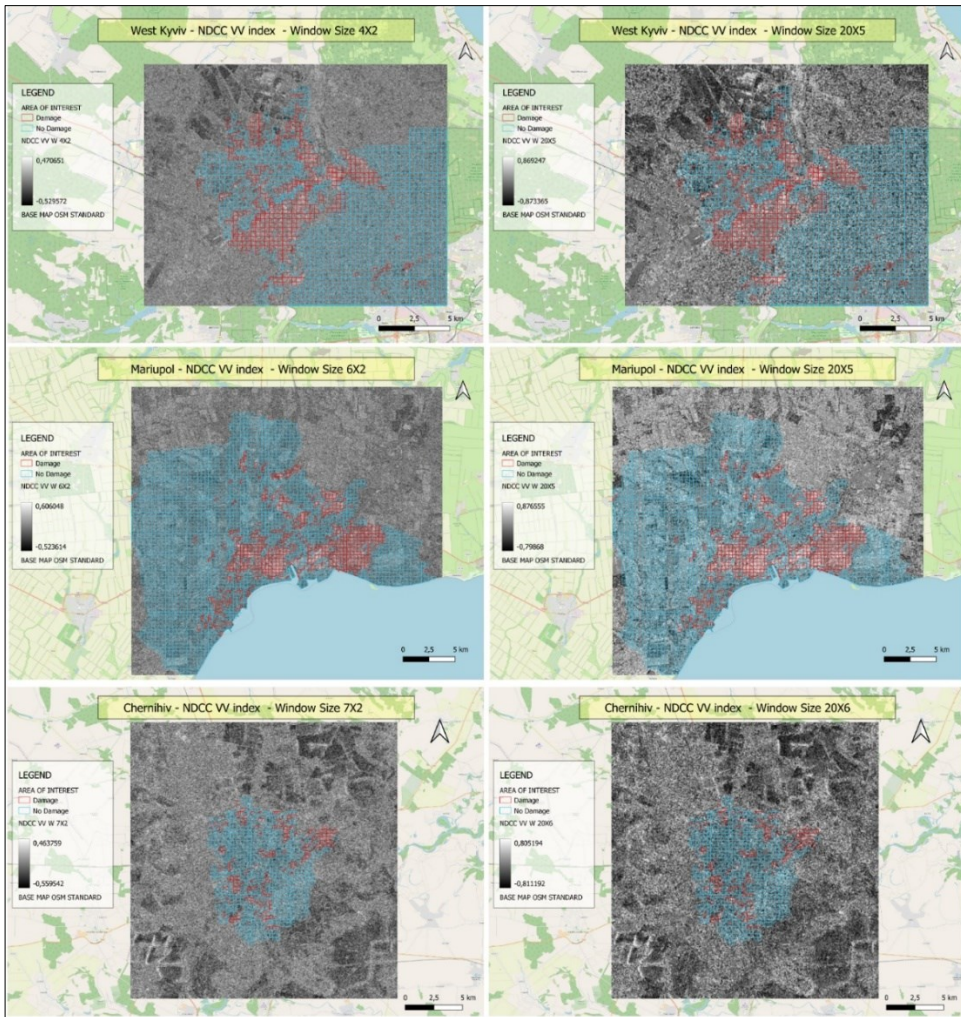


Fig. 53 – Sample maps of the NDCC VV index.

11. INTENSITY VARIABLES

11.1. Correlation Coefficient

The intensity of a SAR signal is the square of the SAR amplitude value A :

$$I = A^2 = Re^2 + Im^2 \quad (57)$$

with Re and Im representing the real and imaginary part of the complex SAR value, respectively (Moreira et al., 2013c). The SAR intensity, or SAR backscattering, is influenced by the imaging geometry of the SAR sensor (e.g., orbit direction (ascending/descending), incidence angle and polarization) as well as by the orientation, size, shape, construction material (especially its dielectric properties) of the object observing on the ground.

The intensity correlation ρ , ranging from 0 to 1 is defined as:

$$\rho = \frac{E\langle I_1 I_2 \rangle}{\sqrt{E\langle I_1^2 \rangle} \sqrt{E\langle I_2^2 \rangle}} \quad (58)$$

where I_1 and I_2 are the corresponding pixel values for the intensity of the two acquisition dates t_1 and t_2 , respectively (Stramondo et al., 2006b; Yonezawa & Takeuchi, n.d.). Intensity Correlation coefficient can be calculated according to eq.(59). Its values range from 0 to 1, with lower values indicating larger ground changes, and a 1 value representing no ground changes:

$$r = \frac{N \sum_{i=1}^N I a_i I b_i - \sum_{i=1}^N I a_i \sum_{i=1}^N I b_i}{\sqrt{(N \sum_{i=1}^N I a_i^2 - (\sum_{i=1}^N I a_i)^2) * (N \sum_{i=1}^N I b_i^2 - (\sum_{i=1}^N I b_i)^2)}} \quad (59)$$

where Ia_i and Ib_i are samples of two backscattering coefficient images in window size $n \times n$, N the number of samples in window size (Akhmadiya & Zeng, 2018).

11.2. Intensity Variables

For damage assessment, the variables derived from the simple difference, ratio and normalized ratio both in VV and VH polarization of the Intensity Correlation Coefficient values between image pair 1 and image pair 2 (Fig. 31) are taken into consideration in eq.(60),(61),(62),(63),(64),(65) (Arciniegas et al., 2007b; Takeuchi et al., n.d.; Suga et al., 2001; Yonezawa & Takeuchi, 2001; Plank, 2014b; Akhmadiya & Zeng, 2018)

$$DI_{VV} = r_{pre}^{VV} - r_{co}^{VV} \quad (60)$$

$$DI_{VH} = r_{pre}^{VH} - r_{co}^{VH} \quad (61)$$

$$RI_{VV} = \frac{r_{pre}^{VV}}{r_{co}^{VV}} \quad (62)$$

$$RI_{VH} = \frac{r_{pre}^{VH}}{r_{co}^{VH}} \quad (63)$$

$$NDIC_{VV} = \frac{r_{pre}^{VV} - r_{co}^{VV}}{r_{pre}^{VV} + r_{co}^{VV}} \quad (64)$$

$$NDIC_{VH} = \frac{r_{pre}^{VH} - r_{co}^{VH}}{r_{pre}^{VH} + r_{co}^{VH}} \quad (65)$$

where r_{pre}^{VV} and r_{pre}^{VH} representing the pre-disaster SAR Intensity Correlation Coefficient calculated for image pair 1 (t_1 and t_2 in Fig. 31) and r_{co}^{VV} and r_{co}^{VH} representing the pre- and post-disaster SAR Intensity Correlation Coefficient calculated for image pair 2 (t_2 and t_3 in Fig. 31) in the VV and VH polarizations, respectively.

11.3. Intensity Image processing

The image processing took place entirely in CATALYST in two phases applied through a single graph for each study area according to the scheme illustrated in Fig. 54.

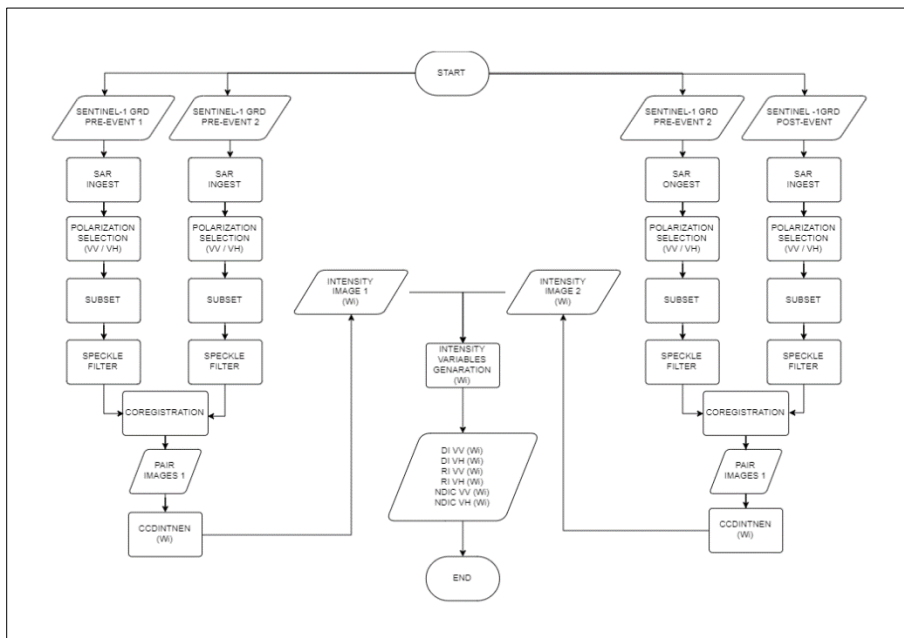


Fig. 54 – Intensity Workflow

Given the preprocessing operations typical of the Sentinel-1 GRDH products illustrated in paragraph 4.3, fewer operations were required in CATALYST than those performed on the Sentinel-1 SLC products in SNAP in order to obtain the coherence variables.

The graph used was implemented both for the pair of Sentinel-1 GRDH images pre-event 1 and pre-event 2 and for the pair pre-event 2 and post-event. The images of each pair were read separately by the software, the VV polarization was selected, a subset was made, the filter was applied to reduce speckle and they were co-registered into a single stack formed by two perfectly overlapping layers.

The CCDINTEN algorithm was applied to each of the two stacks with respect to each of the 15 calculation windows, generating the Intensity Correlation coefficient.

The 3 variables referring to the specific intensity window (DI VV (Wi), RI VV (Wi), NDIC VV (Wi)) were then created using Raster Calculator for a total of 45 variables for the VV polarization.

By repeating the procedure, selecting the VH polarization in the graph, the 3 variables referring to each intensity window (DI VH (Wi), RI VH (Wi), NDIC VH (Wi)) were obtained for a total of 45 variables for the VH polarization.

The Coregistration, Speckle Filter, and Subset operations have been described in Chapter 7, therefore only the detail relating to the Intensity Correlation coefficient Estimation algorithm is reported here.

CCDINTEN measures the change in total radar backscatter between the test and reference SAR images by comparing the sum of the intensities of the input channels. Given two GRDH or SLC SAR images, CCDINTEN determines the overlap area, normalizes the intensity values based on the total span, and calculates the change as a percentile. CCDINTEN is NoData-aware, meaning that pixels that contain a value defined as NoData in the metadata of the input file are excluded from processing. The input and reference layers must be correspondingly comparable; that is, the first layer from each image must have the same polarizations. CCDINTEN algorithm in the preceding table automatically extracts the overlap area between each image pair and writes four channels to the output file: Intensity value (or sum of intensities) of the input test data, Intensity value (or sum of intensities) of the reference data, Change metric (absolute intensity ratio, Wishart metric, or the absolute intensity ratio of the coherence)Change, as percentiles, ranked from zero (no change) to 100 percent (maximum change).

Image quality in detecting change in SAR data depends on the comparability of the source data. As much as is possible, source images should have the same calibration applied, the same georeferencing, pixel size, viewing geometry, and polarization. The quality of the coregistration of each image pair used as input is also a significant factor. Optionally specifies the size of the square window that is moved over the images. All of the pixels in the window are averaged together for the value of the center pixel. The window size value must be an odd integer. By default, no averaging is performed. Fig. 55 shows the settings windows of the CCDINTEN algorithm in CATALYST and in particular the section dedicated to the choice of the calculation window modified from time to time to obtain the different outputs.

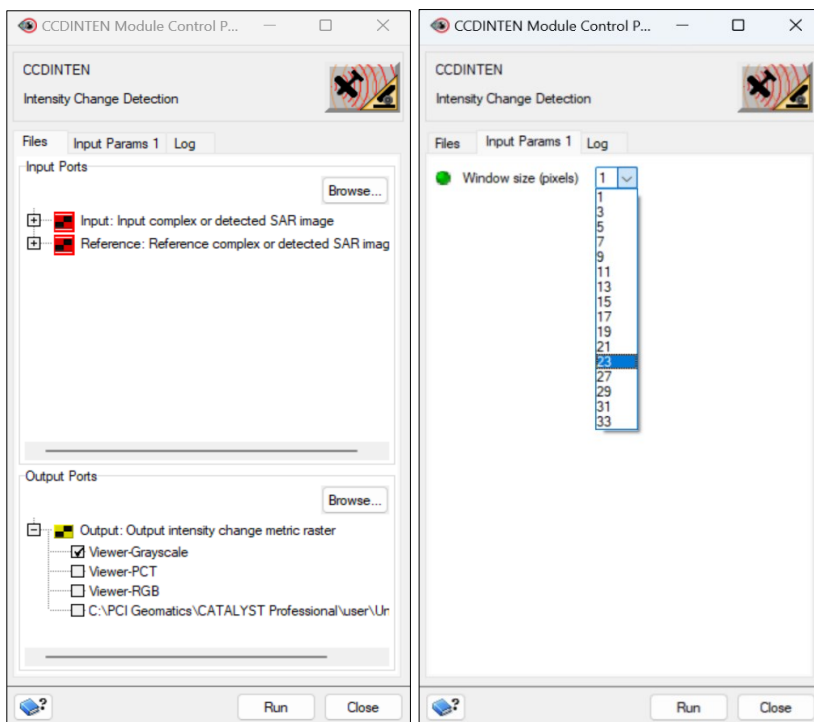


Fig. 55 – CATALYST: CCDINTEN Settings.

11.4. Intensity Results

The outputs of this phase of work made it possible to obtain 90 rasters representing the following variables for each of the 3 areas of interest:

- 15 rasters for the DI VV variable

- 15 rasters for the DI VH variable
 - 15 rasters for the RI VV variable
 - 15 rasters for the RI VH variable
 - 15 rasters for the NDIC VV variable
 - 15 rasters for the NDIC VH variable
- for a total of 270 rasters processed in CATALYST.

The Fig. 56 shows some examples of the DI VH coherence index rasters processed in CATALYST for 2 different calculation windows for each of the 3 study areas and subsequently brought into QGIS for comparison with the UNOSAT map shapefiles.



Fig. 56 – Sample maps of the DI VH index.

In QGIS, for the raster of each index, the average, minimum and maximum values assumed within each 500mX500m cell of the UNOSAT shapefile of each of the study areas were extrapolated. Subsequently, each data table was imported into R and it was possible to create 2 diagrams: the first diagram shows the boxplot sequence of the average values while the second diagram shows the boxplot sequence of the minimum and maximum values. The boxplots have a main grouping referring to the index calculation window and a subgrouping that distinguishes the boxplots of the area investigated as a whole (blue), of the portion defined as damaged (red) and of that defined as undamaged (green) in the references UNOSAT. In Appendix – C, the figures from Fig. 103 to Fig. 120 show the pair of diagrams associated with each index for each of the areas of interest.

12. SNR DISCRIMINATION

12.1. SNR Coefficient

Signal to Noise Ratio (SNR) is a measure, which is used to quantify how much a signal has been corrupted by noise. SNR can be expressed through the following equations (Bentz et al., 2014):

$$SNR = \frac{P_{image}}{P_{noise}} = \left(\frac{A_{image}}{A_{noise}} \right)^2 \quad (66)$$

$$SNR_{DB} = 10 \log_{10} \left(\frac{P_{image}}{P_{noise}} \right) = P_{signal,DB} - P_{noise,DB} \quad (67)$$

$$SNR_{DB} = 10 \log_{10} \left(\frac{A_{image}}{A_{noise}} \right)^2 = 20 \log_{10} \left(\frac{A_{image}}{A_{noise}} \right) \quad (68)$$

Where P_{image} is the image power, P_{noise} is the noise power, A_{image} is the image amplitude and A_{noise} is the noise amplitude.

Since clean image and noise amplitude are unknown, to estimate SNR, the following method is used (Mahesh, 2013; Schroeder, 1999):

$$SNR \approx \frac{m}{\sigma} \quad (69)$$

where m is the mean and σ is the standard deviation of an image.

Notice that such an alternative definition is only useful for variables that are always non-negative (such as photon counts and luminance), and it is only an approximation. It is commonly used in image processing where the SNR of an image is usually calculated

as the ratio of the mean pixel value to the standard deviation of the pixel values over a given neighborhood (Russ, 2010; Raol, 2009; Stathaki, 2008; Gonzalez & Woods, 2007).

The Rose criterion says that if an image has $SNR > 5$, then a level of noise is so small that it shall be considered negligible, and the image shall be considered clean. If $SNR < 5$, then some noise should be expected. The lower is SNR, the stronger is noise. Small-detailed image (for example, satellite images) may have lower SNR because the presence of many small details always leads to the higher standard deviation (Rose, 1973; Mahesh, 2013).

12.2. SNR Determination

The SNR has been fully implemented in R by importing all 540 rasters of the coherence and intensity indices. In particular, for each index two diagrams have been created which both show the coherence or intensity calculation windows on the abscissa (all integer numbers from 1 to 15) and on the ordinate the SNR value assumed by the maximum values of the index in the first diagram and by the minimum values of the index in the second diagram.

The SNR values of the first diagram were calculated as the ratio between the absolute value of the average of the maxima assumed by the coherence or intensity index with respect to the 500X500 meter cells into which the area of interest is divided, and the deviation standard. The SNR values of the second diagram were calculated as the ratio between the absolute value of the average of the minima assumed by the coherence or intensity index with respect to the 500X500 meter cells into which the area of interest is divided, and the deviation standard. Within each diagram there is a horizontal straight line corresponding to the SNR limit value equal to 5.

In Appendix – D, Fig. 121 to Fig. 132 show the two diagrams obtained in R for the SNR referred to each index.

12.3. Variables Discrimination

The analysis proceeded by eliminating for each study area the representative variables of those indices referring to calculation windows such that the result was $SNR = < 5$ for at least one of the maximum or minimum values and consequently keeping only the variables for which the result was $SNR > 5$ for both maximum and minimum values.

The tables below show the number of starting indices in the upper part (which is 180 for all study areas) while the residual indices in the lower part.

WEST KYVIV											
START											
DC VH	DC VV	NDCC VH	NDCC VV	RC VH	RC VV	DI VH	DI VV	NDIC VH	NDIC VV	RI VH	RI VV
W1	W1	W1	W1	W1	W1	W1	W1	W1	W1	W1	W1
W2	W2	W2	W2	W2	W2	W2	W2	W2	W2	W2	W2
W3	W3	W3	W3	W3	W3	W3	W3	W3	W3	W3	W3
W4	W4	W4	W4	W4	W4	W4	W4	W4	W4	W4	W4
W5	W5	W5	W5	W5	W5	W5	W5	W5	W5	W5	W5
W6	W6	W6	W6	W6	W6	W6	W6	W6	W6	W6	W6
W7	W7	W7	W7	W7	W7	W7	W7	W7	W7	W7	W7
W8	W8	W8	W8	W8	W8	W8	W8	W8	W8	W8	W8
W9	W9	W9	W9	W9	W9	W9	W9	W9	W9	W9	W9
W10	W10	W10	W10	W10	W10	W10	W10	W10	W10	W10	W10
W11	W11	W11	W11	W11	W11	W11	W11	W11	W11	W11	W11
W12	W12	W12	W12	W12	W12	W12	W12	W12	W12	W12	W12
W13	W13	W13	W13	W13	W13	W13	W13	W13	W13	W13	W13
W14	W14	W14	W14	W14	W14	W14	W14	W14	W14	W14	W14
W15	W15	W15	W15	W15	W15	W15	W15	W15	W15	W15	W15
TOTAL RASTER = 180											
SNR > 5											
DC VH	DC VV	NDCC VH	NDCC VV	RC VH	RC VV	DI VH	DI VV	NDIC VH	NDIC VV	RI VH	RI VV
-	-	W1	-	W1	W1	W1	W1	W1	W1	-	-
-	-	W2	W2	W2	W2	W2	W2	W2	W2	-	-
-	-	W3	W3	W3	W3	W3	W3	W3	W3	-	-
-	-	W4	W4	W4	W4	W4	W4	W4	W4	-	-
-	-	W5	W5	W5	W5	W5	W5	W5	W5	-	-
-	-	W6	W6	-	-	-	W6	W6	W6	-	-
-	-	W7	W7	-	-	-	-	W7	W7	-	-
-	-	W8	W8	-	-	-	-	-	-	-	-
-	-	W9	-	-	-	-	-	-	-	-	-
-	-	W10	-	-	-	-	-	-	-	-	-
-	-	-	-	-	-	-	-	-	-	-	-
-	-	-	-	-	-	-	-	-	-	-	-
-	-	-	-	-	-	-	-	-	-	-	-
-	-	-	-	-	-	-	-	-	-	-	-
-	-	-	-	-	-	-	-	-	-	-	-
TOTAL RASTER = 52											

Tab. 3 – West Kyviv. Top: initial variables. Bottom: variables with $SNR > 5$.

MARIUPOL											
START											
DC VH	DC VV	NDCC VH	NDCC VV	RC VH	RC VV	DI VH	DI VV	NDIC VH	NDIC VV	RI VH	RI VV
W1	W1	W1	W1	W1	W1	W1	W1	W1	W1	W1	W1
W2	W2	W2	W2	W2	W2	W2	W2	W2	W2	W2	W2
W3	W3	W3	W3	W3	W3	W3	W3	W3	W3	W3	W3
W4	W4	W4	W4	W4	W4	W4	W4	W4	W4	W4	W4
W5	W5	W5	W5	W5	W5	W5	W5	W5	W5	W5	W5
W6	W6	W6	W6	W6	W6	W6	W6	W6	W6	W6	W6
W7	W7	W7	W7	W7	W7	W7	W7	W7	W7	W7	W7
W8	W8	W8	W8	W8	W8	W8	W8	W8	W8	W8	W8
W9	W9	W9	W9	W9	W9	W9	W9	W9	W9	W9	W9
W10	W10	W10	W10	W10	W10	W10	W10	W10	W10	W10	W10
W11	W11	W11	W11	W11	W11	W11	W11	W11	W11	W11	W11
W12	W12	W12	W12	W12	W12	W12	W12	W12	W12	W12	W12
W13	W13	W13	W13	W13	W13	W13	W13	W13	W13	W13	W13
W14	W14	W14	W14	W14	W14	W14	W14	W14	W14	W14	W14
W15	W15	W15	W15	W15	W15	W15	W15	W15	W15	W15	W15
TOTAL RASTER = 180											
SNR > 5											
DC VH	DC VV	NDCC VH	NDCC VV	RC VH	RC VV	DI VH	DI VV	NDIC VH	NDIC VV	RI VH	RI VV
-	-	W1	-	W1	W1	W1	-	W1	-	-	-
-	-	W2	-	W2	W2	W2	-	W2	-	-	-
-	-	W3	-	W3	W3	-	-	-	-	-	-
-	-	W4	-	W4	W4	-	-	-	-	-	-
-	-	W5	-	-	-	-	-	-	-	-	-
-	-	W6	-	-	-	-	-	-	-	-	-
-	-	W7	-	-	-	-	-	-	-	-	-
-	-	W8	-	-	-	-	-	-	-	-	-
-	-	-	-	-	-	-	-	-	-	-	-
-	-	-	-	-	-	-	-	-	-	-	-
-	-	-	-	-	-	-	-	-	-	-	-
-	-	-	-	-	-	-	-	-	-	-	-
-	-	-	-	-	-	-	-	-	-	-	-
-	-	-	-	-	-	-	-	-	-	-	-
-	-	-	-	-	-	-	-	-	-	-	-
TOTAL RASTER = 19											

Tab. 4 – Mariupol. Top: initial variables. Bottom: variables with SNR > 5.

CHERNIHIV											
START											
DC VH	DC VV	NDCC VH	NDCC VV	RC VH	RC VV	DI VH	DI VV	NDIC VH	NDIC VV	RI VH	RI VV
W1	W1	W1	W1	W1	W1	W1	W1	W1	W1	W1	W1
W2	W2	W2	W2	W2	W2	W2	W2	W2	W2	W2	W2
W3	W3	W3	W3	W3	W3	W3	W3	W3	W3	W3	W3
W4	W4	W4	W4	W4	W4	W4	W4	W4	W4	W4	W4
W5	W5	W5	W5	W5	W5	W5	W5	W5	W5	W5	W5
W6	W6	W6	W6	W6	W6	W6	W6	W6	W6	W6	W6
W7	W7	W7	W7	W7	W7	W7	W7	W7	W7	W7	W7
W8	W8	W8	W8	W8	W8	W8	W8	W8	W8	W8	W8
W9	W9	W9	W9	W9	W9	W9	W9	W9	W9	W9	W9
W10	W10	W10	W10	W10	W10	W10	W10	W10	W10	W10	W10
W11	W11	W11	W11	W11	W11	W11	W11	W11	W11	W11	W11
W12	W12	W12	W12	W12	W12	W12	W12	W12	W12	W12	W12
W13	W13	W13	W13	W13	W13	W13	W13	W13	W13	W13	W13
W14	W14	W14	W14	W14	W14	W14	W14	W14	W14	W14	W14
W15	W15	W15	W15	W15	W15	W15	W15	W15	W15	W15	W15
TOTAL RASTER = 180											
SNR > 5											
DC VH	DC VV	NDCC VH	NDCC VV	RC VH	RC VV	DI VH	DI VV	NDIC VH	NDIC VV	RI VH	RI VV
-	-	W1	W1	W1	W1	W1	W1	W1	W1	-	-
-	-	W2	W2	W2	W2	W2	W2	W2	W2	-	-
-	-	W3	W3	W3	W3	-	-	W3	W3	-	-
-	-	W4	-	W4	W4	-	-	W4	W4	-	-
-	-	W5	-	W5	W5	-	-	W5	W5	-	-
-	-	W6	-	W6	-	-	-	W6	W6	-	-
-	-	W7	-	-	-	-	-	W7	W7	-	-
-	-	W8	-	-	-	-	-	W8	W8	-	-
-	-	W9	-	-	-	-	-	-	W9	-	-
-	-	W10	-	-	-	-	-	-	W10	-	-
-	-	W11	-	-	-	-	-	-	-	-	-
-	-	W12	-	-	-	-	-	-	-	-	-
-	-	W13	-	-	-	-	-	-	-	-	-
-	-	-	-	-	-	-	-	-	-	-	-
-	-	-	-	-	-	-	-	-	-	-	-
TOTAL RASTER = 49											

Tab. 5 – Chernihiv. Top: initial variables. Bottom: variables with SNR > 5.

13. PCA ANALYSIS

13.1. Principal Component Analysis

Principal component analysis (PCA) is a technique for analyzing large datasets containing a high number of dimensions/features per observation, increasing the interpretability of data while preserving the maximum amount of information, and enabling the visualization of multidimensional data. Formally, PCA is a statistical technique for reducing the dimensionality of a dataset. This is accomplished by linearly transforming the data into a new coordinate system where (most of) the variation in the data can be described with fewer dimensions than the initial data. Many studies use the first two principal components in order to plot the data in two dimensions and to visually identify clusters of closely related data points. Principal component analysis has applications in many fields such as population genetics, microbiome studies, and atmospheric science (Jolliffe & Cadima, 2016).

PCA is also used in the field of remote sensing. In 2021 Dharani and Sreenivasulu conducted a land use and land cover change detection by using principal component analysis (Dharani & Sreenivasulu, 2021). Uddin et al. have accomplished an information-theoretic feature selection with segmentation-based folded principal component analysis for hyperspectral image classification (Uddin et al., 2021). Frutuoso, Lima and Teodoro implemented band combinations, band ratios, and principal component analysis to the visible, near-infrared, and shortwave infrared bands of Landsat 8 in their application of remote sensing data in gold exploration in Portugal (Frutuoso et al., 2021). Within a study on Hyperspectral Image Classification Using a Hybrid 3D-2D Convolutional Neural Networks, Ghaderizadeh et. all used PCA for data preprocessing (Ghaderizadeh et al., 2021). In 2020 Sam et al. conducted Dimensionality Reduction and Vegetation Monitoring On LISS III Satellite Image Using Principal Component Analysis and Normalized Difference Vegetation Index (Navin et al., 2020).

A raster series can be expressed in matrix format in the following way:

$$X_{n,r} = \begin{bmatrix} x_{1,1} & \dots & \dots & x_{1,n} \\ \dots & \dots & \dots & \dots \\ \dots & \dots & \dots & \dots \\ x_{r,1} & \dots & \dots & x_{r,n} \end{bmatrix} \quad (70)$$

where n represents the number of the pixels and r the number of rasters.

Considering each raster as a vector, the above matrix can be simplified as follows:

$$X_r = \begin{bmatrix} x_1 \\ \dots \\ x_r \end{bmatrix} \quad (71)$$

To reduce the dimensionality of the original bands the eigenvalues of the covariance matrix must be calculated. This matrix can be calculated as follows:

$$C_{b,b} = \begin{bmatrix} \sigma_{1,1} & \dots & \dots & \sigma_{1,r} \\ \dots & \dots & \dots & \dots \\ \dots & \dots & \dots & \dots \\ \sigma_{r,1} & \dots & \dots & \sigma_{r,r} \end{bmatrix} \quad (72)$$

where $\sigma_{i,j}$ is the covariance of each pair of different rasters:

$$\sigma_{i,j} = \frac{1}{N-1} \sum_{p=1}^N (DN_{p,i} - \mu_i) (DN_{p,j} - \mu_j) \quad (73)$$

where $DN_{p,i}$ is a digital number of a pixel p in the raster i , $DN_{p,j}$ is a digital number of a pixel p in the raster j , μ_i and μ_j are the averages of the DN for the rasters i and j , respectively.

From the variance-covariance matrix, the eigenvalues (λ) are calculated as the roots of the characteristic equation:

$$\det(C - \lambda I) = 0 \quad (74)$$

where C is the covariance matrix of the rasters and I is the diagonal identity matrix. The eigenvalues indicate the original information that they retain. From these values the percentage of original variance explained by each principal component can be obtained calculating the ratio of each eigenvalue in relation to the sum of all them (Chuvieco, 2010). Those components which contain minimum variance and thus minimum information can be discarded.

The principal components can be expressed in matrix form:

$$Y_r = \begin{bmatrix} y_1 \\ \dots \\ y_r \end{bmatrix} = \begin{bmatrix} w_{1,1} & \dots & \dots & w_{1,r} \\ \dots & \dots & \dots & \dots \\ \dots & \dots & \dots & \dots \\ w_{r,1} & \dots & \dots & w_{r,r} \end{bmatrix} \begin{bmatrix} x_1 \\ \dots \\ x_r \end{bmatrix} \quad (75)$$

where Y is the vector of the principal components, W the transformation matrix, and X the vector of the original data. The coefficients of the transformation matrix W are the eigen vectors that diagonalizes the covariance matrix of the original rasters. These values provide information on the relationship of the bands with each principal component. From these values it is possible to link a main component with a real variable. The eigenvectors can be calculated from the vector - matrix equation for each eigenvalue λ_k :

$$(C - \lambda_k I)w_k = 0 \quad (76)$$

where C is the covariance matrix, λ_k is the k eigenvalue, I is the diagonal identity matrix, and w_k is the k eigenvector (Estornell et al., 2013) .

13.2. PCA Implementation

PCA has been fully implemented in R by creating a specific script for each area of study. In particular, in each script, the rasters with SNR > 5 were initially imported within a single stack, the dataframe associated with the stack was created and the PCA

algorithm was applied, imposing a maximum number of principal components equal to 15. Subsequently, the outputs necessary for the interpretation of the PCA were created, reported below for each of the areas of interest.

13.3. PCA Results

Scree Plot

Scree Plot is the plot of eigenvalues ordered from largest to the smallest. The number of components is determined at the point, beyond which the remaining eigenvalues are all relatively small and of comparable size (Anon, 2002; Peres-Neto et al., 2005). In general, it is appropriate to consider a number of principal components that allow to reach at least 85% of explained variance.

Fig. 57 shows the scree plots relating to the three study areas.

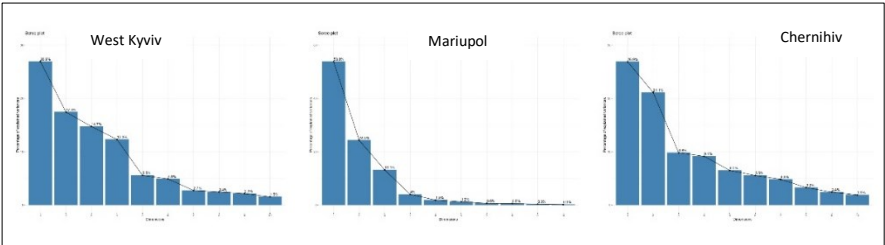


Fig. 57 – Scree Plot of West Kyviv (left), Mariupol (center), Chernihiv (right).

PC Rasters Plot

Fig. 58, Fig. 59 and Fig. 60 show rasters of the main components that allow to reach an overall explained variance greater than or equal to 85% for each of the study areas.

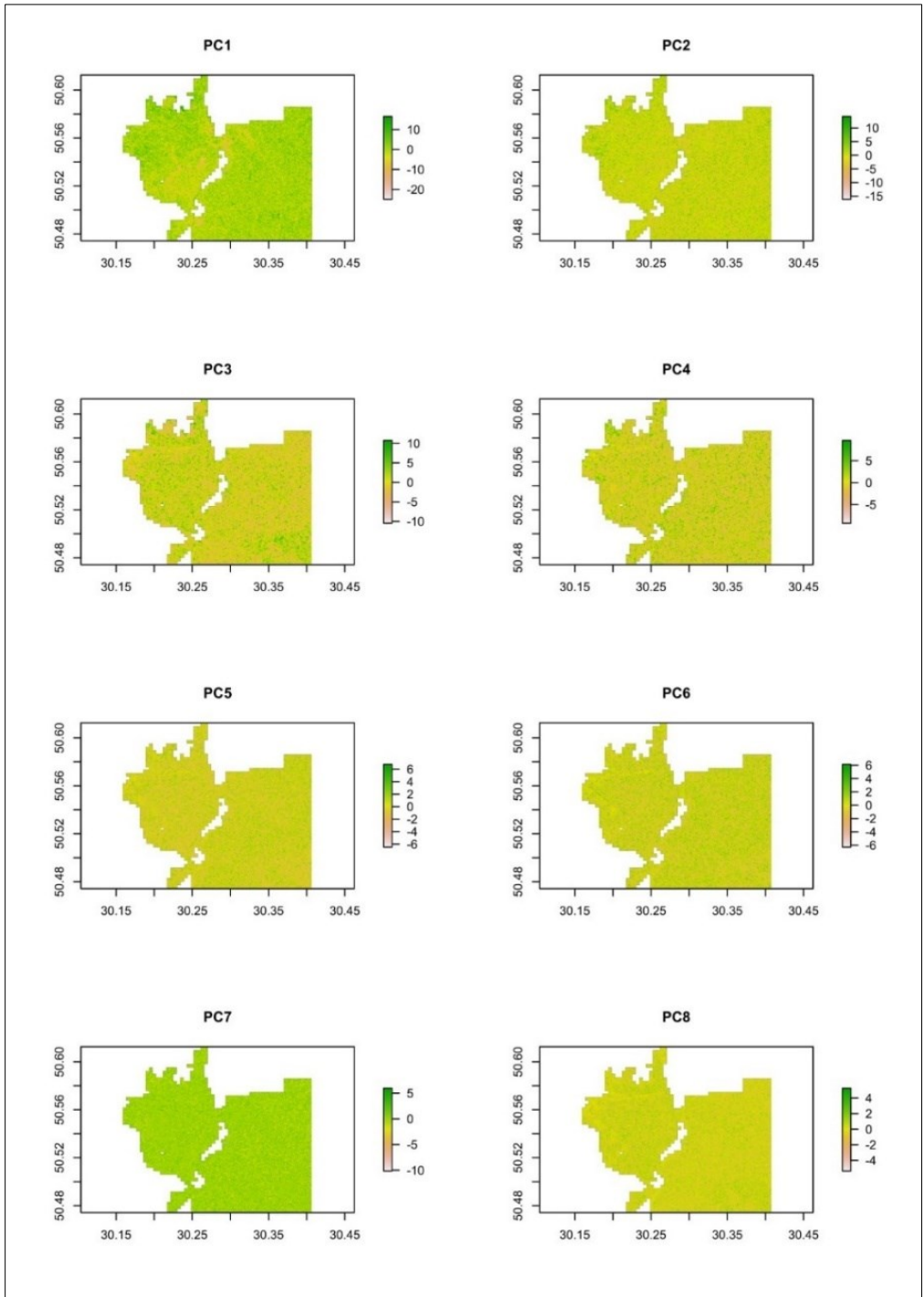


Fig. 58 – West Kyiv: set of principal component rasters with at least 85% variance folded.

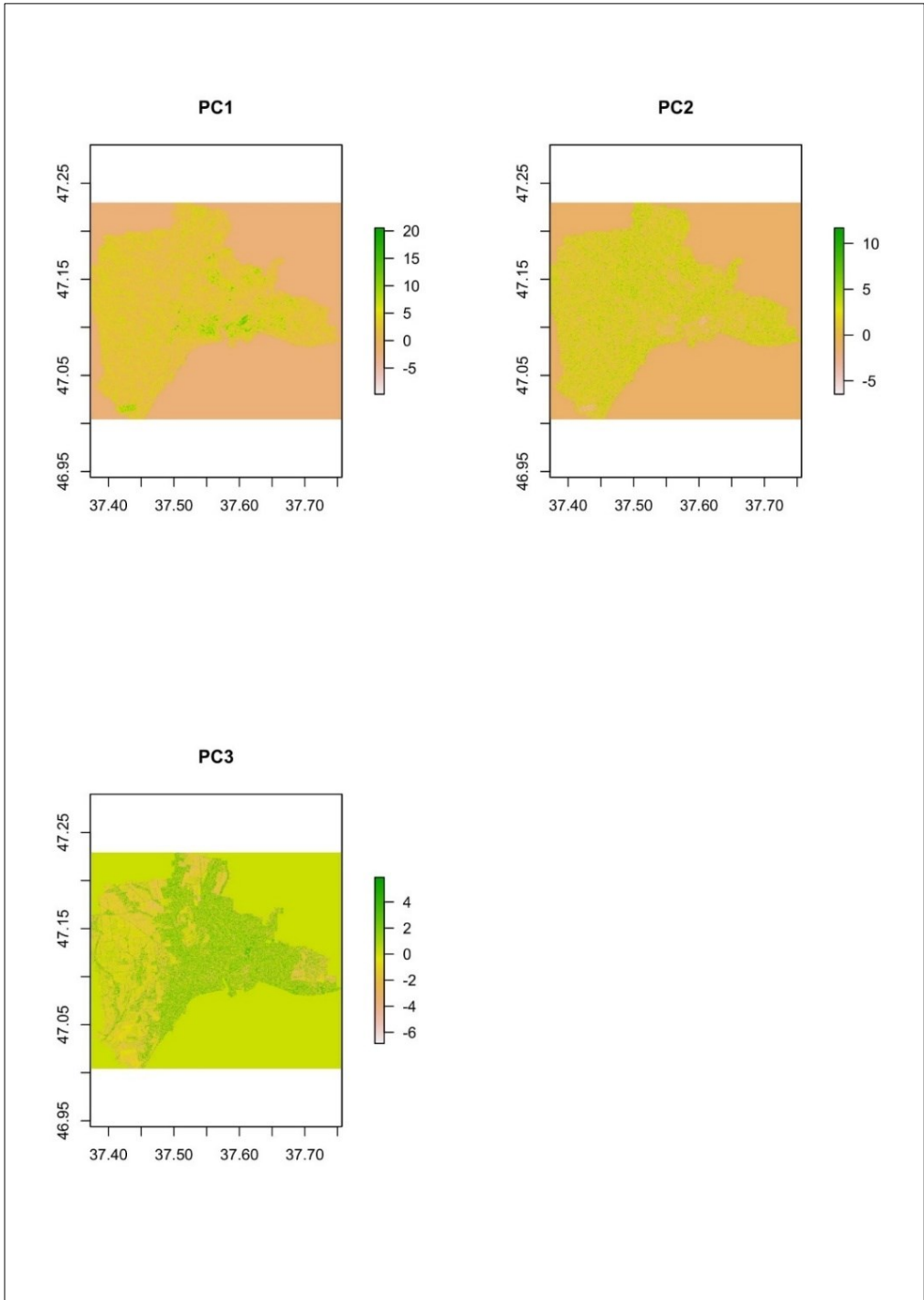


Fig. 59 – Mariupol: set of principal component rasters with at least 85% variance folded.

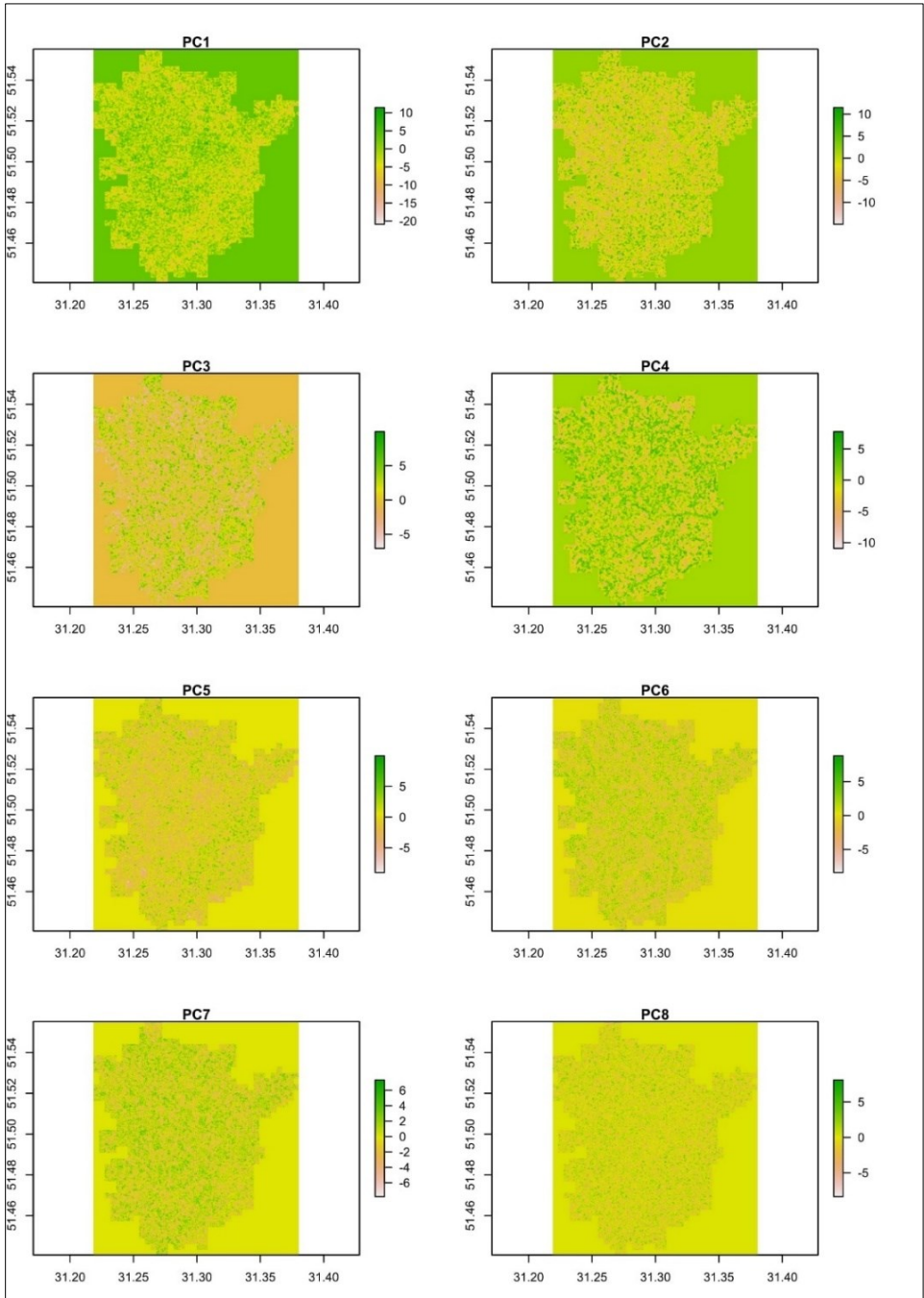


Fig. 60 – Chernihiv: set of principal component rasters with at least 85% variance folded.

Variables Correlation Circle

The correlation between a variable and a principal component (PC) is used as the coordinates of the variable on the PC. The representation of variables differs from the plot of the observations: The observations are represented by their projections, but the variables are represented by their correlations (Abdi & Williams, 2010). The plot above is also known as variable correlation plots. It shows the relationships between all variables. It can be interpreted as follow:

- Positively correlated variables are grouped together.
- Negatively correlated variables are positioned on opposite sides of the plot origin (opposed quadrants).

The distance between variables and the origin measures the quality of the variables on the factor map. Variables that are away from the origin are well represented on the factor map (Kassambara, 2017). Fig. 61, Fig. 62 and Fig. 63 show the correlation circle for the three areas of interest.

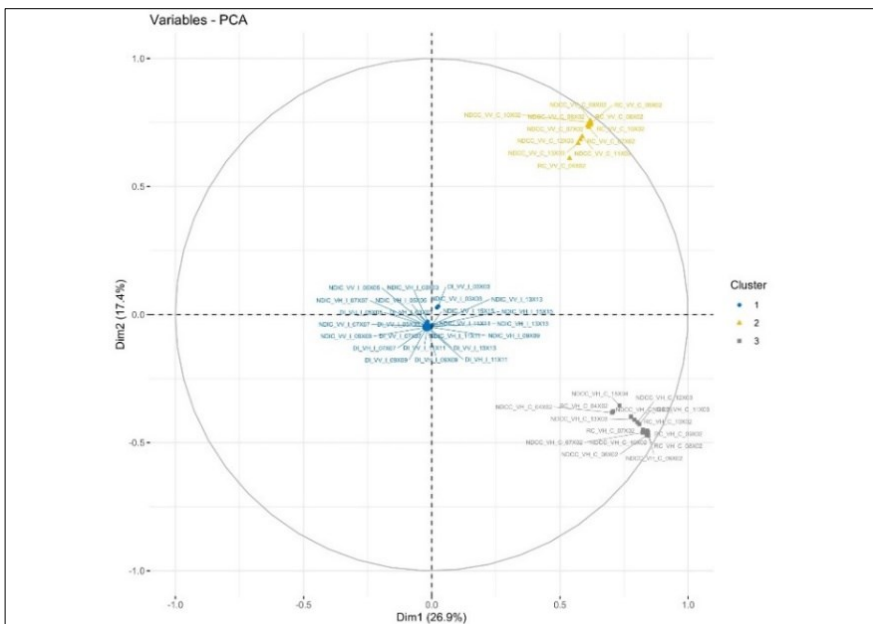


Fig. 61 – West Kyiv. Correlation Circle.

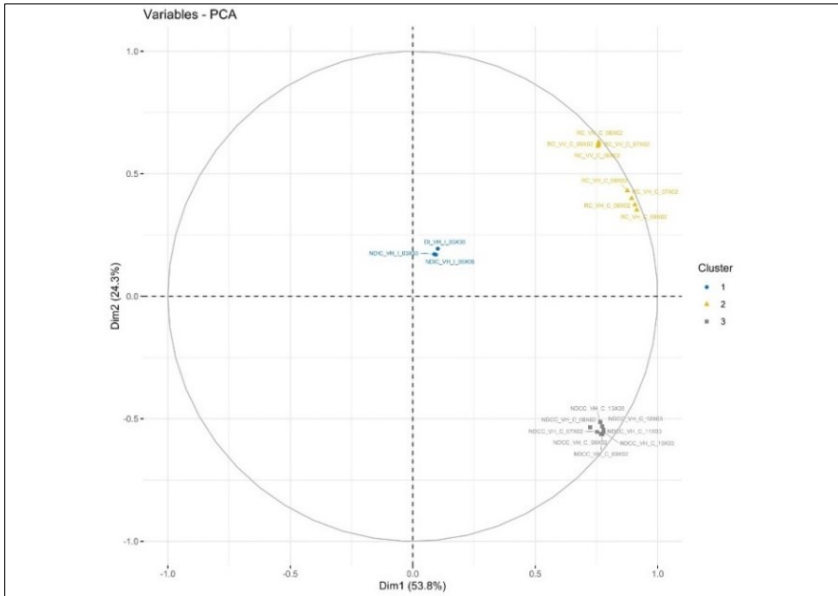


Fig. 62 – Mariupol. Correlation Circle.

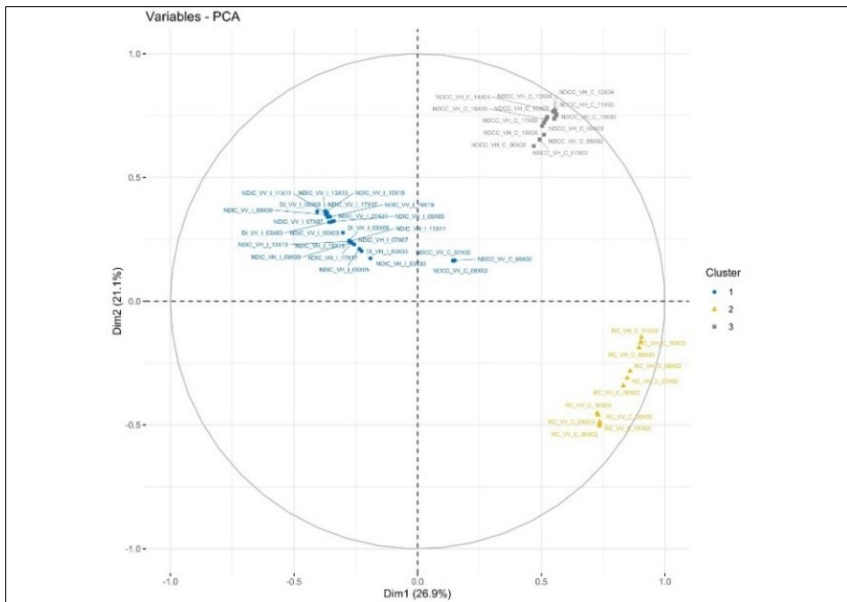


Fig. 63– Chernihiv. Correlation Circle.

Quality of representation

The quality of representation of the variables on factor map is called \cos^2 (square cosine, squared coordinates).

- A high \cos^2 indicates a good representation of the variable on the principal component. In this case the variable is positioned close to the circumference of the correlation circle.
- A low \cos^2 indicates that the variable is not perfectly represented by the PCs. In this case the variable is close to the center of the circle.

For a given variable, the sum of the \cos^2 on all the principal components is equal to one. If a variable is perfectly represented by only two principal components (Dim.1 & Dim.2), the sum of the \cos^2 on these two PCs is equal to one. In this case the variables will be positioned on the circle of correlations. For some of the variables, more than 2 components might be required to perfectly represent the data. In this case the variables are positioned inside the circle of correlations (Kassambara, 2017). Fig. 64, Fig. 65, and Fig. 66 show quality of variables to Dimension 1 (PC1) for each area of interest. Fig. 67 shows the global synthesis of the quality of the variables to Dimensions for each of the study areas.

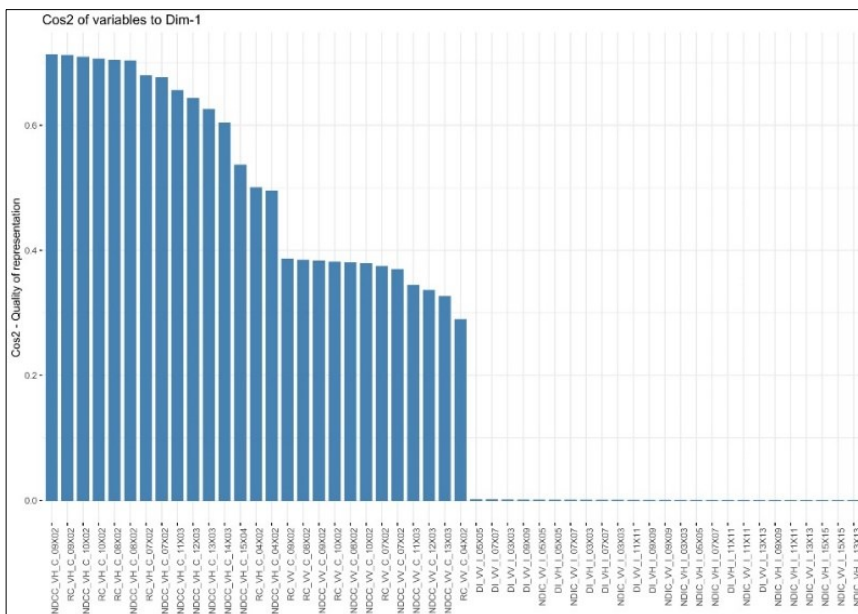


Fig. 64 – Wesy Kyviv. Quality of Variables to Dim.1.

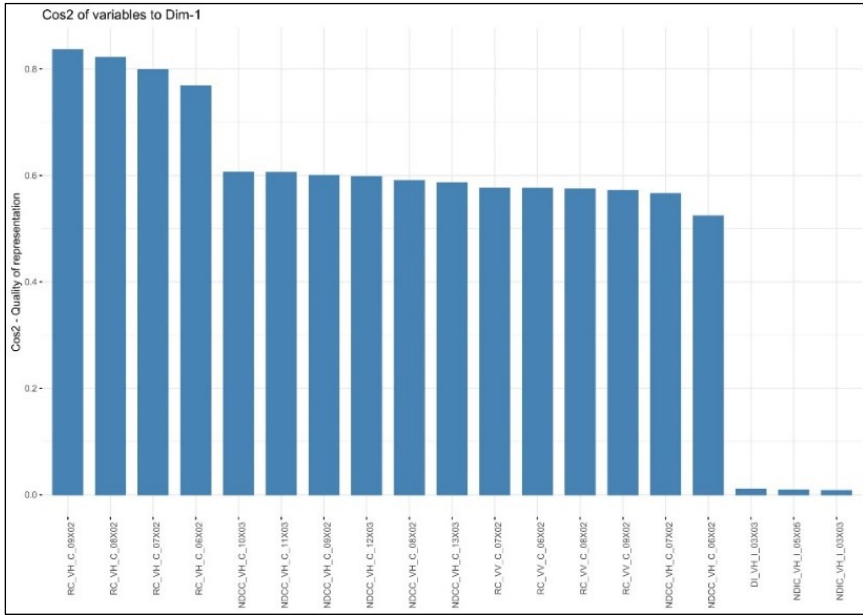


Fig. 65 – Mariupol. Quality of Variables to Dim.1.

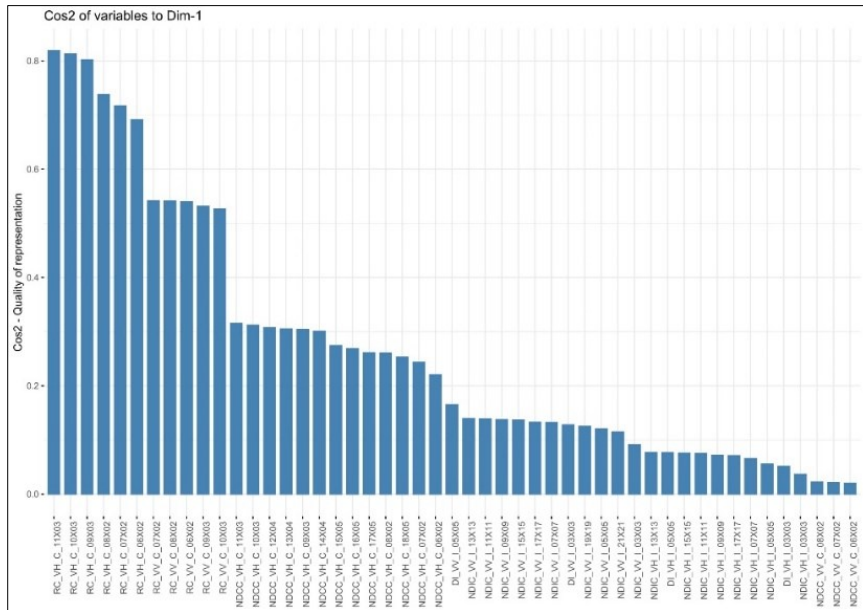


Fig. 66 – Chernihiv. Quality of Variables to Dim.1.

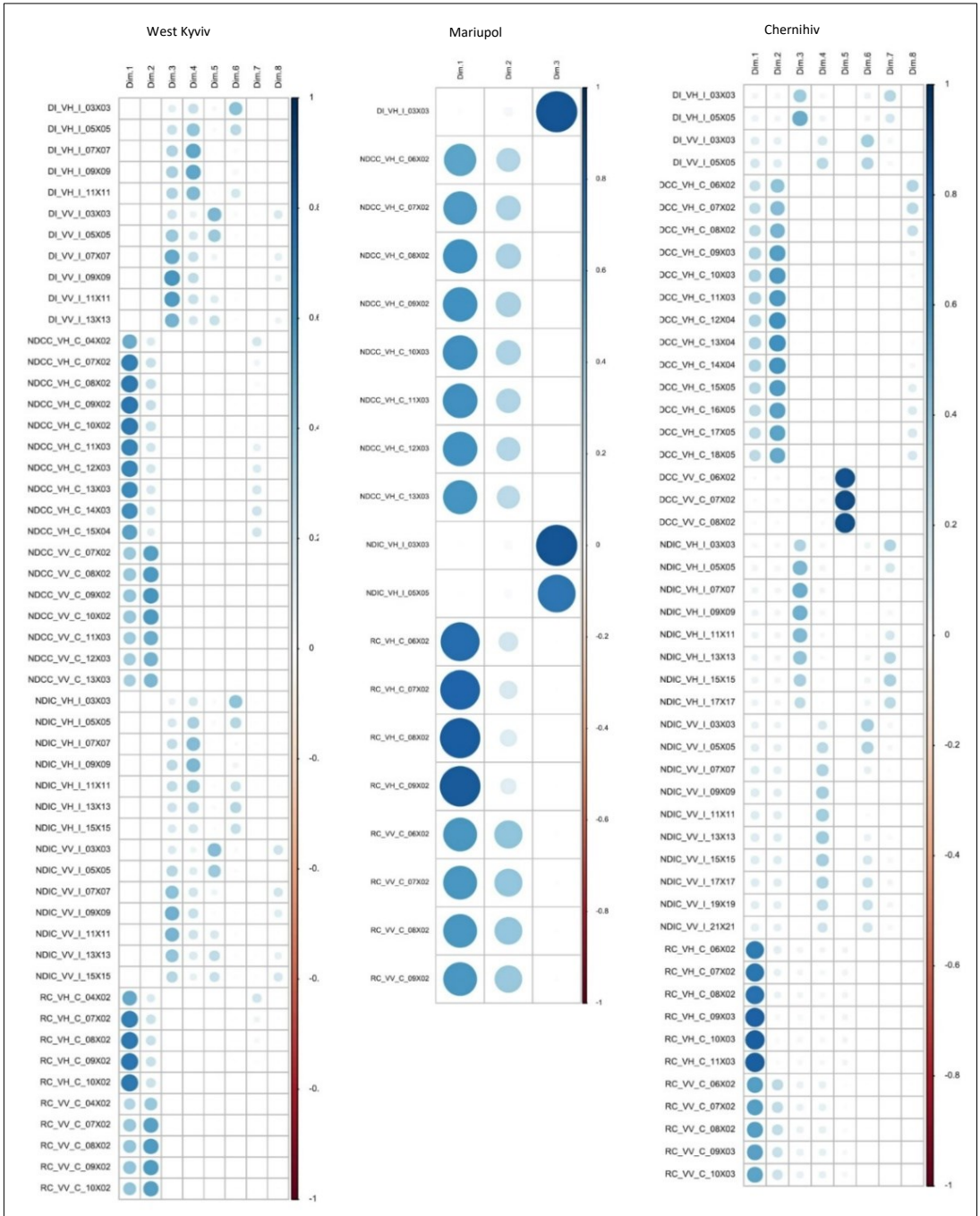


Fig. 67 – Global Quality of Variables to Dims.: West Kyiv (left), Mariupol (center), Chernihiv (right).

Contributions of variables to PCs

The contributions of variables in accounting for the variability in a given principal component are expressed in percentage. Variables that are correlated with PC1 (i.e., Dim.1) and PC2 (i.e., Dim.2) are the most important in explaining the variability in the data set. Variables that do not correlated with any PC or correlated with the last dimensions are variables with low contribution and might be removed to simplify the overall analysis. The red dashed line on the graph above indicates the expected average contribution. If the contribution of the variables were uniform, the expected value would be $1/\text{length}(\text{variables}) = 1/10 = 10\%$. For a given component, a variable with a contribution larger than this cutoff could be considered as important in contributing to the component. Note that, the total contribution of a given variable, on explaining the variations retained by two principal components, say PC1 and PC2, is calculated as $\text{contrib} = [(C1 * Eig1) + (C2 * Eig2)] / (Eig1 + Eig2)$, where C1 and C2 are the contributions of the variable on PC1 and PC2, respectively Eig1 and Eig2 are the eigenvalues of PC1 and PC2, respectively. Recall that eigenvalues measure the amount of variation retained by each PC (Kassambara, 2017). Fig. 68, Fig. 69, and Fig. 70 show contribution of variables to Dimension 1 (PC1) for each area of interest. Fig. 71 shows the global contribution of variables to Dimimesions for each of the study areas.

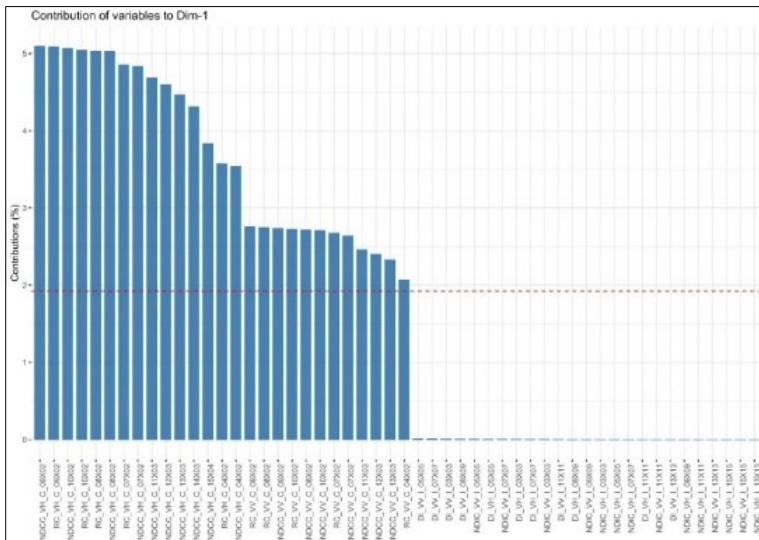


Fig. 68 – West Kyviv. Contribution of Variables to Dim.1.

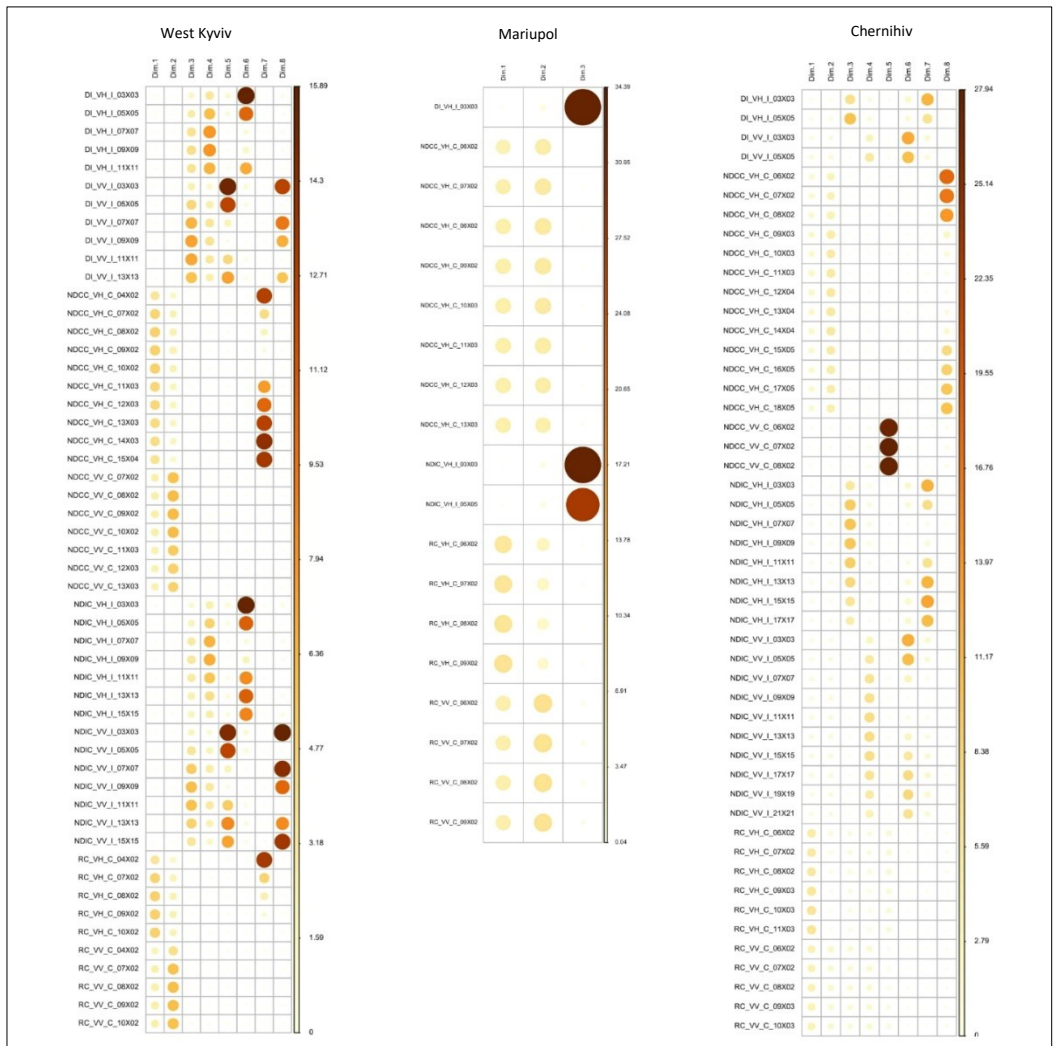


Fig. 71 – Global Contribution of Variables to Dims.: West Kyiv (left), Mariupol (center), Chernihiv (right).

13.4. Damage Maps

The creation of the classification maps for each study area took place in QGIS (Fig. 72, Fig. 73, Fig. 74). For reasons of time, it was decided to proceed with the import of the raster relating to the first principal component to which the greatest value of explained variance is associated. Therefore, the PC1 value interval was searched by trial and error which allowed to obtain damaged areas as similar as possible to those of the shapefiles of the RBDA UNOSAT maps. For the area west of Kyiv, maps were also created that

show the position of the points subject to detailed investigation by UNOSAT both in terms of damage level and confidence (Fig. 75, Fig. 76).

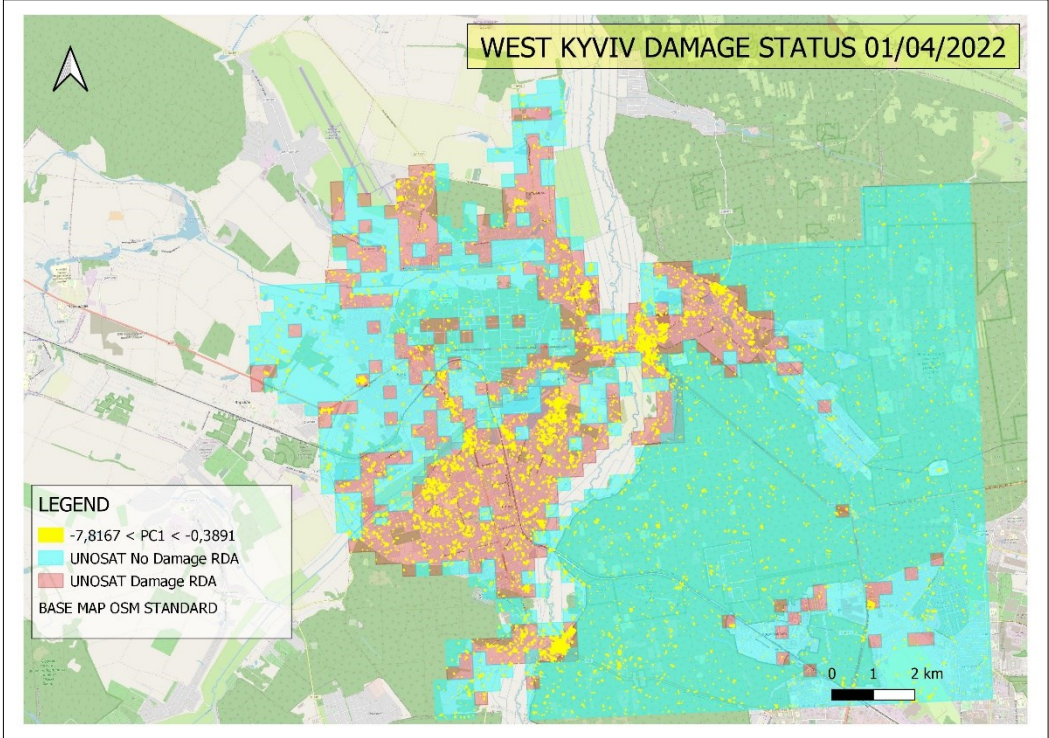


Fig. 72 – West Kyiv 01/04/2022. PC1 Damage Map.

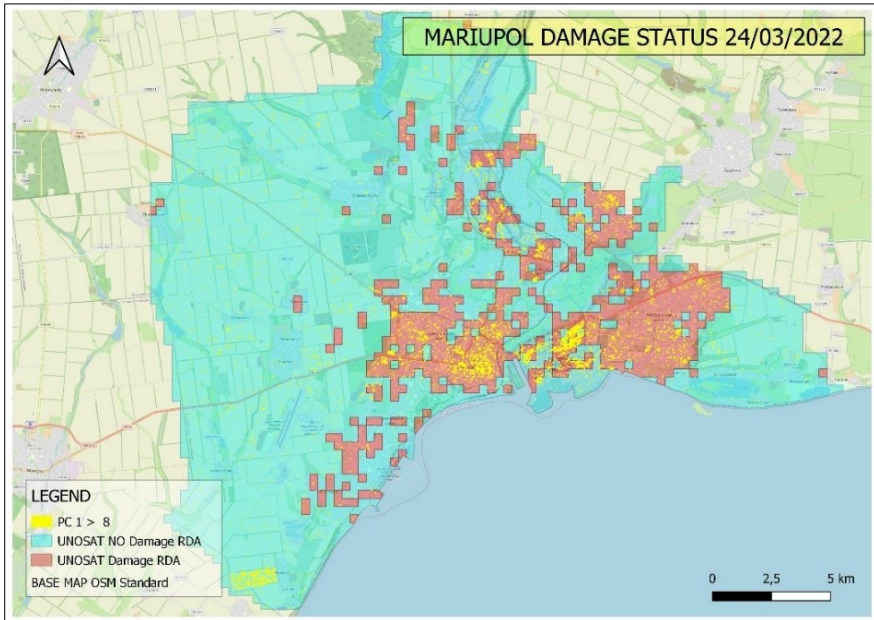


Fig. 73– Mariupol 24/03/2022. PC1 Damage Map.

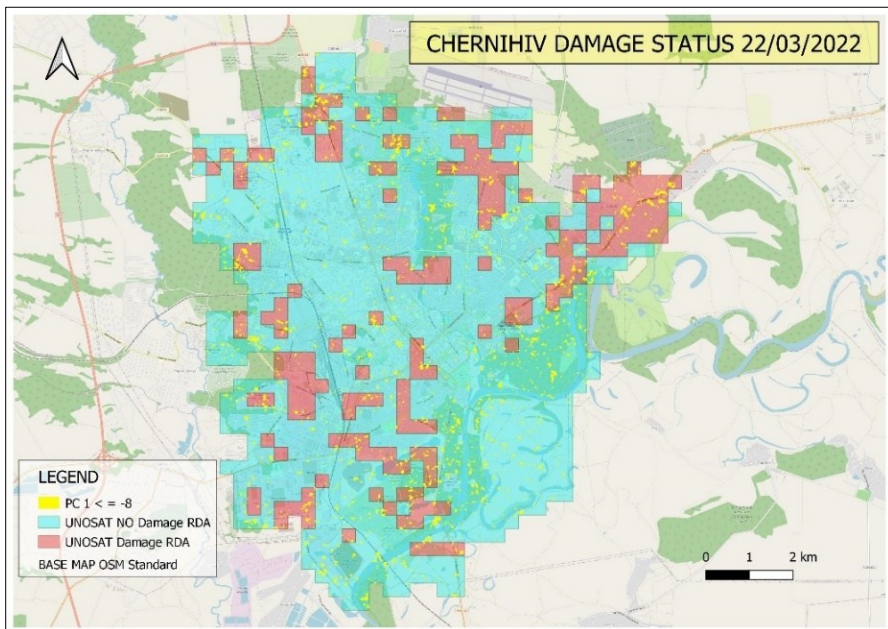


Fig. 74 – Chernihiv 22/03/2022. PC1 Damage Map.

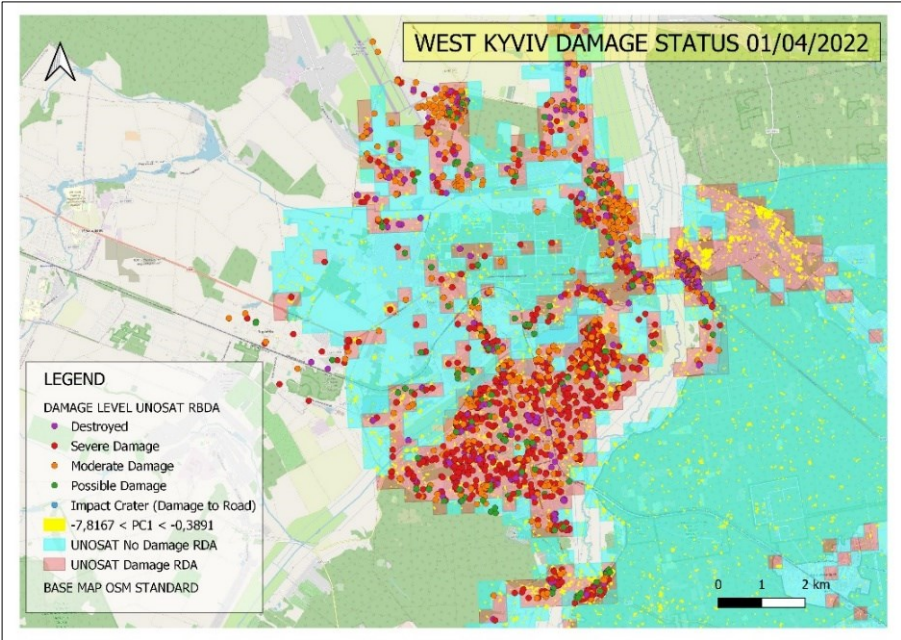


Fig. 75 – West Kyiv 01/04/2022. Damage Level Map

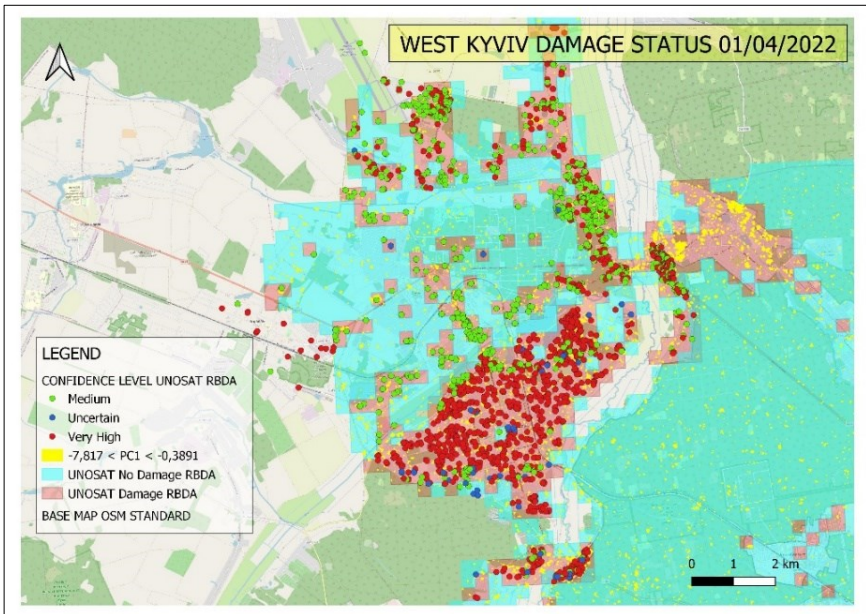


Fig. 76 – West Kyiv 01/04/2022. Confidence Level.

14.DISCUSSION OF THE RESULTS

This chapter discusses the polarimetric analysis results stated in paragraph 9.4 and the damage maps reported in paragraph 13.4 resulting from the examination of the main components of the coherence and intensity variables with $SNR > 5$.

14.1. Polarimetry Discussion

From the Alpha/Entropy graphs in figures Fig. 79, Fig. 80 and Fig. 81 show that the pixel clouds composing the rasters extend into the Z3 - Bragg Surface, Z6 - Random Surface, and Z9 - Non-feasible areas for the three study areas and each of the three reference dates, with a larger concentration in the Z6 area. The cloud of points assumes the same shape for all the pixels of each single area, both the damaged and undamaged portions. Furthermore, no significant variation of the outputs is noted in the three different dates of the analyzed images; thus, it was deemed appropriate to observe in detail the basic statistics of each raster. Therefore, in R, the boxplots of the average values and of the maximum and minimum values assumed by the variables of Entropy, Anisotropy and Alpha were created. In particular, the two series of boxplots were distinguished by study area and with respect to each of them there is an analysis referring to each of the three reference dates. Furthermore, for each date, a grouping was created that allows the boxplots for the full study region to be distinguished for the damaged and undamaged portions. Fig. 82, Fig. 83 and Fig. 84 show the results obtained. The geometric characteristics and positions of the three boxplots (damaged area, undamaged area and total area) of the average and maximum values of Entropy, Anisotropy and Alpha remain almost unchanged in the three dates of the analyzed images (two pre-war dates and one with the war in progress) for each of the three study areas. Similar considerations are given to the minimum values of Anisotropy and Alpha. Instead, it should be observed that the median of the boxplots of the minimum values of Entropy of the damaged areas increases slightly as the conflict progresses from pre-war to post-war conditions.

14.2. PCA Discussion

The results of the principal component analysis in the West Kyiv region show that taking into account 8 principal components (Fig. 57) represented by 8 unique rasters might result in an explained variance higher than or equal to 85%. (Fig. 58). From the correlation plot relating to PC1 and PC2 (Fig. 61) it can be seen that the variables can be grouped into three clusters. The blue cluster consists of the intensity variables and is located in a central position, allowing poor quality to be associated with these variables for the purpose of defining PC1 and PC2. The gray and yellow clusters are located on the periphery of the circle, allowing a good quality to be associated with these variables for the purpose of defining PC1 and PC2. The variable NDCC VH C 09X02 is the one that gives higher quality to the representation of PC1 followed by RC VH C 09X02, NDCC VH C10X02 and RC VH C10X02 (Fig. 64, Fig. 67). Quantitatively it still results that the variables NDCC VH C 09X02, RC VH C 09X02, NDCC VH C10X02 and RC VH C10X02 offer the greatest contribution in the definition of PC1 (Fig. 68, Fig. 71).

For the Mariupol area, an explained variance greater than or equal to 85% can be achieved by taking into consideration 3 principal components (Fig. 61) represented by 3 distinct rasters (Fig. 59). From the correlation plot relating to PC1 and PC2 (Fig. 62) it can be seen that the variables can be grouped into three clusters. The blue cluster consists of the intensity variables and is in a central position, allowing poor quality to be associated with these variables for the purpose of defining PC1 and PC2. The gray and yellow clusters are located on the periphery of the circle, allowing a good quality to be associated with these variables for the purpose of defining PC1 and PC2. The variable RC VH C 09X02 is the one that gives higher quality to the representation of PC1 followed by RC VH C 08X02, RC VH C 07X02 and RC VH C 06X02 (Fig. 65, Fig. 67). Quantitatively it still results that the variables RC VH C 09X02, RC VH C 08X02, RC VH C 07X02 and RC VH C 06X02 offer the greatest contribution in the definition of PC1 (Fig. 69, Fig. 71).

For the Chernihiv area, an explained variance greater than or equal to 85% can be achieved by taking into consideration 8 principal components (Fig. 61) represented by 8 distinct rasters (Fig. 60). From the correlation plot relating to PC1 and PC2 (Fig. 63) it can be noticed that the variables can be grouped into three clusters, one of which is located. The blue cluster consists mostly of intensity variables, is sparse and concentrated in the upper left quadrant with a disconnected core in the upper right quadrant towards the center. . This makes it possible to associate poor quality with these variables for the purpose of defining PC1 and PC2. The gray and yellow clusters are located on the periphery of the circle, allowing a good association with these variables for the purpose of defining PC1 and PC2. The variable RC VH C 11X03 is the one that gives higher quality to the representation of PC1 followed by RC VH C 10X03, RC VH C 09X03 and RC VH C 08X02 (Fig. 66, Fig. 67). Quantitatively it still results that the variables RC VH C 11X03, RC VH C 10X03, RC VH C 09X03 and RC VH C 08X02 offer the greatest contribution in the definition of PC1 (Fig. 70, Fig. 71).

14.3. Damage Map Discussion

The classification maps shown in fig 141, fig 142 and fig 143 were examined by processing the confusion matrices shown in the following tables (Næsset, 1996; Liu & Shriberg, 2007; Congalton, 2001; Story & Congalton, 1986). For each study area, the confusion matrix (Fig. 77) was created by comparing the damaged/undamaged map obtained from PC1 with the UNOSAT one. In detail, in QGIS, the following areas have been determined:

- True Positive (TP): damaged areas identified by both PC maps and UNOSAT maps.
- True Negative (TN): undamaged areas identified by both PC1 maps and UNOSAT maps.
- False Positive (FP): areas classified as damaged by PC1 maps and classified as undamaged by UNOSAT maps.
- False Negative (FN): areas classified as undamaged by PC1 maps and classified as damaged by UNOSAT maps.

Through these values it was possible to calculate the following percentages:

$$\text{Overall Accuracy} = \frac{(TP + TN)}{(TP + TN + FP + FN)} * 100 \quad (77)$$

		GROUND TRUTH	
		Damaged	Undamaged
PREDICTION	Damaged	TP	FP
	Undamaged	FN	TN

Fig. 77 – Confusion Matrix

$$\text{Precision} = \frac{TP}{(TP + FP)} * 100 \quad (78)$$

$$\text{True Damage} = \frac{TP}{(TP + FN)} * 100 \quad (79)$$

$$\text{True Undamaged} = \frac{TN}{(TN + FP)} * 100 \quad (80)$$

The West Kyiv damage map has an overall accuracy of 76.19%, a precision of 69.40%, a percentage of the damaged surface correctly identified equal to 7.61% and a percentage of the undamaged surface correctly identified equal at 98.89% (Tab.). The damage map of Mariupol has an overall accuracy of 82.08%, a precision of 46.17%, a percentage of the damaged surface correctly identified equal to 11.26% and

WEST KYVIV PC1 CLASSIFICATION: CONFUSION MATRIX			
	Damage UNOSAT [m ²]	No Damage UNOSAT [m ²]	Total [m ²]
Damage PC1 [m ²]	3401552	1499915	4901467
No Damage PC1 [m ²]	41275146	133469588	174744734
Total [m ²]	44676698	134969503	179646201
% OVERALL ACCURACY		76,19	
% PRECISION		69,40	
%TRUE DAMAGED		7,61	
%TRUE UNDAMAGED		98,89	

Tab. 6 – West Kyviv. Confusion Matrix.

MARIUPOL PC1 CLASSIFICATION: CONFUSION MATRIX			
	Damage UNOSAT [m ²]	No Damage UNOSAT [m ²]	Total [m ²]
Damage PC1 [m ²]	7203777	8398019	15601796
No Damage PC1 [m ²]	56791209	291365010	348156219
Total [m ²]	63994986	299763029	363758015
% OVERALL ACCURACY		82,08	
% PRECISION		46,17	
%TRUE DAMAGED		11,26	
%TRUE UNDAMAGED		97,20	

Tab. 6 – Mariupol. Confusion Matrix.

CHERNIHIV PC1 CLASSIFICATION: CONFUSION MATRIX			
	Damage UNOSAT [m ²]	No Damage UNOSAT [m ²]	Total [m ²]
Damage PC1 [m ²]	1065723	2512883	3578606
No Damage PC1 [m ²]	17461732	66383402	83845134
Total [m ²]	18527455	68896285	87423740
% OVERALL ACCURACY		77,15	
% PRECISION		29,78	
%TRUE DAMAGED		5,75	
%TRUE UNDAMAGED		96,35	

Tab. 8 – Chernihiv. Confusion Matrix.

a percentage of the undamaged surface correctly identified equal to 97.20% (Tab. 6). The Chernihiv damage map has an overall accuracy of 77.15%, a precision of 29.78%, a percentage of the damaged surface correctly identified equal to 5.75% and a percentage of the undamaged surface correctly identified equal to 96.35% (Tab.). The detailed analysis of the UNOSAT RBDA shapefiles that make up the West Kyviv area of interest revealed what is illustrated in Fig. 78 and quantitatively described in Tab. 7, Tab. 8 and Tab. 9. In particular, it turned out that the shapefiles of the maps of the areas classified as damaged and those classified as undamaged overlap in some areas, resulting in an area of uncertainty equal to about 1% of the investigated area (Tab. 7). Furthermore, it is noted that 2.3% of the BDA points subject to a detailed assessment of the damage with one's own confidence level fall within the UNOSAT area defined as

undamaged while 1% fall within the overlapping area damaged/undamaged (Tab. 8). As regards the Damage Map of PC1, it can be noted that 38.09% of the BDA points fall within the area defined as damaged, 61.91% fall within the area defined as undamaged and 0.49% fall within the zones of PC1 belonging to overlap area (Tab. 9).

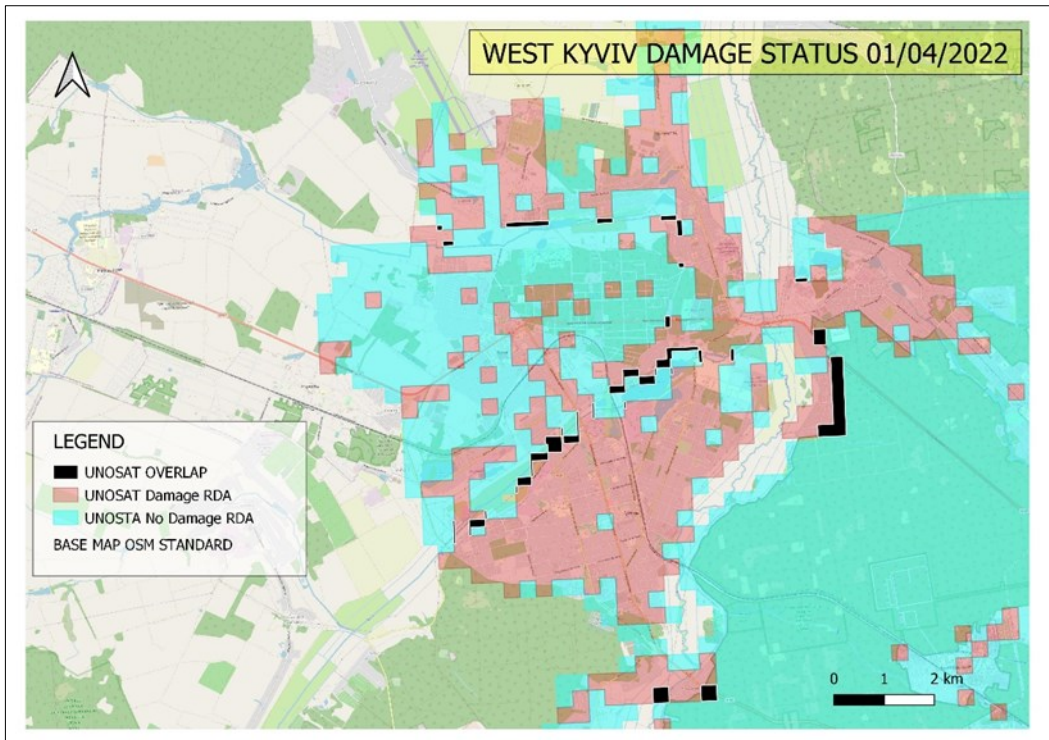


Fig. 78 – West Kyviv. UNOSAT overlap Area.

WEST KYVIV - OVERLAP ANALYSIS		
UNOSAT DATA	[m ²]	%
UNOSAT Total AOI	177955579	100
UNOSAT Damage Area	44676702	25,11
UNOSAT No Damage Area	134969500	75,84
UNOSAT Overlap Area	1690625	0,95

Tab. 7 – West Kyviv. UNOSAT Overlap Area.

WEST KYVIV - OVERLAP ANALYSIS		
UNOSAT DATA	n.	%
Total Point BDA UNOSAT	2292	100,0
Total Point BDA UNOSAT in AOI	2258	98,52
Total Point BDA UNOSAT excluded from AOI	34	1,48
Total Point BDA UNOSAT in Damage Area	2231	98,80
Total Point BDA UNOSAT in No Damage Area	52	2,30
Total Point BDA UNOSAT in Overlap Area	25	1,11

Tab. 8 – West Kyviv. BDA points in UNOSAT RBDA.

WEST KYVIV - OVERLAP ANALYSIS		
PC1 MAP	n.	%
Total Point BDA UNOSAT	2292	100,0
Total Point BDA UNOSAT in AOI	2258	98,52
Total Point BDA UNOSAT excluded from AOI	34	1,48
Total Point BDA UNOSAT in PC1 Damage Area	860	38,09
Total Point BDA UNOSAT in No Damage Area	1398	61,91
Total Point BDA UNOSAT in Overlap Area	11	0,49

Tab. 9 – West Kyviv. BDA points in PC1 map.

CONCLUSIONS

According to the study, the free SAR Sentinel-1 data made accessible to ESA has a high spatial resolution of 10m, which supports the process of identification of damaged regions caused by the war on Ukrainian territory from February 24, 2022. The research evaluated the use of a classification approach for separating damaged from undamaged areas based on the use of polarimetric nature indices, coherence and intensity indices obtained in 15 calculation windows. The analysis conducted in the three distinct study areas of West Kyiv, Mariupol, and Chernihiv revealed striking similarities and divergences that might be relevant for the creation of a general classification approach for the study of realities affected by war events.

The implementation of a polarimetric analysis proved to be appropriate given that collapses and damage to buildings following missile attacks and bomb impacts on the ground most likely determine the change in the scatterometric characteristics of the targets investigated by the SAR signal in terms of bounce mechanisms. The dual-pol nature of the Sentinel-1 data, which sees it equipped with the VV and VH bands but without the HV and HH bands, has only allowed the implementation of the H-Alpha type decomposition whose indices of Entropy, Anisotropy and Alpha they did not show significant variations between the pre-war survey dates and the one with the war in progress in any of the three study areas. Only the Entropy Index increased between pre-war and post-war settings. This confirms what often emerges in the literature for which it would be appropriate to conduct a polarimetric analysis through quad-pol products, i.e. equipped with the VV, VH, HV and HH bands (RADARSAT-2, TerraSAR X, ALOS PALSAR 1&2 etc.) which allow other decompositions and generate indexes able to fully describe the scatterometric behavior of the investigated surfaces (Braun & Offermann, 2022; Xie et al., 2015; Ji & Wu, 2015b; Dhar et al., n.d.; Nasirzadehdizaji et al., 2019).

The idea of generating the six coherence indices (DC VV, DC VH, NDCC VV, NDCC VH, RC VV, RC VH) and the six intensity indices (DI VV, DI VH, NDIC VV, NDIC VH, RI VV, RI VH) for the 15 calculation windows proved to be sensible considering what emerged from the boxplots (sections. 10.4 99and 11.4), from the SNR discrimination (section.12.3) and from the Principal Components Analysis (section 13.3). In fact, the boxplots highlighted the damage/non-damage condition in a different way based on the index considered, the calculation window and the type of value observed (average, minimum or maximum). It turns out that for some indices, in some calculation windows, no difference can be found between the condition of damage/no damage by observing average, minimum or maximum values. Other indices show differences after a specified computation window, while others show differences in correspondence with the highest values but not the average and minimum values, and so on. SNR discrimination reduced the number of indices to operate on, making it clear in each study area that the DC VH, DC VV, RI VH, RI VV indices should not be taken into consideration for any of the 15 coherence or intensity calculation windows, while the NDCC VH index calculated from window 1 to 8, the RC VH index calculated from window 1 to 4, the RC VV index calculated from window 1 to window 4, the DI VH index calculated in window 1, the NDIC VH index calculated in windows 1 and 2, are sensitive. For the remaining indices, it was observed how the SNR discrimination reduces their number in a similar way for the West Kyviv and Chernihiv sites while it significantly reduces the number of indices for the Mariupol site which, unlike the other two, stands on the coast. The Principal Component Analysis confirmed the need to resort to the combination of the residual indices of the SNR discrimination in order to be able to generate a small number of linearly independent variables capable of being able to distinguish the damage/non-damage condition in the three study areas. The RC VH index defined in the fourth coherence calculation window contributes qualitatively and quantitatively to better define the first principal component in the three study areas. The intensity indices do not give qualitative and quantitative contributions to the summary variables of the PCA, while the coherence indices prove to be valid both qualitatively and quantitatively by defining two clusters in each study area. However, it should be

emphasized that the generation of coherence indices starts from the use of Sentinel-1 SLC products processed in SNAP, while the generation of intensity indices refers to Sentinel-1 GRDH products processed in CATALYST to the detriment of a rigorous homogeneity of sources and procedures.

The maps constructed for the three study areas refer only to the first principal component which for the areas of West Kyiv and Chernihiv explains about 27% of the variance, while for Mariupol, it explains about 54% of the variance. The maps assume values of overall accuracy greater than 75% compared to the ground truths consisting of the Rapid Building Damage Assessment Map (RBDA) and the Building Assessment Building Maps (BDA) made available in pdf and shapefile format by the United Nations Satellite Center (UNOSAT) part of the United Nations Institute for Training and Research (UNITAR). It seems appropriate to point out the following with respect to these references:

- The UNOSAT maps come from a visual survey conducted by man and therefore affected by interpretation errors (Magnussen & Russo, 2012; Rizzo & Gasparini, 2022, Anon, 2021).
- The basic satellite image of the UNOSAT maps has a very high resolution (30 cm. x 30 cm.), but the RBDA maps are expressed in terms of damage over relatively high extension units (500 m. x 500 m.). Studies in which the spatial resolution of the satellite data is comparable with the dimensions of the investigated objects are suitable. For example, Tarantino and all made use of WorldView-2 data to analyze the leaf area index (Tarantino et al., 2015b).
- Even the BDA-type maps which attribute a certain level of damage to specific buildings or infrastructures (Destroyed, Severe Damage, Moderate Damage, Possible Damage, Impact Crater) are characterized by a certain level of confidence (Medium, Uncertain and Very High) such not to attribute absolute certainty to what is represented.
- For the area west of Kyiv, the study by Aimaiti et al., (2022) through the SAR log ratio identified exactly 58% of the damaged buildings while in the present

work with only the PC1 map and without any mask that reduces false positives a value greater than 69% is reached.

For the Mariupol and Chernihiv sites, only RBDA-type maps were available which fully capture the surveyed areas, and this did not allow for the detection of the ambiguities which were instead detected at the West Kyviv site. In this study area the shapefiles of the RBDA maps of the western area of Kyviv, of Hostomel, Bucha, Horenka and Irpin were assembled in QGIS environment and the availability of the BDA maps for the areas of Hostomel, Bucha and Irpin was found. Along the edges of each map there are squares or portions of squares that overlap with those of the adjacent maps; the overlays in which the double condition of damage/undamaged (ambiguity) is found have been given the color black. It turns out that there are overlapping areas of the RBDAs in which there is no coherence of expression in terms of damage/undamaged (Fig. 78) and furthermore some points of the BDA fall into undamaged or overlapping areas of the RBDAs (Fig. 75, Fig. 76) (Tab. 8). All of this enables us to avoid treating the UNOSAT maps as absolute and irrefutable truths, making the results of the confusion matrices of the maps generated at the conclusion of the work reasonably questionable. However, given the extent of these problems, resulting in an overlapping area of about 1% in the RBDAs and inaccuracy for about 3.5% of the points in the BDAs, the decision to consider them as valid references was confirmed.

The work carried out could be expanded according to various aspects.

- i. Conduct Polarimetric Analysis with quad-pol products in order to exhaustively describe the scatterometric mechanisms of ground targets.
- ii. Assume ground-truth with level of detail greater than 500m consistently with the objects to be surveyed.
- iii. Design a study based on a single type of images (SLC or GRDH) and on the use of a single software for the generation of the different index categories.

- iv. Create maps based on the use of multiple principal components by increasing the percentage of variance explained for the benefit of overall accuracy and precision of the outputs.
- v. Implement a partial least square in order to define a model with both descriptive characteristics of the investigated reality and with a forecasting character with respect to future events.
- vi. Attempt to determine a single classification index also starting from the indexes examined in the present work.
- vii. It is possible to operate a reduction of false positives by creating a specific mask of the built using the Open Street Map (OSM) and World Settlement Footprint (WSF) data (Aimaiti et al., 2022).

APPENDIX

A – Polarimetry Outputs

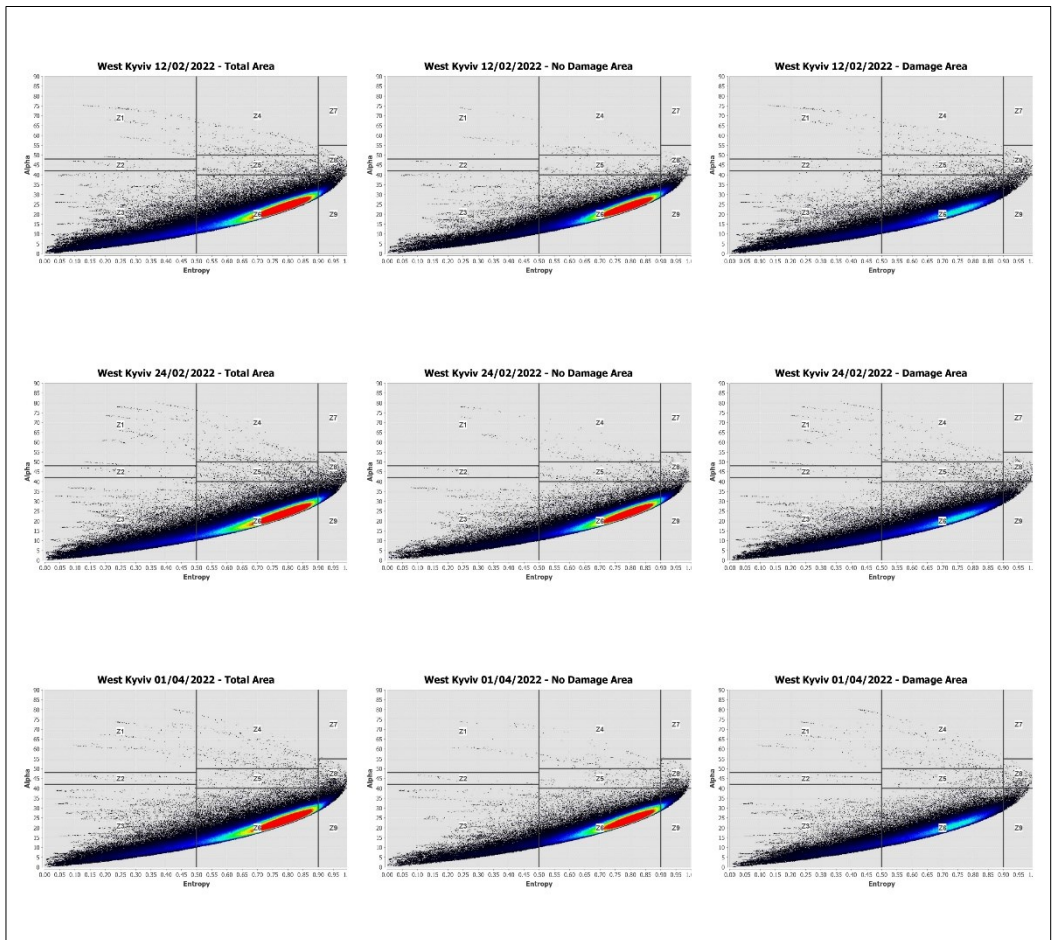


Fig. 79 – SNAP: Alpha Entropy Diagrams for West Kyiv Area.

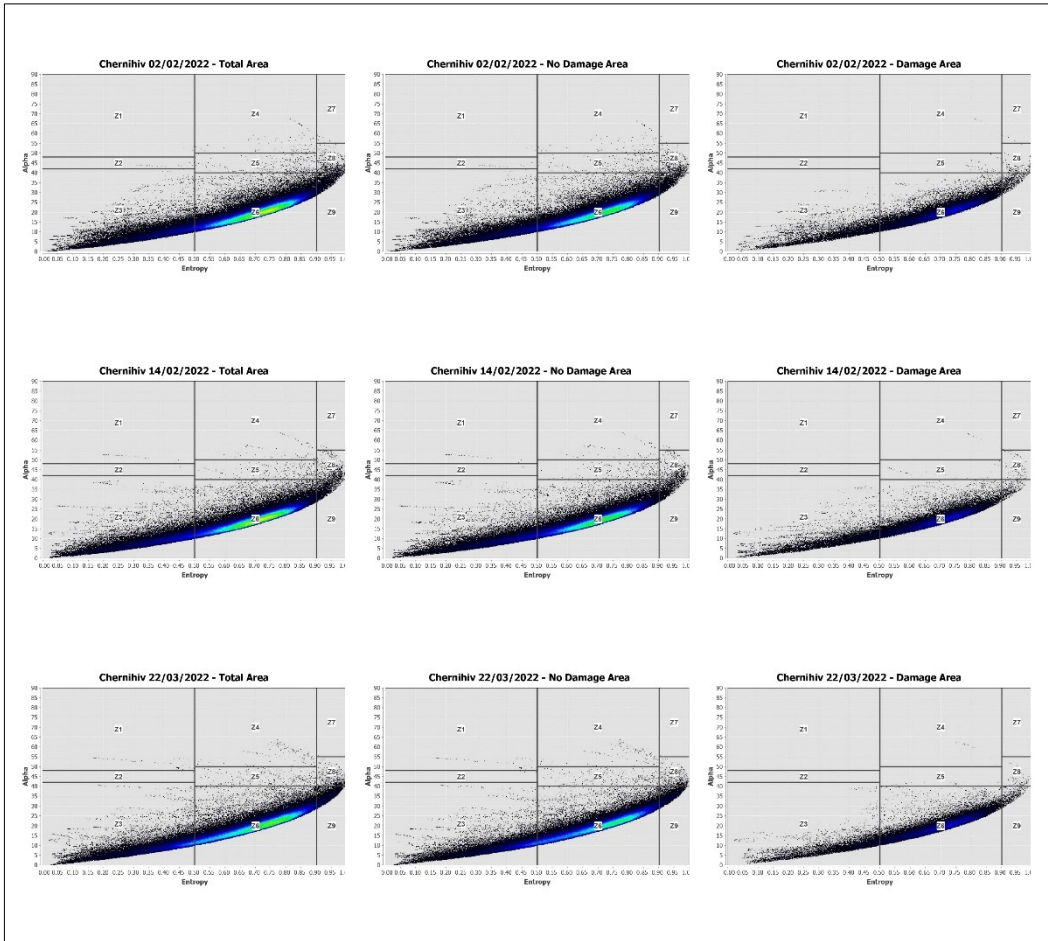


Fig. 80 – SNAP: Alpha Entropy Diagrams for Mariupol Area.

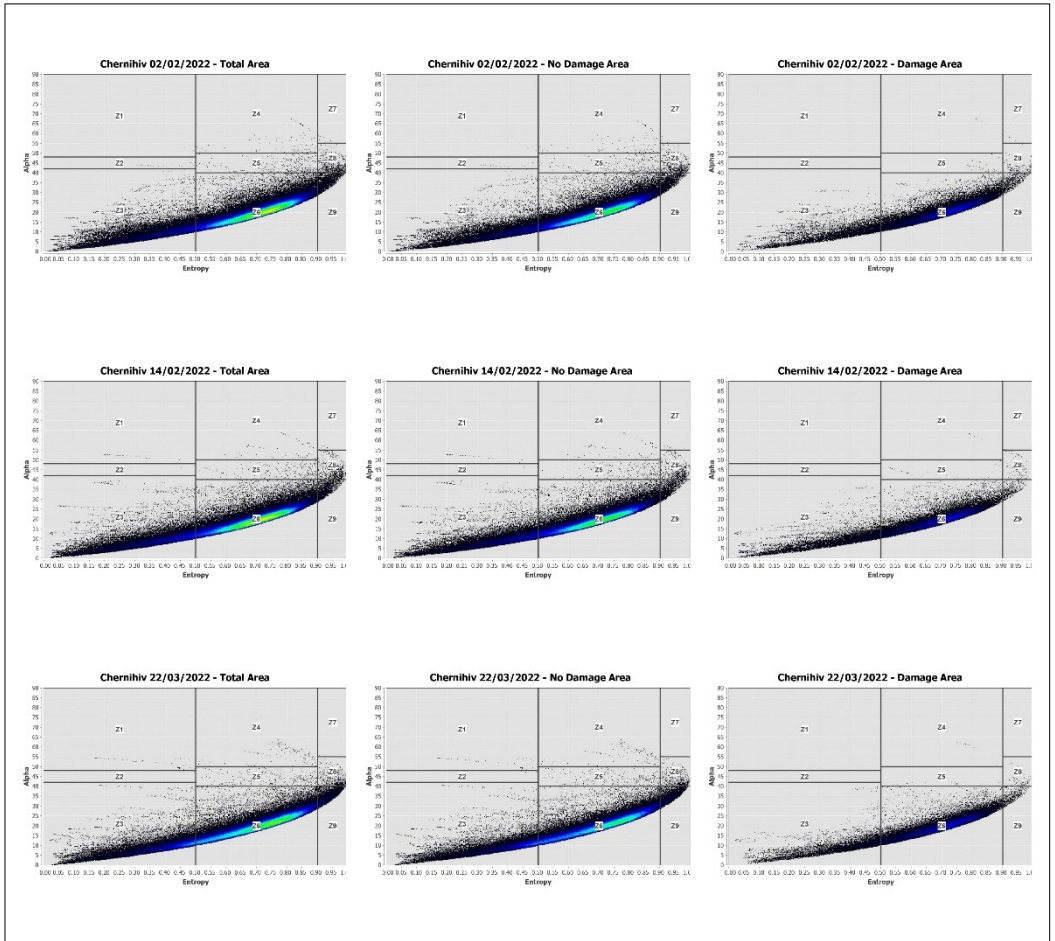


Fig. 81 – SNAP: Alpha Entropy Diagrams for Chernihiv Area.

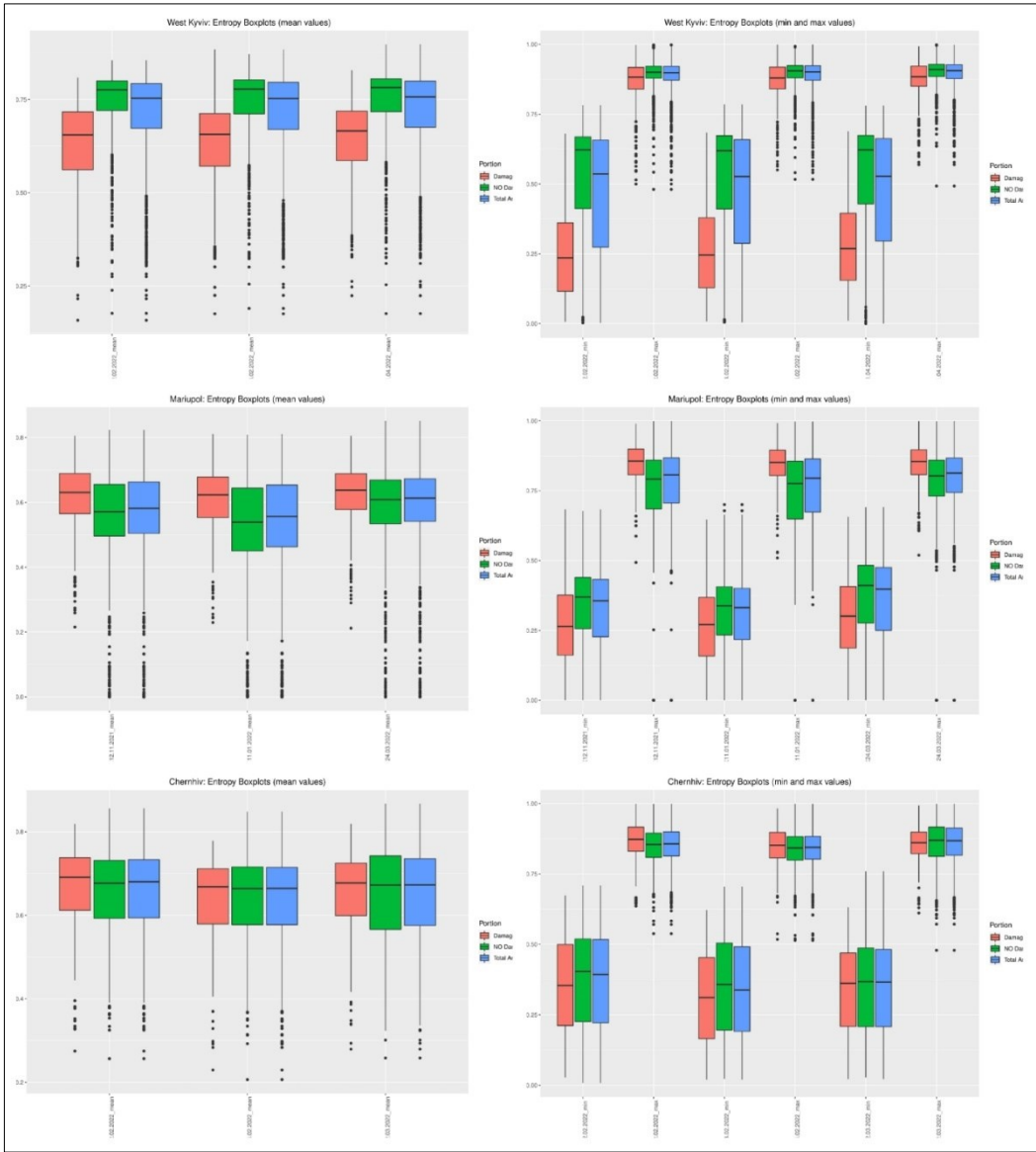


Fig. 82 – Entropy Boxplots.

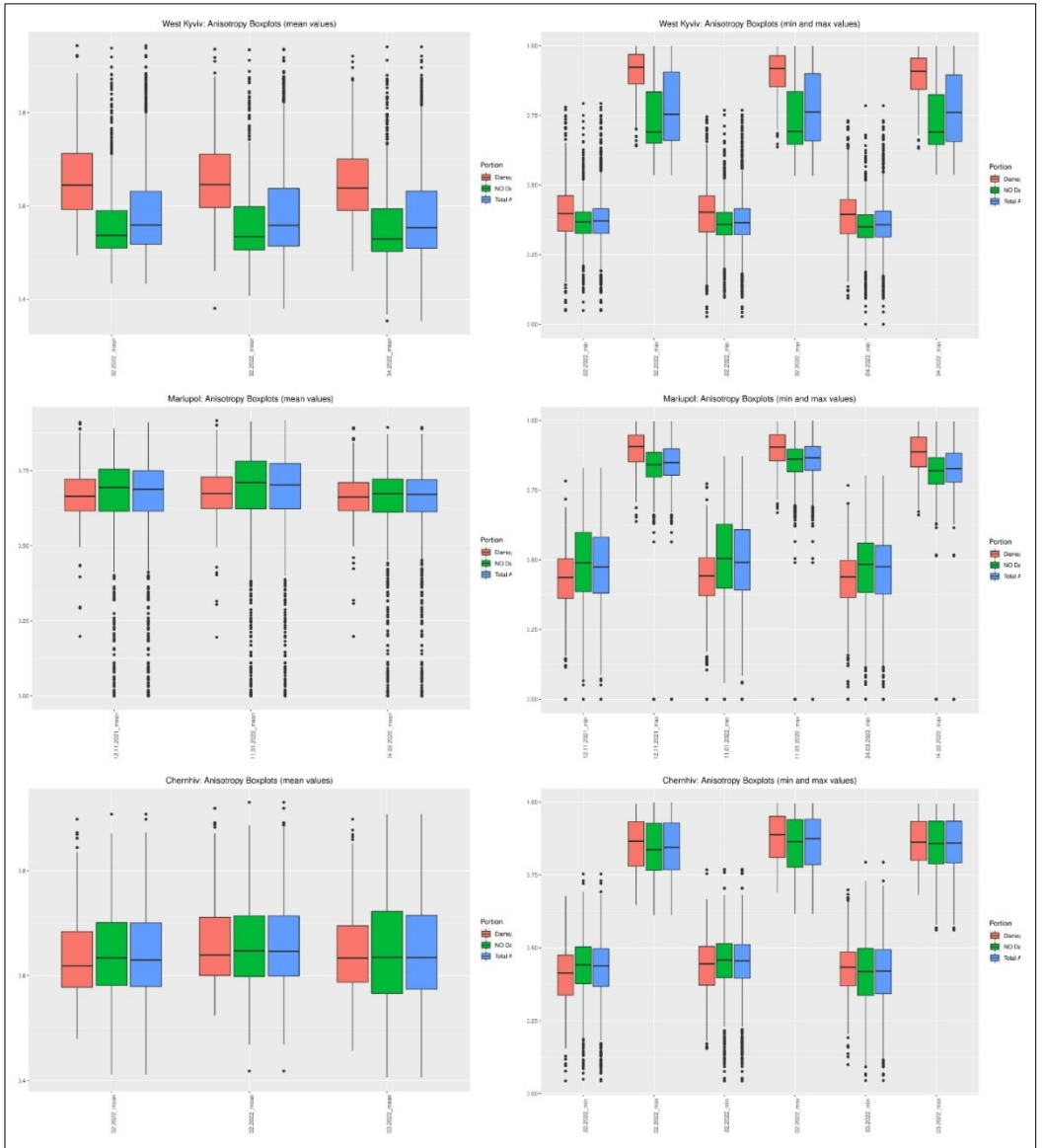


Fig. 83 – Anisotropy Boxplots.

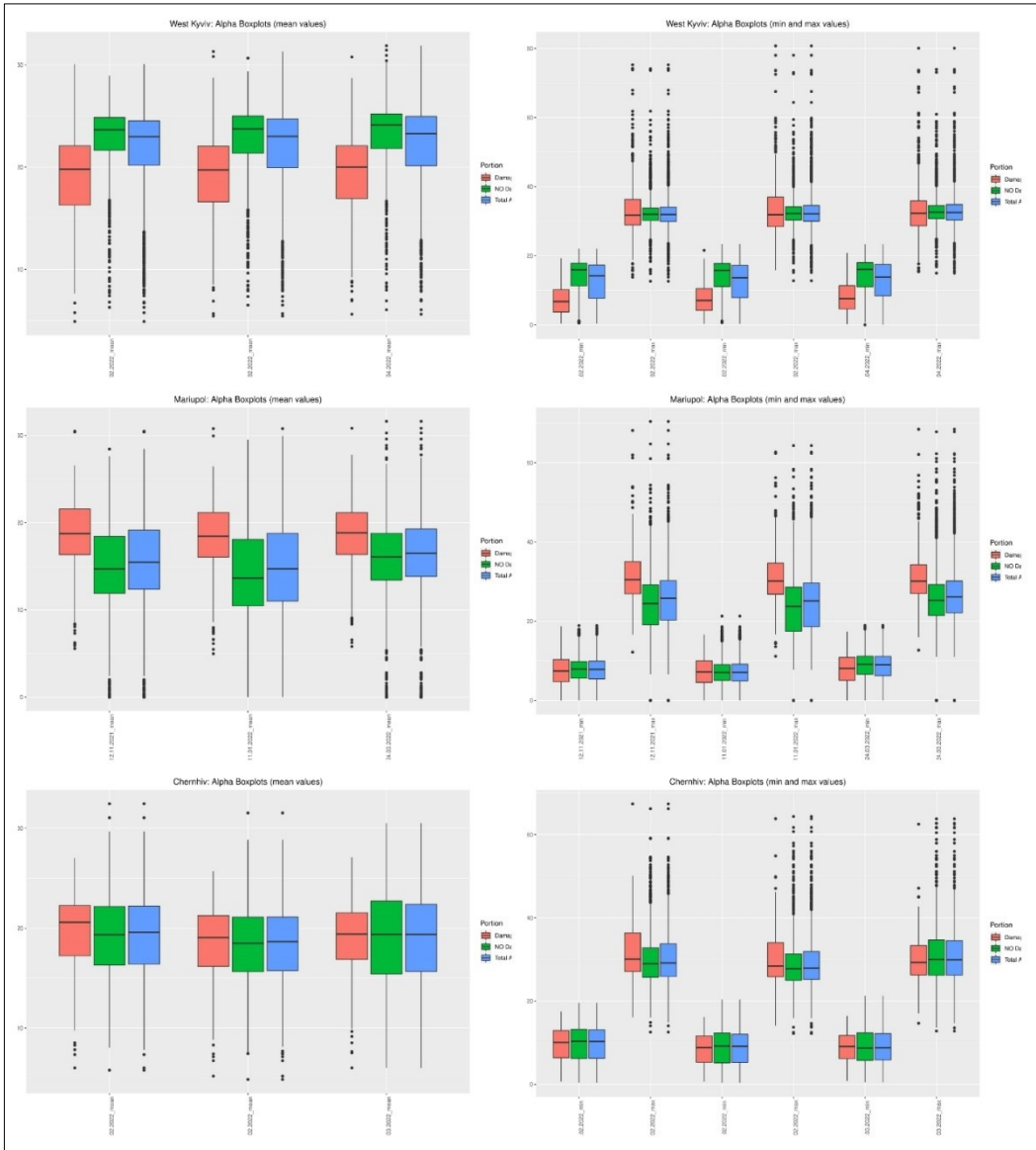


Fig. 84 – Alpha Boxplots.

B – Coherence Boxplots

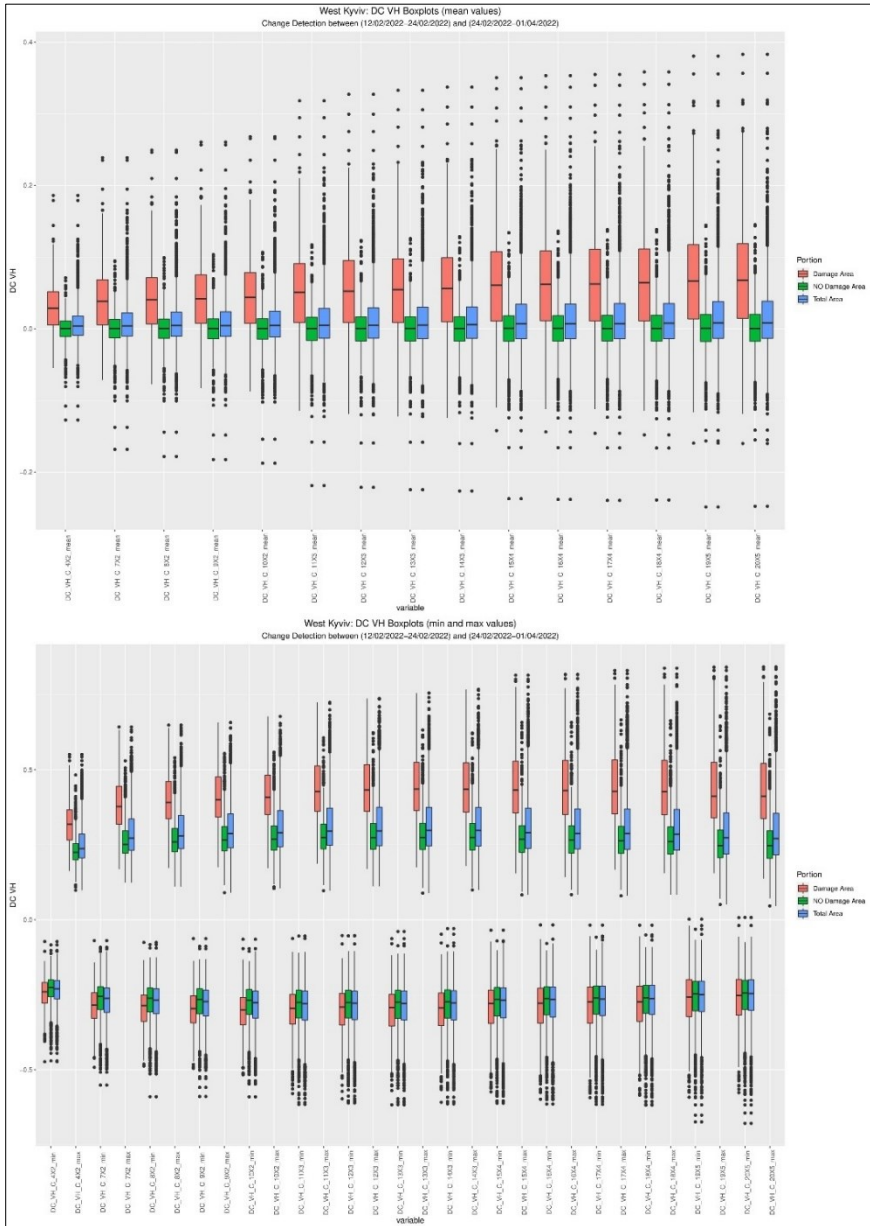


Fig. 85 – West Kyiv, DC VH Index. Top: boxplots of average values. Bottom: boxplots of minimum and maximum values.

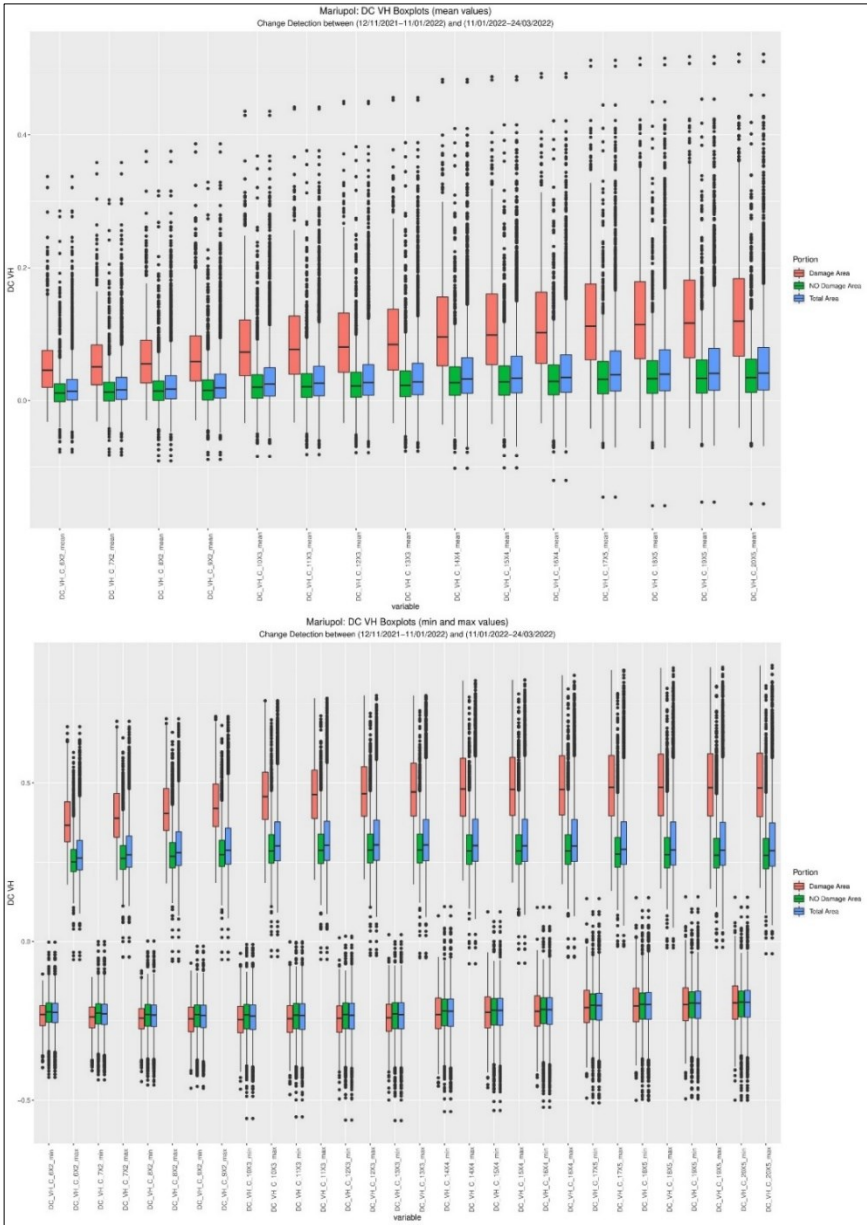


Fig. 86 – Mariupol, DC VH Index. Top: boxplots of average values. Bottom: boxplots of minimum and maximum values.

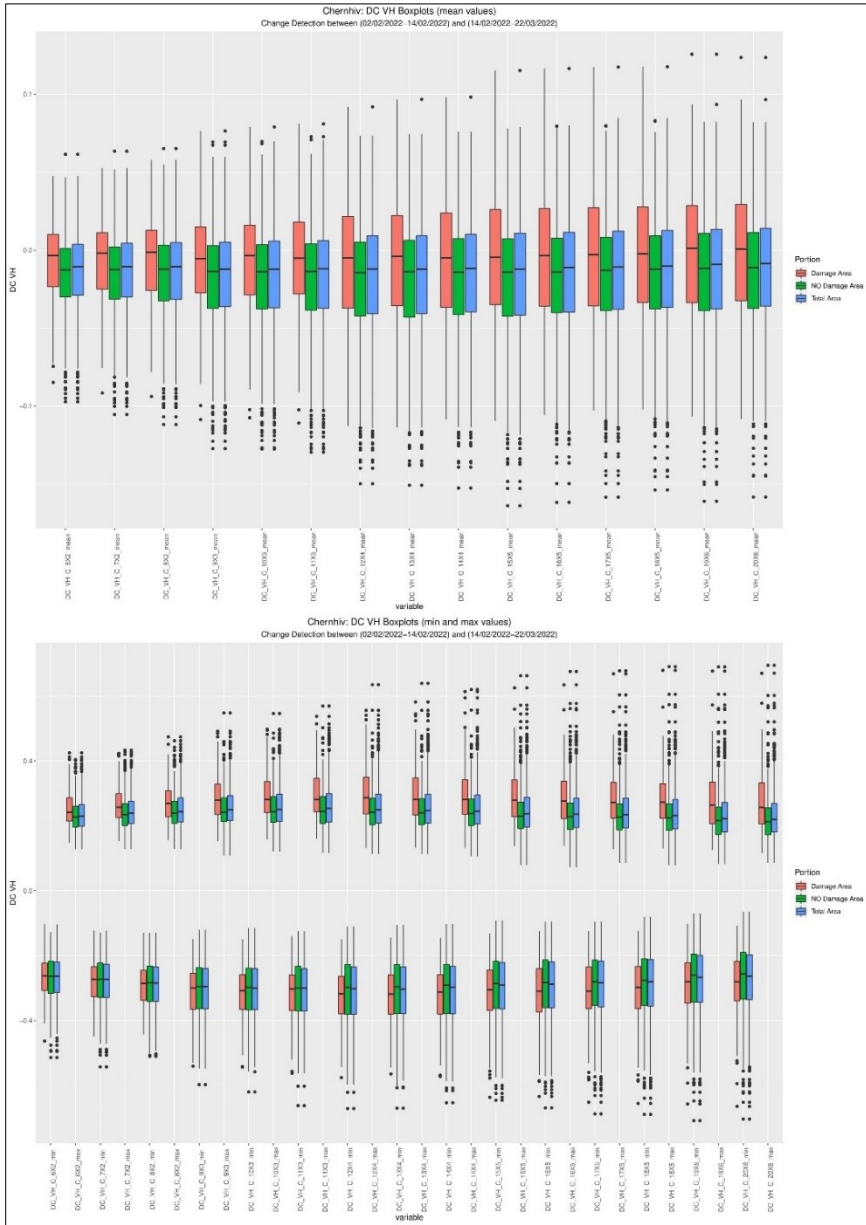


Fig. 87 – Chernihiv, DC VH Index. Top: boxplots of average values. Bottom: boxplots of minimum and maximum values.

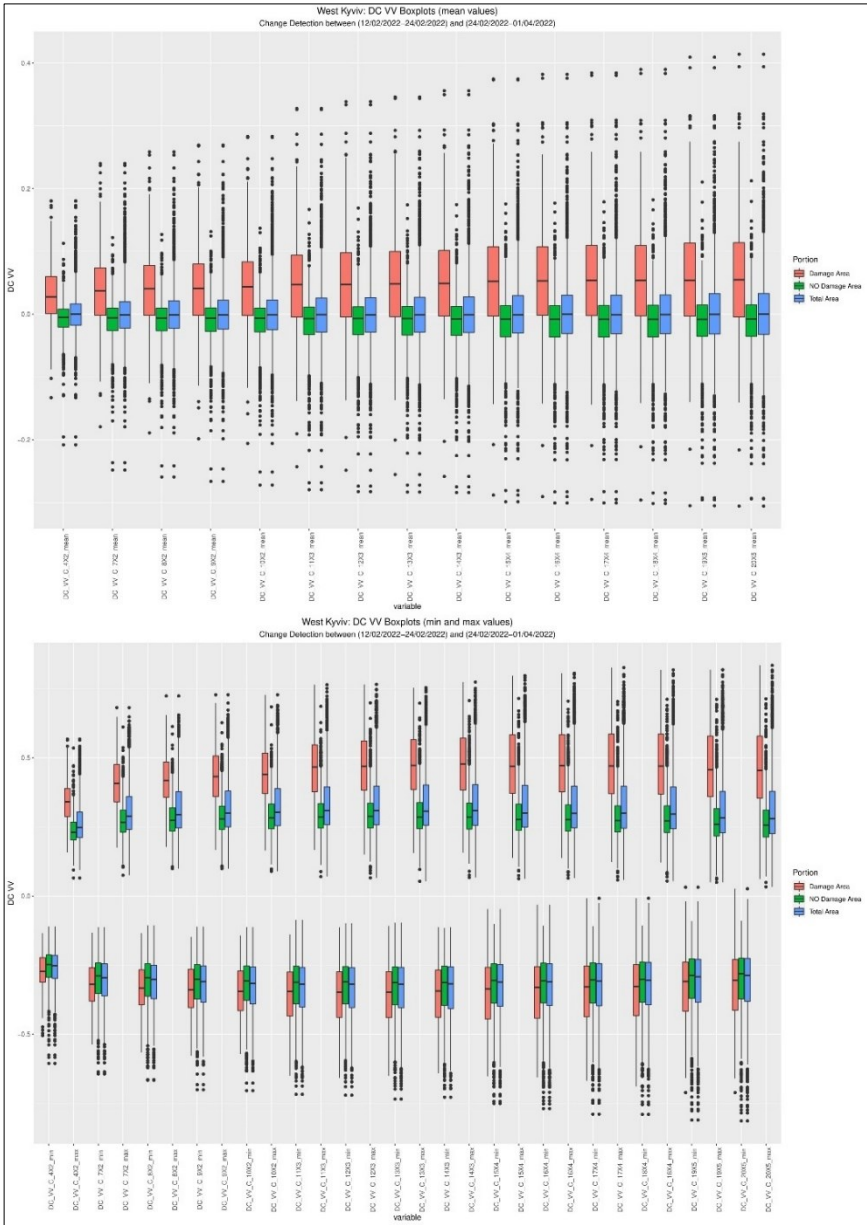


Fig. 88 – West Kyiv, DC VV Index. Top: boxplots of average values. Bottom: boxplots of minimum and maximum values.

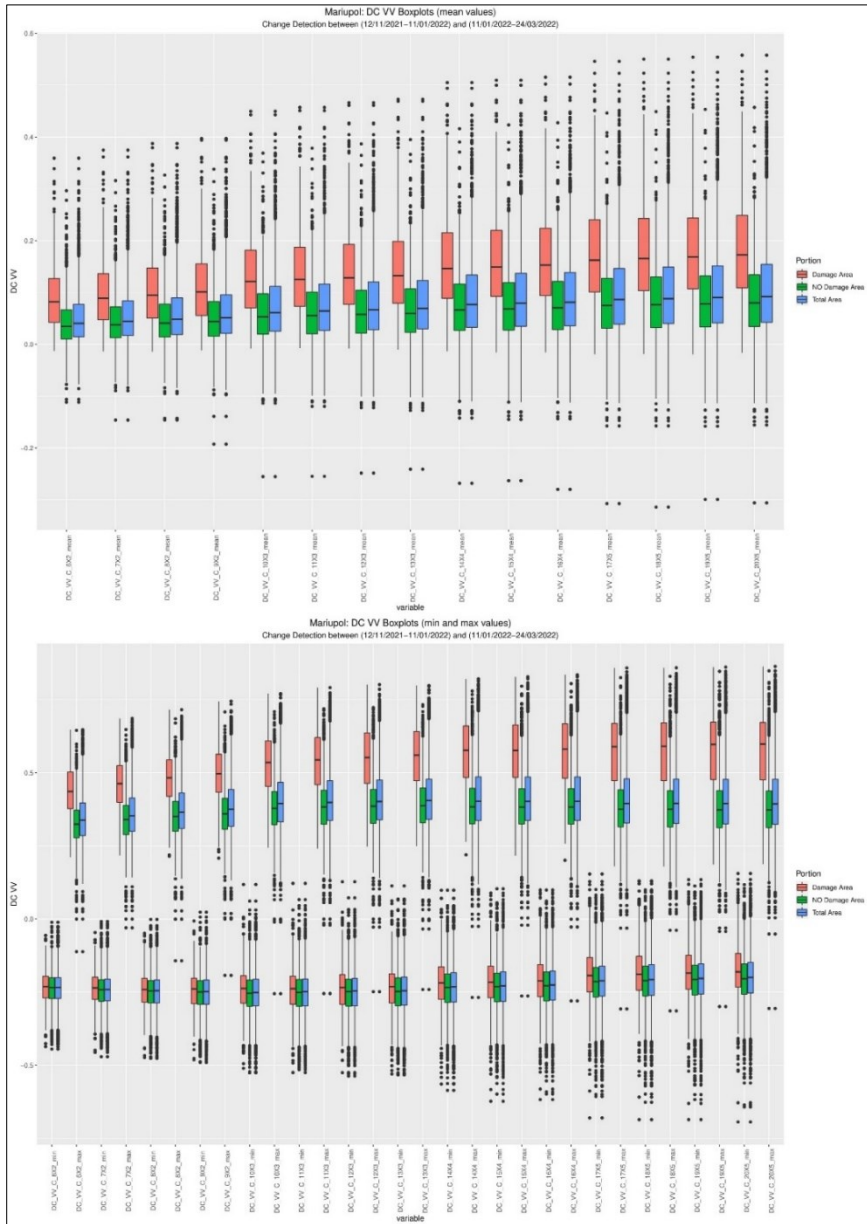


Fig. 89 – Mariupol, DC VV Index. Top: boxplots of average values. Bottom: boxplots of minimum and maximum values.

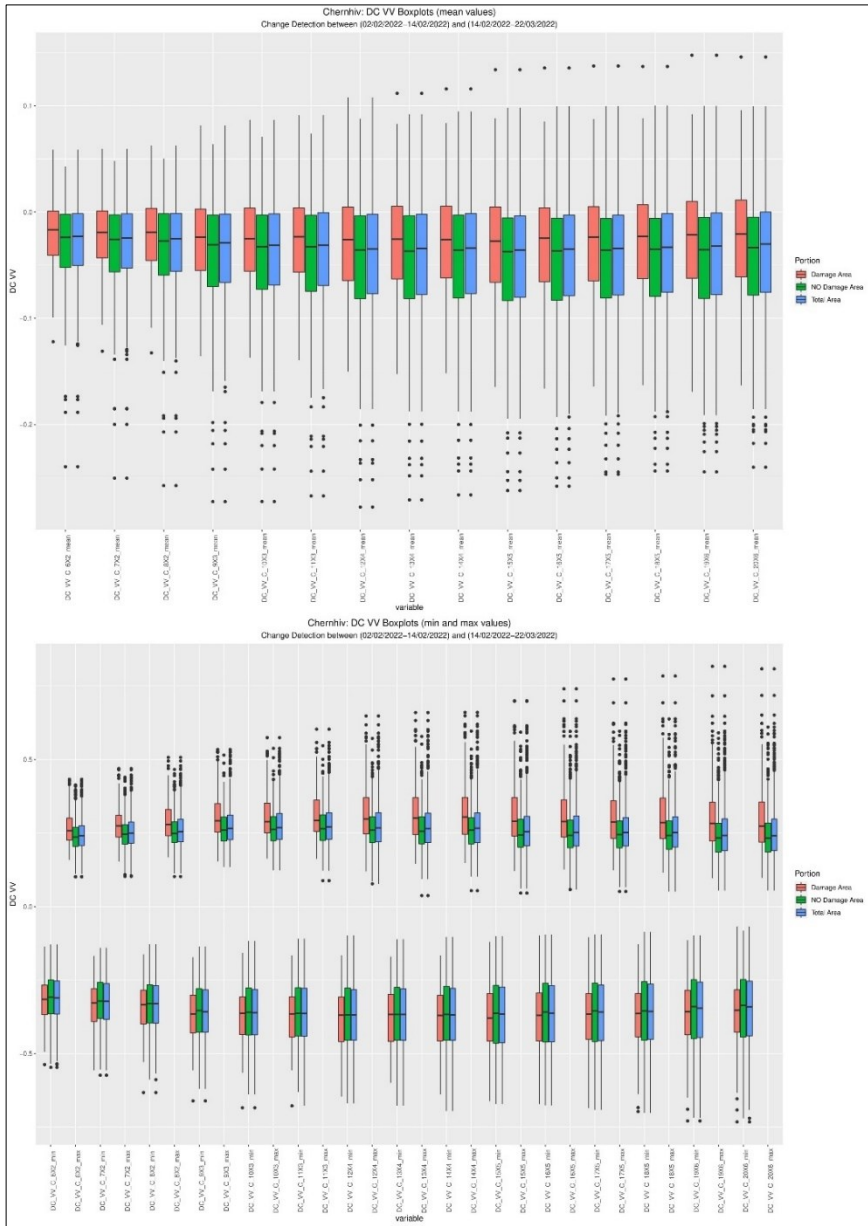


Fig. 90 – Chernihiv, DC VV Index. Top: boxplots of average values. Bottom: boxplots of minimum and maximum values.

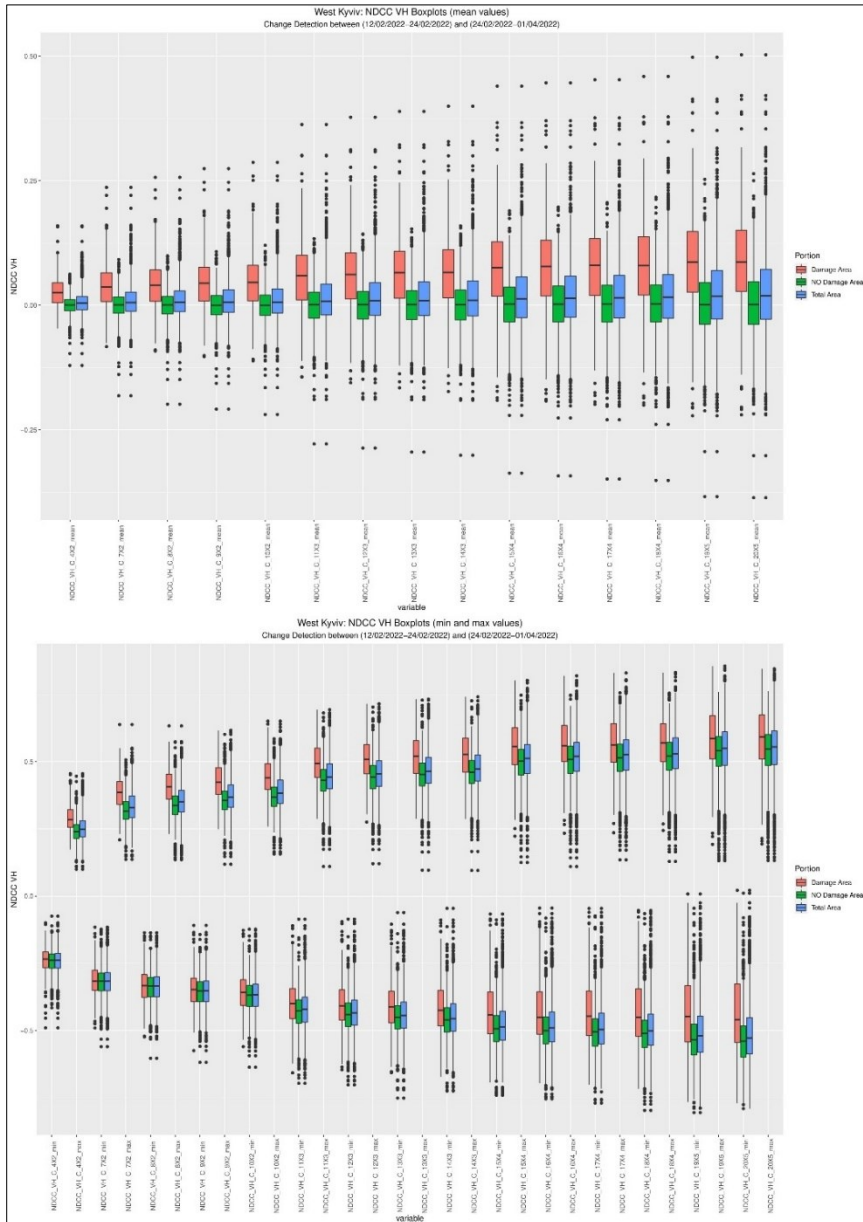


Fig. 91 – West Kyiv, NDCC VH Index. Top: boxplots of average values. Bottom: boxplots of minimum and maximum values.

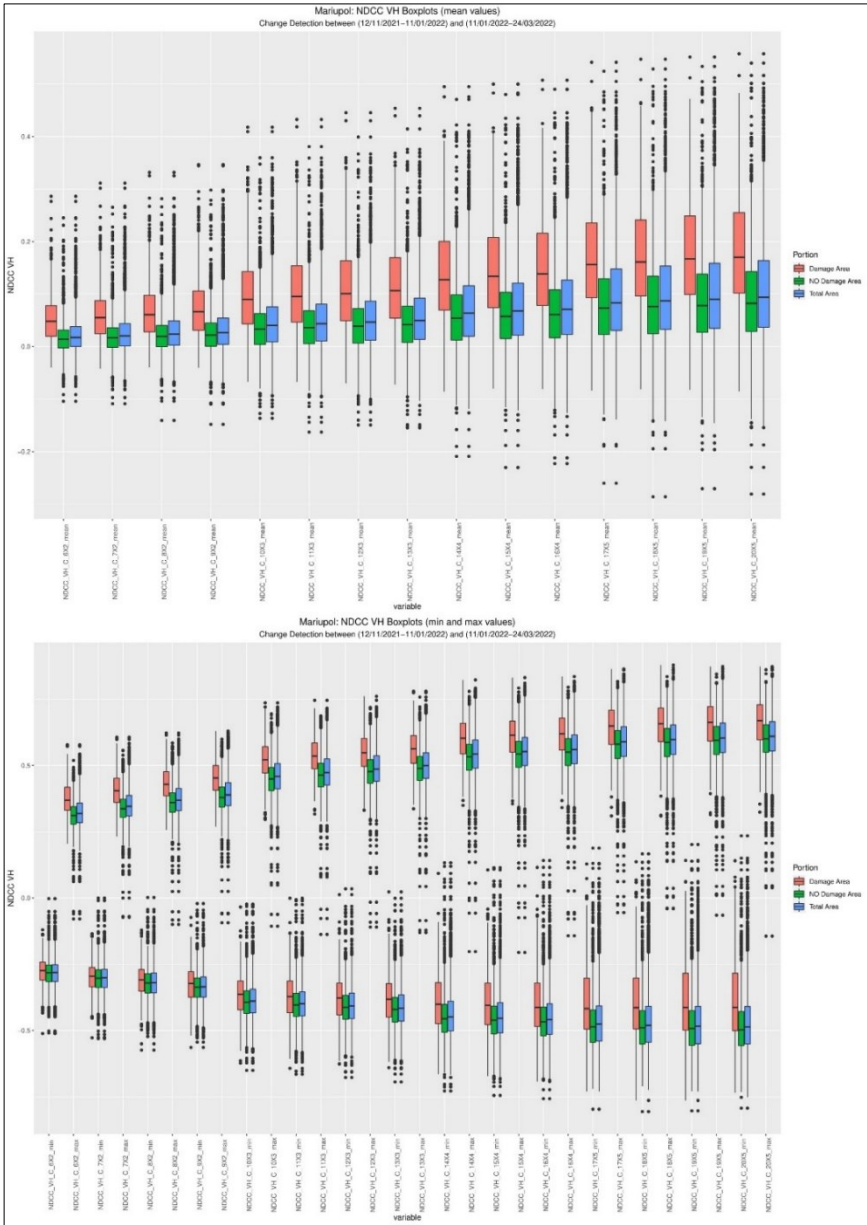


Fig. 92 – Mariupol, NDCC VH Index. Top: boxplots of average values. Bottom: boxplots of minimum and maximum values.

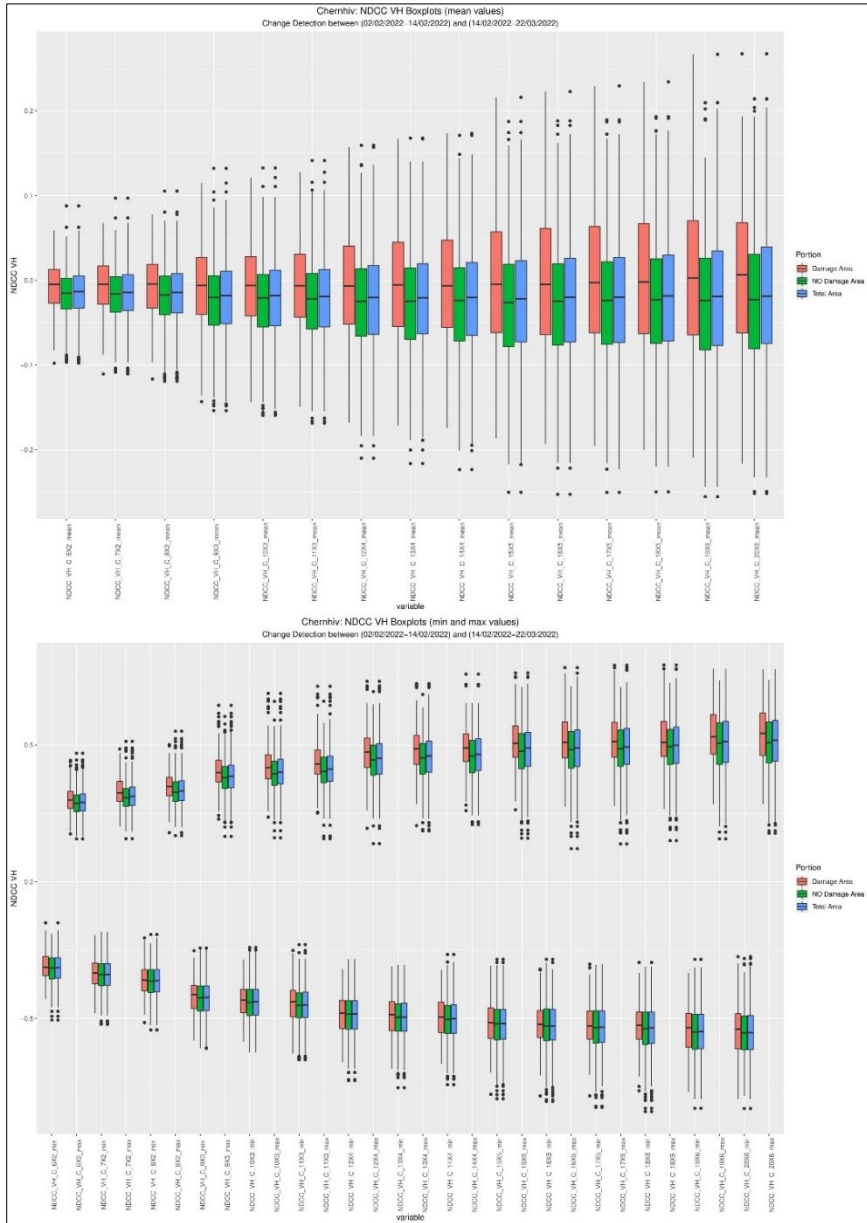


Fig. 93 – Chernihiv, NDCC VH Index. Top: boxplots of average values. Bottom: boxplots of minimum and maximum values.

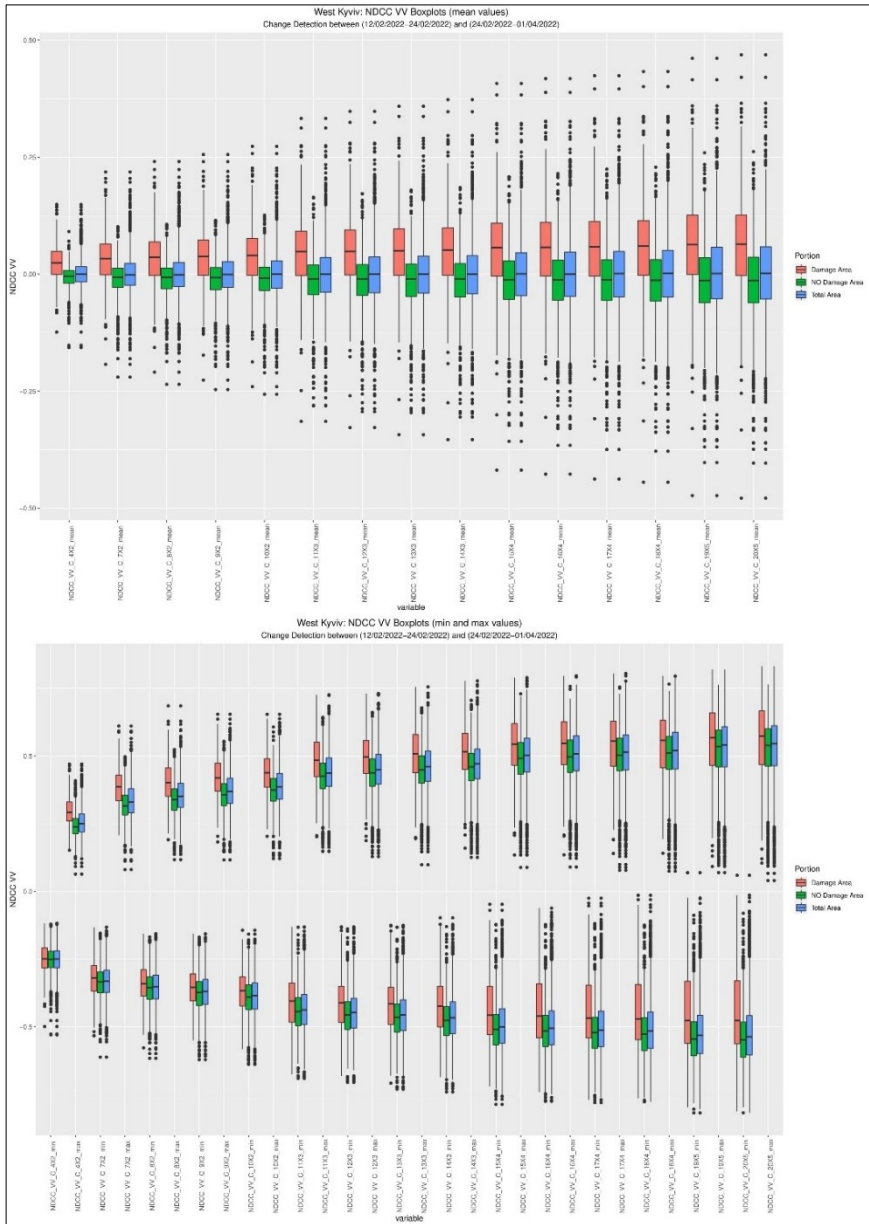


Fig. 94 – West Kyiv, NDCC VV Index. Top: boxplots of average values. Bottom: boxplots of minimum and maximum values.

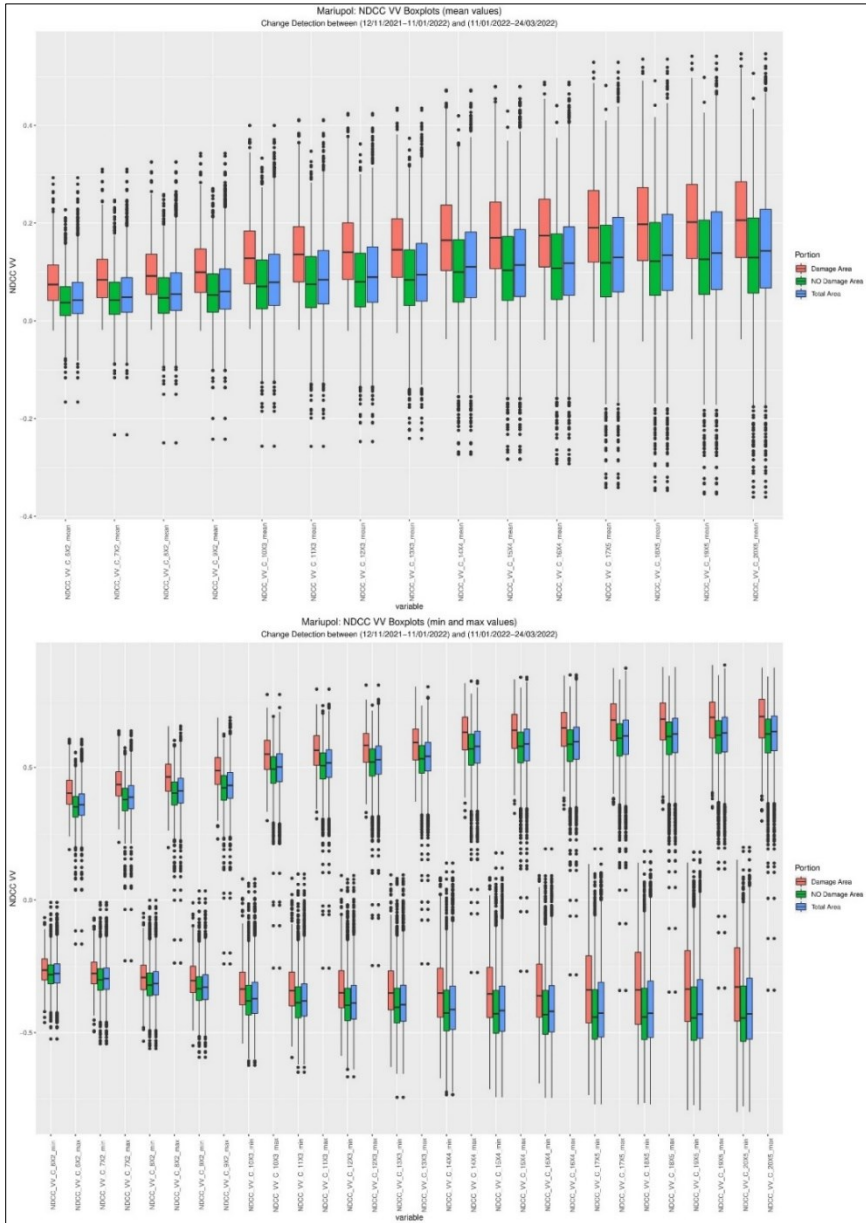


Fig. 95 – Mariupol, NDCC VV Index. Top: boxplots of average values. Bottom: boxplots of minimum and maximum values.

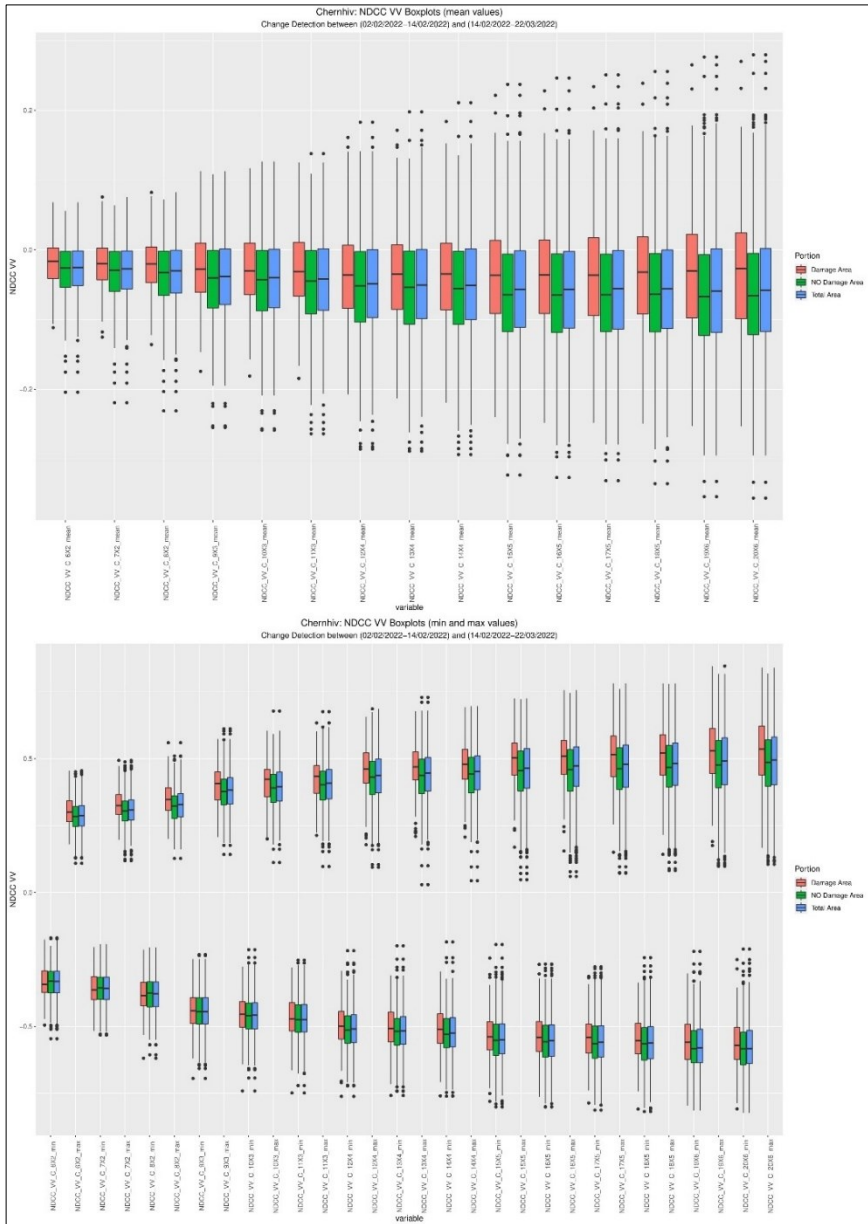


Fig. 96 – Chernihiv, NDCC VV Index. Top: boxplots of average values. Bottom: boxplots of minimum and maximum values.

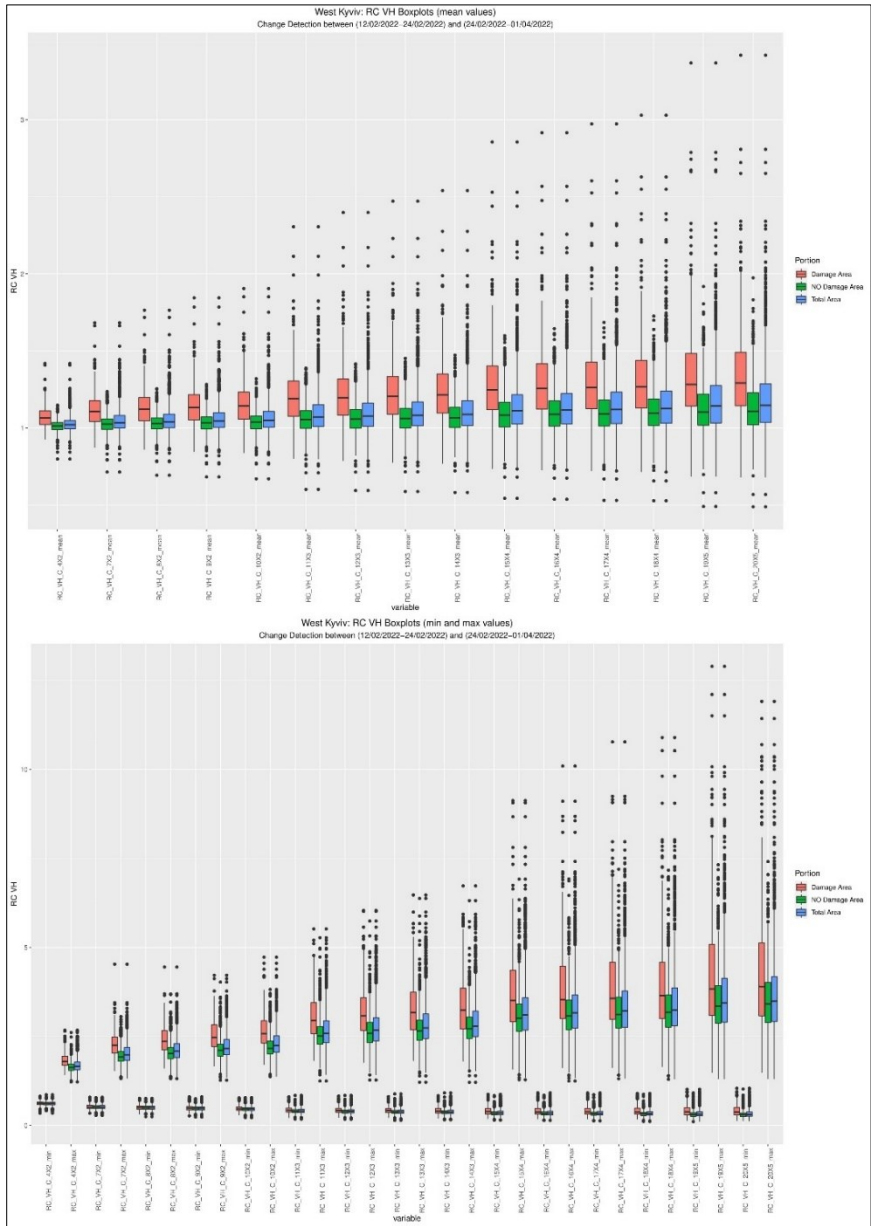


Fig. 97 – West Kyiv, RC VH Index. Top: boxplots of average values. Bottom: boxplots of minimum and maximum values.

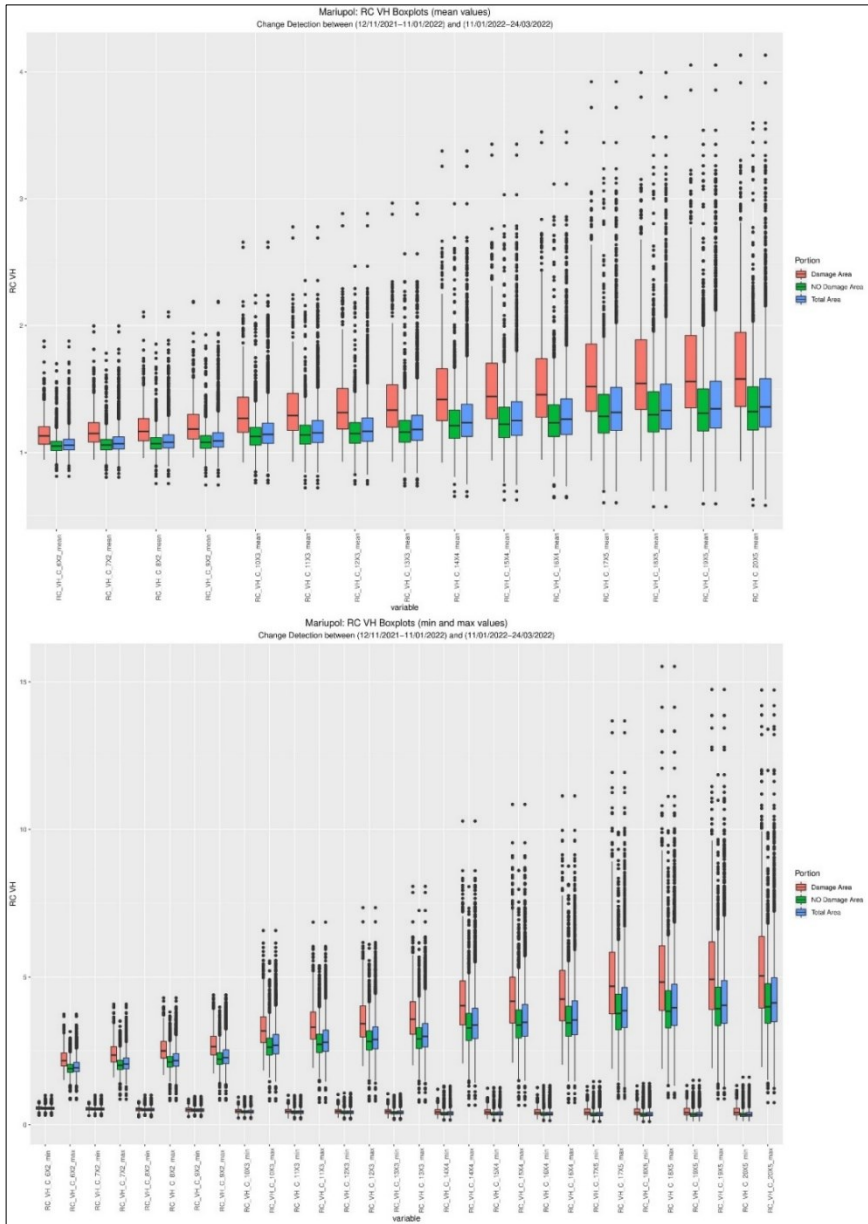


Fig. 98 – Mariupol, RC VH Index. Top: boxplots of average values. Bottom: boxplots of minimum and maximum values.

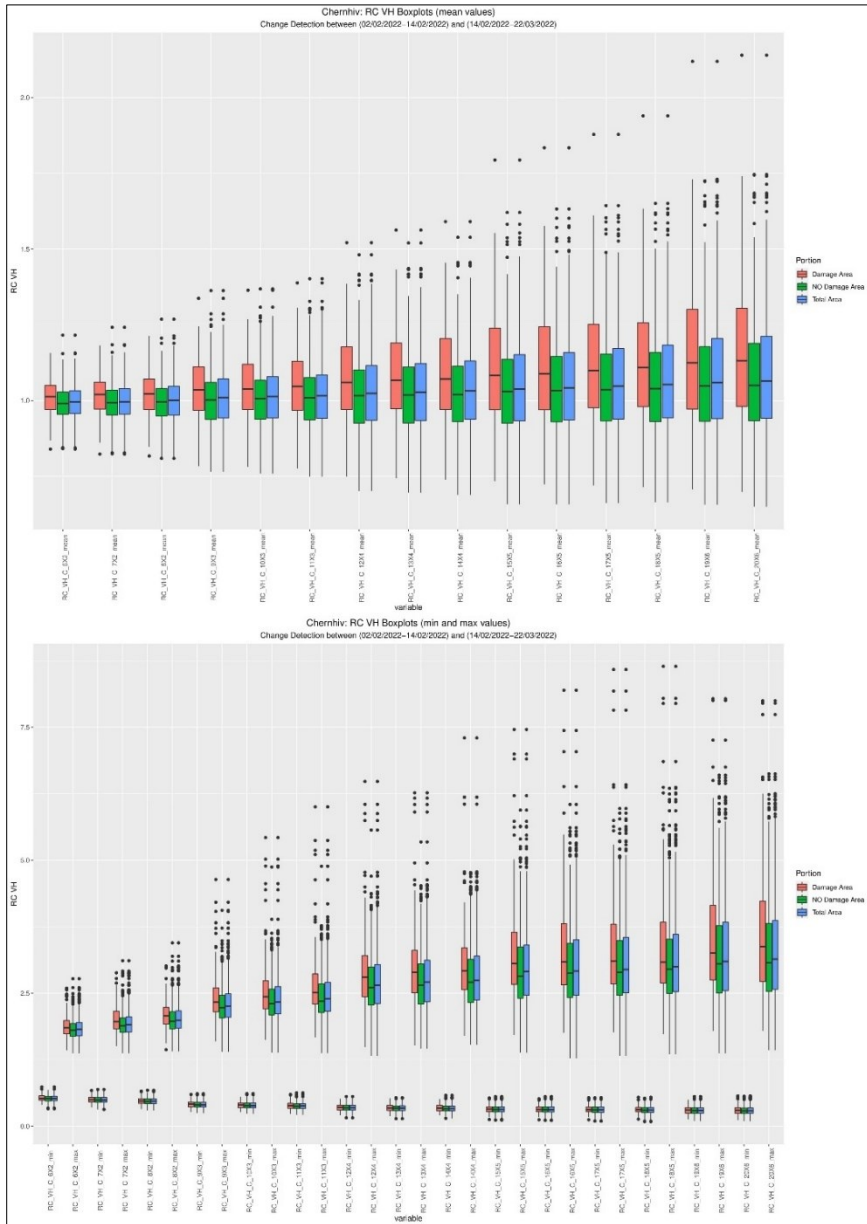


Fig. 99 – Chernihiv, RC VH Index. Top: boxplots of average values. Bottom: boxplots of minimum and maximum values.

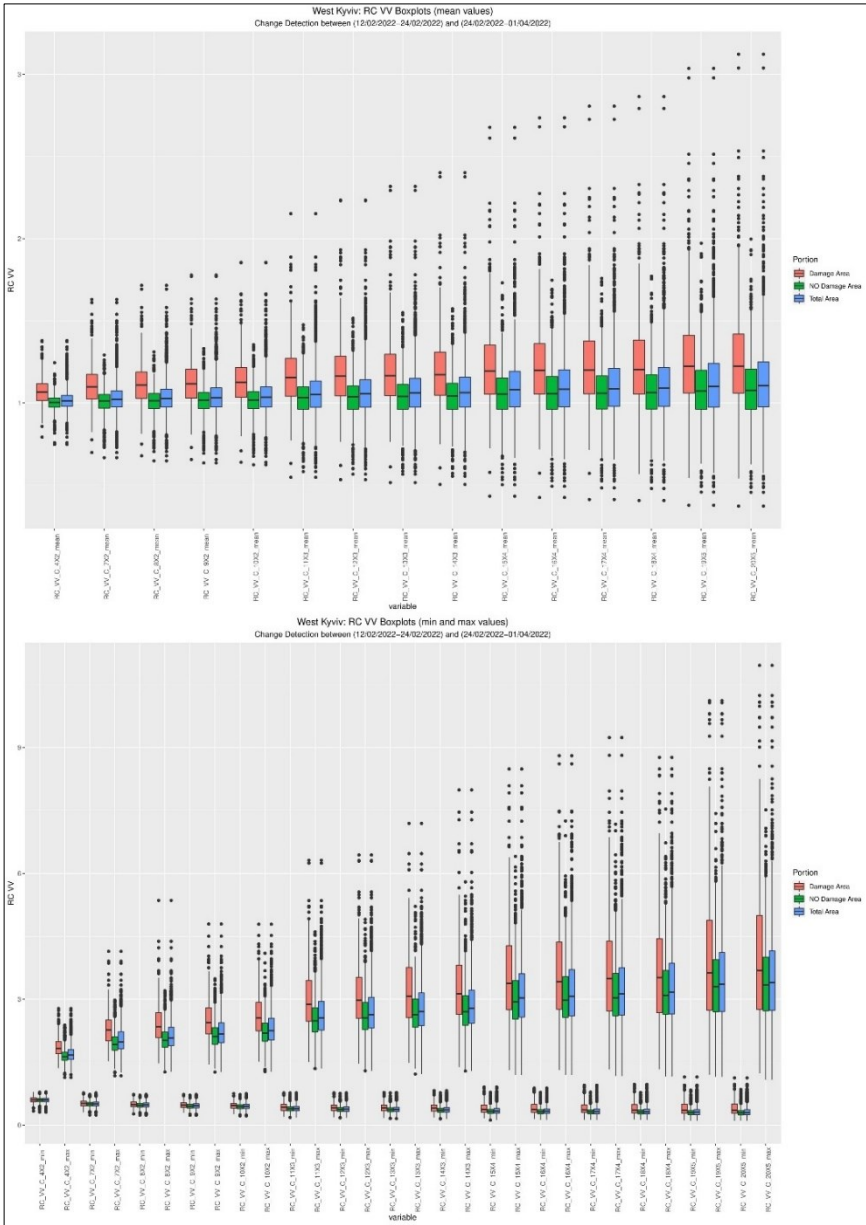


Fig. 100 – West Kyiv, RC VV Index. Top: boxplots of average values. Bottom: boxplots of minimum and maximum values.

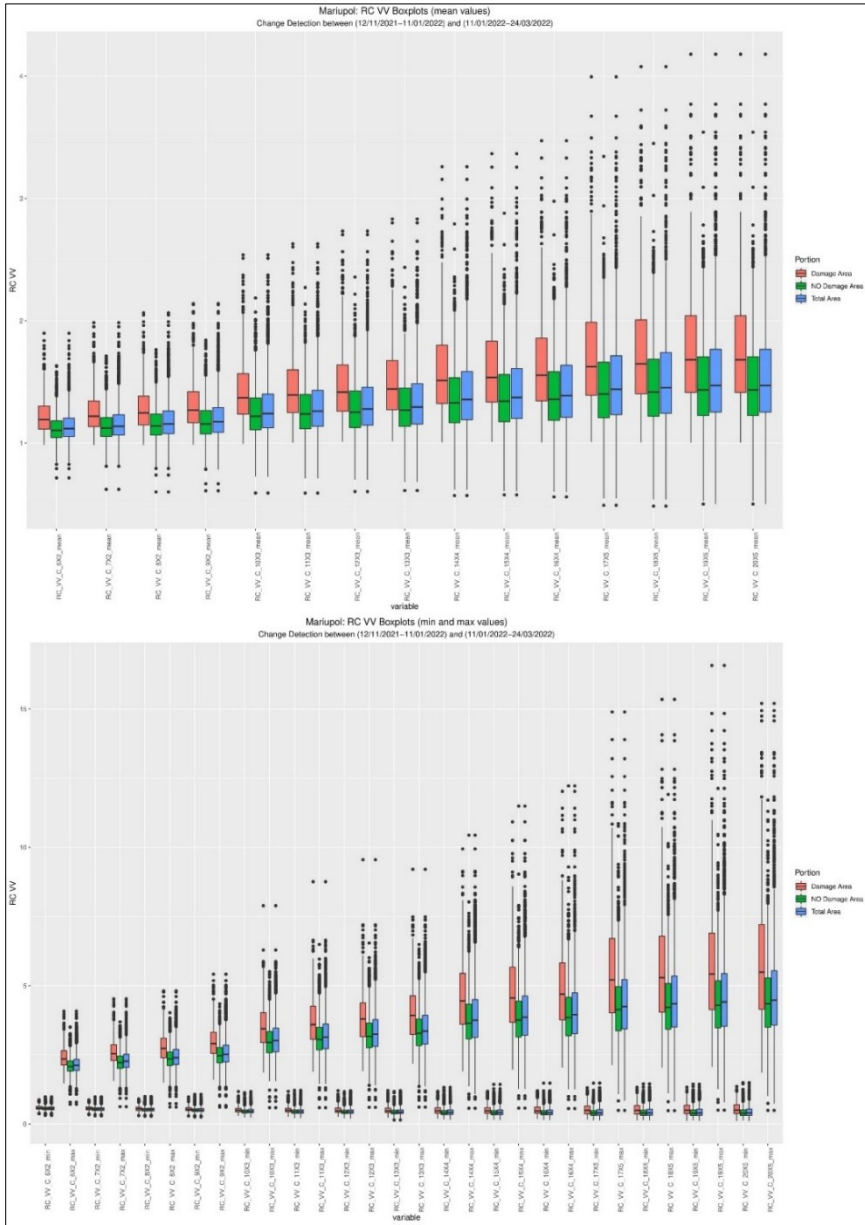


Fig. 101 – Mariupol RC VV Index. Top: boxplots of average values. Bottom: boxplots of minimum and maximum values.

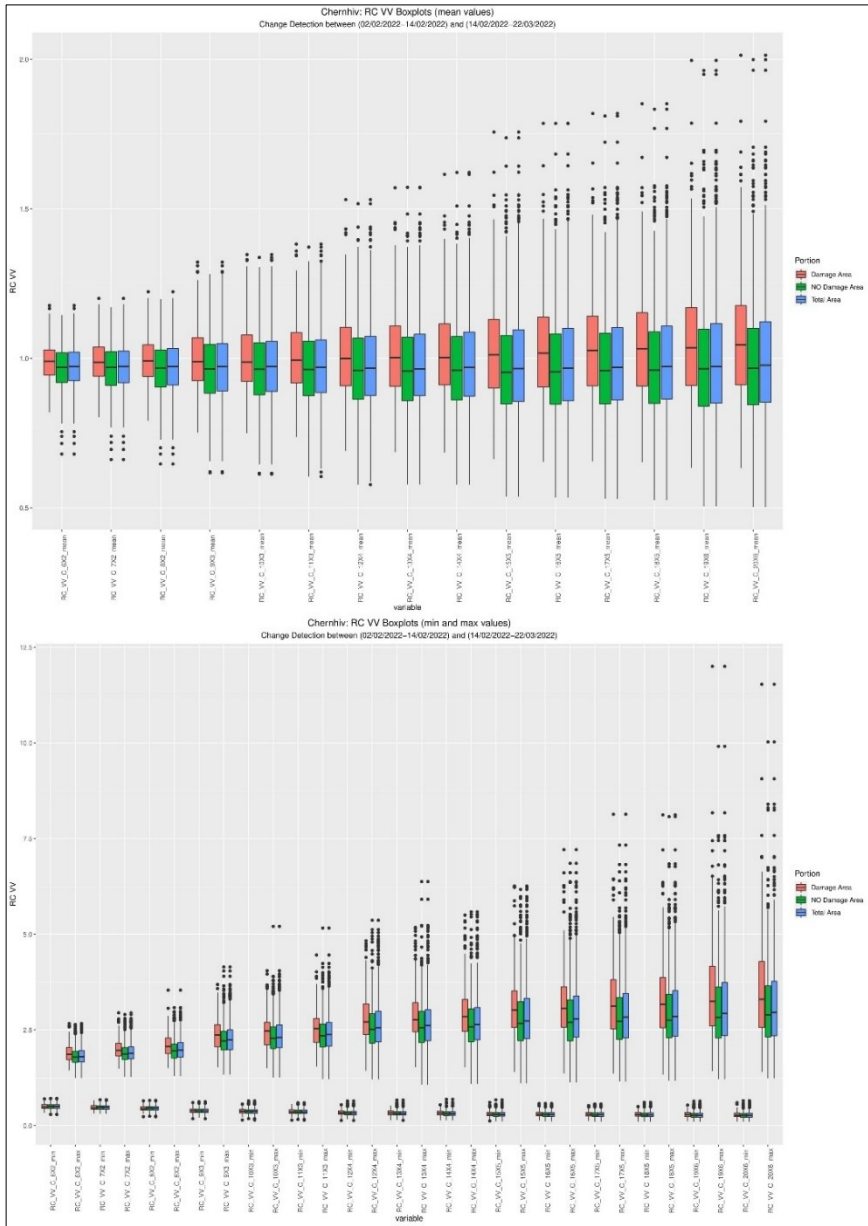


Fig. 102 – Chernihiv, RC VV Index. Top: boxplots of average values. Bottom: boxplots of minimum and maximum values.

C – Intensity Boxplots

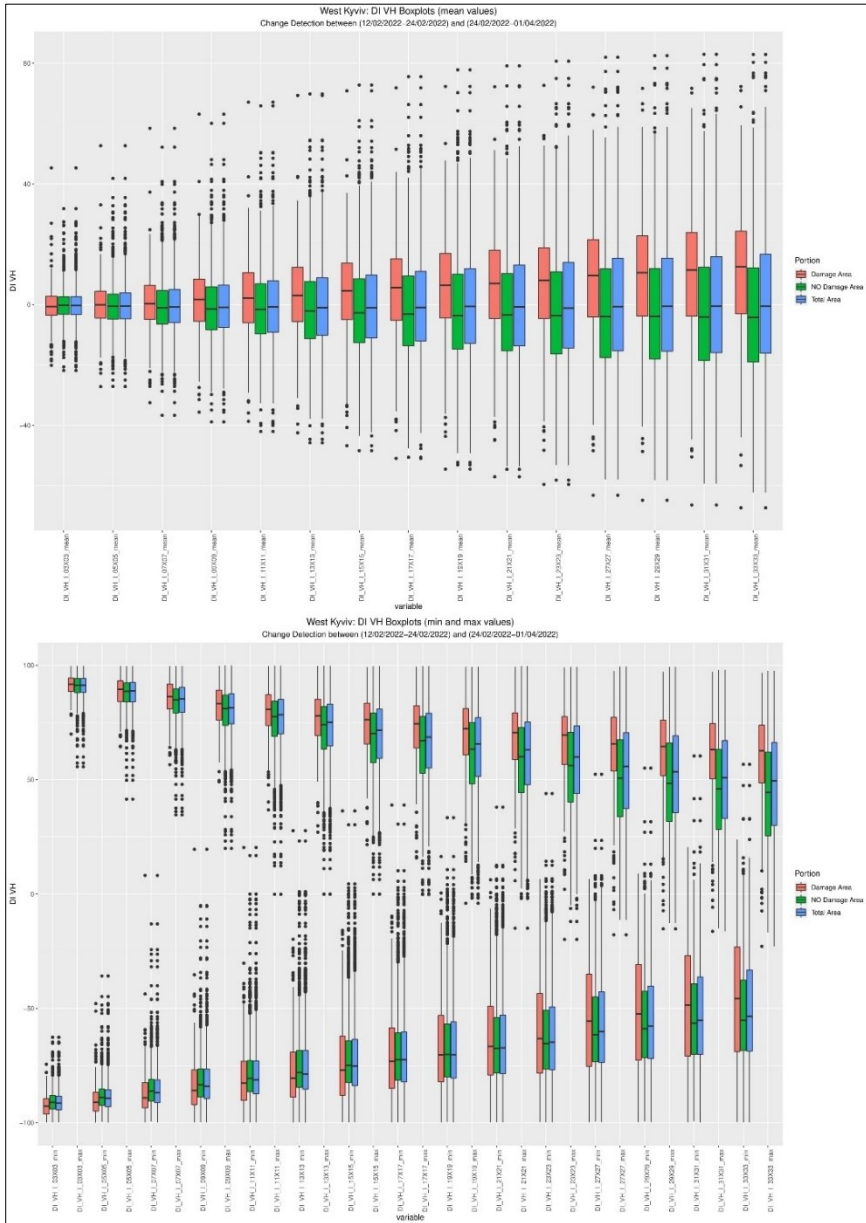


Fig. 103 – West Kyiv, DI VH Index. Top: boxplots of average values. Bottom: boxplots of minimum and maximum values.

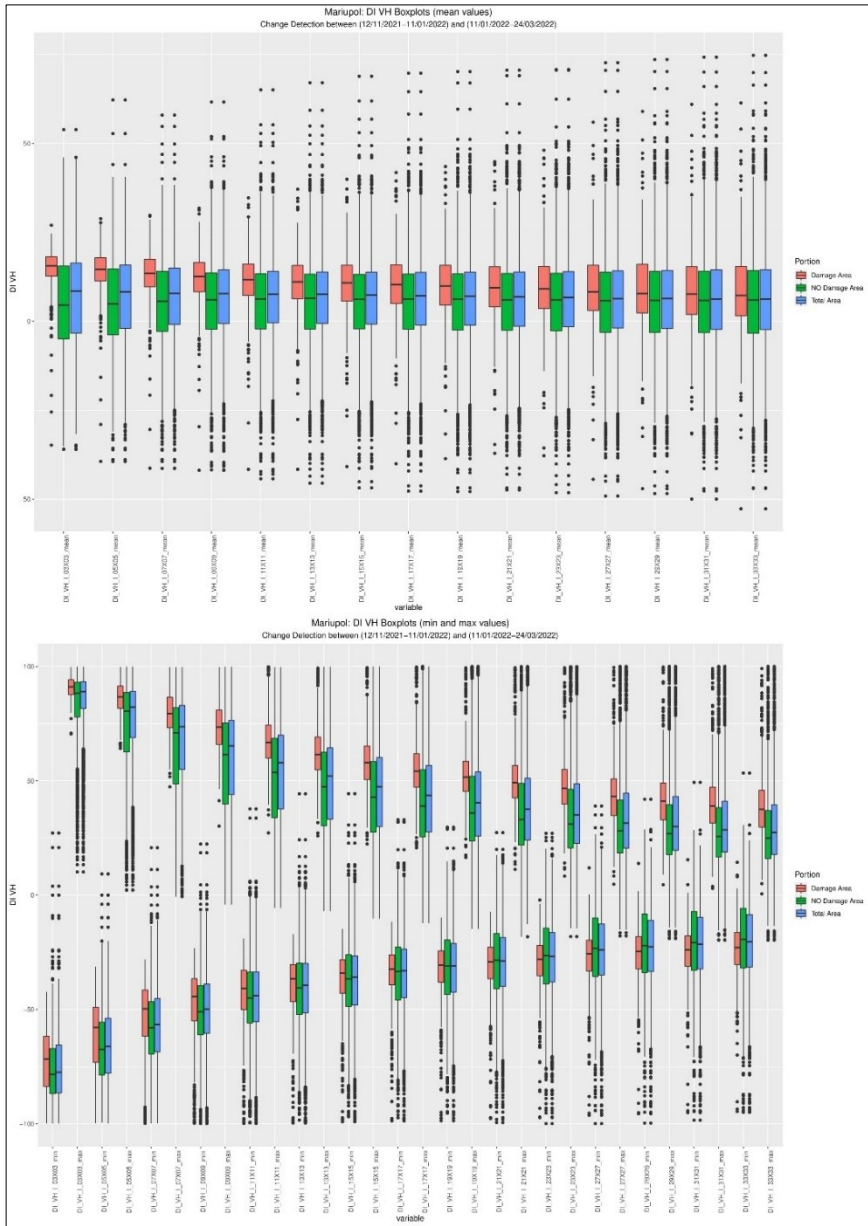


Fig. 104 – Mariupol, DI VH Index. Top: boxplots of average values. Bottom: boxplots of minimum and maximum values.

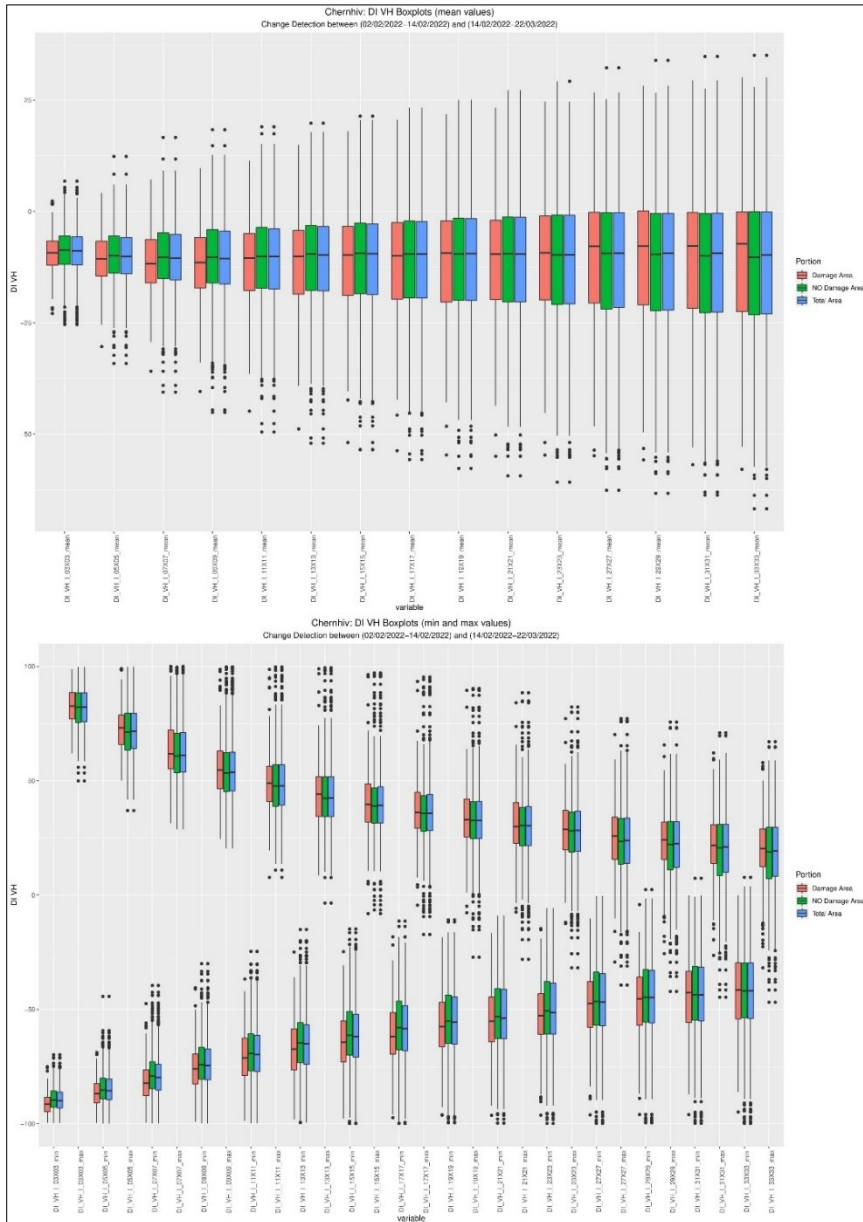


Fig. 105 – Chernihiv, DI VH Index. Top: boxpolts of average values. Bottom: boxplots of minimum and maximum values.

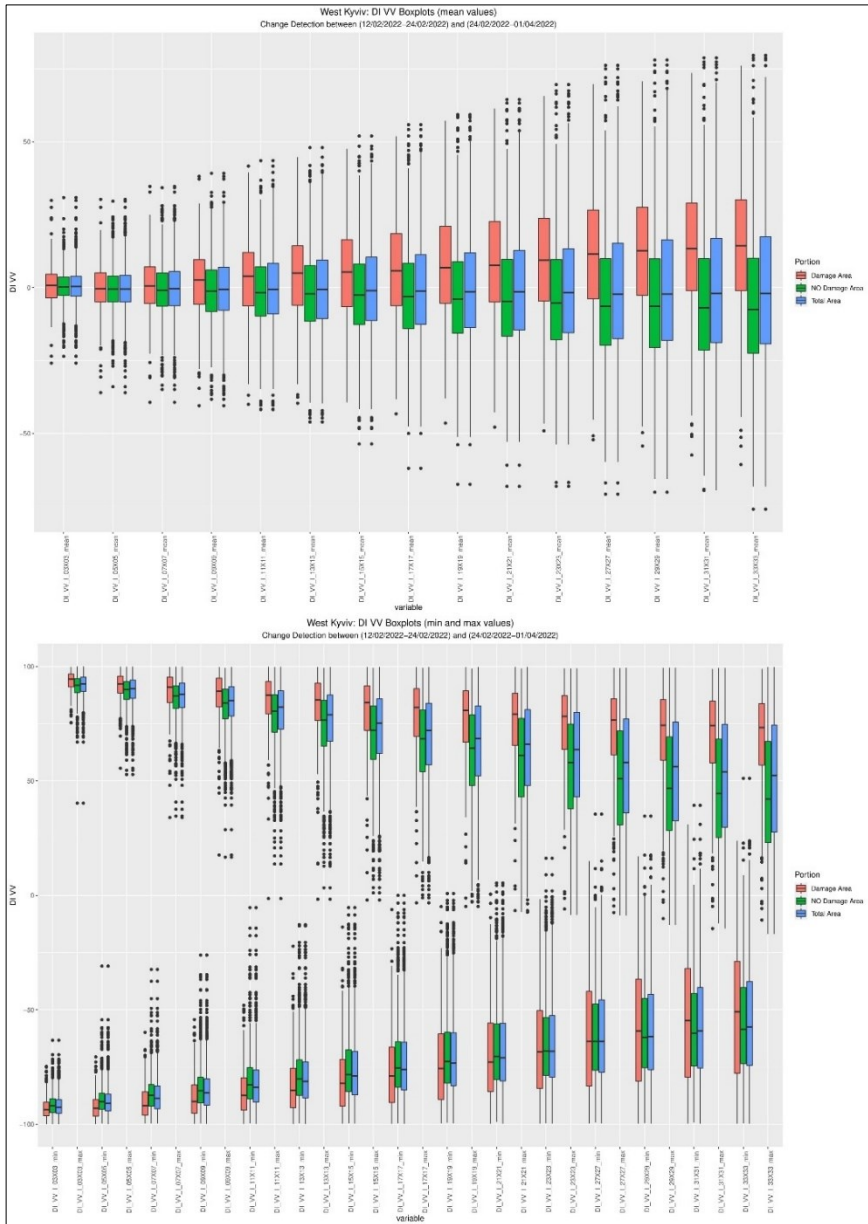


Fig. 106 – West Kyiv, DI VV Index. Top: boxplots of average values. Bottom: boxplots of minimum and maximum values.

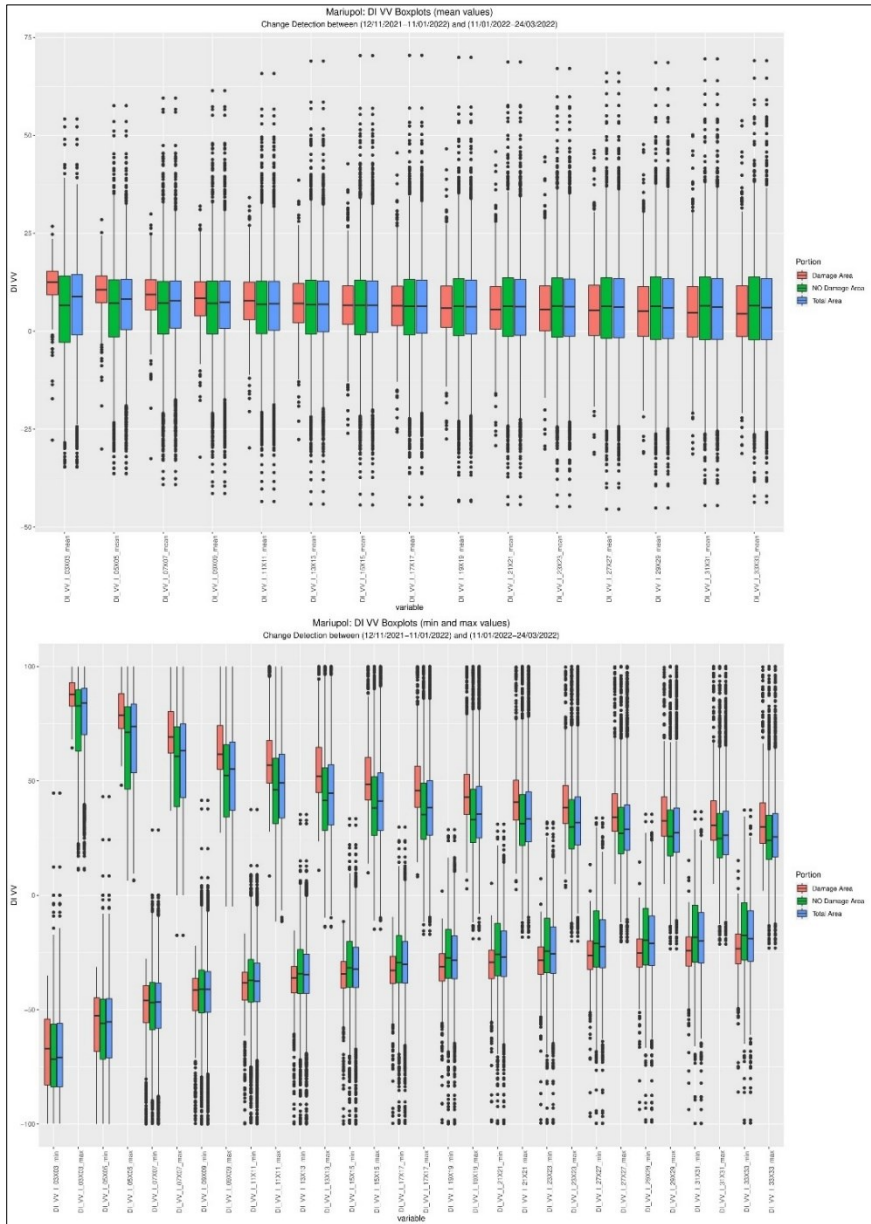


Fig. 107 – Mariupol, DI VV Index. Top: boxplots of average values. Bottom: boxplots of minimum and maximum values.

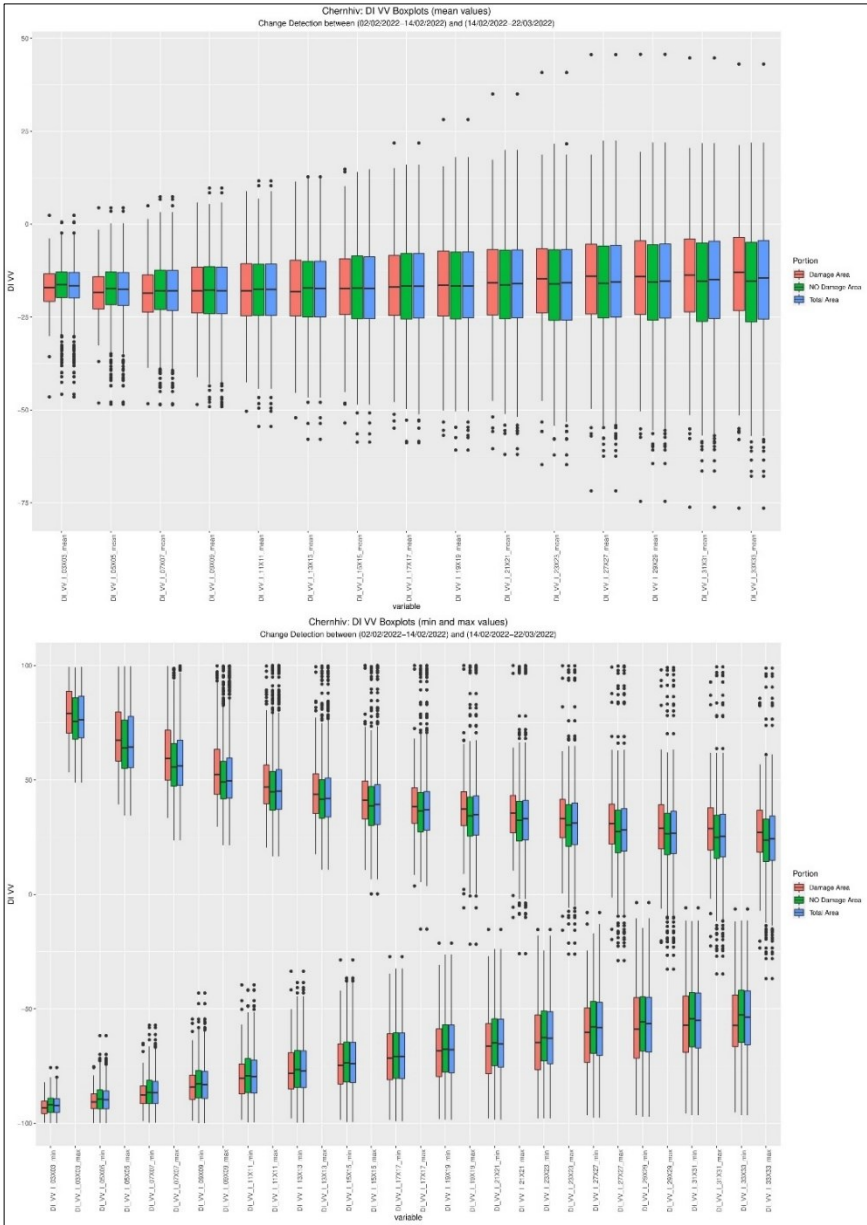


Fig. 108 – Chernihiv, DI VV Index. Top: boxplots of average values. Bottom: boxplots of minimum and maximum values.

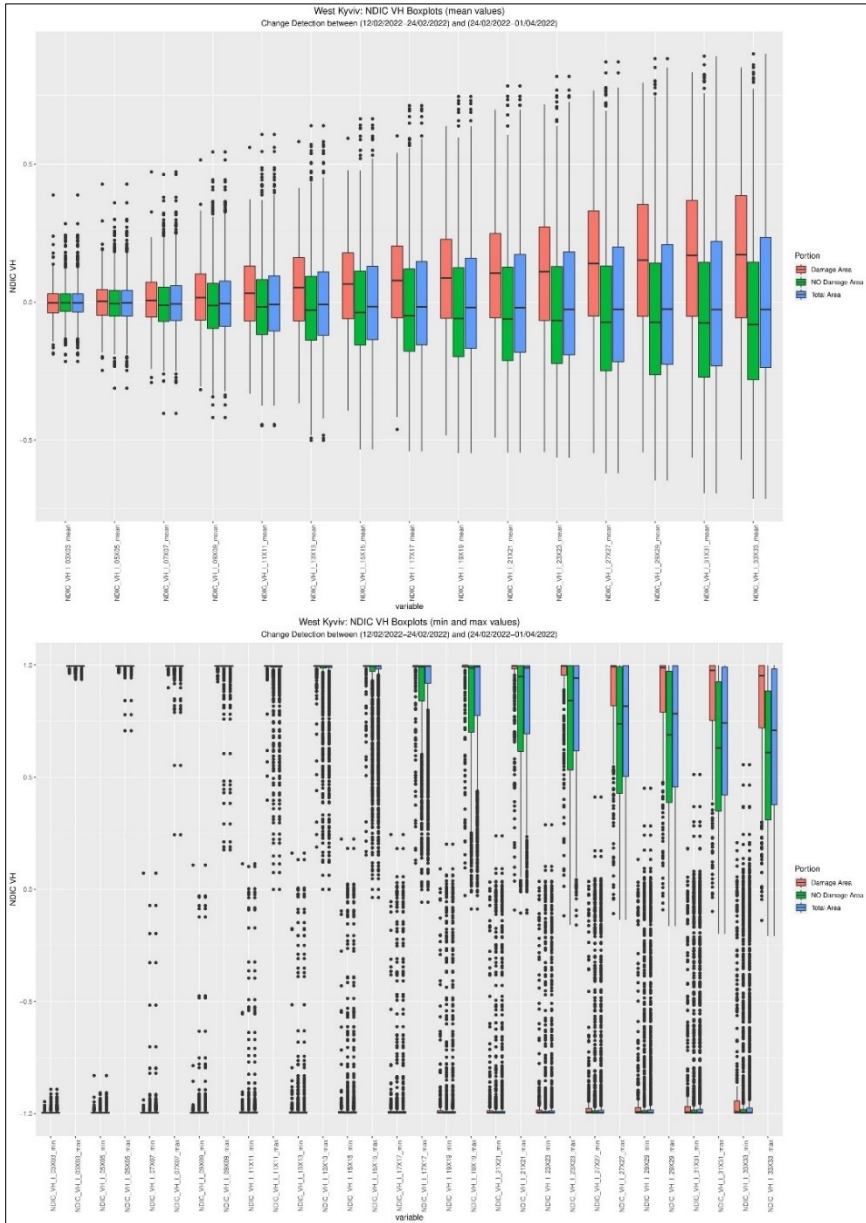


Fig. 109 – West Kyiv, NDIC VH Index. Top: boxplots of average values. Bottom: boxplots of minimum and maximum values.

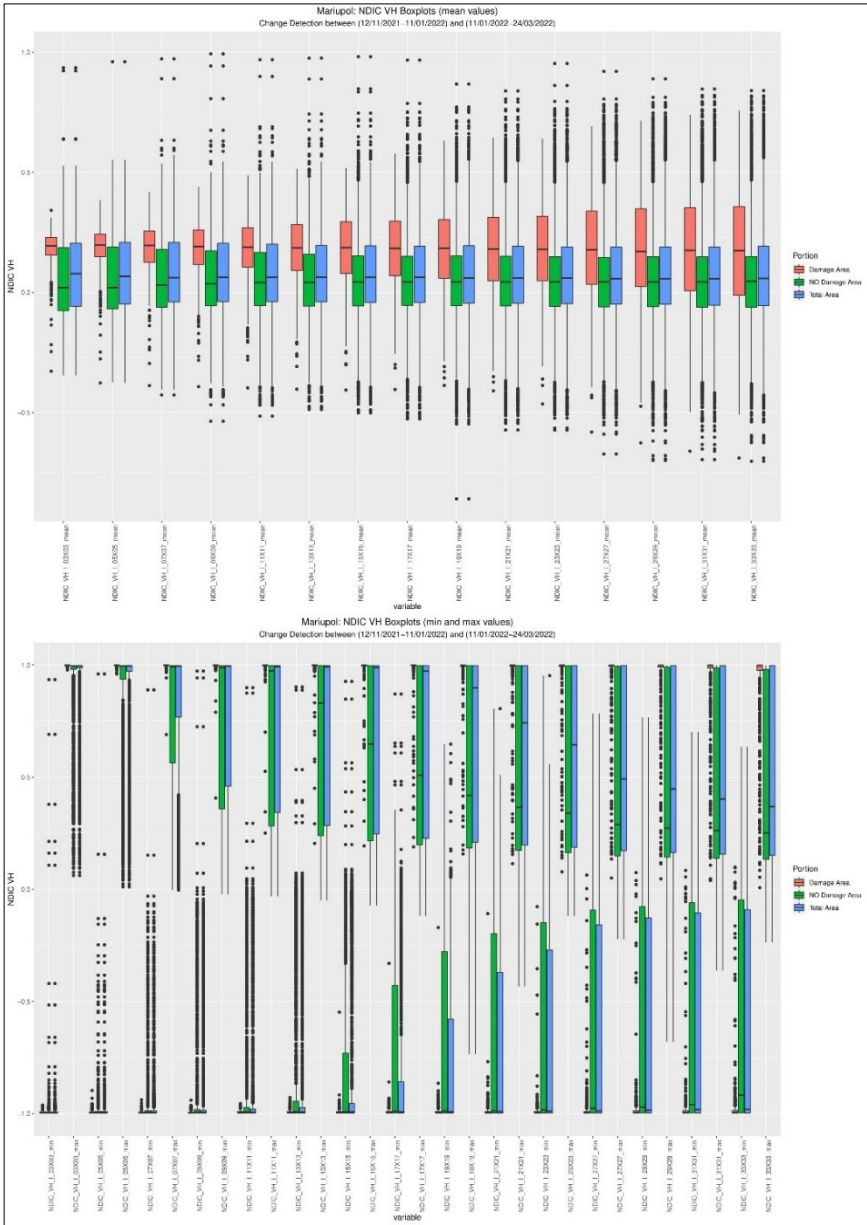


Fig. 110 – Mariupol, NDIC VH Index. Top: boxplots of average values. Bottom: boxplots of minimum and maximum values.

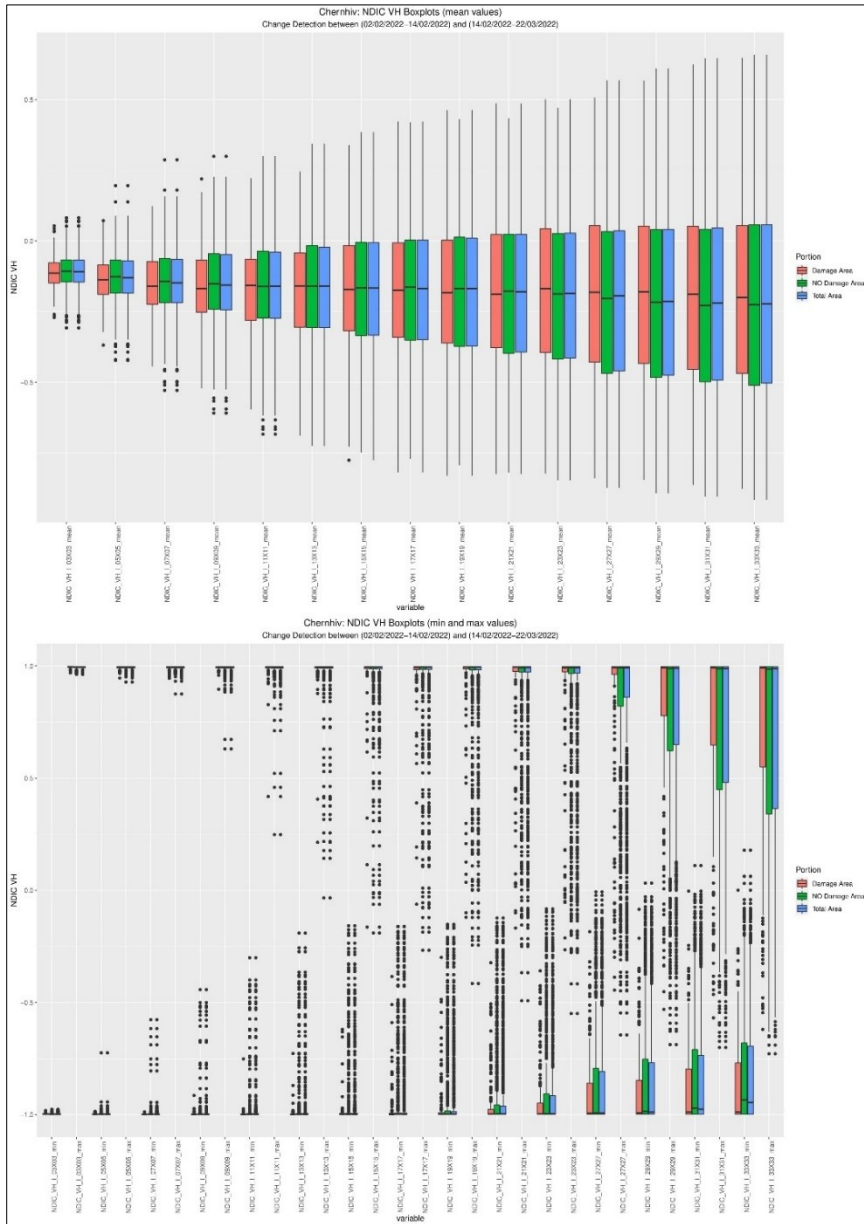


Fig. 111 – Chernihiv, NDIC VH Index. Top: boxplots of average values. Bottom: boxplots of minimum and maximum values.

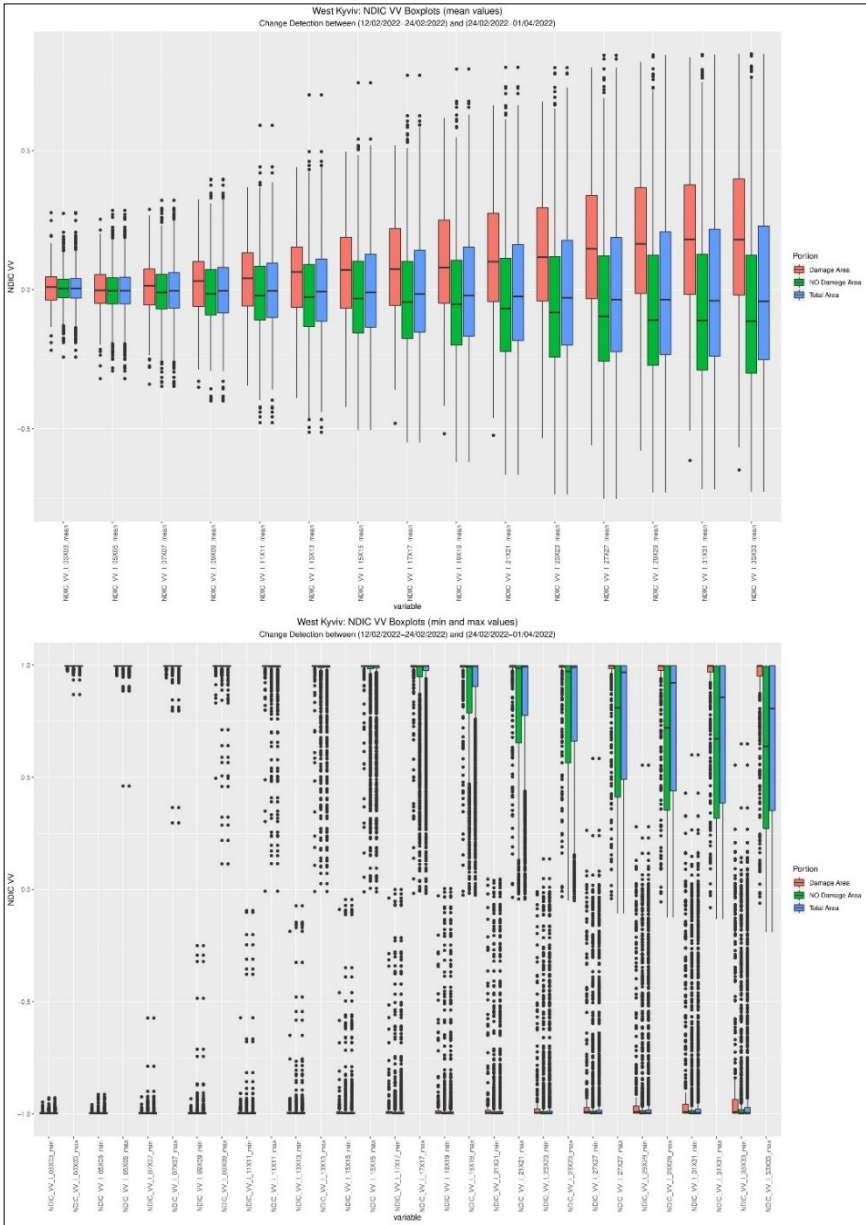


Fig. 112 – West Kyiv, NDIC VV Index. Top: boxplots of average values. Bottom: boxplots of minimum and maximum values.

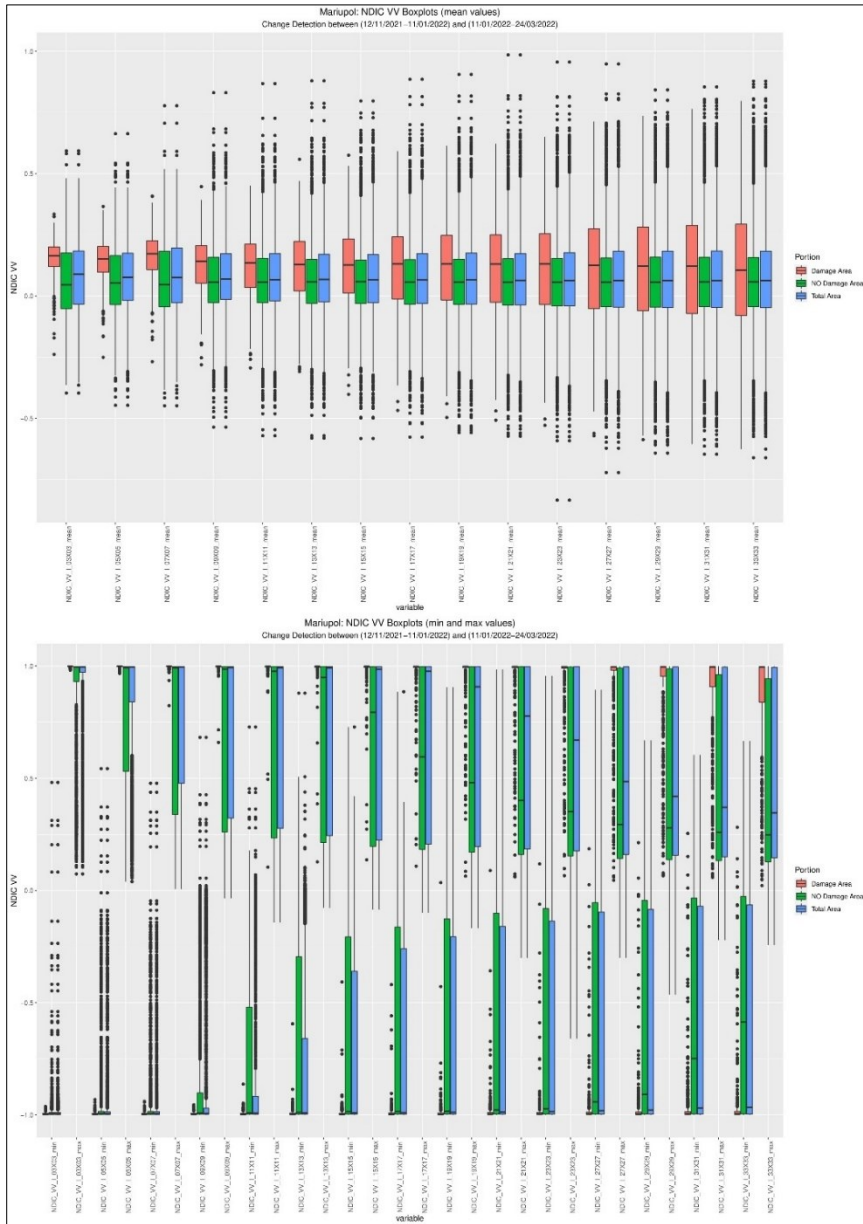


Fig. 113 – Mariupol, NDIC VV Index. Top: boxplots of average values. Bottom: boxplots of minimum and maximum values.

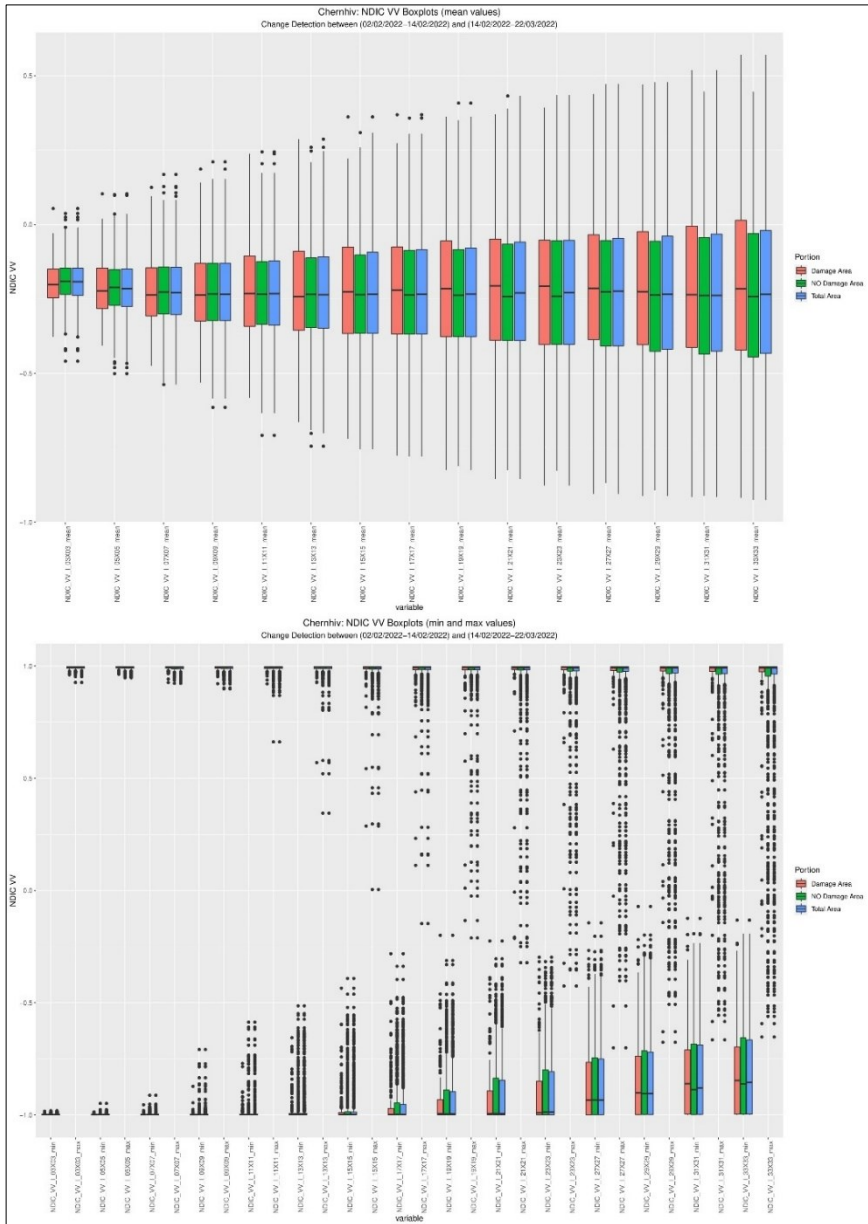


Fig. 114 – Chernihiv, NDIC VV Index. Top: boxplots of average values. Bottom: boxplots of minimum and maximum values.

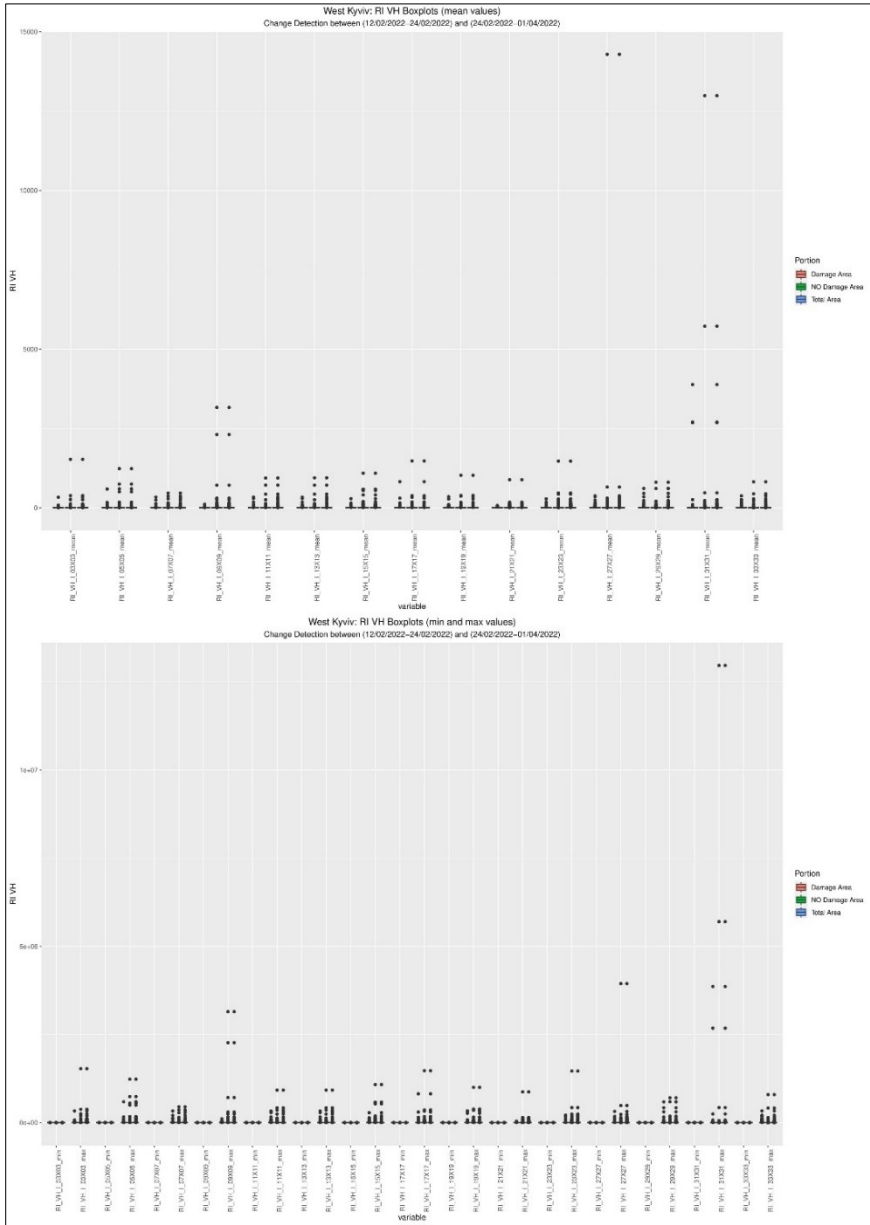


Fig. 115 – West Kyiv, RI VH Index. Top: boxplots of average values. Bottom: boxplots of minimum and maximum values.

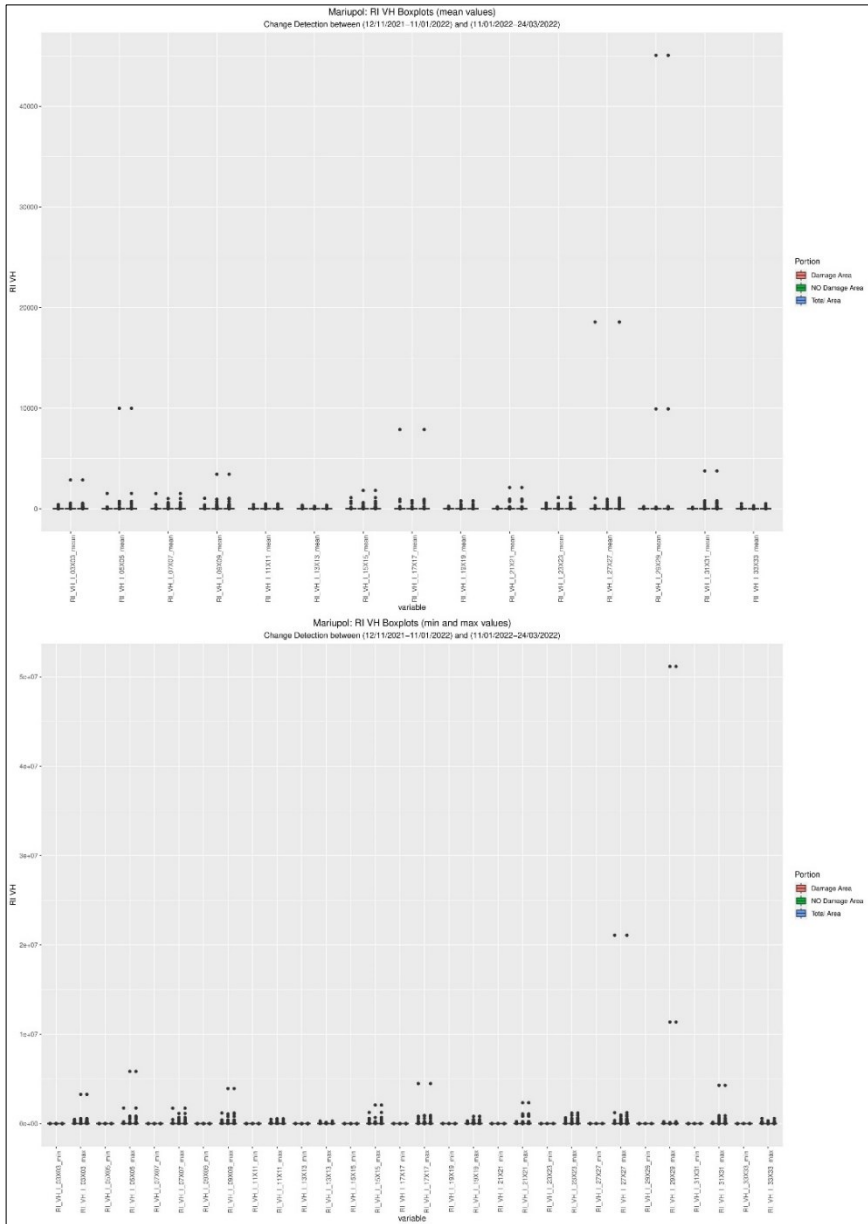


Fig. 116 – Mariupol, RI VH Index. Top: boxplots of average values. Bottom: boxplots of minimum and maximum values.

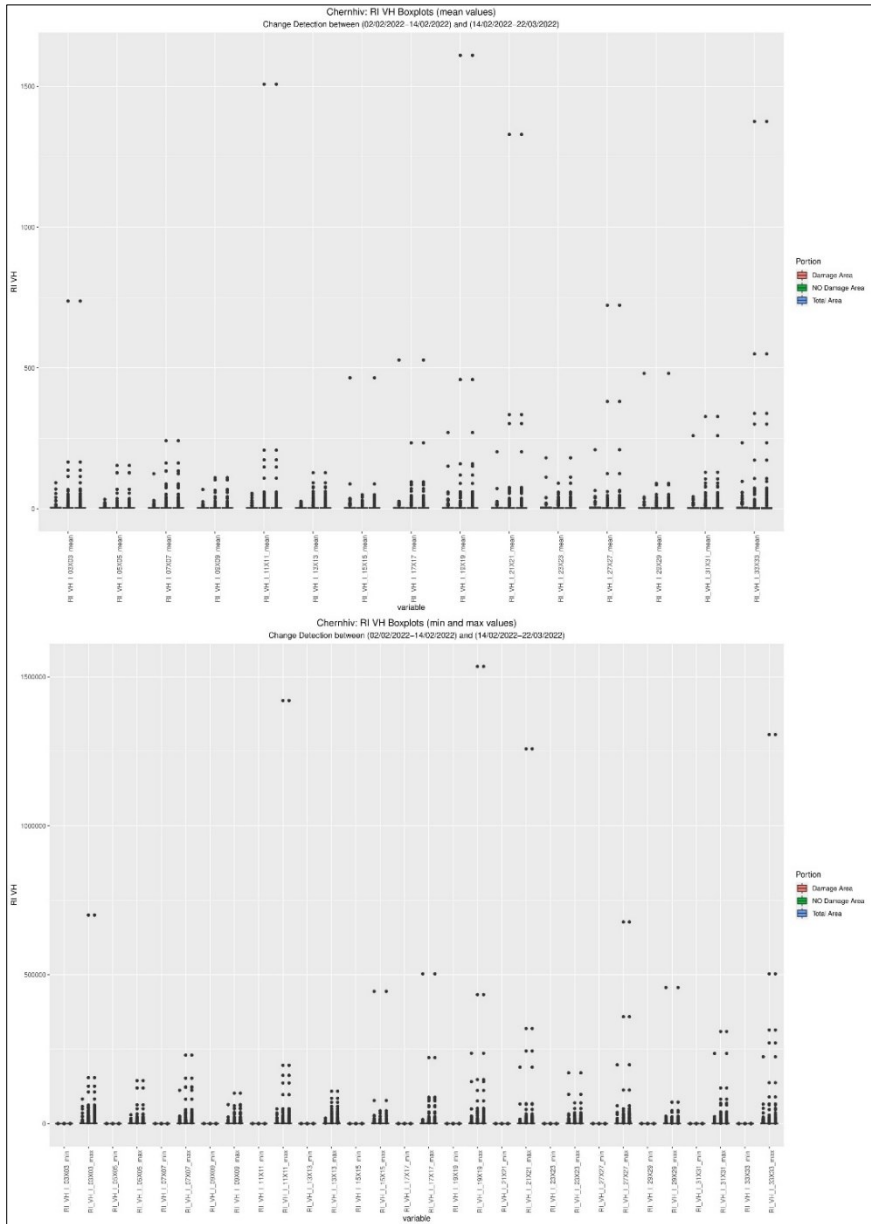


Fig. 117 – Chernihiv, RI VH Index. Top: boxplots of average values. Bottom: boxplots of minimum and maximum values.

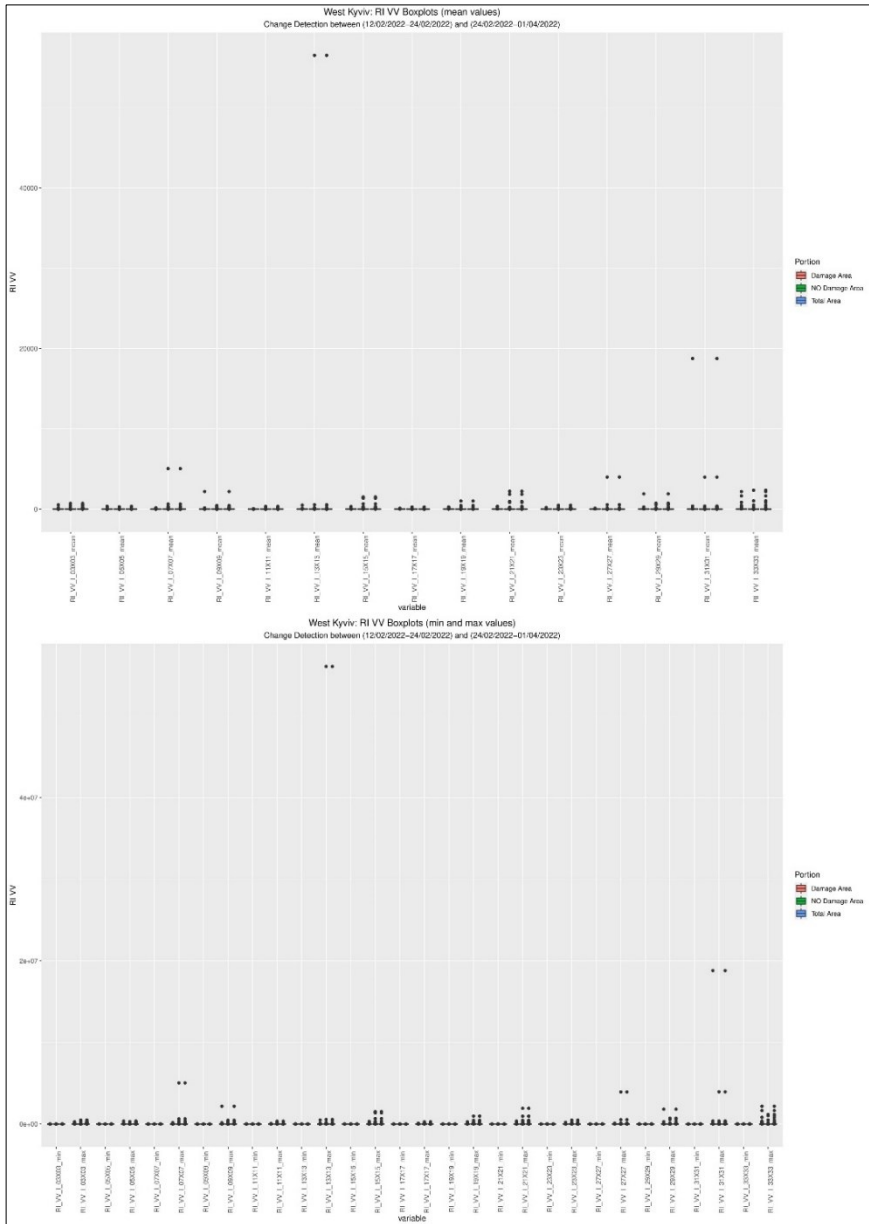


Fig. 118 – West Kyiv, RI VV Index. Top: boxplots of average values. Bottom: boxplots of minimum and maximum values.

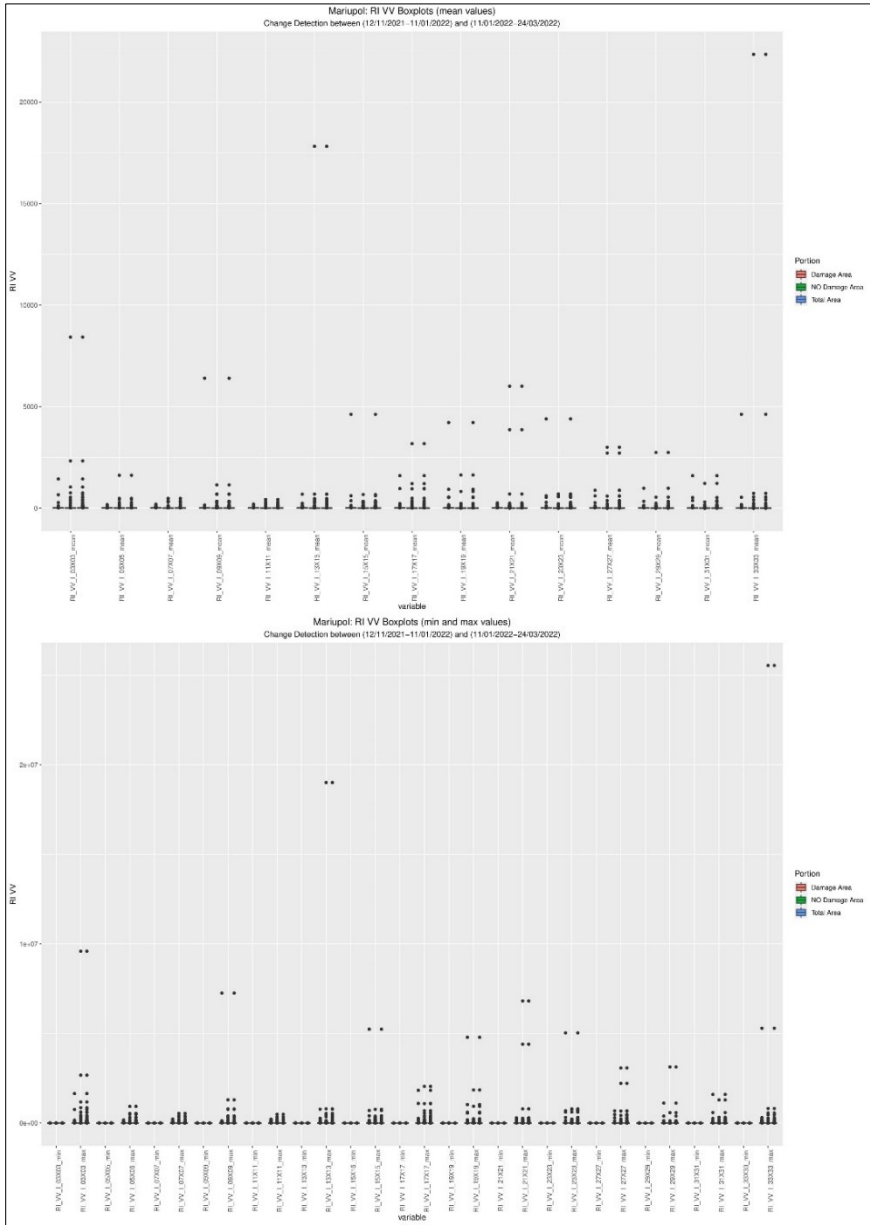


Fig. 119 – Mariupol, RI VV Index. Top: boxplots of average values. Bottom: boxplots of minimum and maximum values.

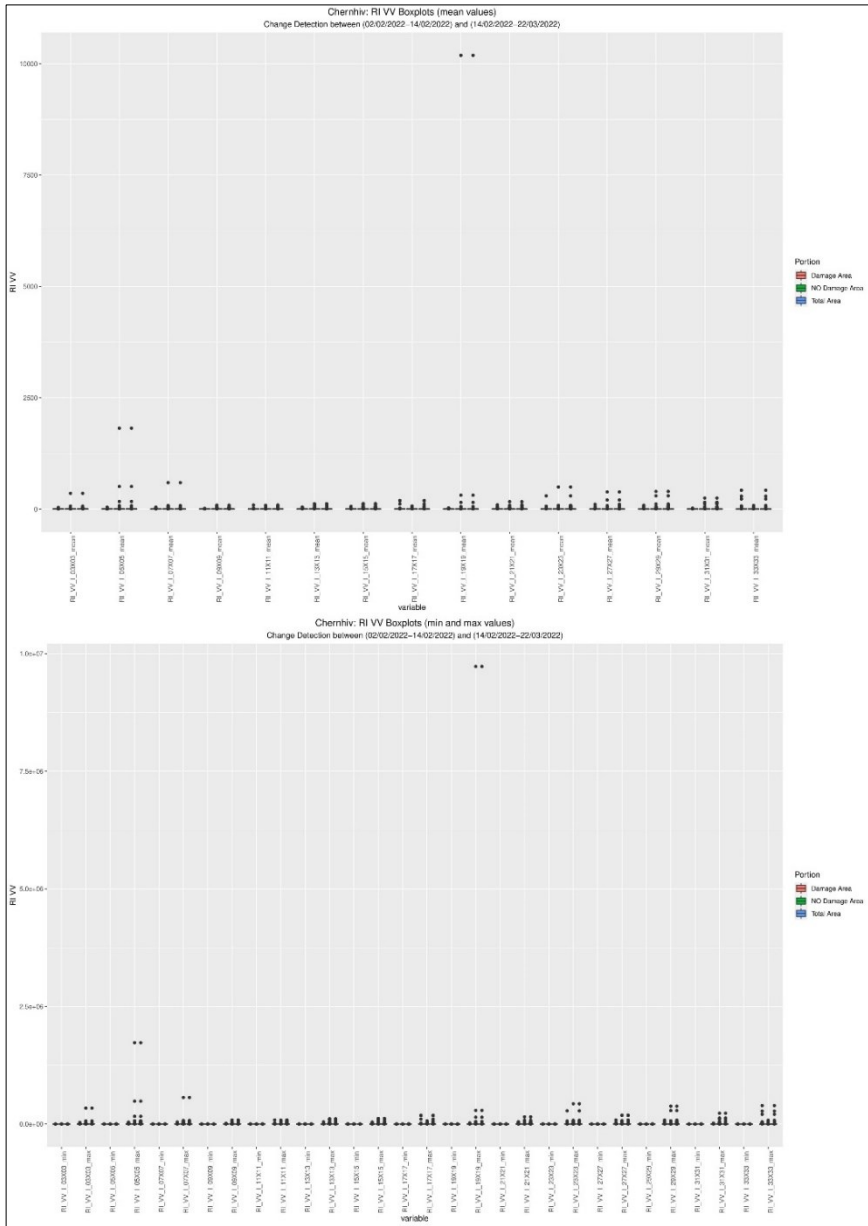


Fig. 120 – Chernihiv, RI VV Index. Top: boxplots of average values. Bottom: boxplots of minimum and maximum values.

D – SNR Graphs

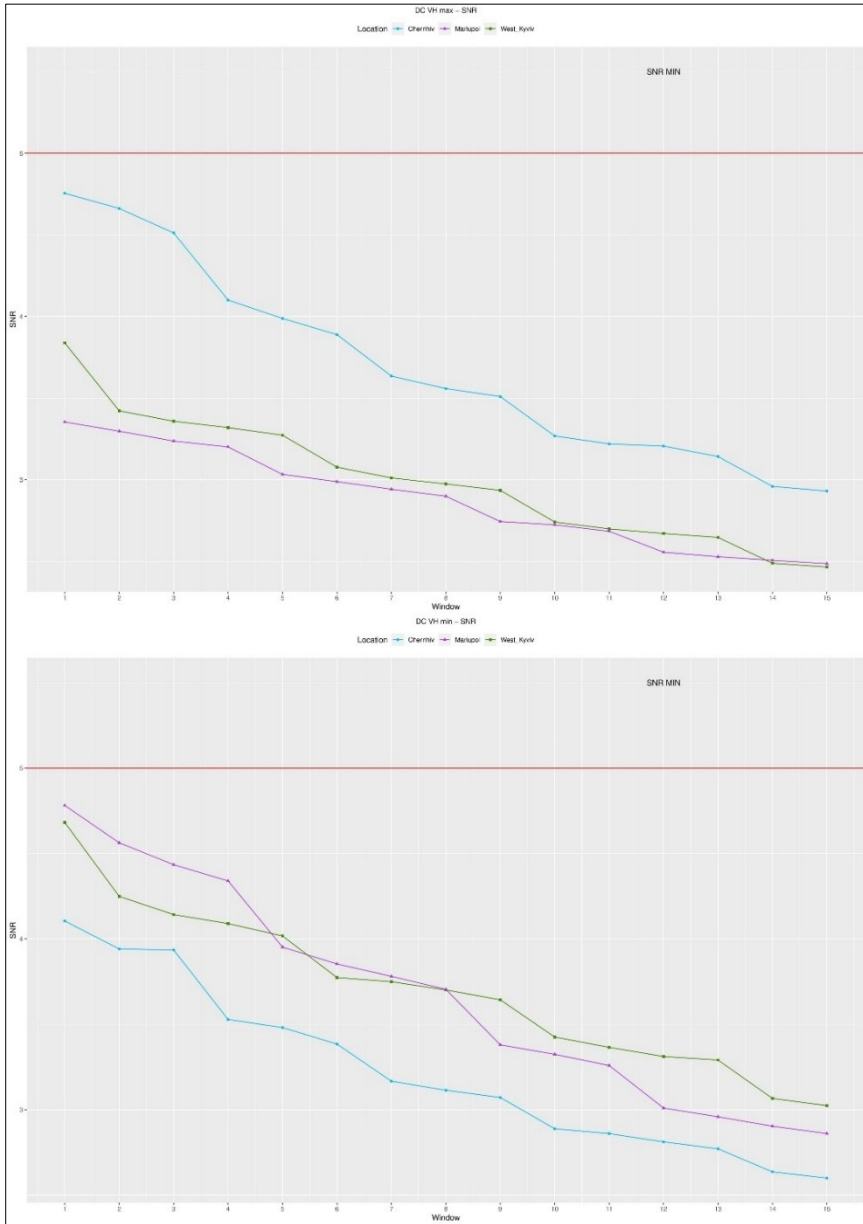


Fig. 121 – DC VH Index. Top: SNR of maximum values. Bottom: SNR of minimum values.

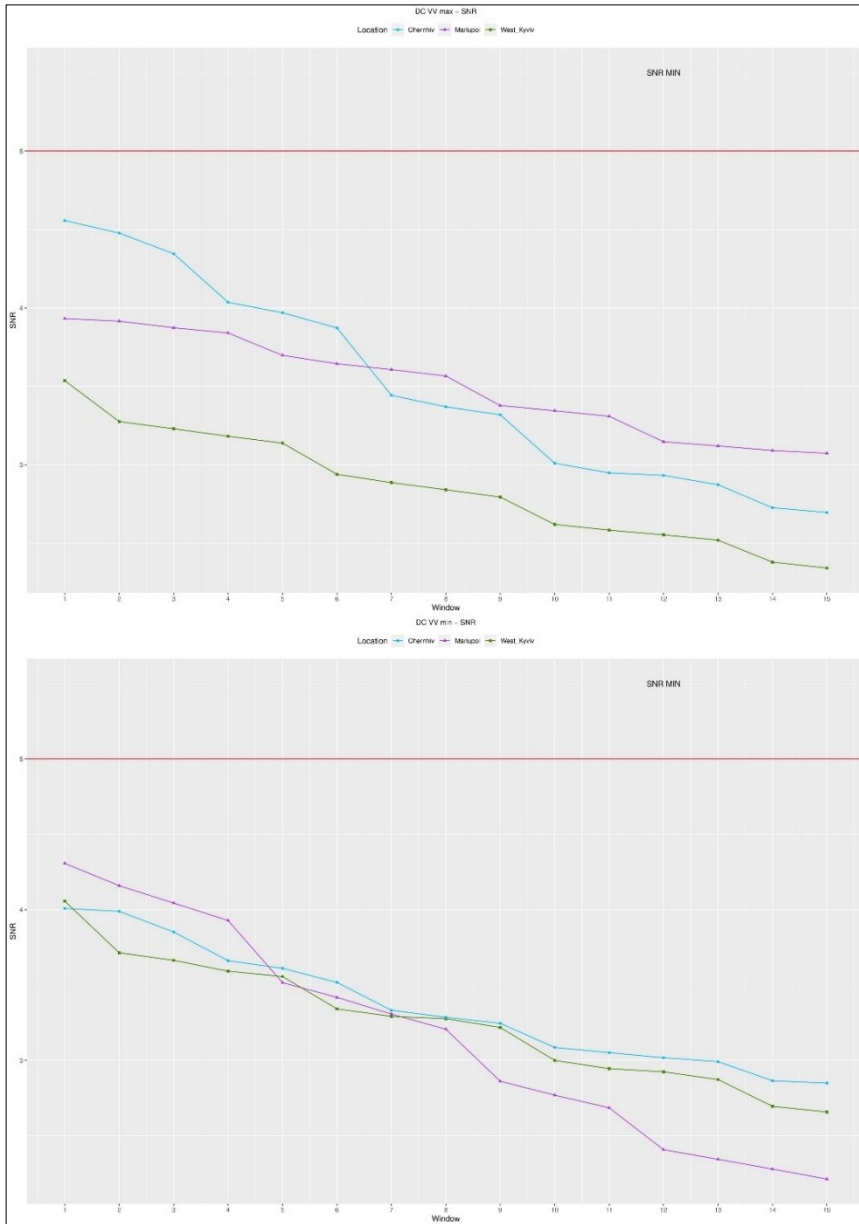


Fig. 122 – DC VV Index. Top: SNR of maximum values. Bottom: SNR of minimum values.



Fig. 123 – NDCC VH Index. Top: SNR of maximum values. Bottom: SNR of minimum values.

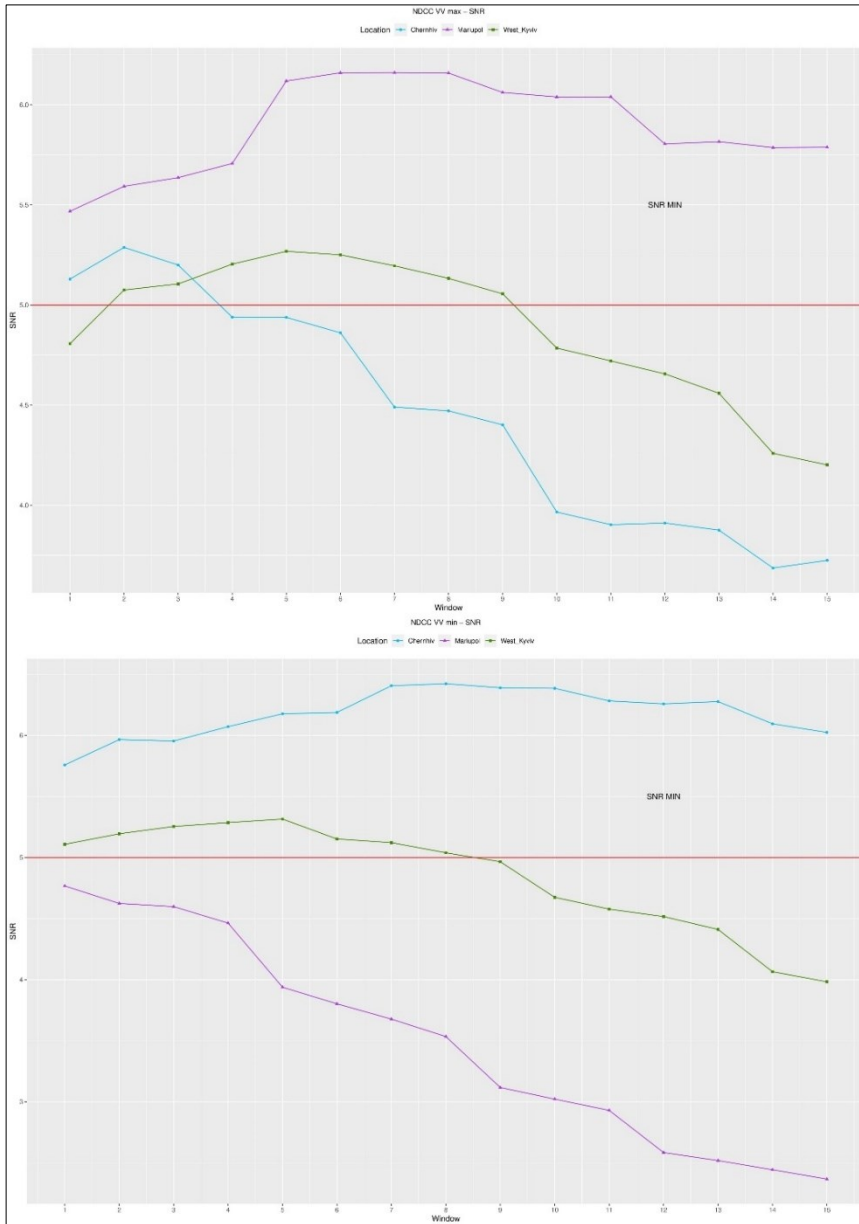


Fig. 124 – NDCC VV Index. Top: SNR of maximum values. Bottom: SNR of minimum values.

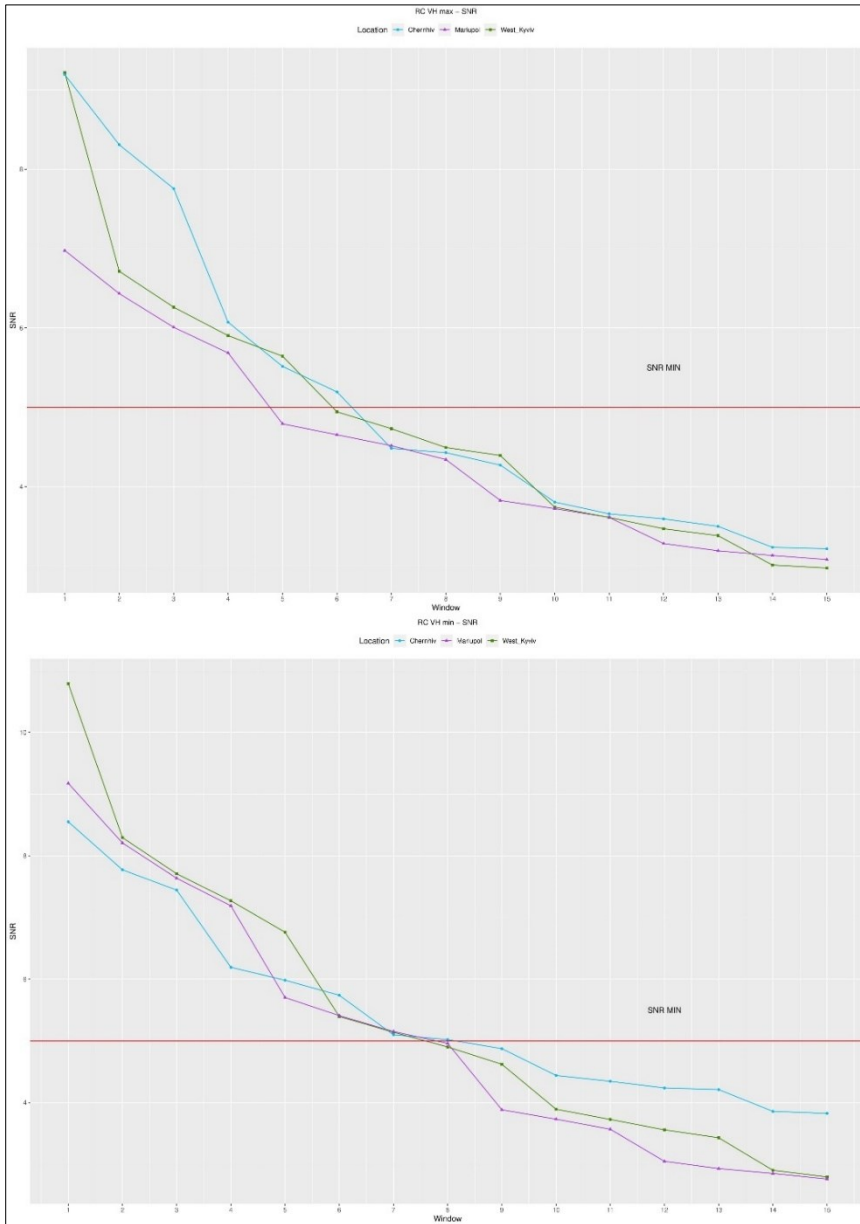


Fig. 125 – RC VH Index. Top: SNR of maximum values. Bottom: SNR of minimum values.

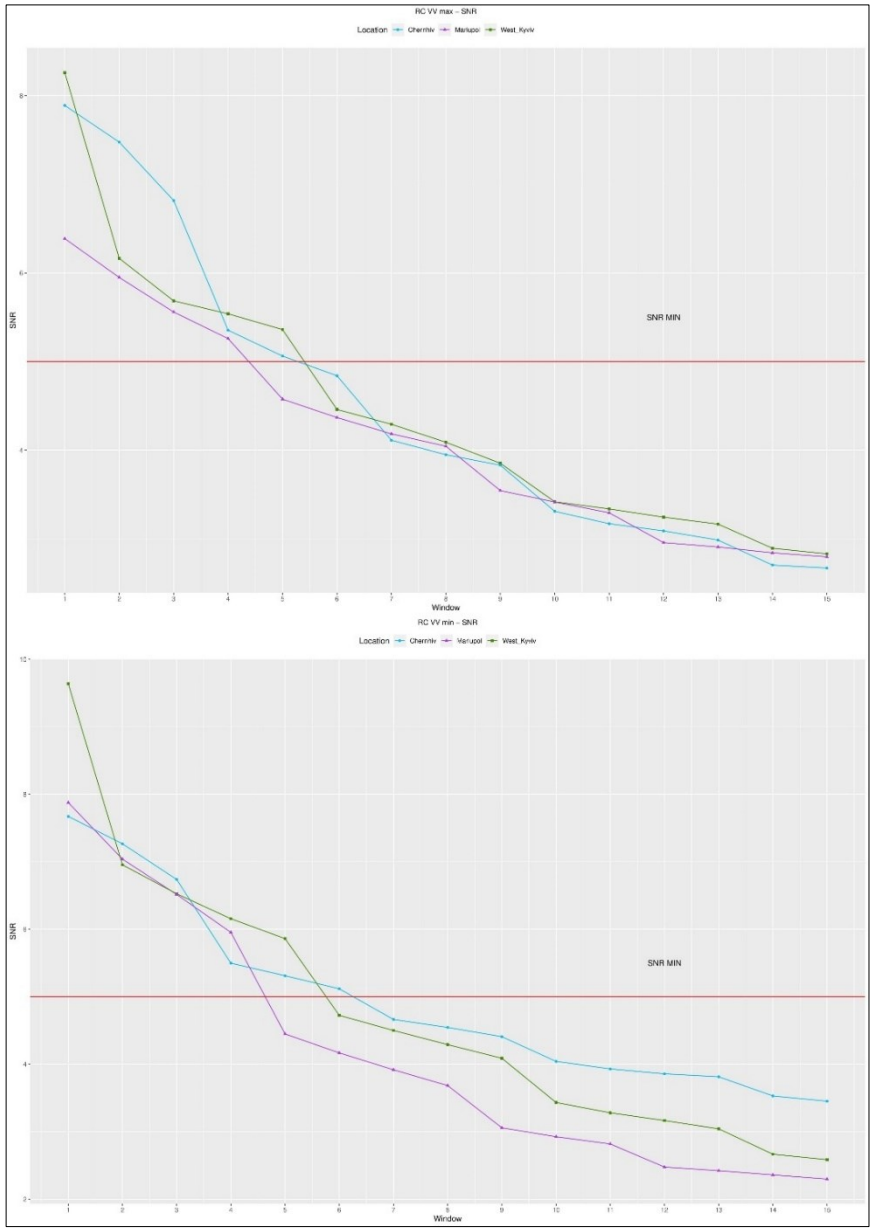


Fig. 126 – RC VV Index. Top: SNR of maximum values. Bottom: SNR of minimum values.

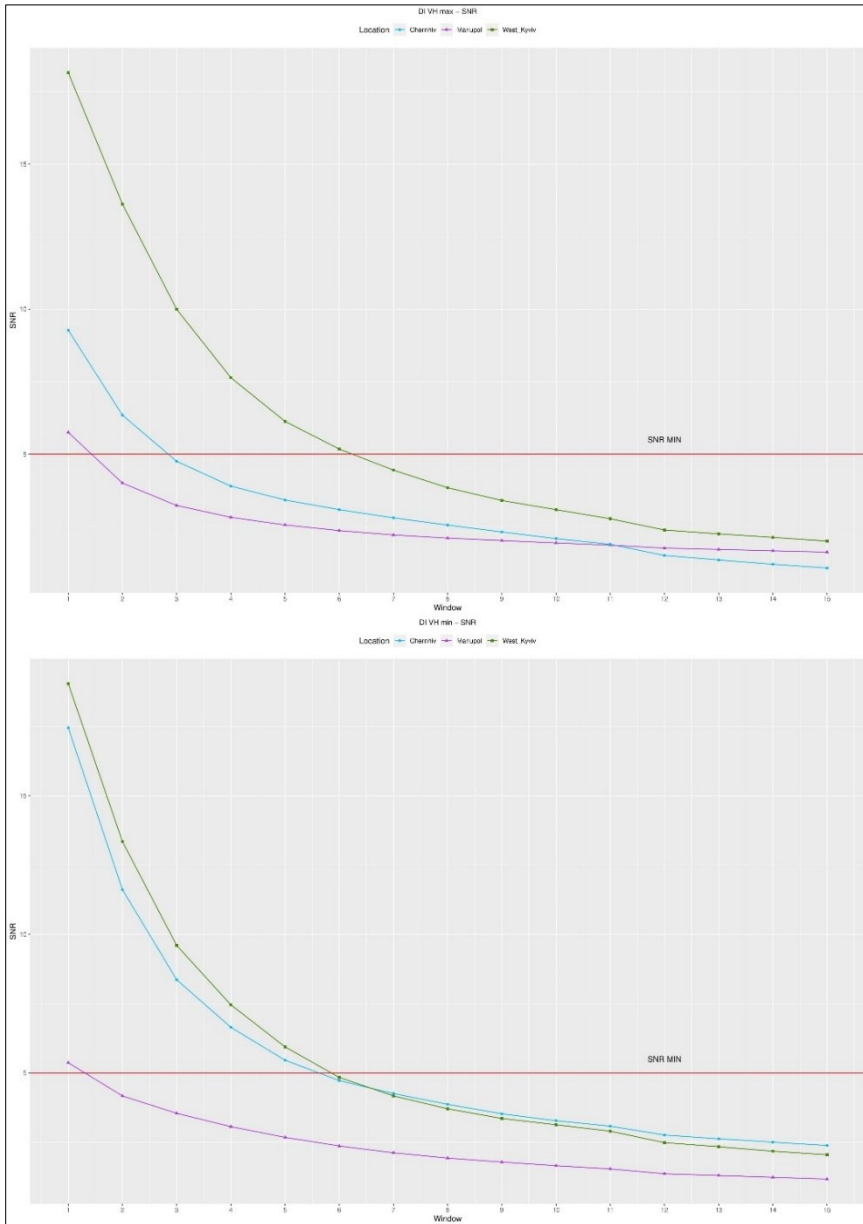


Fig. 127 – DI VH Index. Top: SNR of maximum values. Bottom: SNR of minimum values.

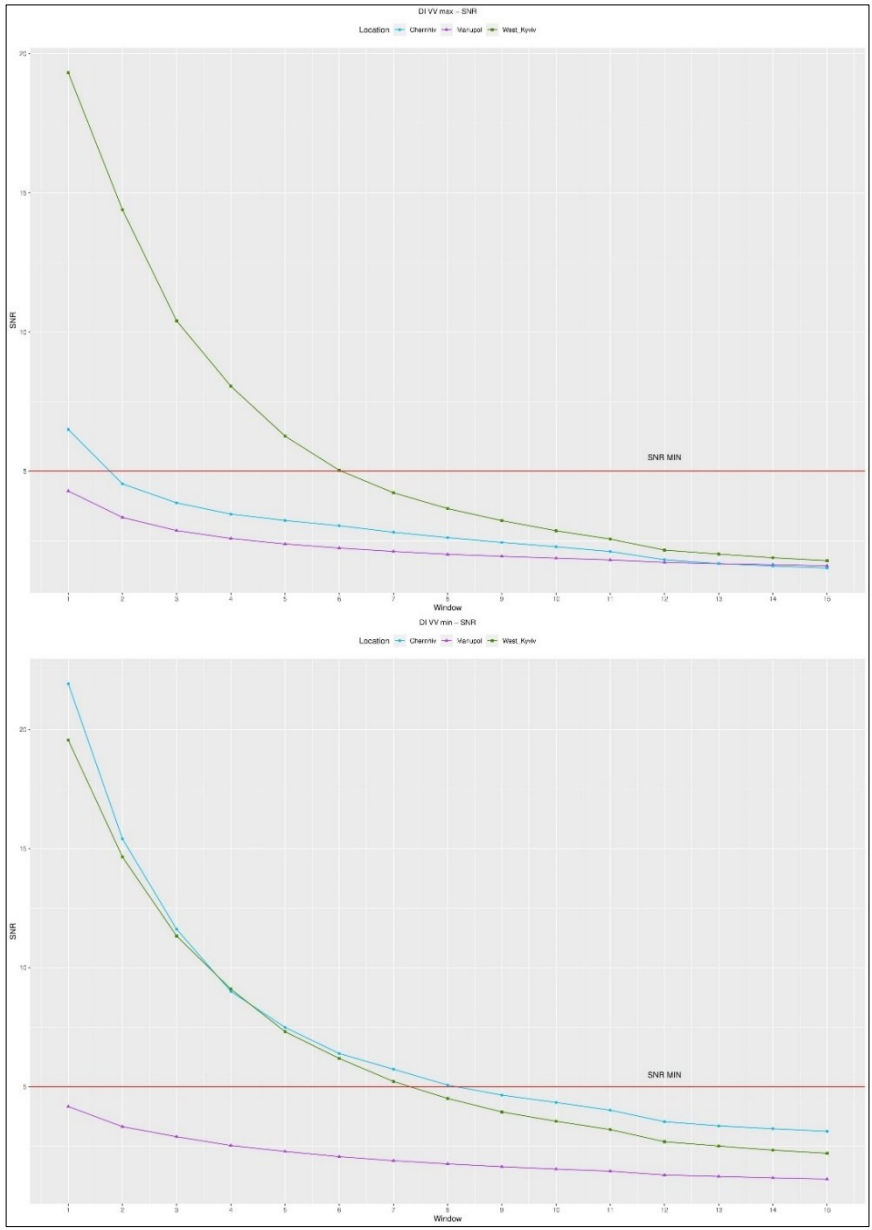


Fig. 128 – DI VV Index. Top: SNR of maximum values. Bottom: SNR of minimum values.

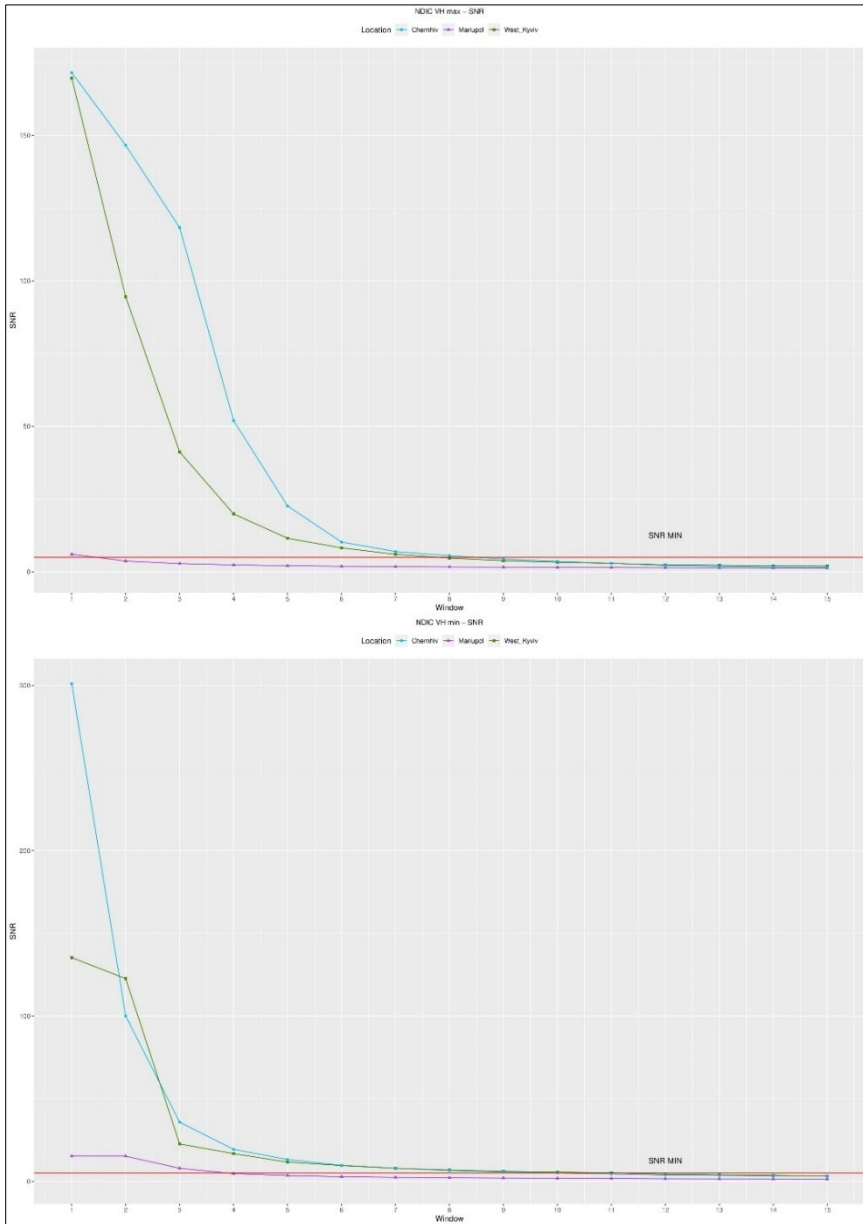


Fig. 129 – NDIC VH Index. Top: SNR of maximum values. Bottom: SNR of minimum values.

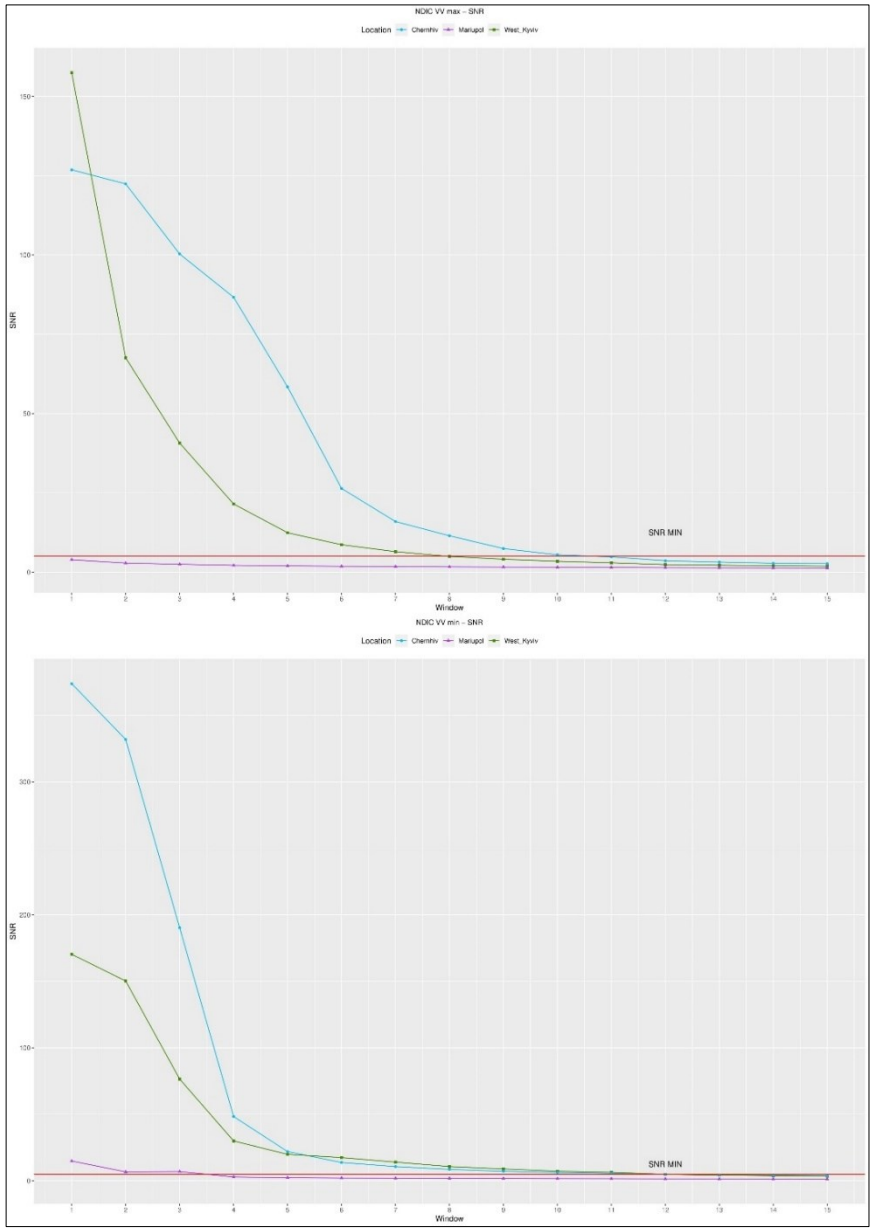


Fig. 130 – NDIC VV Index. Top: SNR of maximum values. Bottom: SNR of minimum values.

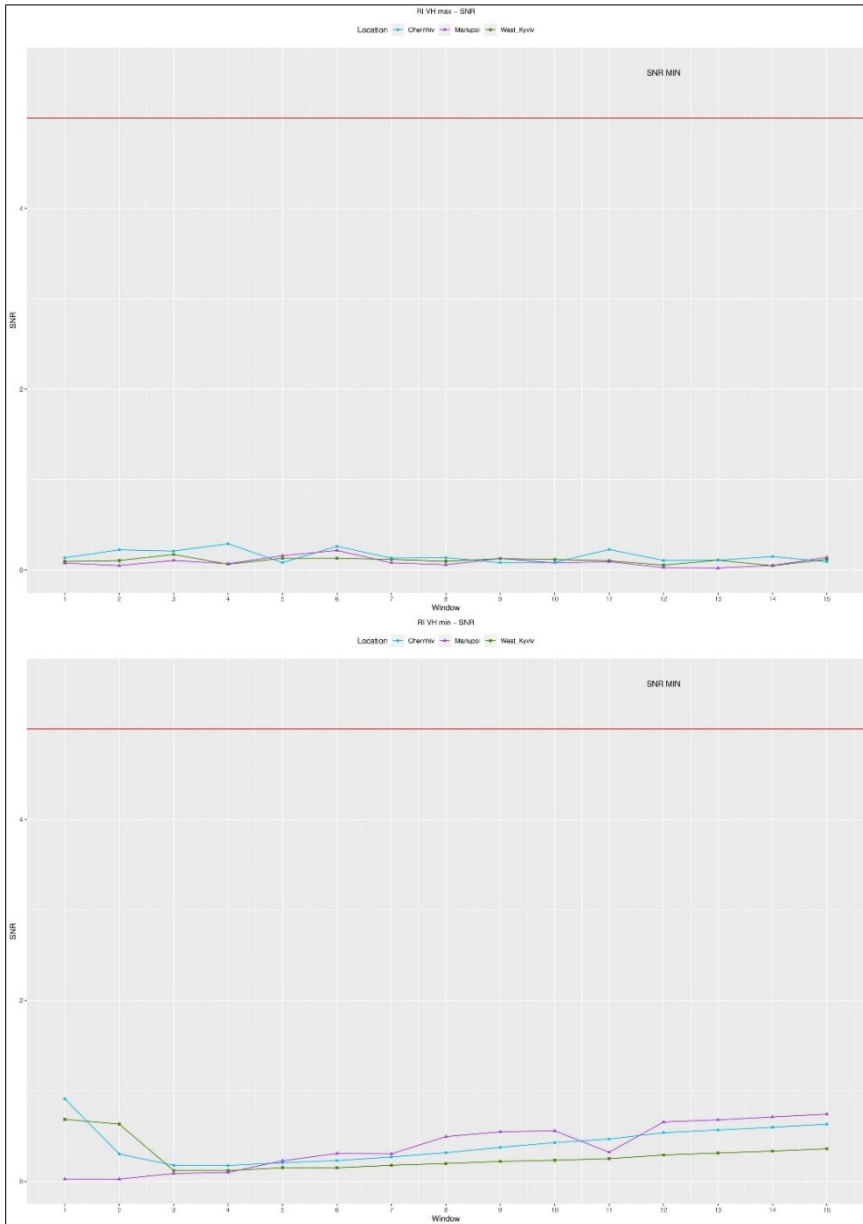


Fig. 131 – RI VH Index. Top: SNR of maximum values. Bottom: SNR of minimum values.

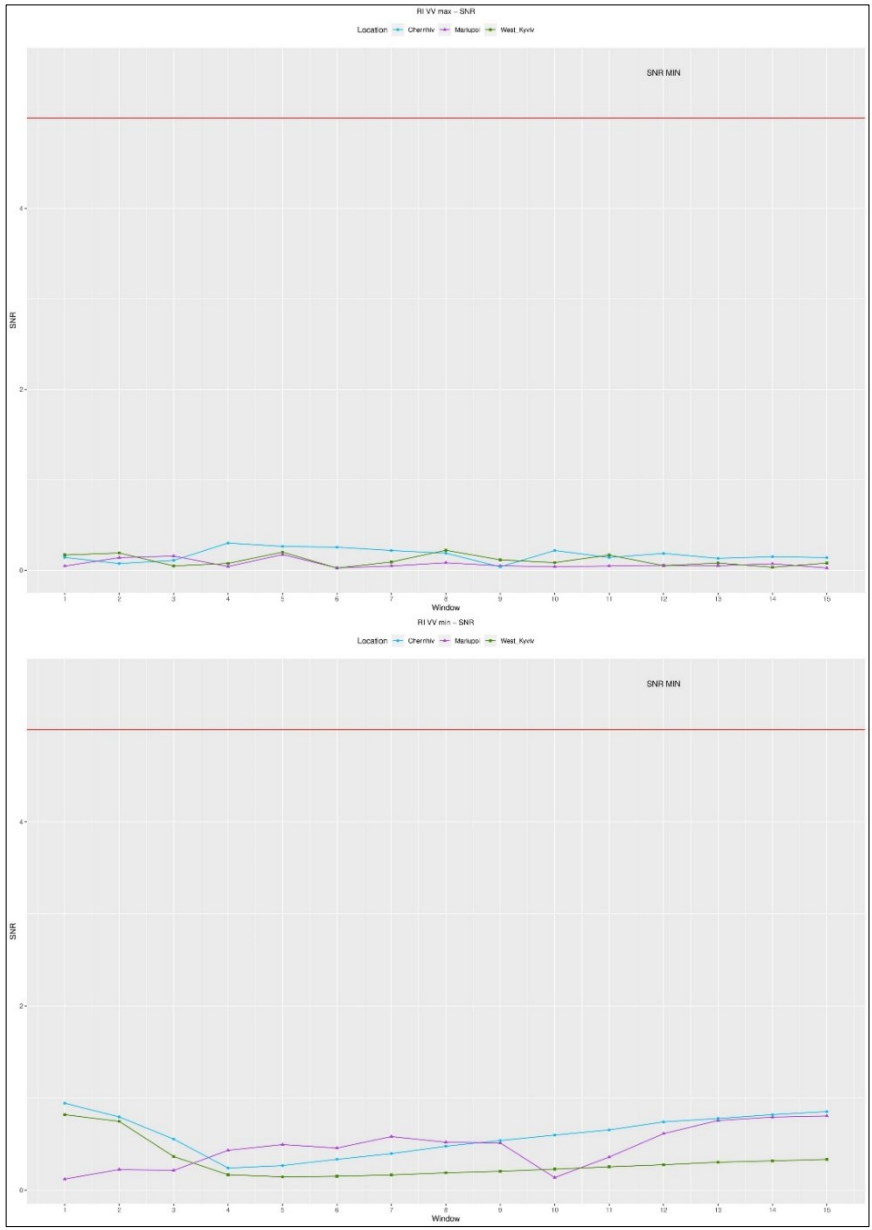


Fig. 132 – RI VV Index. Top: SNR of maximum values. Bottom: SNR of minimum values.

ACKNOWLEDGEMENTS

I wish to thank Prof.ssa Eufemia Tarantino for bringing enthusiasm and Dott.ssa Alessandra Capolupo for her assistance and suggestions.

For the constant availability and kindness I thank the Coordinator of the Doctoral Course Prof. Micele Mossa.

REFERENCES

BIBLIOGRAPHY

- Abdi, H. & Williams, L.J. (2010). Principal component analysis. *Wiley Interdisciplinary Reviews: Computational Statistics*. [Online]. 2 (4). p.pp. 433–459.
- Aimaiti, Y., Sanon, C., Koch, M., Baise, L.G. & Moaveni, B. (2022). War Related Building Damage Assessment in Kyiv, Ukraine, Using Sentinel-1 Radar and Sentinel-2 Optical Images. *Remote Sensing 2022, Vol. 14, Page 6239*. [Online]. 14 (24). p.p. 6239.
- Akhmadiya, A. & Zeng, Q. (2018). Use of Sentinel-1 Data for Earthquake Damage Assessment in Cases of Amatrice and Sarpol-E Zahab. In: *IGARSS 2018 - 2018 IEEE International Geoscience and Remote Sensing Symposium*. July 2018, IEEE, pp. 4877–4880.
- Anon (2021). Application of Remote Sensing Technology in Engineering Geological Surveying and Surveying. 6 (1).
- Anon (2002). Choosing a Subset of Principal Components or Variables. [Online]. p.pp. 111–149. Available from: https://link.springer.com/chapter/10.1007/0-387-22440-8_6.
- Arciniegas, G.A., Bijker, W., Kerle, N. & Tolpekin, V.A. (2007a). Coherence- and Amplitude-Based Analysis of Seismogenic Damage in Bam, Iran, Using ENVISAT ASAR Data. *IEEE Transactions on Geoscience and Remote Sensing*. 45 (6). p.pp. 1571–1581.
- Arciniegas, G.A., Bijker, W., Kerle, N. & Tolpekin, V.A. (2007b). Coherence- and Amplitude-Based Analysis of Seismogenic Damage in Bam, Iran, Using ENVISAT ASAR Data. *IEEE Transactions on Geoscience and Remote Sensing*. 45 (6). p.pp. 1571–1581.
- Arjasakusuma, S., Kusuma, S.S., Rafif, R., Saringatin, S. & Wicaksono, P. (2021). Time-series Cross-orbit Sentinel-1 Synthetic-Aperture Radar (SAR) Data for

- Mapping Paddy Extent: Case Study of Magelang District, Central Java. *IOP Conference Series: Earth and Environmental Science*. 686 (1). p.p. 012053.
- Arturo, F., Garzón, M. & Valánszki, I. (2020). REMOTE SENSING TENDENCIES IN THE ASSESSMENT OF AREAS DAMAGED BY ARMED CONFLICTS. *Scientific Papers, Series E. Land Reclamation, Earth Observation & Surveying, Environmental Engineering*. IX.
- Ashbindu, S. (1989). Review article digital change detection techniques using remotely-sensed data. *Remote Sensing*. [Online]. 10 (6). p.pp. 989–1003.
- Atwood, D.K., Small, D. & Gens, R. (2012). Improving PolSAR Land Cover Classification With Radiometric Correction of the Coherency Matrix. *IEEE Journal of Selected Topics in Applied Earth Observations and Remote Sensing*. 5 (3). p.pp. 848–856.
- Azzam, R.M.A., Bashara, N.M. & Ballard, S.S. (1978a). Ellipsometry and Polarized Light. *Physics Today*. 31 (11). p.pp. 72–72.
- Azzam, R.M.A., Bashara, N.M. & Ballard, S.S. (1978b). Ellipsometry and Polarized Light. *Physics Today*. 31 (11). p.pp. 72–72.
- Bajwa, I.S. & Hyder, S.I. (2005). PCA based image classification of single-layered cloud types. *Proceedings - IEEE 2005 International Conference on Emerging Technologies, ICET 2005*. 2005. p.pp. 365–369.
- Ball, D.W. (2007). The electromagnetic spectrum: a history. *Spectroscopy*. [Online]. Available from: http://alfresco-static-files.s3.amazonaws.com/alfresco_images/pharma/2014/08/21/32f98d89-422d-4e07-af11-0211ecfc26e8/article-411659.pdf.
- Beckmann, P. & Keller, J.B. (1972). The Depolarization of Electromagnetic Waves. *American Journal of Physics*. 40 (10). p.pp. 1557–1557.
- Bender, N., Yilmaz, H., Bromberg, Y. & Cao, H. (2019). Creating and controlling complex light. *APL Photonics*. 4 (11). p.p. 110806.
- Bender, N., Yilmaz, H., Bromberg, Y. & Cao, H. (2018). Customizing speckle intensity statistics. *Optica*. 5 (5). p.pp. 595–600.

- Bentz, C.M., Baudzus, L. & Krummrich, P.M. (2014). Signal to Noise Ratio (SNR) Enhancement Comparison of Impulse-, Coding- and Novel Linear-Frequency-Chirp-Based Optical Time Domain Reflectometry (OTDR) for Passive Optical Network (PON) Monitoring Based on Unique Combinations of Wavelength Selective Mirrors. *Photonics 2014, Vol. 1, Pages 33-46*. [Online]. 1 (1). p.pp. 33–46. Available from: <https://www.mdpi.com/2304-6732/1/1/33/htm>.
- Boerner, W.-M. (2007). *Basics of sar polarimetry I*. [Online]. Available from: <https://apps.dtic.mil/sti/citations/ADA471015>.
- Boerner, W.-M. (1981). Use of polarization in electromagnetic inverse scattering. *Radio Science*. 16 (6). p.pp. 1037–1045.
- Boerner, W.M., Cram, L.A., Holm, W.A., Stein, D.E., Wiesbeck, W., Keydel, W., Giuli, D., Gjessing, D.T., Molinet, A. & Brand, H. (1988). *Direct and Inverse Methods in Radar Polarimetry*. NATO ASI Series. W.-M. Boerner, H. Brand, L. A. Cram, W. A. Holm, D. E. Stein, W. Wiesbeck, W. Keydel, D. Giuli, D. T. Gjessing, & F. A. Molinet (eds.). [Online]. Dordrecht: Springer Netherlands. Available from: <http://link.springer.com/10.1007/978-94-010-9243-2>.
- Boerner, W.-M., El-Arini, M., Chung-Yee Chan & Mastoris, P. (1981). Polarization dependence in electromagnetic inverse problems. *IEEE Transactions on Antennas and Propagation*. 29 (2). p.pp. 262–271.
- Boerner, W.-M., Mott, H. & Luneburg, E. (n.d.). Polarimetry in remote sensing: basic and applied concepts. In: *IGARSS'97. 1997 IEEE International Geoscience and Remote Sensing Symposium Proceedings. Remote Sensing - A Scientific Vision for Sustainable Development*. IEEE, pp. 1401–1403.
- Boerner, W.M. & North Atlantic Treaty Organization. Scientific Affairs Division. (1985). *Inverse methods in electromagnetic imaging*. [Online]. p.p. 1347. Available from: https://books.google.com/books/about/Inverse_Methods_in_Electromagnetic_Imagi.html?hl=it&id=AaD6CAAQBAJ.
- Bloorani, A.D., Darvishi, M., Weng, Q. & Liu, X. (2021). Post-War Urban Damage Mapping Using InSAR: The Case of Mosul City in Iraq. *ISPRS International Journal of Geo-Information*. 10 (3). p.p. 140.

- Braun, A. (2018). *Assessment of Building Damage in Raqqa during the Syrian Civil War Using Time-Series of Radar Satellite Imagery*. (1).
- Braun, A. & Offermann, E. (2022). Polarimetric information content of Sentinel-1 for land cover mapping: An experimental case study using quad-pol data synthesized from complementary repeat-pass acquisitions. *Frontiers in Remote Sensing*. 3. p.p. 90.
- Braun, A. & Veci, L. (2021). *Sentinel-1 Toolbox TOPS Interferometry Tutorial*. [Online]. Available from: <https://skywatch.co>.
- Capolupo, A., Saponaro, M., Borgogno Mondino, E. & Tarantino, E. (2020). Combining Interior Orientation Variables to Predict the Accuracy of Rpas–Sfm 3D Models. *Remote Sensing*. 12 (17). p.p. 2674.
- Caporusso, G., Dell’Olio, M. & Tarantino, E. (2022a). *Use of the Sentinel-1 Satellite Data in the SNAP Platform and the WebGNOME Simulation Model for Change Detection Analyses on the Persian Gulf Oil Spill*.
- Caporusso, G., Gallo, C. & Tarantino, E. (2022b). *Change Detection Analysis Using Sentinel-1 Satellite Data with SNAP and GEE Regarding Oil Spill in Venezuela*.
- Cascini, L., Fornaro, G. & Peduto, D. (2009). Analysis at medium scale of low-resolution DInSAR data in slow-moving landslide-affected areas. *ISPRS Journal of Photogrammetry*. [Online]. 64. p.pp. 598–611. Available from: https://www.sciencedirect.com/science/article/pii/S0924271609000628?casa_token=U-C0bY0GWX8AAAAA:Hg6tXpQ4HxYbrDoJLBeldhv-4a8lkFZ6Ykmhxm-Y_rgZTvBpU4eEYrGGtX7F6BKKj_0WJy3Aw.
- catalyst.earth (2022). *Catalyst Professional*. [Online]. 2022. Available from: <https://catalyst.earth/products/catalyst-pro/>.
- Chae, S.-H., Lee, W.-J., Baek, W.-K. & Jung, H.-S. (2019). An Improvement of the Performance of SAR Offset Tracking Approach to Measure Optimal Surface Displacements. *IEEE Access*. 7. p.pp. 131627–131637.
- Chandrasekhar, S. (1960). *Radiative Transfer*. Dover Publications.
- Cheney, M. & Borden, B. (2009). *Fundamentals of Radar Imaging*. Society for Industrial and Applied Mathematics.

- Chipman, R.A. (1990). Polarimetry: Radar, infrared, visible, ultraviolet, X-ray. *Proc. SPIE*. [Online]. Available from: <https://cir.nii.ac.jp/crid/1570291224531696768>.
- Chuvieco, E. (2010). *Teledetección Ambiental: La Observación de la Tierra Desde el Espacio*. Editorial Ariel S.A. (ed.). Barcelona.
- Chuvieco, E., Mouillot, F., van der Werf, G.R., San Miguel, J., Tanasse, M., Koutsias, N., García, M., Yebra, M., Padilla, M., Gitas, I., Heil, A., Hawbaker, T.J. & Giglio, L. (2019). Historical background and current developments for mapping burned area from satellite Earth observation. *Remote Sensing of Environment*. 225. p.p. 45–64.
- Cloude, S.R. & Pottier, E. (1996). A review of target decomposition theorems in radar polarimetry. *IEEE Transactions on Geoscience and Remote Sensing*. 34 (2). p.p. 498–518.
- Collett, E. & Society of Photo-optical Instrumentation Engineers. (2005). *Field guide to polarization*. p.p. 134.
- Congalton, R.G. (2001). Accuracy assessment and validation of remotely sensed and other spatial information. *International Journal of Wildland Fire*. 10 (4). p.p. 321.
- Crecraft, D. & Gergely, S. (2002). *Analog Electronics - 1st Edition*. [Online]. Available from: <http://www.sciencedirect.com:5070/book/9780750650953/analog-electronics>.
- Dainty, J.C. (1984). *Laser speckle and related phenomena*. 2nd Ed. Springer-Verlag.
- Darwish, N., Kaiser, M., Koch, M. & Gaber, A. (2021). Assessing the Accuracy of ALOS/PALSAR-2 and Sentinel-1 Radar Images in Estimating the Land Subsidence of Coastal Areas: A Case Study in Alexandria City, Egypt. *Remote Sensing*. 13 (9). p.p. 1838.
- Delgado Blasco, J.M., Fitrzyk, M., Patruno, J., Ruiz-Armenteros, A.M. & Marconcini, M. (2020). Effects on the Double Bounce Detection in Urban Areas Based on SAR Polarimetric Characteristics. *Remote Sensing*. 12 (7). p.p. 1187.
- Devrani, T. (2018). *Development of automated mapping methods for birch woodlands in the Norourhraun lava field, Hekla*. [Online]. Available from:

https://www.researchgate.net/profile/Tarun-Devrani/publication/329169115_Development_of_automated_mapping_methods_for_birch_woodlands_in_the_Nordurhraun_lava_field_Hekla/links/5c34641292851c22a3639b3f/Development-of-automated-mapping-methods-for-birch-woodlands-in-the-Nordurhraun-lava-field-Hekla.pdf.

- Dhar, A., Gray, B., International, C.M.-2011 I. & 2011, undefined (n.d.). Comparison of dual and full polarimetric entropy/alpha decompositions with TerraSAR-X, suitability for use in classification. *ieeexplore.ieee.org*. [Online]. Available from: https://ieeexplore.ieee.org/abstract/document/6049163/?casa_token=LkgfAoz2ApsAAAAA:idAOhzFdjxGAcdrK0oRmN-6V5XfBqNt6n4pJgGVL7VUk7f3VK7W9sGELRD059gJfR1gwGlePw.
- Dharani, M. & Sreenivasulu, G. (2021). Land use and land cover change detection by using principal component analysis and morphological operations in remote sensing applications. *International Journal of Computers and Applications*. 43 (5). p.pp. 462–471.
- Dubovik, O., Schuster, G.L., Xu, F., Hu, Y., Bösch, H., Landgraf, J. & Li, Z. (2021). Grand Challenges in Satellite Remote Sensing. *Frontiers in Remote Sensing*. 2. p.p. 1.
- ElGharbawi, T. & Zarzoura, F. (2021). Damage detection using SAR coherence statistical analysis, application to Beirut, Lebanon. *ISPRS Journal of Photogrammetry and Remote Sensing*. 173. p.pp. 1–9.
- ESA (2022). *SNAP Help Content*.
- Espín Bedón, P.A., Audin, L., Doin, M.P., Pinel, V., Pathier, E., Mothes, P., García, A., Samaniego, P. & Pacheco, D. (2022). Unrest at Cayambe Volcano revealed by SAR imagery and seismic activity after the Pedernales subduction earthquake, Ecuador (2016). *Journal of Volcanology and Geothermal Research*. 428. p.p. 107577.
- Estornell, J., Martí-Gavliá, J.M., Sebastiá, M.T. & Mengual, J. (2013). Principal component analysis applied to remote sensing. *Modelling in Science Education and Learning*. 6. p.p. 83.

- Fattahi, H., Agram, P. & Simons, M. (2017). A Network-Based Enhanced Spectral Diversity Approach for TOPS Time-Series Analysis. *IEEE Transactions on Geoscience and Remote Sensing*. 55 (2). p.pp. 777–786.
- Ferguson, J.E. & Gunn, G.E. (2022a). Polarimetric decomposition of microwave-band freshwater ice SAR data: Review, analysis, and future directions. *Remote Sensing of Environment*. 280. p.p. 113176.
- Ferguson, J.E. & Gunn, G.E. (2022b). Polarimetric decomposition of microwave-band freshwater ice SAR data: Review, analysis, and future directions. *Remote Sensing of Environment*. 280. p.p. 113176.
- Ferretti, A., Prati, C. & Rocca, F. (2001). Permanent scatterers in SAR interferometry. *IEEE Transactions on Geoscience and Remote Sensing*. 39 (1). p.pp. 8–20.
- Filipponi, F. (2019). Sentinel-1 GRD Preprocessing Workflow. In: *3rd International Electronic Conference on Remote Sensing*. 4 June 2019, Basel Switzerland: MDPI, p. 11.
- Frost, V.S., Stiles, J.A., Shanmugan, K.S. & Holtzman, J.C. (1982). A Model for Radar Images and Its Application to Adaptive Digital Filtering of Multiplicative Noise. *IEEE Transactions on Pattern Analysis and Machine Intelligence*. PAMI-4 (2). p.pp. 157–166.
- Frutuoso, R., Lima, A. & Teodoro, A.C. (2021). Application of remote sensing data in gold exploration: targeting hydrothermal alteration using Landsat 8 imagery in northern Portugal. *Arabian Journal of Geosciences*. 14 (6). p.p. 459.
- Fujiwara, H. (2007). *Spectroscopic Ellipsometry*. Wiley.
- Gandrud, C. (2018). *Reproducible Research with R and RStudio*. [Online]. Available from: <https://www.taylorfrancis.com/books/9781315363295>.
- Ge, P., Gokon, H. & Meguro, K. (2019). Building Damage Assessment Using Intensity SAR Data with Different Incidence Angles and Longtime Interval. *Journal of Disaster Research*. 14 (3). p.pp. 456–465.
- GENS, R. & van GENDEREN, J.L. (1996). Review Article SAR interferometry—issues, techniques, applications. *International Journal of Remote Sensing*. 17 (10). p.pp. 1803–1835.

- Ghaderizadeh, S., Abbasi-Moghadam, D., Sharifi, A., Zhao, N. & Tariq, A. (2021). Hyperspectral Image Classification Using a Hybrid 3D-2D Convolutional Neural Networks. *IEEE Journal of Selected Topics in Applied Earth Observations and Remote Sensing*. 14. p.pp. 7570–7588.
- Ghandour, A. & Jezzini, A. (2018). Post-War Building Damage Detection. In: *The 2nd International Electronic Conference on Remote Sensing*. 22 March 2018, Basel Switzerland: MDPI, p. 359.
- Gonzalez, R.C. & Woods, R.E. (2007). Digital Image Processing (3rd Edition). *Prentice-Hall, Inc. Upper Saddle River, NJ, USA ©2006*. [Online]. p.p. 976. Available from: https://books.google.com/books/about/Digital_Image_Processing.html?hl=it&id=8uGOnjRGEzoC.
- Goodman, J.W. (1976). Some fundamental properties of speckle*. *Journal of the Optical Society of America*. 66 (11). p.pp. 1145–1150.
- Gunn, G.E., Duguay, C.R., Atwood, D.K., King, J. & Toose, P. (2018). Observing Scattering Mechanisms of Bubbled Freshwater Lake Ice Using Polarimetric RADARSAT-2 (C-Band) and UW-Scat (X- and Ku-Bands). *IEEE Transactions on Geoscience and Remote Sensing*. 56 (5). p.pp. 2887–2903.
- Guo, H., Huang, Q., Li, X., Sun, Z. & Zhang, Y. (2013). Spatiotemporal analysis of urban environment based on the vegetation–impervious surface–soil model. *Journal of Applied Remote Sensing*. [Online]. 8 (1). p.p. 084597. Available from: <https://api.semanticscholar.org/CorpusID:28430037#id-name=S2CID>.
- Haal, D.K. (1996). Remote sensing applications to hydrology; imaging radar. *Hydrological Science Journal*. [Online]. 41 (4). p.pp. 609–624. Available from: <https://www.tandfonline.com/doi/abs/10.1080/02626669609491528>.
- Hajeb, M., Karimzadeh, S. & Fallahi, A. (2020). Seismic damage assessment in Sarpole-Zahab town (Iran) using synthetic aperture radar (SAR) images and texture analysis. *Natural Hazards*. 103 (1). p.pp. 347–366.
- Hanssen, R. (2001). *Radar interferometry: data interpretation and error analysis*. [Online]. Available from: <https://books.google.com/books?hl=it&lr=&id=bqNkJUk4wtMC&oi=fnd&pg>

=PA4&dq=HANSEN+R.,+2001+-
+RADAR+Interferometry.+Data+Interpretation+and+Error+Analysis.+Klu
wer+Academic+Publishers,+New+York,+pp.+327.&ots=8PiqkAC_dU&sig=O8ELOxVK7S5pOHZ-y4Y_YxhVkl0.

- Harfenmeister, K., Itzerott, S., Weltzien, C. & Spengler, D. (2021). Agricultural Monitoring Using Polarimetric Decomposition Parameters of Sentinel-1 Data. *Remote Sensing*. 13 (4). p.p. 575.
- Hasanlou, M., Shah-Hosseini, R., Seydi, S.T., Karimzadeh, S. & Matsuoka, M. (2021). Earthquake Damage Region Detection by Multitemporal Coherence Map Analysis of Radar and Multispectral Imagery. *Remote Sensing*. 13 (6). p.p. 1195.
- Heiselberg, P., Sørensen, K.A., Heiselberg, H. & Andersen, O.B. (2022). SAR Ship–Iceberg Discrimination in Arctic Conditions Using Deep Learning. *Remote Sensing*. 14 (9). p.p. 2236.
- Hoffmann, J. (2007). Mapping damage during the Bam (Iran) earthquake using interferometric coherence. *International Journal of Remote Sensing*. 28 (6). p.pp. 1199–1216.
- Hua, T., Xie, H., Wang, S., Hu, Z., Chen, P. & Zhang, Q. (2011). Evaluation of the quality of a speckle pattern in the digital image correlation method by mean subset fluctuation. *Optics & Laser Technology*. 43 (1). p.pp. 9–13.
- Ji, K. & Wu, Y. (2015a). Scattering Mechanism Extraction by a Modified Cloude–Pottier Decomposition for Dual Polarization SAR. *Remote Sensing*. 7 (6). p.pp. 7447–7470.
- Ji, K. & Wu, Y. (2015b). Scattering Mechanism Extraction by a Modified Cloude–Pottier Decomposition for Dual Polarization SAR. *Remote Sensing*. 7 (6). p.pp. 7447–7470.
- Jolliffe, I.T. & Cadima, J. (2016). Principal component analysis: a review and recent developments. *Philosophical Transactions of the Royal Society A: Mathematical, Physical and Engineering Sciences*. 374 (2065). p.p. 20150202.
- Kang, M. & Baek, J. (2021). SAR Image Change Detection via Multiple-Window Processing with Structural Similarity. *Sensors*. 21 (19). p.p. 6645.

- Karimzadeh, S., Matsuoka, M., Miyajima, M., Adriano, B., Fallahi, A. & Karashi, J. (2018). Sequential SAR Coherence Method for the Monitoring of Buildings in Sarpole-Zahab, Iran. *Remote Sensing*. 10 (8). p.p. 1255.
- Kassambara, A. (2017). *Practical Guide To Principal Component Methods in R: PCA, M (CA), FAMD, MFA, HCPC, factoextra*. Sthada (ed.).
- Kellndorfer, J.M., Pierce, L.E., Dobson, M.C. & Ulaby, F.T. (1998). Toward consistent regional-to-global-scale vegetation characterization using orbital SAR systems. *IEEE Transactions on Geoscience and Remote Sensing*. 36 (5). p.pp. 1396–1411.
- Kim, J., Kim, H., Jeon, H., Jeong, S.-H., Song, J., Vadivel, S.K.P. & Kim, D. (2021). Synergistic Use of Geospatial Data for Water Body Extraction from Sentinel-1 Images for Operational Flood Monitoring across Southeast Asia Using Deep Neural Networks. *Remote Sensing*. 13 (23). p.p. 4759.
- Lacoste, H., International Workshop on Science and Applications of SAR Polarimetry and Polarimetric Interferometry (3 : 2007.01.22-26 : Frascati) & PolInSAR 2007 (3 : 2007.01.22-26 : Frascati) (2007). The Dual Polarization Entropy/Alpha Decomposition: A PALSAR Case Study. *ESASP*. [Online]. 644. p.p. 2. Available from: <https://ui.adsabs.harvard.edu/abs/2007ESASP.644E...2C/abstract>.
- Lecompte, D., Smits, A., Bossuyt, S., Sol, H., Vantomme, J., van Hemelrijck, D. & Habraken, A.M. (2006). Quality assessment of speckle patterns for digital image correlation. *Optics and Lasers in Engineering*. 44 (11). p.pp. 1132–1145.
- Lee, J., Kim, W., Im, J., Kwon, C. & Kim, S. (2021). Detection of Forest Fire Damage from Sentinel-1 SAR Data through the Synergistic Use of Principal Component Analysis and K-means Clustering. *Korean Journal of Remote Sensing*. 37 (5). p.pp. 1373–1387.
- Lee, J. sen & Pottier, E. (2017a). *Polarimetric radar imaging: From basics to applications*. CRC Press.
- Lee, J.-S. (1980). Digital Image Enhancement and Noise Filtering by Use of Local Statistics. *IEEE Transactions on Pattern Analysis and Machine Intelligence*. PAMI-2 (2). p.pp. 165–168.

- Lee, J.-S. (1981). Refined filtering of image noise using local statistics. *Computer Graphics and Image Processing*. 15 (4). p.pp. 380–389.
- Lee, J.S., Jurkevich, I., Dewaele, P., Wambacq, P. & Oosterlinck, A. (1994). Speckle filtering of synthetic aperture radar images: a review. *Remote Sensing Reviews*. 8 (4). p.pp. 313–340.
- Lee, J.-S. & Pottier, E. (2017b). *Polarimetric Radar Imaging*. J.-S. Lee & E. Pottier (eds.). CRC Press.
- Liang, S. (2017). *Comprehensive Remote Sensing*. [Online]. Available from: [https://books.google.it/books?hl=it&lr=&id=x9skDwAAQBAJ&oi=fnd&pg=PP1&dq=%09Liang,+S.+\(2017\).+Comprehensive+Remote+Sensing.+Elsevier.&ots=qSW8PsoM5f&sig=8iWaCxzeSgFhkygpggMH_shsbMA](https://books.google.it/books?hl=it&lr=&id=x9skDwAAQBAJ&oi=fnd&pg=PP1&dq=%09Liang,+S.+(2017).+Comprehensive+Remote+Sensing.+Elsevier.&ots=qSW8PsoM5f&sig=8iWaCxzeSgFhkygpggMH_shsbMA).
- Liang, X., Lin, Y. & Zhang, H. (2022). Mapping Urban Impervious Surface with an Unsupervised Approach Using Interferometric Coherence of SAR Images. *IEEE Journal of Selected Topics in Applied Earth Observations and Remote Sensing*. 15. p.pp. 2734–2744.
- Liu, J.G. & Mason, P.J. (2009). *Essential Image Processing and GIS for Remote Sensing*.
- Liu, N., Li, X., Peng, X. & Hong, W. (2022a). SAR Tomography Based on Atomic Norm Minimization in Urban Areas. *Remote Sensing*. 14 (14). p.p. 3439.
- Liu, Q., Li, Q., Yu, W. & Hong, W. (2022b). Automatic Building Detection for Multi-Aspect SAR Images Based on the Variation Features. *Remote Sensing*. 14 (6). p.p. 1409.
- Liu, Y. & Shriberg, E. (2007). Comparing Evaluation Metrics for Sentence Boundary Detection. In: 2007 IEEE International Conference on Acoustics, Speech and Signal Processing - ICASSP '07. April 2007, IEEE, pp. IV-185-IV–188.
- Long, S., Tong, A., Yuan, Y., Li, Z., Wu, W. & Zhu, C. (2018). New Approaches to Processing Ground-based SAR (GBSAR) Data for Deformation Monitoring. *Remote Sensing*. 10 (12). p.p. 1936.

- Lu, C.-H., Ni, C.-F., Chang, C.-P., Yen, J.-Y. & Chuang, R. (2018). Coherence Difference Analysis of Sentinel-1 SAR Interferogram to Identify Earthquake-Induced Disasters in Urban Areas. *Remote Sensing*. 10 (8). p.p. 1318.
- Lu, Z. & Kwoun, O. (2008). Radarsat-1 and ERS InSAR Analysis Over Southeastern Coastal Louisiana: Implications for Mapping Water-Level Changes Beneath Swamp Forests. *IEEE Transactions on Geoscience and Remote Sensing*. 46 (8). p.pp. 2167–2184.
- Lubin, A. & Saleem, A. (2019). Remote sensing-based mapping of the destruction to Aleppo during the Syrian Civil War between 2011 and 2017. *Applied Geography*. 108. p.pp. 30–38.
- Magnussen, S. & Russo, G. (2012). Uncertainty in photo-interpreted forest inventory variables and effects on estimates of error in Canada's national forest inventory. *Forestry Chronicle*. 88 (4). p.pp. 439–447.
- Mahesh, M. (2013). The Essential Physics of Medical Imaging, Third Edition. *Medical Physics*. 40 (7). p.p. 077301.
- Malmgren-Hansen, D., Sohnesen, T., Fisker, P. & Baez, J. (2020). Sentinel-1 Change Detection Analysis for Cyclone Damage Assessment in Urban Environments. *Remote Sensing*. 12 (15). p.p. 2409.
- Mansourpour, M., Blais, R., Mansourpour, M., Rajabi, M.A. & Blais, J.A.R. (2006). Effects and performance of speckle noise reduction filters on active radar and SAR images.
- Marchionni, D.S. & Cavayas, F. (2014). La teledetección por radar como fuente de información litológica y estructural: Análisis espacial de imágenes SAR de RADARSAT-1. *Geoacta*. [Online]. 39 (1). p.p. 70. Available from: http://www.scielo.org.ar/scielo.php?script=sci_arttext&pid=S1852-77442014000100007&lang=pt.
- Martone, M. (2019). *Onboard Quantization for Interferometric and Multichannel Synthetic Aperture Radar (SAR) Systems*.
- Mayer, F. (2019). *Spaceborne Synthetic Aperture Radar – Principles, Data Access, and Basic Processing Techniques.* SAR Handbook: Comprehensive Methodologies for Forest Monitoring and Biomass Estimation.

- McKechnie, T.S. (1976). Image-plane speckle in partially coherent illumination. *Optical and Quantum Electronics*. 8 (1). p.pp. 61–67.
- Meneses III, S.F. & Blanco, A.C. (2022). RAPID MAPPING AND ASSESSMENT OF DAMAGES DUE TO TYPHOON RAI USING SENTINEL-1 SYNTHETIC APERTURE RADAR DATA. *The International Archives of the Photogrammetry, Remote Sensing and Spatial Information Sciences*. XLIII-B3-2022. p.pp. 1139–1146.
- Mengen, D., Ottinger, M., Leinenkugel, P. & Ribbe, L. (2020). Modeling River Discharge Using Automated River Width Measurements Derived from Sentinel-1 Time Series. *Remote Sensing*. 12 (19). p.p. 3236.
- Migliaccio, M., Nunziata, F. & Buono, A. (2015). SAR polarimetry for sea oil slick observation. *International Journal of Remote Sensing*. 36 (12). p.pp. 3243–3273.
- Moreira, A., Prats-Iraola, P., Younis, M., Krieger, G., Hajnsek, I. & Papathanassiou, K.P. (2013a). A tutorial on synthetic aperture radar. *IEEE Geoscience and Remote Sensing Magazine*. 1 (1). p.pp. 6–43.
- Moreira, A., Prats-Iraola, P., Younis, M., Krieger, G., Hajnsek, I. & Papathanassiou, K.P. (2013b). A tutorial on synthetic aperture radar. *IEEE Geoscience and Remote Sensing Magazine*. 1 (1). p.pp. 6–43.
- Moreira, A., Prats-Iraola, P., Younis, M., Krieger, G., Hajnsek, I. & Papathanassiou, K.P. (2013c). A tutorial on synthetic aperture radar. *IEEE Geoscience and Remote Sensing Magazine*. 1 (1). p.pp. 6–43.
- Mott, H. (1992). *Antennas for Radar and Communications: A Polarimetric Approach*. Business Physics.
- Mueller, H., Groeger, A., Hersh, J., Matranga, A. & Serrat, J. (2021). Monitoring war destruction from space using machine learning. *Proceedings of the National Academy of Sciences of the United States of America*. [Online]. 118 (23). p.p. e2025400118. Available from: <https://www.pnas.org/doi/abs/10.1073/pnas.2025400118>.

- Næsset, E. (1996). Conditional tau coefficient for assessment of producer's accuracy of classified remotely sensed data. *ISPRS Journal of Photogrammetry and Remote Sensing*. 51 (2). p.pp. 91–98.
- Nasirzadehdizaji, R., Balik Sanli, F., Abdikan, S., Cakir, Z., Sekertekin, A. & Ustuner, M. (2019). Sensitivity Analysis of Multi-Temporal Sentinel-1 SAR Parameters to Crop Height and Canopy Coverage. *Applied Sciences*. 9 (4). p.p. 655.
- Natsuaki, R., Nagai, H., Tomii, N. & Tadono, T. (2018). Sensitivity and Limitation in Damage Detection for Individual Buildings Using InSAR Coherence—A Case Study in 2016 Kumamoto Earthquakes. *Remote Sensing*. 10 (2). p.p. 245.
- Navin, M.S., Agilandeswari, L. & Anjaneyulu, G.S.G.N. (2020). Dimensionality Reduction and Vegetation Monitoring On LISS III Satellite Image Using Principal Component Analysis and Normalized Difference Vegetation Index. In: *2020 International Conference on Emerging Trends in Information Technology and Engineering (ic-ETITE)*. February 2020, IEEE, pp. 1–5.
- Nielsen, A.A., Canty, M.J., Skriver, H. & Conradsen, K. (2017). Change detection in multi-temporal dual polarization Sentinel-1 data. In: *2017 IEEE International Geoscience and Remote Sensing Symposium (IGARSS)*. July 2017, IEEE, pp. 3901–3908.
- Oliver, C. & Quegan, S. (1998). *Understanding Synthetic Aperture Radar Images*. Norwood, MA, USA: Artech House.
- Ottinger, M. & Kuenzer, C. (2020). Spaceborne L-Band Synthetic Aperture Radar Data for Geoscientific Analyses in Coastal Land Applications: A Review. *Remote Sensing*. 12 (14). p.p. 2228.
- Oxoli, D., Boccardo, P., Brovelli, M.A., Molinari, M.E. & Monti Guarnieri, A. (2020). Coherent Change Detection for repeated-pass interferometric SAR images: An application to earthquake damage assessment on buildings. *INTERNATIONAL ARCHIVES OF THE PHOTOGRAMMETRY, REMOTE SENSING AND SPATIAL INFORMATION SCIENCES*. [Online]. 42 (3W4). p.pp. 383–388. Available from: <https://re.public.polimi.it/handle/11311/1052405>.

- Pan, Z., Fan, H. & Zhang, Z. (2020). Nonuniformly-Rotating Ship Refocusing in SAR Imagery Based on the Bilinear Extended Fractional Fourier Transform. *Sensors*. 20 (2). p.p. 550.
- Peduto, D. (2008). *Analysis of ground deformations related to subsidence...* - Google Scholar. [Online]. University of Salerno. Available from: https://scholar.google.com/scholar?hl=it&as_sdt=0%2C5&q=Analysis+of+ground+deformations+related+to+subsidence+and+landslide+phenomena+via+DInSAR+techniques&btnG=#d=gs_cit&t=1670350879976&u=%2Fscholar%3Fq%3Dinfo%3Ahe4sds93eoYJ%3Ascholar.google.com%2F%26output%3Dcite%26scirp%3D0%26hl%3Dit.
- Peres-Neto, P.R., Jackson, D.A. & Somers, K.M. (2005). How many principal components? stopping rules for determining the number of non-trivial axes revisited. *Computational Statistics & Data Analysis*. 49 (4). p.pp. 974–997.
- Pettorelli, N., Ryan, S., Mueller, T., Bunnefeld, N., Jedrzejewska, B., Lima, M. & Kausrud, K. (2011). The Normalized Difference Vegetation Index (NDVI): unforeseen successes in animal ecology. *Climate Research*. [Online]. 46 (1). p.pp. 15–27. Available from: <https://www.int-res.com/abstracts/cr/v46/n1/p15-27/>.
- Plank, S. (2014a). Rapid Damage Assessment by Means of Multi-Temporal SAR — A Comprehensive Review and Outlook to Sentinel-1. *Remote Sensing*. 6 (6). p.pp. 4870–4906.
- Plank, S. (2014b). Rapid Damage Assessment by Means of Multi-Temporal SAR — A Comprehensive Review and Outlook to Sentinel-1. *Remote Sensing*. 6 (6). p.pp. 4870–4906.
- Plank, S., Singer, J., Minet, C. & Thuro, K. (2012). Pre-survey suitability evaluation of the differential synthetic aperture radar interferometry method for landslide monitoring. *International Journal of Remote Sensing*. 33 (20). p.pp. 6623–6637.
- Poelman, A.J., Guy, J.R.F., Poelman, A.J. & Guy, J.R.F. (1985). Polarization information utilization in primary radar - An introduction and up-date to activities at SHAPE Technical Centre. *imei*. [Online]. p.pp. 521–572. Available from: <https://ui.adsabs.harvard.edu/abs/1985imei.rept..521P/abstract>.

- Pulvirenti, L., Chini, M. & Pierdicca, N. (2020). InSAR Multitemporal Data over Persistent Scatterers to Detect Floodwater in Urban Areas: A Case Study in Beletweyne, Somalia. *Remote Sensing*. 13 (1). p.p. 37.
- Purcell, E.M. & Morin D.J. (2013). *Electricity and Magnetism*. Cambridge University (ed.).
- Ramakrishnan, S., Demarcus, V., Ny, J.L., Patwari, N. & Gussy, J. (2002). *Synthetic Aperture Radar Imaging Using Spectral Estimation Techniques*.
- Raol, J.R. (2009). Multi-sensor data fusion with MATLAB®. *Multi-Sensor Data Fusion with MATLAB*. p.pp. 1–535.
- Refice, A., Zingaro, M., D’Addabbo, A. & Chini, M. (2020). Integrating C- and L-Band SAR Imagery for Detailed Flood Monitoring of Remote Vegetated Areas. *Water*. 12 (10). p.p. 2745.
- Richards, J. (2009). *Remote sensing with imaging radar*. [Online]. Available from: <https://link.springer.com/content/pdf/10.1007/978-3-642-02020-9.pdf>.
- Rizzo, M. & Gasparini, P. (2022). Land Use and Land Cover Photointerpretation: Fotointerpretazione dell’uso e copertura del suolo. *Springer Tracts in Civil Engineering*. [Online]. p.pp. 49–66. Available from: https://link.springer.com/chapter/10.1007/978-3-030-98678-0_3.
- Robinson, G.S. (1977). Edge detection by compass gradient masks. *Computer Graphics and Image Processing*. 6 (5). p.pp. 492–501.
- Rose, A. (1973). *Vision – Human and Electronic*. Plenum Press (ed.).
- Russ, J.C. (2010). *The Image Processing Handbook, Fifth Edition (Livre numérique Google)*. [Online]. p.p. 832. Available from: https://books.google.com/books/about/The_Image_Processing_Handbook.html?hl=it&id=Vs2AM2cWl1AC.
- Russelle, M.P., Wilhelm, W.W., Olson, R.A. & Power, J.F. (1984). Growth Analysis Based on Degree Days¹. *Crop Science*. 24 (1). p.pp. 28–32.
- Sarscape (2009). *Synthetic Aperture Radar and SARscape Guidebook*. Available from: [Accessed: 6 December 2022].

- Schmitt, A. & Brisco, B. (2013). Wetland monitoring using the curvelet-based change detection method on polarimetric SAR imagery. *Water*. [Online]. 5. p.pp. 1036–1051. Available from: <https://www.mdpi.com/2073-4441/5/3/1036>.
- Schott, J.R. (John R. (2007). *Remote sensing: the image chain approach*. p.p. 666.
- Schowengerdt, R.A. (2007). *Remote sensing: models and methods for image processing*. p.p. 515. Available from: [Accessed: 3 December 2022].
- Schroeder, D.J. (1999). *Astronomical Optics*. 2nd Ed. Academic Press (ed.).
- sentinel.copernicus.eu (2022a). *About Copernicus*. [Online]. 2022. Copernicus.eu. Available from: <https://www.copernicus.eu/en/about-copernicus>.
- sentinel.copernicus.eu (2022b). *Instrument Payload*. [Online]. 2022. ESA. Available from: <https://sentinels.copernicus.eu/web/sentinel/missions/sentinel-1/instrument-payload>.
- sentinel.copernicus.eu (2022c). *Mission Objectives*. [Online]. 2022. Available from: <https://sentinels.copernicus.eu/web/sentinel/missions/sentinel-1/mission-objectives>.
- sentinel.copernicus.eu (2022d). *Sentinel-1 Overview*. [Online]. 2022. Available from: <https://sentinel.esa.int/web/sentinel/missions/sentinel-1/overview>.
- sentinels.copernicus.eu (2022). *Data Products*. [Online]. 2022. Available from: <https://sentinels.copernicus.eu/web/sentinel/missions/sentinel-1/data-products>.
- Shokr, M. & Dabboor, M. (2020). Observations of SAR polarimetric parameters of lake and fast sea ice during the early growth phase. *Remote Sensing of Environment*. 247. p.p. 111910.
- Singh, P., Diwakar, M., Achyut Shankar, ·, Shree, · Raj & Kumar, M. (2021a). *A Review on SAR Image and its Despeckling*. [Online]. 28. p.pp. 4633–4653. Available from: <https://doi.org/10.1007/s11831-021-09548-z>.
- Singh, P., Diwakar, M., Achyut Shankar, ·, Shree, · Raj & Kumar, M. (2021b). *A Review on SAR Image and its Despeckling*. [Online]. 28. p.p. 4639. Available from: <https://doi.org/10.1007/s11831-021-09548-z>.

- Skolnik, M.I. (1980). *Introduction to radar systems*. McGraw Hill Book Co. (ed.). [Online]. New York. Available from: <https://ui.adsabs.harvard.edu/abs/1980mgh..book.....S/abstract>.
- Sletten, M.A. & Mc Laughlin, D.J. (2005). Radar Polarimetry. In: *Encyclopedia of RF and Microwave Engineering*. Hoboken, NJ, USA: John Wiley & Sons, Inc.
- Small, D. (2011). Flattening Gamma: Radiometric Terrain Correction for SAR Imagery. *IEEE Transactions on Geoscience and Remote Sensing*. 49 (8). p.pp. 3081–3093.
- Small, D., RSL-ASAR-GC-AD, A.S.-E.-E.T.N. & 2008, undefined (2008). Guide to ASAR geocoding. *geo.uzh.ch*. [Online]. Available from: http://www.geo.uzh.ch/microsite/rsl-documents/research/publications/other-sci-communications/2008_RSL-ASAR-GC-AD-v101-0335607552/2008_RSL-ASAR-GC-AD-v101.pdf.
- Stathaki, Tania. (2008). *Image fusion: algorithms and applications*. [Online]. p.p. 500. Available from: https://books.google.com/books/about/Image_Fusion.html?hl=it&id=VmvY4MTMFTwC.
- Story, M. & Congalton, R.G. (1986). Accuracy assessment: a user's perspective. *Photogrammetric Engineering and Remote Sensing*. [Online]. 52 (3). p.pp. 397–399. Available from: http://www.asprs.org/wp-content/uploads/pers/1986journal/mar/1986_mar_397-399.pdf. [Accessed: 10 February 2023].
- Stramondo, S., Bignami, C., Chini, M., Pierdicca, N. & Tertulliani, A. (2006a). Satellite radar and optical remote sensing for earthquake damage detection: results from different case studies. *International Journal of Remote Sensing*. 27 (20). p.pp. 4433–4447.
- Stramondo, S., Bignami, C., Chini, M., Pierdicca, N. & Tertulliani, A. (2006b). Satellite radar and optical remote sensing for earthquake damage detection: results from different case studies. *International Journal of Remote Sensing*. 27 (20). p.pp. 4433–4447.
- Stratton, J.A. (1941). *Electromagnetic theory*. p.p. 615.

- Suga, Y., Takeuchi, S., Oguro, Y., Chen, A.J., Ogawa, M., Konishi, T. & Yonezawa, C. (2001). Application of ERS-2/SAR data for the 1999 Taiwan earthquake. *Advances in Space Research*. 28 (1). p.pp. 155–163.
- Takeuchi, S., Suga, Y., Yonezawa, C. & Chen, A.J. (n.d.). Detection of urban disaster using InSAR. A case study for the 1999 Great Taiwan Earthquake. In: *IGARSS 2000. IEEE 2000 International Geoscience and Remote Sensing Symposium. Taking the Pulse of the Planet: The Role of Remote Sensing in Managing the Environment. Proceedings (Cat. No.00CH37120)*. IEEE, pp. 339–341.
- Takeuchi, S., Suga, Y., Yonezawa, C. & Chen, A.J. (n.d.). Detection of urban disaster using InSAR. A case study for the 1999 Great Taiwan Earthquake. In: *IGARSS 2000. IEEE 2000 International Geoscience and Remote Sensing Symposium. Taking the Pulse of the Planet: The Role of Remote Sensing in Managing the Environment. Proceedings (Cat. No.00CH37120)*. IEEE, pp. 339–341.
- Tamkuan, N. & Nagai, M. (2017). Fusion of Multi-Temporal Interferometric Coherence and Optical Image Data for the 2016 Kumamoto Earthquake Damage Assessment. *ISPRS International Journal of Geo-Information*. 6 (7). p.p. 188.
- Tarantino, E., Novelli, A., Laterza, M. & Gioia, A. (2015a). *Testing high spatial resolution WorldView-2 imagery for retrieving the leaf area index*. In: D. G. Hadjimitsis, K. Themistocleous, S. Michaelides, & G. Papadavid (eds.). 19 June 2015, p. 95351N.
- Tarantino, E., Novelli, A., Laterza, M. & Gioia, A. (2015b). *Testing high spatial resolution WorldView-2 imagery for retrieving the leaf area index*. In: D. G. Hadjimitsis, K. Themistocleous, S. Michaelides, & G. Papadavid (eds.). 19 June 2015, p. 95351N.
- Tempfli, K., Huurneman, G., Bakker, W. & Janssen, L. (2009). *Principles of remote sensing: an introductory textbook*. [Online]. Available from: <https://research.utwente.nl/en/publications/principles-of-remote-sensing-an-introductory-textbook-4>.
- The European Space Agency (2022a). *SNAP Description*. [Online]. 2022. Available from: <https://earth.esa.int/eogateway/tools/snap>.

- The European Space Agency (2022b). *The Sentinel-1 Toolbox*. [Online]. 2022. Available from: <https://sentinel.esa.int/web/sentinel/toolboxes/sentinel-1>.
- Touzi, R., Lopes, A., Bruniquel, J. & Vachon, P.W. (1999). Coherence estimation for SAR imagery. *IEEE Transactions on Geoscience and Remote Sensing*. 37 (1). p.pp. 135–149.
- Töyrä, J. & Pietroniro, A. (2005). Towards operational monitoring of a northern wetland using geomatics-based techniques. *Remote Sensing Environment*. [Online]. 97. p.pp. 174–191. Available from: https://www.sciencedirect.com/science/article/pii/S0034425705001343?casa_token=idKnwY5qAC0AAAAA:g9K8ipmjnSOH2udl82w0sTgHp4dfRaPepA9sFdG_so3ZRyoZXZB-ovy2HUsQlecRiEPkpNJO2w.
- Uddin, M., Rahman, T., Dharmalingam, M., Jaybhay, J. & Shastri, R. (2015). A STUDY OF SPECKLE NOISE REDUCTION FILTERS Related papers Effect ive Techniques for Reduct ion of Impulse, Gaussian and Speckle Noises A DENOISING FRAMEWORK USING LINEAR AND NON-LINEAR FILT ERS Comparat ive Analysis of Image Denoising Algorit hms using Reference Based Image Qualit y Measures. *An International Journal (SIPIJ) Signal & Image Processing*. 6 (3).
- Uddin, Md.P., Mamun, Md. al, Afjal, M.I. & Hossain, Md.A. (2021). Information-theoretic feature selection with segmentation-based folded principal component analysis (PCA) for hyperspectral image classification. *International Journal of Remote Sensing*. 42 (1). p.pp. 286–321.
- USGS (2022). *What is remote sensing and what is it used for?* [Online]. 2022. Available from: https://www.usgs.gov/faqs/what-remote-sensing-and-what-it-used?qt-news_science_products=0#qt-news_science_products.
- Washaya, P., Balz, T. & Mohamadi, B. (2018). Coherence Change-Detection with Sentinel-1 for Natural and Anthropogenic Disaster Monitoring in Urban Areas. *Remote Sensing*. 10 (7). p.p. 1026.
- Woodhouse, I.H. (2017a). *Introduction to Microwave Remote Sensing*. CRC Press.
- Woodhouse, I.H. (2017b). *Introduction to Microwave Remote Sensing*. CRC Press.

- Wu, S., Huang, X., Sun, J. & Wang, H. (2021). Building Monitoring Method based On Interferometric SAR Shadow. In: *2021 2nd China International SAR Symposium (CISS)*. 3 November 2021, IEEE, pp. 1–4.
- Xie, L., Zhang, H., Wang, C. & Shan, Z. (2015). Similarity analysis of entropy/alpha decomposition between HH/VV dual- and quad-polarization SAR data. *Remote Sensing Letters*. 6 (3). p.pp. 228–237.
- Yamaguchi, Y., Moriyama, T., ... M.I.-I.T. on & 2005, undefined (n.d.). Four-component scattering model for polarimetric SAR image decomposition. *ieeexplore.ieee.org*. [Online]. Available from: <https://ieeexplore.ieee.org/abstract/document/1487628/>.
- Yonezawa, C. & Takeuchi, S. (2001). Decorrelation of SAR data by urban damages caused by the 1995 Hyogoken-nanbu earthquake. *International Journal of Remote Sensing*. 22 (8). p.pp. 1585–1600.
- Yonezawa, C. & Takeuchi, S. (n.d.). Detection of urban damage using interferometric SAR decorrelation. In: *IEEE 1999 International Geoscience and Remote Sensing Symposium. IGARSS'99 (Cat. No.99CH36293)*. IEEE, pp. 925–927.
- Zhang, F., Li, Z. & Lindenschmidt, K.-E. (2019). Potential of RADARSAT-2 to Improve Ice Thickness Calculations in Remote, Poorly Accessible Areas: A Case Study on the Slave River, Canada. *Canadian Journal of Remote Sensing*. 45 (2). p.pp. 234–245.
- Zhao, W. (2019). *Multitemporal SAR images denoising and change detection: applications to Sentinel-1 data*. [Online]. Available from: <https://www.theses.fr/2019SACL003>. [Accessed: 5 December 2022].
- Zhou, X., Chang, N.-B. & Li, S. (2009). Applications of SAR Interferometry in Earth and Environmental Science Research. *Sensors*. 9 (3). p.pp. 1876–1912.
- van Zyl, J. & Kim, Yunjin. (2011). *Synthetic aperture radar polarimetry*. Wiley.

SOURCES OF WAR NEWS

- 24tv (2022). *A child died and a woman was wounded as a result of enemy shelling in Irpen*. https://24tv.ua/vnaslidok-obstrilu-irpenya-zaginula-ditina-poranili-zhinku-prokuratura_n1889013. [Online]. 3 March. Available from: https://24tv.ua/vnaslidok-obstrilu-irpenya-zaginula-ditina-poranili-zhinku-prokuratura_n1889013. [Accessed: 10 November 2022].
- ABC News (2022a). Russia orders troops to hasten their advance as Mariupol remains under heavy shelling. *ABC News*. [Online]. 26 February. Available from: <https://www.abc.net.au/news/2022-02-27/russia-commands-troops-advance-faster-kyiv-long-curfew/100865104>. [Accessed: 10 November 2022].
- ABC News (2022b). *Russian troops close on Kyiv as Ukrainian President Volodymyr Zelenskyy calls for humanitarian ceasefire to be upheld*. [Online]. 12 March. Available from: <https://www.abc.net.au/news/2022-03-13/russians-shell-kyiv-capture-outskirts-mariupol-ukraine/100906016>. [Accessed: 11 November 2022].
- ABC News. Associated Press (2022). Sorting fact, disinformation amid Russian war on Ukraine. *ABC News. Associated Press*. [Online]. 3 March. Available from: <https://abcnews.go.com/International/wireStory/sorting-fact-disinformation-amid-russian-war-ukraine-83200673>. [Accessed: 11 November 2022].
- Agence France Presse (2022). One Dead In Strike On Residential Building In Kyiv. *Barron's*. [Online]. 14 March. Available from: <https://www.barrons.com/news/at-least-two-dead-in-strike-on-residential-building-in-kyiv-01647241207?refsec=afp-news>. [Accessed: 10 November 2022].
- Andrea, R. (2022). Ukraine rescuers search Mariupol theater rubble as Russian attacks continue. *PBS Associated Press*. [Online]. 18 March. Available from: <https://www.pbs.org/newshour/world/ukraine-rescuers-search-mariupol-theater-rubble-as-russian-attacks-continue>. [Accessed: 10 November 2022].
- Ari Gross, J. (2022). Russian bombing of Kyiv damages Babi Yar Holocaust memorial site. *The Time of Israel*. [Online]. 1 March. Available from: https://www.timesofisrael.com/liveblog_entry/russian-bombing-of-kyiv-damages-babi-yar-holocaust-memorial/. [Accessed: 10 November 2022].

- Balachuk, I. (2022). Russia shells Bucha, no mercy for children. *Ukrayinska Pravda*. [Online]. 6 March. Available from: <https://www.pravda.com.ua/eng/news/2022/03/6/7328710/>. [Accessed: 10 November 2022].
- Balachuk, I. (2022a). In Kiev, a shell hit a 9-storey building and the Antonov plant, killing a man. *Ukrayinska Pravda*. [Online]. 14 March. Available from: <https://www.pravda.com.ua/rus/news/2022/03/14/7331160/>. [Accessed: 10 November 2022].
- Balachuk, I. (2022b). The enemy shelled Kiev: a burning administrative building in Podil, a drone was shot down there. *Ukrayinska Pravda*. [Online]. 12 March. Available from: <https://www.pravda.com.ua/rus/news/2022/03/12/7330632/>. [Accessed: 10 November 2022].
- BBC News (2022a). *Mass grave set up in Mariupol as morgues overflow*. [Online]. 9 March. Available from: <https://www.bbc.com/news/live/world-europe-60657155>. [Accessed: 10 November 2022].
- BBC News (2022b). *Ukraine war in maps: Tracking the Russian invasion*. [Online]. 25 March. Available from: <https://www.bbc.com/news/world-europe-60506682>. [Accessed: 10 November 2022].
- BBC News (2022c). War in Ukraine, Day 26: Missile Strike on Kiev; ammonia leakage in Sumy; 96-year-old prisoner of Buchenwald died in Kharkiv. *BBC News*. [Online]. 21 March. Available from: <https://www.bbc.com/russian/news-60823227>. [Accessed: 10 November 2022].
- BBC News (2022d). War in Ukraine, Day 26: Missile Strike on Kiev; ammonia leakage in Sumy; 96-year-old prisoner of Buchenwald died in Kharkiv. *BB News*. [Online]. 21 March. Available from: <https://www.bbc.com/russian/news-60823227>. [Accessed: 10 November 2022].
- Bondarenko, K., Watson, I. & Stapleton, A. (2022). *'Bombs falling every 10 minutes,' says Ukrainian officer in Mariupol*. [Online]. 21 March. Available from: https://edition.cnn.com/europe/live-news/ukraine-russia-putin-news-03-21-22/h_aa76393e1b16e6be6d04b0acb9fb96d4. [Accessed: 10 November 2022].

- Braithwaite, S. (2022). *Ukrainian MP: Russia has damaged Donetsk-Mariupol pipeline, leaving over 700,000 people without heat*. [Online]. 6 March. Available from: https://edition.cnn.com/europe/live-news/ukraine-russia-putin-news-03-06-22/h_0270b55168bce7fce3c9226a2874d715. [Accessed: 10 November 2022].
- Brown, M. (2022). Babi Yar, Kyiv's Holocaust memorial to victims of Nazis, damaged in Russian bombing attack. *USA Today*. [Online]. 2 March. Available from: <https://eu.usatoday.com/story/news/politics/2022/03/01/ukraine-holocaust-babi-yar/6979800001/>. [Accessed: 10 November 2022].
- Chernihiv Society (2022). *2 shells hit the SBU building in Chernihiv: a fire broke out*. [Online]. 25 February. Available from: https://24tv.ua/ru/zdanie-sbu-chernigove-popali-2-snarjada-proizoshel-pozhar_n1879042. [Accessed: 11 November 2022].
- CHERNIHIV REGIONAL MILITARY ADMINISTRATION (2022). *Another senseless attack on the center of Chernihiv*. [Online]. Available from: <https://www.cg.gov.ua/index.php?id=452585&tp=page>. [Accessed: 11 November 2022].
- Crane, E. (2022). Hundreds feared dead from 15-hour Russian attack on Mariupol, Ukraine. *New York Post*. [Online]. 2 March. Available from: <https://nypost.com/2022/03/02/hundreds-feared-dead-in-mariupol-ukraine-from-russian-shelling/>. [Accessed: 10 November 2022].
- Deutsche Welle (2022). Mariupol evacuations fail for second time. *Deutsche Welle*. [Online]. 6 March. Available from: <https://www.dw.com/en/ukraine-second-attempt-to-evacuate-civilians-from-mariupol-fails-as-it-happened/a-61030032>. [Accessed: 10 November 2022].
- Devdiscourse (2022). *Ukraine's Mariupol city says 2,187 residents killed since start of war*. [Online]. 13 March 2022. Devdiscourse. Available from: <https://www.devdiscourse.com/article/law-order/1960811-ukraines-mariupol-city-says-2187-residents-killed-since-start-of-war>. [Accessed: 10 November 2022].
- Dreier, N. (2022). *Russia attacks Ukraine: Mariupol theater used as shelter bombed*. [Online]. 17 March. Available from: <https://www.kiro7.com/news/trending/russia->

attacks-ukraine-mariupol-theater-used-shelter-bombed/FCCS554IAVBJDK6NWAU6ALSXI/. [Accessed: 10 November 2022].

FC Chernihiv (2022). *Following the Gagarin Stadium, the Rashists shelled the Chernihiv Arena*. [Online]. 10 March 2022. chesport.cn.ua. Available from: <https://www.chesport.cn.ua/2022/03/10/slidom-za-stadionom-gagarina-rashysty-obstrilyaly-chernigiv-arenu/>. [Accessed: 11 November 2022].

Gavirelov, N. (2022). Jewish groups condemn strike near Babyn Yar Holocaust Memorial. *The New York Times*. [Online]. 2 March. Available from: <https://www.nytimes.com/2022/03/01/world/europe/kyiv-babyn-yar-holocaust-memorial.html>. [Accessed: 10 November 2022].

Gerashchenko, P. (2022). *In Podil in Kiev, shot down a 'kamikaze drone' filled with explosives: a photo was published*. [Online]. 12 March. Available from: <https://tsn.ua/ru/ato/gumanitarnye-koridory-dlya-zhiteley-naibolee-postradavshih-ot-voyny-regionov-vereschuk-rasskazala-o-mashrutah-2006713.html>. [Accessed: 10 November 2022].

Government of Ukraine. (2022). Russian invasion update: Russian troops fire on Chernihiv city center, damaging dentistry and houses. *Ukrinform*. [Online]. 27 February. Available from: <https://www.ukrinform.net/rubric-ato/3414897-russian-invasion-update-russian-troops-fire-on-chernihiv-city-center-damaging-dentistry-and-houses.html>. [Accessed: 11 November 2022].

Gunter, J. (2022a). Siege of Mariupol: Fresh Russian attacks throw evacuation into chaos. *BBC News*. [Online]. 5 March. Available from: <https://www.bbc.com/news/world-europe-60629851>. [Accessed: 10 November 2022].

Gunter, J. (2022b). Mariupol under siege: 'We are being completely cut off' Published 3 March. *BBC News*. [Online]. 3 March. Available from: <https://www.bbc.com/news/world-europe-60601235>. [Accessed: 10 November 2022].

Gunter, J. (2022c). *Ukrainian city of Mariupol 'near to humanitarian catastrophe' after bombardment*. [Online]. 2 March. Available from: <https://www.bbc.com/news/world-europe-60585603>. [Accessed: 10 November 2022].

- Harding, L. (2022a). 'Pure genocide': civilian targets in Mariupol 'annihilated' by Russian attacks. *The Guardian*. [Online]. 9 March. Available from: <https://www.theguardian.com/world/2022/mar/09/pure-genocide-civilian-targets-in-mariupol-annihilated-by-russian-attacks>. [Accessed: 10 November 2022].
- Harding, L. (2022b). Ukraine says Russia targeting civilians as missiles hit Kyiv TV tower. *The Guardian*. [Online]. 1 March. Available from: <https://www.theguardian.com/world/2022/mar/01/ukraine-russia-civilians-missiles-kyiv-tv-tower>. [Accessed: 10 November 2022].
- Horbach, N. (2022). The column of the invaders is blocked: the Armed Forces blew up the bridge between Bucha and Irpen (VIDEO). *Depo Kyviv*. [Online]. 27 February. Available from: <https://kyiv.depo.ua/ukr/kyiv/kolona-okupantiv-zablokovana-zsu-pidirvali-mist-mizh-bucheyu-ta-irpenem-video-202202271429488>. [Accessed: 10 November 2022].
- Interfax Ukraine (2022). Fiberglass institute blown up in Bucha, chemical fumes go up in sky – Irpin ex-mayor Karpliuk. *Interfax Ukraine*. [Online]. 8 March. Available from: <https://en.interfax.com.ua/news/general/809602.html>. [Accessed: 10 November 2022].
- Interfax Ukraine news agency (2022). *Russian army uses Grad missile launchers hitting hospitals, kindergartens, residential buildings in Chernihiv – State Emergency Service*. [Online]. Available from: <https://en.interfax.com.ua/news/general/802783.html>. [Accessed: 10 November 2022].
- Kesaieva, Y. & Carey, A. (2022). *Russian forces bomb school sheltering 400 people in Mariupol, city council says*. [Online]. 20 March. Available from: https://edition.cnn.com/europe/live-news/ukraine-russia-putin-news-03-20-22/h_b1c1cd7201927da836d75f3e95f324f9. [Accessed: 10 November 2022].
- Khudaykulov, A., Khudaykulova, M. & Yuanqiong, H. (2022). International Journal of Management Science and Business Administration View project inorganic chemistry View project Economic Consequences and Implications of the Ukraine-Russia War. *International Journal of Management Science and Business Administration*. [Online]. 8 (4). p.pp. 44–52. Available from:

<https://doi.org/10.18775/ijmsba.1849-5664-5419.2014.84.1005>. [Accessed: 20 December 2022].

Kurpita, T. (2022). *Russian aviation bombed Chernihiv: a dormitory was damaged, one person was killed*. [Online]. 13 March. Available from: <https://tsn.ua/ato/rosiyska-aviaciya-bombila-chernigiv-poshkodzheno-gurtozhitok-odin-zagibliy-2007667.html>. [Accessed: 11 November 2022].

Kyiv School of Economics (2022). *The total amount of damage caused to Bucha city in the Kyiv region due to the war is estimated at \$191,3 mln*. [Online]. Available from: <https://kse.ua/about-the-school/news/the-total-amount-of-damage-caused-to-bucha-city-in-the-kyiv-region-due-to-the-war-is-estimated-at-191-3-mln/>. [Accessed: 10 November 2022].

Liam, J. (2022). Ukraine-Russia war: Explosion rocks Kyiv near train station where thousands are being evacuated. *The Independent*. [Online]. 2 March. Available from: <https://www.independent.co.uk/news/world/europe/ukraine-kyiv-train-station-explosion-b2027252.html>. [Accessed: 10 November 2022].

Lysyckina, L. (2022). Bucha is Bucha. How the Russian occupiers entered into battle with the monument to the Afghans. *Big Kyviv*. [Online]. 27 February. Available from: <https://bigkyiv.com.ua/bucha-ye-bucha-yak-rosijski-okupanty-vstupyly-v-bij-z-pamyatnykom-afgancyam/?exp=1668077142799>. [Accessed: 10 November 2022].

Mackenzie, J. (2022). At least eight killed as Kyiv shopping centre wrecked by shelling. *Reuters*. [Online]. 21 March. Available from: <https://www.reuters.com/world/europe/kyivs-mayor-says-shelling-kills-least-one-podil-district-2022-03-20/>. [Accessed: 10 November 2022].

Magnussen, S. & Russo, G. (2012). Uncertainty in photo-interpreted forest inventory variables and effects on estimates of error in Canada's national forest inventory. *Forestry Chronicle*. 88 (4). p.pp. 439–447. Available from: [Accessed: 19 December 2022].

Maloletka, E. (2022a). Ukrainians evacuate Kyiv suburbs amid deepening crisis. *Associated Press*. [Online]. 10 March. Available from: <https://apnews.com/article/russia-ukraine-kyiv-europe-2bed71c00916d44ea951c5809b446db3>. [Accessed: 10 November 2022].

- Maloletka, E. (2022b). Airstrike hits Ukraine maternity hospital, 17 reported hurt. *AP News*. [Online]. 10 March. Available from: <https://apnews.com/article/russia-ukraine-kyiv-europe-2bed71c00916d44ea951c5809b446db3>. [Accessed: 10 November 2022].
- Marsi, F. (2022). *Anguished Ukrainians await news of relatives in besieged Mariupol*. [Online]. 9 March 2022. www.aljazeera.com. Available from: <https://www.aljazeera.com/news/2022/3/9/anguished-ukrainians-await-news-of-relatives-in-besieged-mariupol>. [Accessed: 10 November 2022].
- Meduza (2022). 'Putin destroyed evidence of Nazi crimes' Meduza talks to historian Gregory Aimaro-Parmut about the destruction of Chernihiv's SBU archive. *Meduza*. [Online]. 28 March. Available from: <https://meduza.io/en/feature/2022/04/07/putin-destroyed-evidence-of-nazi-crimes>. [Accessed: 11 November 2022].
- Myronchuk, R. (2022). Russia drops bombs intended for fortifications on houses in Chernihiv. *RBC-Ukraine*. [Online]. 6 March. Available from: <https://www.rbc.ua/ukr/news/azerbaydzhanskie-aviakompanii-otkazalis-letat-1646534934.html>. [Accessed: 11 November 2022].
- National Post (2022a). Kyiv mayor says one killed, two wounded in carpark shelling. *National post*. [Online]. 23 March. Available from: <https://nationalpost.com/pmnl/news-pmn/kyiv-mayor-says-one-killed-two-wounded-in-carpark-shelling>. [Accessed: 10 November 2022].
- National Post (2022b). Mariupol says children's hospital destroyed by Russian bombing. *National Post*. [Online]. 9 March. Available from: <https://nationalpost.com/pmnl/news-pmn/mariupol-says-childrens-hospital-destroyed-by-russian-bombing>. [Accessed: 10 November 2022].
- Novynarnia (2022). Mariupol is under a flurry of Russian jet artillery, non-stop shelling. VIDEO. *Novynarnia*. [Online]. 1 March. Available from: <https://novynarnia.com/2022/03/01/mariupol-pid-shkvalom/>. [Accessed: 10 November 2022].
- O'Grady, S., Stern, D.L., Dixon, R., Harlan, C., Cheng, A., Lamothe, D., Iati, M., Beachum, L., Kornfield, M., Paul, M.L. & Francis, E. (26AD). Blasts heard in Kyiv as Russian forces close in. *The Washington Post*. [Online]. 26 February. Available

from: <https://www.washingtonpost.com/world/2022/02/25/ukraine-invasion-russia-news/#link-TAIGHCFPGRBUVBQRFBISDQJSL4>. [Accessed: 9 November 2022].

Petrenko, R. (2022). A rocket was shot down over Kiev, its wreckage hit the house, a person was killed. *Ukrayinska Pravda*. [Online]. 14 March. Available from: <https://www.pravda.com.ua/rus/news/2022/03/14/7331216/>. [Accessed: 10 November 2022].

Polishchuk, V. (2022). In Kiev, a drone was shot down in Podil: the building of Oschadbank caught fire from the explosion. *RBK-Ukraine*. [Online]. 12 March. Available from: <https://www.rbc.ua/rus/news/kieve-podole-sbili-besipilotnik-vzryva-zagorelos-1647069560.html>. [Accessed: 10 November 2022].

Polityuk, P., Prentice, A. & Chopra, T. (2022). At least 22 killed in air strikes in Ukraine's Chernihiv region, say emergency services. *Reuters*. [Online]. 3 March. Available from: <https://www.reuters.com/world/europe/least-22-killed-air-strikes-ukraines-chernihiv-region-say-emergency-services-2022-03-03/>. [Accessed: 11 November 2022].

Romanenko, V. (2022). A Russian fighter jet was shot down during an air raid on Chernihiv. *Ukrayinska Pravda*. [Online]. 13 March. Available from: <https://www.pravda.com.ua/news/2022/03/13/7331049/>. [Accessed: 11 November 2022].

Roshchina, O. (2022). Chernihiv Polytechnic destroyed by an airstrike, Nizhyn shelled by Uragan MLRSs. *Ukrayinska Pravda*. [Online]. 14 March. Available from: <https://www.pravda.com.ua/eng/news/2022/03/14/7331185/>. [Accessed: 11 November 2022].

Sagal, A., Vogt, A., Regan, H., Renton, A., Yeung, J., Picheta, R., Upright, E., Macaya, M. & Wagner, M. (2022). *A maternity clinic near Kyiv hit by a missile, clinic chief says*. [Online]. 2 March. Available from: https://edition.cnn.com/europe/live-news/ukraine-russia-putin-news-03-01-22/h_76604390f2fb2983f6b3141ce0627a92. [Accessed: 10 November 2022].

Sangal, A., Vogt, A., Wagner, M., Macaya, M., Hollingsworth, J., Yeung, J., Renton, A., Ravindran, J. & Kurtz, J. (2022). *March 11, 2022 Russia-Ukraine news*. [Online]. 12 March. Available from: <https://edition.cnn.com/europe/live-news/ukraine->

russia-putin-news-03-11-22/h_3a9fc0898b3fc040b2c8b216ef1fe6ea.
[Accessed: 11 November 2022].

Santora, M. (2022). Ukraine Live Updates: Russian Forces Encircle Some Cities as Diplomacy Falter. *The New York Times*. [Online]. 11 March. Available from: <https://www.nytimes.com/live/2022/03/10/world/ukraine-russia-war?smid=tw-nytimesworld&smtyp=cur#chernihiv-russia-troops>. [Accessed: 11 November 2022].

Singh, N. (2022). Kyiv's Antonov aircraft plant shelled by Russian forces, city says. *The Independent*. [Online]. 14 March. Available from: <https://www.independent.co.uk/news/world/europe/kyiv-antonov-aircraft-plant-russia-b2035108.html>. [Accessed: 10 November 2022].

Skotnikova, O. (2022). An explosion occurred in Kyiv in Troyeshchyna. *Вечірній Київ*. [Online]. 27 February. Available from: <https://vechirniy.kyiv.ua/news/61909/>. [Accessed: 9 November 2022].

SKY News (2022). *Russia's invasion of Ukraine mapped - what happened on day eight*. [Online]. 4 March. Available from: <https://news.sky.com/story/russias-invasion-of-ukraine-mapped-what-happened-on-day-eight-12556318>. [Accessed: 11 November 2022].

Spektor, A. (2022). *US father watches as premature twin boys born in Kyiv: incredibly worried and incredibly hopeful*. [Online]. 2 March. Available from: https://edition.cnn.com/europe/live-news/ukraine-russia-putin-news-03-01-22/h_705bae0177721092ab81d874b708c2dc. [Accessed: 10 November 2022].

TCH Ukraine (2022). *Russian occupiers shelled Irpin with rockets: details*. [Online]. 2 March. Available from: <https://tsn.ua/ukrayina/rosiyski-okupanti-raketami-obstrilyali-irpin-podrobici-1994761.html>. [Accessed: 10 November 2022].

The Associated Press (2022a). AP PHOTOS: Day 28: As bombs fall over Kyiv, some seek solace. *The Associated Press*. [Online]. 23 March. Available from: <https://apnews.com/article/russia-ukraine-kyiv-europe-2e00ce0127d4cb748a0e5845ae47edec>. [Accessed: 10 November 2022].

The Associated Press (2022b). *Russian forces target major cities, take out important infrastructure*. [Online]. 1 March. Available from:

<https://www.cbc.ca/news/world/ukraine-russia-invasion-mar1-2022-1.6368172>. [Accessed: 10 November 2022].

The Associated Press (2022c). Russia-Ukraine War: What to know as Russians advance on Kyiv. *Associated Press*. [Online]. 1 March. Available from: <https://web.archive.org/web/20220301030118/https://apnews.com/article/russia-a-ukraine-war-what-to-know-1c7a5fc5e9cf84134592c855c363e791>. [Accessed: 10 November 2022].

The Free Press Journal (2022). Russia – Ukraine War: Kyiv burns as Russian bombardment damages metro station, residential areas. *The Free Press Journal*. [Online]. 15 March. Available from: <https://www.freepressjournal.in/world/russia-ukraine-war-kyiv-burns-as-russian-bombardment-damages-metro-station-residential-areas>. [Accessed: 10 November 2022].

Tiefenthaler, A., Willis, H. & Cardia, A. (2022). Videos show Russian losses on outskirts of Kyiv. *The New York Times*. [Online]. 27 February. Available from: https://en.wikipedia.org/wiki/Battle_of_Bucha#cite_note-24. [Accessed: 10 November 2022].

Trevithick, J. (2022). Strategic Ukrainian Port Of Mariupol Now Surrounded By Russian Forces. *The Drive*. [Online]. 28 February. Available from: <https://www.thedrive.com/the-war-zone/44475/putin-orders-russias-strategic-deterrence-forces-on-alert>. [Accessed: 10 November 2022].

Trofimov, Y. & Marson, J. (2022). Russia Batters Ukraine's No. 2 City Kharkiv, as Kyiv Offensive Stalls. *The Wall Street Journal*. [Online]. 2 March. Available from: <https://www.wsj.com/articles/russia-resumes-kharkiv-bombardment-in-bid-to-break-ukrainian-resistance-11646208607>. [Accessed: 10 November 2022].

Tyschenko, K. (2022). Advisor to the President of Ukraine: Russian invaders broke through into Bucha, Irpin, and Hostomil, their advance was stopped. *Ukrayinska Pravda*. [Online]. 27 February. Available from: <https://www.pravda.com.ua/eng/news/2022/02/27/7326440/>. [Accessed: 10 November 2022].

Ukrayinska Pravda (2022). *Azov Regiment Commander Denys Prokopenko hands over his command*. [Online]. 15 September 2022. yahoo!news. Available from: <https://news.yahoo.com/azov-regiment-commander-denys-prokopenko->

193657362.html?guccounter=1&guce_referrer=aHR0cHM6Ly9lbi53aWtpcGVkaWEub3JnLw&guce_referrer_sig=AQAAAIKJ-LV8src-TfJRt3pXwagzNvy0xWpB9kCTbVb4iyKu3_OjnNfcNVdfOc5FjalW5xKYg8sQeyuqx dWjoqxRVyc3wnj8yEg9EiiyOt3WUHtXQfuql80X5FVLO4DzlgAhcbeoJFW1Et-Q0UI4cCl1Det1crPGaDqBweSVRgZ73YL8. [Accessed: 10 November 2022].

Ukrinform (2022). *Enemies dropped cluster bombs on a village in Chernihiv Oblast*. [Online]. Available from: <https://www.ukrinform.ua/rubic-ato/3415991-vorogiskinuli-kasetni-bombi-na-selo-na-cernigivsini.html>. [Accessed: 11 November 2022].

ukrinform.net (2022). Results in talks on humanitarian corridors for Mariupol not yet achieved – adviser to interior minister. *ukrinform.net*. [Online]. 4 March. Available from: <https://www.ukrinform.net/rubic-ato/3420367-results-in-talks-on-humanitarian-corridors-for-mariupol-not-yet-achieved-adviser-to-interior-minister.html>. [Accessed: 10 November 2022].

ukrinform.net (2022). Russian invasion update: Mariupol remains Ukrainian controlled, Russian invaders shell urban quarters and villages. *ukrinform.net*. [Online]. 28 February. Available from: <https://www.ukrinform.net/rubic-ato/3415622-russian-invasion-update-mariupol-remains-ukrainian-controlled-russian-invaders-shell-urban-quarters-and-villages.html>. [Accessed: 10 November 2022].

UN News (2022). Ukraine Crisis: Protecting civilians ‘Priority Number One’; Guterres releases \$20M for humanitarian support. *UN News*. [Online]. 24 February. Available from: <https://web.archive.org/web/20220301084123/https://news.un.org/en/story/2022/02/1112662>. [Accessed: 10 November 2022].

UNESCO (2022). *Damages and Victims*. [Online]. Available from: <https://www.unesco.org/en/ukraine-war/damages-and-victims>. [Accessed: 20 December 2022].

United Nations. Regional Information Centre for Western Europe (2022). *The UN and the war in Ukraine: key information*. [Online]. Available from: <https://unric.org/en/the-un-and-the-war-in-ukraine-key-information/#:~:text=According%20to%20the%20office%20of,%E2%80%9Cpotential%20danger%20of%20death%E2%80%9C>. [Accessed: 20 December 2022].

- UN News (2022). Ukraine Crisis: Protecting civilians 'Priority Number One'; Guterres releases \$20M for humanitarian support. *UN News*. [Online]. 24 February. Available from: <https://web.archive.org/web/20220301084123/https://news.un.org/en/story/2022/02/1112662>. [Accessed: 10 November 2022].
- Vasovic, A. (2022a). Port city of Mariupol comes under fire after Russia invades Ukraine. *Reuters*. [Online]. 24 February. Available from: <https://www.reuters.com/world/europe/strategic-city-mariupol-wakes-blasts-russia-invades-ukraine-2022-02-24/>. [Accessed: 10 November 2022].
- Vasovic, A. (2022b). More explosions heard in Kyiv in sign assault is intensifying. *National Post*. [Online]. 4 March. Available from: <https://nationalpost.com/pmnn/news-pmn/more-explosions-heard-in-kyiv-in-sign-assault-is-intensifying>. [Accessed: 10 November 2022].
- Yeung, J., Hollingsworth, J., Renton, A., Berlinger, J., Noor Haq, S., Healy Blathnaid, Vogt, A., Wagner, M. & Macaya, M. (2022). *Videos show large explosion in western outskirts of Kyiv*. [Online]. 4 March. Available from: https://edition.cnn.com/europe/live-news/ukraine-russia-putin-news-03-04-22/h_be0bd075c61b6c910435929ee239b892. [Accessed: 10 November 2022].
- Yurichenko, N. (2022). In Kiev, occupants shot the plant 'Antonov'. *RBK-Ukraine*. [Online]. 14 March. Available from: <https://www.rbc.ua/rus/news/kieve-okkupanty-obstrelyali-zavod-antonov-1647239216.html>. [Accessed: 10 November 2022].
- Zaks, D. & Clark, D. (2022). Ukraine accuses Russia of attacking humanitarian corridors as civilians flee cities. *The Times of Israel*. [Online]. 8 March. Available from: <https://www.timesofisrael.com/ukraine-accuses-russia-of-attacking-humanitarian-corridors-as-civilians-flee-cities/>. [Accessed: 10 November 2022].
- Zinets, N., Prentice, A. & Lawson, H. (2022). Ukraine's Mariupol says city's last reserves of food and water are running out. *Reuters*. [Online]. 13 March. Available from: <https://www.reuters.com/world/europe/ukraines-mariupol-says-citys-last-reserves-food-water-are-running-out-2022-03-13/>. [Accessed: 10 November 2022].

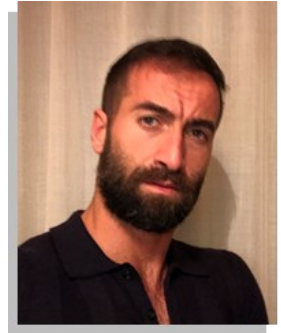
CURRICULUM

COGNOME: Caporusso

NOME: Giacomo

LUOGO E DATA DI NASCITA: BARLETTA: 18/07/1982

Mail: giacomo.caporusso@poliba.it cel: +39 320 8897141



ESPERIENZE LAVORATIVE:

- dal 01/09/2013 ad oggi: Docente di ruolo di scuola superiore Classe A037 - Scienze e tecnologie delle costruzioni, tecnologie e tecniche di rappresentazione grafica – (ruolo ottenuto tramite superamento di concorso pubblico per esami e titoli relativo bandito ai sensi del D.D.G. n. 82 del 24/09/2012) in posizione di congedo per assegno di ricerca presso in CNR IREA di Bari;
- Dicembre 2020: docente di Topografia del corso di preparazione all'esame di abilitazione per la professione di Geometra presso il Collegio dei Geometri e Geometri Laureati della Provincia BT;
- Dicembre 2019: docente di Topografia del corso di preparazione all'esame di abilitazione per la professione di Geometra presso il Collegio dei Geometri e Geometri Laureati della Provincia BT;
- Dicembre 2018: docente di Topografia del corso di preparazione all'esame di abilitazione per la professione di Geometra presso il Collegio dei Geometri e Geometri Laureati della Provincia BT;
- A.A. 2018/2019 Docente a Contratto presso il Politecnico di Bari della disciplina di Trattamento delle Osservazioni Topografiche ICAR/06 6CFU Cds L7;
- 05/05/2013 – 31/08/2013 software tester presso la MERMEC Group di Monopoli.

FORMAZIONE:

- DOTTORATO DI RICERCA IN CORSO:
- Dal 01/11/2019 ad oggi: Dottorando presso il Politecnico di Bari in Rischio e Sviluppo Ambientale, Territoriale ed Edilizio, XXXV Ciclo, matricola 580018, tutor Prof.ssa Eufemia Tarantino. Tema di ricerca: “Il SAR come strumento di analisi dei disastri dell’Ambiente e del Territorio”. Conclusione del corso prevista per il 31/01/2023.
- ABILITAZIONE NELLA CLASSE DI CONCORSO DI A072 PER SCUOLA SUPERIORE - Topografia Generale, Costruzioni Rurali e Disegno (confluita nella classe A-37 – Scienze e Tecnologie delle Costruzioni, Tecnologie e Tecniche di Rappresentazione Grafica) conseguita in seguito alla partecipazione al TFA indetto con del D.M. prot.n. 487 del 20 giugno 2014. nella provincia/regione Bari, presso il Politecnico di Bari in data 13/07/2015, con punti 99/100.
- ABILITAZIONE ALL’ESERCIZIO DELLA PROFESSIONE DI INGEGNERE CIVILE presso il Politecnico di Bari in data 12/04/2011 con la votazione di 221/240.
- DIPLOMA DI LAUREA SPECIALISTICA IN INGEGNERIA CIVILE conseguito presso il Politecnico di Bari in data 22/04/2010 con punti 110/110 e lode.
- DIPLOMA DI LAUREA TRIENNALE IN INGEGNERIA CIVILE conseguito presso il Politecnico di Bari in data 07/11/2006 con punti 110/110 e lode.
- DIPLOMA DI SCUOLA SUPERIORE DI GEOMETRA conseguito l’11/07/2001 presso l’ITG Nervi di Barletta e di aver riportato la seguente votazione totale 100/100.

CERTIFICAZIONI LINGUISTICHE:

certificazione di lingua inglese livello B2 conseguita il 20/11/2014 presso il Trinity College London.

CERTIFICAZIONI INFORMATICHE:

- ICDL Essentials IT 2461137 31/08/2020
- ICDL Certificato ECDL Base IT 2461137 31/08/2020
- ICDL Certificato ECDL Standard IT 2461137 31/08/2020

- ICDL Certificato ECDL Full Standard IT 2461137 31/08/2020
- ICDL Certificato IT Security IT 2461137 31/08/2020

PUBBLICAZIONI SCIENTIFICHE:

1. Caporusso, G., Gallo, C., & Tarantino, E. (2022). Change Detection Analysis Using Sentinel-1 Satellite Data with SNAP and GEE Regarding Oil Spill in Venezuela. In International Conference on Computational Science and Its Applications (pp. 387-404). Springer, Cham.
2. Caporusso, G., Dell'Olio, M., & Tarantino, E. (2022). Use of the Sentinel-1 Satellite Data in the SNAP Platform and the WebGNOME Simulation Model for Change Detection Analyses on the Persian Gulf Oil Spill. In International Conference on Computational Science and Its Applications (pp. 369-386). Springer, Cham.
3. Capolupo, A., Monterisi, C., Sonnessa, A., Caporusso, G., & Tarantino, E. (2021, September). Modeling land cover impact on albedo changes in Google Earth Engine environment. In International Conference on Computational Science and Its Applications (pp. 89-101). Springer, Cham.
4. Saponaro, M., Capolupo, A., Caporusso, G., & Tarantino, E. (2021). Influence of Co-Alignment Procedures on the Co-Registration Accuracy of Multi-Epoch SFM Points Clouds. The International Archives of Photogrammetry, Remote Sensing and Spatial Information Sciences, 43, 231-238.
5. Rząsa, K., Caporusso, G., Ogryzek, M. P., & Tarantino, E. (2021). Spatial planning systems in Poland and Italy-comparative analysis on the example of Olsztyn and Bari. Acta Scientiarum Polonorum Administratio Locorum, 20(2).
6. Capolupo, A., Monterisi, C., Caporusso, G., & Tarantino, E. (2020, July). Extracting Land Cover Data Using GEE: A Review of the Classification Indices. In International Conference on Computational Science and Its Applications (pp. 782-796). Springer, Cham.
7. Saponaro, M., Capolupo, A., Caporusso, G., Reina, A., Fratino, U., & Tarantino, E. (2020) Exploring UAV and cloud platform potentialities for

detecting geomorphological changes in coastal environment. In XV Protection and Restoration of the Environment Conference

8. Saponaro, M., Capolupo, A., Caporusso, G., Borgogno Mondino, E., & Tarantino, E. (2020). Predicting the Accuracy of Photogrammetric 3d Reconstruction from Camera Calibration Parameters Through a Multivariate Statistical Approach. In XXIV ISPRS Congress (Vol. 43, pp. 479-486). ISPRS.
9. Giacomo, C., Ettore, L., Rino, L., Rosa, L., Rocchina, G., Girolamo, D. M., & Patrizia, S. (2020, September). The hyperspectral prisma mission in operations. In IGARSS 2020-2020 IEEE International Geoscience and Remote Sensing Symposium (pp. 3282-3285). IEEE.